Titre: Title:	Characterization of High Power Impulse Magnetron Sputtering Discharges
Auteur: Author:	Matej Hala
Date:	2011
Type:	Mémoire ou thèse / Dissertation or Thesis
Référence: Citation:	Hala, M. (2011). Characterization of High Power Impulse Magnetron Sputtering Discharges [Thèse de doctorat, École Polytechnique de Montréal]. PolyPublie. https://publications.polymtl.ca/742/

UNIVERSITÉ DE MONTRÉAL

CHARACTERIZATION OF HIGH POWER IMPULSE MAGNETRON SPUTTERING DISCHARGES

MATEJ HALA
DÉPARTEMENT DE GÉNIE PHYSIQUE
ÉCOLE POLYTECHNIQUE DE MONTRÉAL

THÈSE PRÉSENTÉE EN VUE DE L'OBTENTION
DU DIPLÔME DE PHILOSOPHIÆ DOCTOR
DÉCEMBRE 2011

UNIVERSITÉ DE MONTRÉAL

ÉCOLE POLYTECHNIQUE DE MONTRÉAL

Cette thèse intitulée :

CHARACTERIZATION OF HIGH POWER IMPULSE MAGNETRON SPUTTERING DISCHARGES

présentée par : HALA, Matej
en vue de l'obtention du diplôme de : Philosophiæ Doctor
a été dûment acceptée par le jury d'examen constitué de :

M. WERTHEIMER, Michael R., D. Sc. A., président
M. MARTINU, Ludvik, Ph.D., membre et directeur de recherche
Mme. SAPIEHA, Jolanta Ewa, Ph.D., membre et codirectrice de recherche
M. STAFFORD, Luc, Ph.D., membre
M. HELMERSSON, Ulf, Ph.D., membre

To my mother.

Věnováno mamince.

ACKNOWLEDGEMENTS

I wish to thank my supervisors Jolanta Sapieha and Ludvik Martinu for giving me the opportunity to work on an exciting research project, and for their patient guidance and support throughout my studies at École Polytechnique. I have learned a lot from you, both on professional and personal levels.

Equally, I wish to thank Oleg Zabeida who was my plasma teacher, advisor as well as a good friend. I admire your critical mind, positive attitude and patience to help everyone who seeks for your advice. Without your assistance, I would never make it.

I would furthermore like to thank Prof. Michael Wertheimer, Prof. Ulf Helmersson and Prof. Luc Stafford for their kind acceptance to read my thesis and to be my jury members.

I would like to acknowledge my co-workers who have substantially contributed to the progress in my work, specifically Nicolas Viau and Jiří Čapek. Thank you for your great help, inspiring discussions and friendship.

Many thanks go to my colleagues and all the technicians in the Functional Coating and Surface Engineering Laboratory. I have been truly fortunate to have the chance to work with so many talented, great people! In particular, I wish to express my gratitude to the following friends, whose support (and patience with me) was invaluable to me: Bill Baloukas, Etienne Bousser, Jean-Michel Lamarre and Richard Vernhes. Thank you for being there whenever I needed your help.

Last but not least, I am very grateful towards my mom and Manal who have shared with me the ups and downs of these years. Thank you for your love, care and encouragement.

ABSTRACT

Recent development in the field of physical vapor deposition has shown a great interest in processes that provide high level ionization of the sputtered material, enabling thus the fabrication of dense coatings exhibiting superior material and functional characteristics. This is particularly the case of high power pulsed magnetron sputtering (HiPIMS), recently introduced to both academia and industry, that combines magnetron sputtering and pulsed power technology. The high power dissipated on the target during each HiPIMS pulse leads to the generation of high-density plasma and to a significant ionization of the sputtered target material. Hence, the HiPIMS plasma can be rich in metal ions which, in turn, contribute to target self-sputtering.

Despite great advances in the understanding as well as in the application of this novel deposition technique, there remain numerous open questions related to the complex dynamics of the pulsed HiPIMS discharges, particularly if operated in the reactive gas mixtures employed in the preparation of functional protective and optical films. For instance, there is still little information available about the propagation of the metal-rich plasma in between the target and the substrate during individual HiPIMS pulses, an important criterion for facilitating the optimization of the deposition conditions. Furthermore, there exists a variety of commercial HiPIMS power supplies exhibiting very different pulse shape-, voltage- and current characteristics. However, a rigorous analysis of the respective discharges – that could identify their particular benefits and drawbacks with respect to the deposition process – is missing.

This work addresses the issues and needs defined above. First, we perform an in-depth investigation of the gas-phase processes during the HiPIMS pulses operated above a Cr target in Ar, O_2, N_2 and in N_2/Ar mixtures, mostly using optical emission emanating from different plasma-excited species. Afterwards, we focus on the critical assessment of the two principal types of high power pulsed discharges generated by the commercially available power supplies: (i) a shorter (200 μs) square voltage pulse generator permitting higher cathode voltage values (denoted here as HiPIMS), and (ii) a modulated pulse power generator with longer (800 − 3000 μs) custom-shaped pulses (MPPMS). We investigate these two discharges applied to a

Nb target in the various non-reactive conditions, as well as in the reactive O_2/Ar mixtures, and compare them with the standard DC magnetron sputtering (DCMS). In addition, the discharge monitoring by electrical and optical methods is complemented by the analysis of the characteristics of the prepared Nb and NbO_x films. The following paragraphs summarize the main results, presented in the form of five articles at the core of this thesis.

Paper I: In the first paper, we present a new approach in the characterization of the HiPIMS discharge evolution – time- and species-resolved plasma imaging – employing a set of band-pass optical interference filters suitable for the isolation of the emission originating from different species populating the plasma. We demonstrate that the introduction of such filters can be used to distinguish different phases of the discharge, and to visualize numerous plasma effects including background gas excitations during the discharge ignition, gas shock waves, and expansion of metal-rich plasmas. In particular, the application of this technique is shown on the diagnostics of the 200 μs long non-reactive HiPIMS discharges using a Cr target.

Paper II: In order to gain further information about the dynamics of reactive HiPIMS discharges, both fast plasma imaging and time- and space-resolved optical emission spectroscopy (OES) are used for a systematic investigation of the 200 μs long HiPIMS pulses operated in Ar, N_2 and N_2/Ar mixtures and at various pressures. It is observed that the dense metal plasma created next to the target propagates in the reactor at a speed ranging from 0.7 to 3.5 $\mathrm{km\,s^{-1}}$, depending on the working gas composition and the pressure. In fact, it increases with higher N_2 concentration and with lower pressure. The visible form of the propagating plasma wave changes from a hemispherical shape in Ar to a drop-like shape extending far from the target with increasing N_2 concentration, owing to the significant emission from molecular N_2. Interestingly, the evidence of the target self-sputtering is found for all investigated conditions, including pure N_2 atmosphere.

Paper III: Here, we report on the time- and species-resolved plasma imaging analysis of the dynamics of the 200 μs long HiPIMS discharges above a Cr target ignited in pure O_2. It is shown that the discharge emission is dominated solely by neutral and ionized oxygen, since the monitored discharge is operated above a fully poisoned (oxidized) target from which only a minimum of Cr is sputtered. No signs of self-sputtering have been detected, in contrast to the discharges in Ar, N_2 and N_2/Ar mixtures previously investigated.

Paper IV: In the fourth paper, we study different power management approaches in HiPIMS and MPPMS and their effects on the pulsed discharge evolution, plasma composition, and metal ionization estimated by OES. It is shown that HiPIMS is the only technique that enables the discharge operation in self-sputtering mode within the investigated range of applied powers, resulting in a significantly higher ionization of the sputtered metal than that reached with MPPMS. In contrast to HiPIMS, MPPMS provides a higher versatility in adjusting the pulse shape and pulse length. This feature can be particularly beneficial, for instance, in the discharge ignition. Nb coatings prepared by HiPIMS and MPPMS have very similar deposition rates that are lower than in DCMS. All films prepared at $p = 1\,\mathrm{Pa}$ possess a dense columnar structure. Coatings deposited by the two high power pulsed discharges exhibit higher compressive stress and larger out-of-plane lattice spacing than those prepared by DC sputtering under comparable conditions. At higher pressure, $p = 2\,\mathrm{Pa}$, DCMS-grown films show a tensile stress due to a porous microstructure, while films prepared by HiPIMS and MPPMS are dense and in compression, most probably due to the substantial ion bombardment.

Paper V: In the last paper, we analyze the behavior of the HiPIMS, MPPMS and DCMS discharges in reactive O_2/Ar gas mixtures and evaluate the characteristics of the fabricated NbO_x films. We demonstrate that the surface metal oxides can be effectively sputter-eroded from the target during both HiPIMS and MPPMS pulses, and that sputtering from a partially oxide-free target is possible even at high oxygen concentrations. This results in a hysteresis-free deposition process which allows one to prepare optically transparent Nb_2O_5 coatings at a high growth rate without the need of feedback control commonly used in reactive DCMS. Nb_2O_5 coatings prepared by both reactive high power pulsed discharges exhibited a high index of refraction, a low extinction coefficient, a near-zero internal stress, and high hardness and Young's modulus. The HiPIMS-deposited coatings showed the highest deposition rate and the highest index of refraction. The latter observation was related to the higher film density. In comparison, MPPMS exhibited the highest power-normalized deposition rate among the three investigated deposition techniques, possibly due to the longer period that is available for the gradual target cleaning. Finally, the cathode voltage was identified as a principal parameter that affects the reactive discharge behavior.

RÉSUMÉ

La tendance actuelle dans le domaine du dépôt physique en phase vapeur porte en partie sur le développement de processus permettant une ionisation élevée du matériau pulvérisé. Cette forte ionisation permet d'obtenir des conditions favorables à la fabrication de couches minces très denses. C'est le cas de la pulvérisation magnétron pulsée de grande puissance (HiPIMS), une technique de dépôt récemment introduite dans les milieux académiques et industriels. Ainsi, une forte dissipation de puissance au niveau de la cible durant chaque impulsion HiPIMS mène à la génération d'un plasma de haute densité et à une ionisation considérable du matériau pulvérisé. Pour cette raison principale, la concetration en ions métalliques d'un plasma HiPIMS peut être élevée, ce qui peut mener à une auto-pulvérisation de la cible.

Malgré les importants progrès tant dans la compréhension que dans l'application de cette nouvelle technique de dépôt, une multitude de questions reliées à la dynamique complexe des décharges HiPIMS restent ouvertes. Ces questions concernent nottement les décharges opérées dans des mélanges gazeux réactifs employés dans la préparation de revêtements protecteurs et optiques. Ainsi, à titre d'exemple, il existe très peu d'information concernant la propagation entre la cible et le substrat d'un plasma riche en métal lors de chaque impulsion HiPIMS. Ceci est pourtant un critère important facilitant l'optimisation des conditions de dépôt. Ajoutons qu'il existe plusieurs types de sources de puissance offrant des formes d'impulsion en courant et en tension très différentes, mais qu'acune analyse rigoureuse de leur décharge respective menant à l'identification des avantages et de s inconvénients sur le processus de dépôt n'est disponible en ce moment.

Le but de la présente thèse consiste ainsi à répondre aux problématiques et aux besoins définis plus-haut. En premier lieu nous menons une étude approfondie des processus en phase gazeuse durant des impulsions HiPIMS opérées avec une cible de Cr dans des milieux de Ar, de O_2/Ar, de N_2 et un mélange de N_2 et Ar (N_2/Ar) en utilisant primordialement l'émission optique émanant des différentes espèces excitées par le plasma. Nous nous concentrons ensuite sur l'évaluation critique des deux types de décharges pulsées à grande puissance générées par

les deux sources principales disponibles sur le marché : (i) un générateur d'impulsions carrées très courtes (200 μs) permettant d'atteindre de grandes valeurs de tension cathodique (noté ici HiPIMS), et (ii) un générateur de pulsations modulées plus longues (800 – 3000 μs) aux formes personnalisées (MPPMS). Nous examinons ces deux décharges appliquées à une cible de Nb dans une variété de conditions non-réactives, ainsi que dans des mélanges réactifs de O_2/Ar. Par la suite, nous comparons ces dernières décharges à la pulvérisation magnétron DC (DCMS) standard. De plus, l'observation de la décharge à travers des méthodes électriques et optiques est complémentée par une analyse approfondie des caractéristiques des couches de Nb et de NbO_x déposées. Les paragraphes suivants résument les résultats principaux présentés dans la thèse sous la forme de cinq articles.

Article I : Dans le premier article, nous présentons une approche innovatrice permettant la caractérisation de l'évolution d'une décharge HiPIMS – l'imagerie de plasma résolue en temps et en espèces atomiques – l'observation ciblée des différentes espèces du plasma est réalisée grâce à l'utilisation d'un ensemble de filtres interférentiels passe-bande. Nous démontrons par la suite que l'introduction de tels filtres peut être utile à la fois pour la distinction des différentes étapes de la décharge et pour la visualisation de nombreux effets du plasma incluant : l'excitation du gaz de travail durant l'ignition de la décharge, la présence d'ondes de chocs gazeuses et l'expansion d'un plasma riche en métal. Nous avons démontré que cette technique est applicable au diagnostique de pulsations HiPIMS longues de 200 μs dans un milieu non-réactif en utilisant une cible de Cr.

Article II : Dans le deuxième article, afin d'acquérir de plus amples informations concernant la dynamique des décharges réactives HiPIMS, l'imagerie de plasma énergétique ainsi que la spectroscopie optique (OES) résolue dans le temps et dans l'espace sont utilisées afin d'étudier systématiquement des pulsations longues de 200 μs opérées à diverses pressions dans divers milieux (Ar, N_2 et mélange N_2/Ar). Nous remarquons ainsi que le plasma métallique dense créé au voisinage de la cible se propage dans le réacteur à une vitesse allant de 0.7 à 3.5 $\mathrm{km\,s^{-1}}$ dépendamment de la composition et de la pression du gaz de travail. En effet, cette vitesse croît avec l'augmentation de la concentration de N_2 ainsi qu'avec une diminution de la pression. La forme de l'onde plasma se propageant dans la chambre de dépôt varie d'une

forme hémisphérique dans le Ar pur à une forme de goutte dans le N_2 liée à l'émission considérable des molécules de N_2 excitées. Il est intéressant de noter que nous avons observé la présence d'une auto-pulvérisation de la cible et ce quelque soit la composition de gaz utilisée (même pour N_2 pur).

Article III : Dans le troisième article, nous analysons, au moyen de l'imagerie de plasma résolue en temps et en espèce atomiques, des décharges longues de 200 μs au-dessus d'une cible de Cr dans le O_2 pur. Nous observons que l'émission de la décharge est principalement dominée par l'émission de le O_2 neutre et ionisé ; Comme la cible est complètement oxydée seulement très peu de Cr est pulvérisé. Aucun signe d'auto-pulvérisation n'a été détecté dans le O_2 contrairement aux décharges dans le Ar, le N_2 et les mélanges de N_2/Ar précédemment investigués.

Article IV : Dans le quatrième article, nous étudions les différentes approches de gestion des pulses de la puissance dans des générateurs HiPIMS et MPPMS ainsi que leurs effets sur l'évolution de la décharge, la composition du plasma et l'ionisation métallique estimée par l'OES. Nous démontrons que le HiPIMS est la seule technique qui permet l'obtention d'une décharge en mode d'auto-pulvérisation dans l'intervalle de puissances étudié. Il en résulte ainsi une ionisation du métal pulvérisé significativement plus importante que dans le cas du MPPMS. Au contraire du HiPIMS, le générateur MPPMS présente une plus grande versatilité dans l'ajustement de la forme et de la taille des impulsions. Cette caractéristique peut être particulièrement avantageuse lors de l'ignition de la décharge. Les revêtements de Nb préparés par HiPIMS et MPPMS ont des taux de dépôt très similaires mais plus faibles que ceux obtenus par DCMS. Tous les films préparés à une pression de 1 Pa possèdent une structure colonnaire dense. Les revêtements déposés par les deux décharges pulsées de grande puissance présentent une contrainte en compression plus élevée et une plus grande distance interplanaire dans la direction hors du plan de la couche que ceux préparés par la pulvérisation DC sous des conditions comparables. À une pression plus élevée de 2 Pa, les couches préparées par DCMS montrent une contrainte en tension due à une microstructure poreuse tandis que celles préparées par HiPIMS et MPPMS sont denses et en compression, probablement en raison du bombardement ionique substantiel.

Article V : Dans le cinquième et dernier article, nous analysons le comportement des décharges HiPIMS, MPPMS et DCMS dans des mélanges gazeux réactifs de O_2/Ar, et nous évaluons les caractéristiques des couches de NbO_x déposées. Nous démontrons que les oxydes métalliques sur la surface de la cible peuvent être effectivement pulvérisés que ce soit en HiPIMS ou en MPPMS, et que la pulvérisation d'une cible partiellement métallique reste possible même avec des concentrations élevées de O_2. Il en résulte un processus de dépôt sans courbe d'hystérésis ce qui permet la préparation de revêtements de Nb_2O_5 optiquement transparents, à un taux de dépôt élevé, et ce sans l'utilisation d'un contrôle rétroactif fréquemment utilisé lors de la pulvérisation DCMS réactive. Les revêtements de Nb_2O_5 préparés par les deux décharges pulsées de grande puissance manifestent également un haut indice de réfraction, un faible coefficient d'extinction, une contrainte interne négligeable, ainsi qu'une dureté et un module d'Young élevés. Les couches déposées par HiPIMS présentent les taux de dépôt et les indices de réfraction les plus élevés. Cette dernière observation semble être liée à une plus grande densité des couches. En comparaison, les couches déposées par MPPMS ont les taux de dépôt normalisés par la puissance les plus élevés parmi les trois techniques étudiées. Ceci est probablement dû à un plus long nettoyage progressif de la cible. Finalement, la tension cathodique a été identifiée comme l'un des critères les plus importants affectant le comportement d'une décharge réactive.

CONTENTS

LIST OF TABLES

LIST OF FIGURES

LIST OF APPENDICES

LIST OF SYMBOLS AND ACRONYMS

Acronyms

2D	two-dimensional
3D	three-dimensional
AC	alternating current
DC	direct current
DCMS	direct current magnetron sputtering
DIBS	dual ion beam sputtering
CA	cathodic arc
CCD	charge coupled device
CVD	chemical vapor deposition
CRT	cathode ray tube
EEDF	electron energy distribution function
FCSEL	Functional Coating and Surface Engineering Laboratory
HD	high density
HiPIMS	high power impulse magnetron sputtering
HPPMS	high power pulsed magnetron sputtering
IBS	ion beam sputtering
ICCD	intensified charge coupled device
IEDF	ion energy distribution function
IPVD	ionized physical vapor deposition
ISEE	ion-induced secondary electron emission
LD	low density
Nb_2O_5	niobium pentoxide or niobium oxide
NbO_x	substoichiometric niobium oxide
MCP	micro-channel plate of the ICCD detector
MEMS	microelectromechanical systems
MF	mid-frequency
MPP	modulated pulse power
MPPMS	modulated pulse power magnetron sputtering
MS	magnetron sputtering
MW	microwave
OES	optical emission spectroscopy

PECVD	plasma enhanced chemical vapor deposition
PEM	plasma emission monitoring
PMS	pulsed magnetron sputtering
PS	power supply
PVD	physical vapor deposition
RF	radio frequency
RT	room temperature
SE	secondary electrons
SEM	scanning electron microscopy
SS	self-sputtering
SZM	structure zone model
TCO	transparent conducting oxide
TEM	transmission electron microscopy
TR	time-resolved
TRG-OES	trace rare gases optical emission spectroscopy
TRIM	computer program "Transport of ions in matter"
UV	ultraviolet range of the electromagnetic spectrum
XRD	X-ray diffraction

Symbols

A	denotes particle A
A_{kl}	Einstein coefficient for electronic transition from level k to l
B	denotes particle B
$\vec{B}$	magnetic field vector
c	velocity of light
C	nitrogen concentration in N_2/Ar mixture
d	distance from the target surface
$d_{(110)}$	out-of-plane lattice spacing
D	duty cycle
e	denotes electron
e	elemental electron charge
E	electron energy
E^*	normalized energy flux towards substrate
E_0	energy of ion leaving plasma
E_{b}	binding energy

E_{C}	cohesion energy
E_{dis}	dissociation energy of molecule
E_{g}	bandgap energy
E_{i}	ionization energy threshold
E_{k}	excited energy level k
E_{kin}	kinetic energy of arriving particle
E_{l}	excited energy level l
E_{pot}	potential energy of arriving particle
E_{P}	energy per deposited particle
E_{r}	reduced Young's modulus of prepared film
E_{s}	Young's modulus of substrate
f	repetition frequency
f_{e}	electron energy distribution function
F	energy distribution of sputtered atoms
h	Planck's constant
H	hardness of prepared film
I	optical emission intensity
I_{A}	radiation intensity from excited species A
I_{C}	cathode current
I_{d}	discharge current density
J	current density
J_{C}	cathode current density
J_{α}	flux of particles α
k	Boltzmann constant
k	extinction coefficient
K	constant
K_{ea}	electron-atom excitation/ionization rate coefficient
K_{d}	response constant of the detector
m	particle mass
m_{e}	mass of electron
m_{i}	mass of ion
m_{s}	mass of surface atom
m_{α}	mass of particle α
n	index of refraction
n^*	density of excited atoms
n_{A}	density of species A

n_e	density of electrons
n_i	density of ionized atoms
n_n	density of neutrals
n_x	density of excited or ionized atoms
N_dis	number of displaced atoms
p	pressure
P	power
q	particle charge
Q	ion charge state
Q_e	quantum yield for the photon emission
r	deposition rate
$r^\star_\mathrm{HiPIMS}$	theoretical value of maximal deposition rate of the HiPIMS technique if operated at the same power as DCMS
r_n	deposition rate normalized to power
r_L	Larmor radius
s	sheath thickness
S	surface area
t	time
t_f	film thickness
t_s	substrate thickness
T	pulse duration
T	temperature
T^*	generalized substrate temperature
T_0	background gas temperature
T_e	electron temperature
T_h	homologous substrate temperature
T_i	ion temperature
T_m	material melting point
T_s	substrate temperature
U_b	substrate bias potential
U_C	cathode potential
U_f	floating potential
U_output	potential on the output of power supply
U_p	plasma potential
$\vec{v}$	velocity vector
$v_\perp$	projection of velocity vector to a plane perpendicular to $\vec{B}$

v_0	thermal velocity of neutrals
$\mathrm{v_B}$	Bohm velocity
v_e	thermal velocity of electrons
v_i	thermal velocity of ions
v_A	propagation velocity of the emission peak of neutral A
$v_{\mathrm{A}+}$	propagation velocity of the emission peak of ion A^+
Y	material sputtering yield
Y_S	material self-sputtering yield

Greek symbols

α_eA	proportionality constant between I_A and n_A for electron excitation
γ_SE	secondary electron emission yield
Δ	ellipsometric angle
ϵ	energy of sputtered atom
ϵ_0	permittivity of vacuum
θ	angle of incidence
λ	wavelength of the photon
λ_D	Debye length
λ_i	ion mean free path
λ_kl	wavelength of radiation due to electronic transition from level k to l
ν	frequency of the emitted light
ν_s	Poisson's ratio of substrate
σ	inplane residual stress of prepared film
σ_ea	interaction cross section for electron excitation/ionization of A
σ_eA	interaction cross section for electron excitation of A
σ_n	interaction cross section for particle collision
ϕ	material work function
$\Phi(\mathrm{Ar})$	argon flow
$\Phi(\mathrm{O_2})$	oxygen flow
Φ_i	fluxes of ions bombarding growing film
Φ_n	fluxes of condensing film atoms
Ψ	ellipsometric angle
ω_C	cyclotron frequency

CHAPTER 1

Introduction

1.1 Importance of thin films

Thin films can be found in a vast number of applications where specific surface properties of the materials are needed. For instance, manufacturing tools deployed in machining or drilling are commonly coated by protective hard thin films in order to reach higher hardness, toughness and elevated wear-, erosion- or corrosion resistance. Furthermore, the coatings have to withstand a large range of working temperatures without delamination from the underlying material. Such properties are also required in the automotive and aerospace applications, where the durability of various engine, transmission and external parts exposed to hostile environments are crucial. Moreover, the protective films are used in biomedical applications, e.g. bio-implant coatings, where the above-mentioned properties should be coupled with material compatibility with the biological environment.

Thin films generally possess different optical, electrical and magnetic properties than the substrate material. They are widely used as decorative coatings, mirrors, antireflective coatings on eyewear, optical interference filters in telecommunication, or as segments of the photovoltaic cells, just to list a few applications. Perhaps, the most commonly known use of thin films is in the semiconductor device fabrication, in microelectronics and in microelectromechanical systems (MEMS). In fact, it was the boom of the integrated circuit technology in the late 1960s that started massive invasion of thin films into the commercial applications [1]. Nowadays, both conductive and insulating films form essential parts of the integrated circuits within various computer components, such as microprocessors. Thin ferromagnetic films are also used as magnetic storage medium in hard disk drives and as the read/write devices in the hard disk heads.

It should be stressed, that the above-mentioned list of applications is limited and by far not exhaustive. In fact, thin films are gradually expanding in many industrial domains. This expansion is driven by the ever-increasing demand for higher production and performance ef-

ficiency, and for lower environmental impact. For instance, the coating of the manufacturing tool will extend its lifetime. In this way, both material and machining costs necessary for the tool fabrication can be significantly diminished, as well as the off-time required for the tool replacement.

1.2 Techniques of thin film fabrication

There are numerous ways how to prepare thin films. The most common methods used in industry are electrodeposition and different forms of plasma enhanced chemical vapor deposition (CVD) and physical vapor deposition (PVD) techniques. In the following paragraphs, these deposition techniques will be briefly introduced.

Electrodeposition is widely applied for surface metallization. Its principle is based on the reversed galvanic cell. Positive metal ions dissolved in a liquid solution are attracted to the negatively charged part to be coated. The popularity of the electrodeposition is based on the high metal growth rate and on its simplicity in comparison to other techniques requiring the use of sophisticated and costly vacuum equipment. The principal disadvantages are the limitation to single metallic elements (with an exception of brass and solder) and the low uniformity of the resulting films, specifically on the steps or faceted surfaces. Another drawback is the use of environmentally aggressive agents and toxic effluents.

In CVD, the film is formed from a volatile gaseous precursor which is decomposed at the substrate surface to be coated. Typically, the precursor is activated by heat and/or by plasma. In the latter case, the process is called Plasma Enhanced Chemical Vapor Deposition (PECVD). The advantage of this technique is its capacity to prepare metallic, dielectric and even organic compound coatings of well defined stoichiometry [1, 2]. Another interesting feature is good coating coverage of the complex-shaped substrates exhibiting curved features, holes and trenches, and even of the interior of tubes. The principal limitation of CVD is the need for high process temperature in order to facilitate the gas-phase and surface reactions of different film constituents. This means that coating of temperature-sensitive materials, or of the substrates exhibiting a different thermal expansion coefficient than that of the deposited film, is hindered. PECVD partially overcomes this obstacle since the process temperature can be substantially lowered, down to room temperature (RT). Both CVD and PECVD also

require vacuum system and pumps for operation.

In PVD, the deposited material is vaporized from a solid or liquid surface by thermal or electron beam evaporation, by ion bombardment-induced sputtering or by laser ablation. The vaporized material (mostly neutral atoms) travels in a line-of-sight manner through the deposition chamber and subsequently condenses on the substrates that usually face the material's source. In the case of a reactive deposition process, condensation involves reaction of the condensing material with a reactive gaseous species (e.g. dissociated N_2, O_2) in order to create a compound. In comparison to electrodeposition and CVD techniques, no toxic effluents and pollutants are involved. A possible limitation is the necessity for rather complicated equipment, including vacuum chamber and pumps and sophisticated power supply(ies).

In conventional (thermal) evaporation, the source material is usually positioned inside of the crucible made from a material with a much higher melting point (e.g. W, Mo, C, ceramic). The former one is then evaporated by resistive heating or by an intense electron beam. The main advantage is the high deposition rate and the relative simplicity of the process compared to other PVD techniques. Its drawbacks are low coating packing density and moderate adhesion to the substrate. Also, the deposition of alloys is rather difficult; This often demands the use of multiple evaporation sources [3]. In addition, the materials exhibiting high melting temperature are difficult to evaporate.

Another variant of the evaporation technique is called cathodic arc (CA). Here, the material in the form of a conductive cylinder or a circular plate called *target* is evaporated by high currents flowing from the discharge maintained above its surface. In fact, the target atoms are ejected from the small melting spots on its surface (*cathodic spots*). The deposition of metallic and compound films by CA reach elevated deposition rates. The obtained coatings exhibit high density and excellent adhesion [4]. CA can also be employed for substrate cleaning for adhesion enhancement pre-treatment before the coating deposition. In such a case, the arc discharge is used as a source of metal ions which are then accelerated towards the substrate in order to erode its surface (*plasma etching*). The major limitation is the generation of macroparticles or liquid droplets which are the by-products of microexplosions at the cathodic spots. Their incorporation in the growing film is highly undesirable and even unacceptable in some applications, e.g., in the fabrication of semiconductor devices or in

optical coatings. A solution to this problem is application of sophisticated magnetic filters for the selection of the ejected ionized material. However, such filtering adds complexity to the deposition apparatus and it significantly reduces the deposition rate [5, 6].

Sputtering is the most flexible PVD technique that allows one to deposit a large number of materials, including those with a high melting point, metal alloys and even dielectrics. The target atoms are liberated from the surface by physical bombardment by energetic ions impacting its surface (the effect called momentum transfer sputtering or simply *sputtering*). These ions can be created from a separate ion source (e.g., ion beam sputtering (IBS) or its ion-assisted version dual ion beam sputtering (DIBS)) or from the discharge maintained directly above the sputtered target (e.g. magnetron sputtering (MS)). In the latter case, the target serves as the driving cathode, and the substrate holder that faces the target, as well as all the walls of the surrounding deposition chamber, act as the anode.

The principal advantage of sputtering compared to evaporation is the higher kinetic energy of the vaporized species [3, 7]. This can result in higher packing density of the deposited film since the condensing atoms have higher energy for surface diffusion on the underlying material. Furthermore, the absence of the growth defects (e.g., macroparticles) and the capacity to scale the sputtering sources (cathodes) make sputtering, and especially MS, a suitable technique for a wide range of industrial applications; this includes large area glass coatings, automotive and tool coatings, and microelectronics component fabrication. This is why the popularity of this deposition technique keeps steadily increasing [7, 8]. Further advances of the MS technique is the subject of this work.

1.3 Challenges in coating fabrication

Great progress in technology during the last years stimulated the development of novel coating solutions based on heterostructures, such as film multilayers and nanocomposites, in order to profit from the synergy of different properties of the individual forming materials; Each of the constituents has different functions, such as conductivity, hardness, environmental protection, biocompatibility, color, or their combination.

The term multilayer stands for a layered structure composed of several up to several thousand of film layers. If the thickness of the individual layers is in the nanometer scale, the

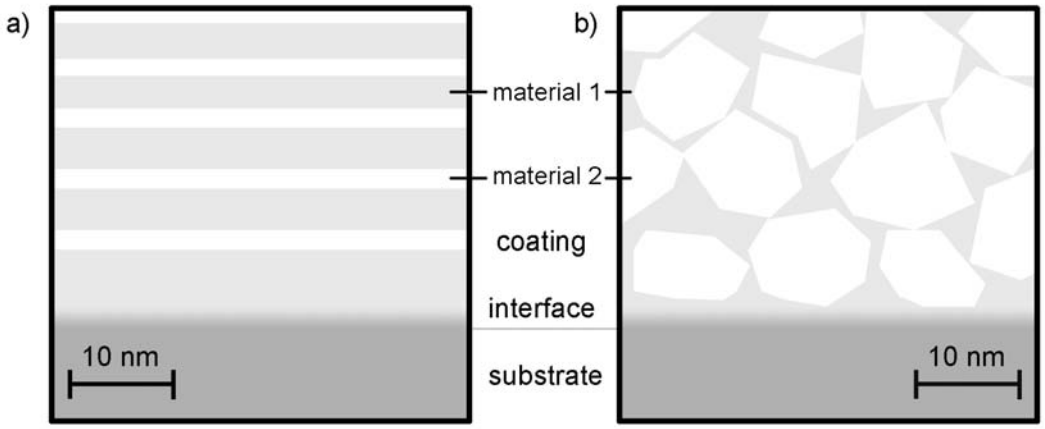

Figure 1.1 Schematics of the nano-scaled multilayer coating (nanolaminate, superlattice) (a) and of the nanocomposite coating (b) composed of two different materials deposited on a substrate. The interface region is highlighted.

resulting structure is called nanolaminate [Fig. 1.1(a)]. Furthermore, if the constituent layers are crystallographically matched, the resulting structure is called superlattice. In contrast, nanocomposite coatings consist of a matrix (crystalline or amorphous) of one material in which nanometer-size particles of a second material are embedded [Fig. 1.1(b)]. All these new structures can provide exceptional properties (e.g., hardness, wear resistance, environmental stability) that are difficult to achieve by single phase coatings [9].

The ever-growing requirements on the performance of the fabricated coatings implies a need for new technological processes suitable for their production. Research is therefore moving towards the exploration and development of new sophisticated deposition techniques capable of synthesizing coatings with fine tuned composition and microstructure, in order to obtain requested properties. In addition, the fabrication technique should be suitable for tailoring the coating-substrate interface and/or interfaces in multilayer systems in order to secure the coating durability and environmental stability. Moreover, the capacity for coating complex-shaped substrates, which may exhibit deep trenches, holes or 3D structures is frequently demanded.

1.4 Ionized physical vapor deposition

One of the approaches that can be used for modification and control of the microstructure and hence the properties of the deposited films and interfaces, is to employ the ionized sputtered-material atoms, also called *film ions*, in the deposition process. The film ions can be accelerated and collimated via the electric field of the plasma sheath near the substrate. In this way, both energy and direction control of the film-forming species are ensured simply by applying a substrate bias. The energy conveyed locally to the place of the arriving atoms affects the nucleation and film growth mechanisms [10]. The localized energy transfer permits to lower the deposition temperature and to improve the film quality in terms of higher density [11, 12], lower surface roughness [13, 12] and better adhesion to the underlying material [14]. The possibility to control the direction of the arriving film ions also enables coating of parts with complicated geometries even when using a standard planar source of material as magnetron target [13, 15].

Among the plasma-based coating techniques generating substantial fluxes of ionized film atoms can be classified PECVD and several advanced modifications of PVD that are referred to as ionized physical vapor deposition (IPVD) methods. The most common IPVD technique, which exhibits the highest vaporized material ionization is filtered CA. Unfortunately, CA has a major drawback in generating macroparticles which have to be filtered away, as discussed previously. However, there are numerous applications of both unfiltered and filtered CA, such as those summarized in [4, 6].

Other IPVD techniques are mostly based on the conventional direct current magnetron sputtering (DCMS) where the discharge plasma density is intentionally increased in order to enhance the sputtered material ionization on its way through the plasma region towards the substrate. This is usually done by either a specific shape of the cathode (hollow cathode [16]) or by the application of a secondary discharge within the deposition chamber, e.g., by the radio frequency (RF)-powered inductive coils or by the microwave (MW) applicator, as summarized in Ref. [17]. However, these IPVD techniques never became popular in the industry due to the complexity of the required deposition apparatus and the consequent difficulty to scale up to industrial-size coaters.

Another way how to reach higher plasma density is to substantially increase the power applied to the magnetron target. This is the basic idea behind the recently introduced HiPIMS technique that is increasingly gaining attention from both academia and industry and that became the "hot topic" of many conferences during the past years.

1.5 High power impulse magnetron sputtering

The origins of HiPIMS, by some referred to as high power pulsed magnetron sputtering (HPPMS), go back to the middle of 1990s when the experiments with pulsed glow and magnetron discharges were first reported [18, 19, 20]. However, it has not gained popularity until 1999 when uniform filling of 1 μm deep and 1 μm wide trenches with a dense Cu coating by HiPIMS was demonstrated by Kouznetsov et *al.* [21].

The principal difference of HiPIMS from DCMS is the use of much higher power densities applied to the magnetron. In order to avoid target overheating, the power is applied in pulses of short duration with a low duty cycle (ratio of pulse on-time over off-time), usually in the range of 0.5 to 5%. In this way, power densities up to few kW·cm^{-2} can be reached. For illustration, a typical power delivery in DCMS and HiPIMS, together with its recent modification called modulated pulse power magnetron sputtering (MPPMS), is depicted in Fig. 1.2.

The high power dissipated on the target during each pulse leads to the generation of high-

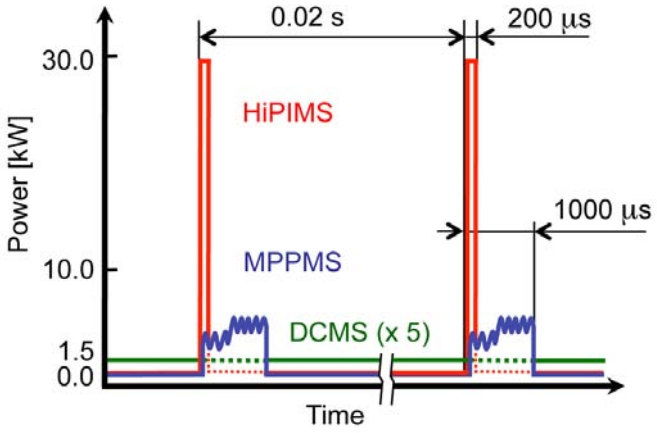

Figure 1.2 Schematic representation of the power delivery during the pulsed discharges above a magnetron powered by HiPIMS, MPPMS and DCMS power supplies operated at the same average power $P = 300$ W. Reprinted from Paper IV (Chapter 7).

density plasma, e.g., $n_e \approx 10^{12} - 10^{13}\,cm^{-3}$ [22, 23, 24, 25, 26, 27]. This enables a significant ionization of sputtered-material, which can become available to the deposition process. A high metal ion fraction in the sputtered flux by HiPIMS, reaching up to 30% for Cr [28], 60% for Cu [29] and above 90% for Ti, has been reported [30, 31]. As well, the detection of multiple (up to four-fold [32]) charged metal ions has been shown [33, 34]. Such observations contrast sharply with the conventional DCMS, in which the metal ionization is very low ($n_e \approx 10^9 - 10^{11}\,cm^{-3}$).

The application of HiPIMS for coating non-flat and inclined substrates was demonstrated to significantly improve film homogeneity and decrease surface roughness [13, 15]. This is illustrated in Fig. 1.3(a) by an example of two Ta films grown on 90° inclined surfaces with respect to the plane of the material source (cathode's surface) . While the microstructure of the film grown by DCMS shows apparently inclined columns and high surface roughness, the HiPIMS-prepared film appears dense with a smooth surface, and the visible columns have a perpendicular direction to the substrate. The authors of the study have also claimed a higher packing density in the case of HiPIMS-deposited films [13]. This indicates that HiPIMS is a suitable deposition technique for filling small trenches in microelectronics and in MEMS fabrication, and for coating components with complex shapes (e.g. drilling bits, turbine engine blades).

The HiPIMS discharge was found very beneficial if applied for substrate pre-treatment (plasma etching). Films deposited on the HiPIMS pre-treated substrates exhibited an enhanced adhesion [14] and a substantially improved corrosion-, oxidation- and erosion-corrosion resistance [35, 36, 37, 38, 39]. For illustration, Fig. 1.3(b) shows the interface area of the stainless steel substrate and the deposited CrN film. No voids, lattice misalignment or other defects can be observed. In fact, the atomic layers in both materials are visibly aligned. This is a sign of the cube-on-cube epitaxial growth preserved throughout the substrate-coating interface region [14]. Such interface provides the best adhesion and an excellent protection against the harsh environment.

Protective metal nitride-based coatings prepared by HiPIMS exhibited dense droplet-free microstructure, high hardness and low surface roughness [40, 41, 42]. Recently, HiPIMS was also used in the preparation of advanced nanolayered [35, 36, 37, 38, 39] and nanocom-

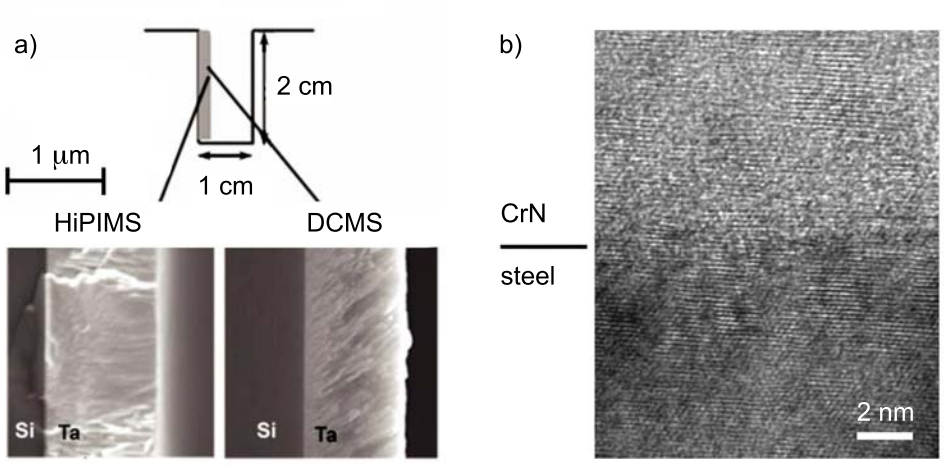

Figure 1.3 (a) Film morphology of a Ta coating deposited on the wall of a 1 cm wide and 2 cm deep rectangular trench prepared by HiPIMS and by DCMS. Both films were grown on crystalline Si substrates at room temperature with a bias $U_b = -250$ V. Modified from [13]. (b) Cross-sectional lattice image with atomic resolution of stainless steel substrate - CrN film interface that was pre-treated by HiPIMS with Nb ions at $U_b = -1000$ V. The substrate temperature was maintained at 400°C. Modified from [14].

posite [43, 15, 44, 45] coatings exhibiting dense microstructure and outstanding mechanical properties (wear-, corrosion-, erosion-, or corrosion-erosion resistance, and dry milling) if compared with other common deposition techniques. This demonstrates the capacity of this deposition technique to synthesise advanced compound materials, while benefiting from all advantages of the highly energetic nature of the IPVD process.

HiPIMS was also applied for the preparation of various transparent metal oxides. In general, optical coatings deposited by HiPIMS exhibited higher packing density, higher index of refraction, and lower surface roughness than those prepared by DCMS [46, 12, 47, 48, 49, 50]. Other studies showed a diminished resistivity of the HiPIMS-deposited transparent conducting oxide (TCO) films in comparison to DCMS-deposited films [51, 52].

Due to the steadily growing attention that HiPIMS technique received during the first decade of its existence, a variety of power supplies (PS) from different manufacturers and with different pulse shape, voltage and current characteristics were introduced to the market [53, 54, 55, 56, 57]. However, among the great number of commercially available PS, one can distinguish two principal types according to the specific form of the produced voltage pulse; Square voltage pulse generator and modulated pulse power (MPP) generator. The former

is commonly referred to as HiPIMS PS and the latter is often called MPPMS PS. Further details about the principal differences between the two kinds of PS can be found in section 3.1 (Chapter 3). Moreover, several companies already offer the built-in HiPIMS PS within their industrial-size coaters using large-scale cathodes (CemeCon [58], Hauzer [59], PLT [57]). This demonstrates that HiPIMS is becoming a well established and popular deposition technique.

1.6 Motivation of this work

HiPIMS is truly at the cutting edge of nowadays surface engineering and functional coating fabrication technology. Its benefits for the preparation of protective and optical coatings, briefly summarized above, are the main motivation for this work.

Despite the great advances in the understanding as well as in the application of this novel deposition technique, there are numerous open questions related to the dynamics of the pulsed HiPIMS discharges, specifically when operated in the reactive gas mixtures. For instance, there is still little information available about the discharge evolution, and particularly, about the propagation of the metal-rich plasma in between the target and the substrates. In order to facilitate such investigation, a convenient diagnostic approach suitable for both time- and space-resolved monitoring of various physical processes in the gas phase of HiPIMS discharge (e.g., gas rarefaction by sputtered material and subsequent plasma expansion) is needed. Here, it should be stressed that the in depth characterization of the reactive HiPIMS discharges is of primordial importance for the optimization of the deposition conditions suitable for the preparation of functional protective and optical films.

The existence of the two commercially available types of HiPIMS PSs exhibiting different power management strategies implies a need for a rigorous comparison of the respective HiPIMS and MPPMS discharges, that would ease the coating manufacturer's task to choose the most suitable approach for the deposition process. An appropriate comparison with a standard coating process used in the industry (e.g., DCMS) is also required. Such an investigation, still missing in today's literature, should employ both discharge diagnostics and fabricated thin films characterization. In addition, a proper understanding of the hysteresis behavior of HiPIMS and MPPMS discharges operated in reactive gas mixtures is necessary for a judicious control of the corresponding deposition processes.

Previous research in the Functional Coating and Surface Engineering Laboratory (FCSEL) at École Polytechnique has focused, among many other topics, on the understanding of pulsed RF and MW plasmas. For instance, Zabeida *et al.* [60, 61] have studied the dynamics of the non-reactive and reactive discharges excited by pulsed MW by the time-resolved (TR) mass spectrometry; They have shown that different features of ion energy distribution function (IEDF) originate from different periods of the MW pulse [60]. The authors have also demonstrated that energy of the bombarding ions - and hence the related plasma-surface interactions - can be selectively adjusted by modifying the duty cycle of the pulsed MW power [61]. In another work, the modification of the duty cycle of the RF-powered PECVD discharge was used for tailoring the characteristics of the amorphous SiN_x:H alloy coatings [62]. Pulsed dual-mode MW/RF discharges were also applied for surface treatment of SiN_x:H films in order to fabricate porous-dense multilayer structures, such as Fabry-Perot filters [63]. The background expertise in the characterization as well as in the application of the pulsed plasma discharges in FCSEL hence serves as a driving force and motivation for the current work.

1.7 Objectives

The main objective of the present thesis is to enhance understanding of the HiPIMS process by characterizing the discharge dynamics during individual pulses with a special focus on plasma propagation in the reactive gas mixtures. In this work, we also perform a critical analysis of the two main types of HiPIMS discharges, namely those produced by either a square voltage pulse generator or an MPP generator, operated under both non-reactive and reactive conditions. This will help to identify their respective benefits and drawbacks, an important aspect for the implementation of this technology in industry.

Specific objectives are then defined as follows:

1. Develop a diagnostic approach suitable for the visualization of the spatial evolution of the HiPIMS discharge, and specifically, of the expanding metal plasma.
2. Characterize various physical processes in the gas phase of the HiPIMS discharge under both non-reactive and reactive conditions.
3. Critically assess HiPIMS discharges exhibiting different pulse power management approaches and compare them to the DCMS discharge.
4. Investigate the HiPIMS process in various O_2/Ar gas mixtures in terms of the hysteresis behavior and of the properties of the deposited metal oxide coatings.

1.8 Organization of the thesis

The thesis is divided into 9 chapters. In the following Chapter 2, the theoretical background of the plasma discharges for materials processing, and the principles of sputtering and thin film deposition are presented. Furthermore, a brief overview of the present knowledge on HiPIMS is offered.

Chapter 3 details the characteristics of the two HiPIMS PS employed in this work, namely the square voltage pulse generator and the MPP generator, and also the principles of the used analytical techniques. Special attention is given to the optical monitoring of the discharge.

The principal results of this thesis are then presented in the form of five papers, either already published or submitted to peer-reviewed journals:

Paper I (Chapter 4) describes a novel approach in HiPIMS discharge diagnostics based on fast plasma imaging using the bandpass filters in order to separate optical emission from different plasma-excited species. Application of this technique is demonstrated by analyzing the evolution of the HiPIMS discharge operated above a Cr target in Ar.

Paper II (Chapter 5) is devoted to the investigation of the gas-phase processes within the pulsed HiPIMS discharges above a Cr target in Ar, N_2 and in N_2/Ar mixtures, and at various pressures. Different phases of the HiPIMS discharge are identified and discussed.

Paper III (Chapter 6) uses the insight and methodology developed in Paper 1 for the characterization of the HiPIMS discharge evolution in pure O_2.

Paper IV (Chapter 7) offers a critical comparison of HiPIMS discharges, that are excited by the two types of PS exhibiting different power delivery managements - square voltage pulse generator and MPP generator - with the standard DCMS discharge. Both the discharge characteristics and the properties of Nb coatings are evaluated.

Paper V (Chapter 8) extends the comparative study introduced in Paper 4 for discharge diagnostics in reactive O_2/Ar gas mixtures. Special attention is given to the discussion of the hysteresis suppression observed in both HiPIMS and MPPMS discharges. In addition, optically transparent high refractive index Nb_2O_5 coatings are characterized and their properties compared.

Finally, Chapter 9 offers a general discussion of the accomplished work and conclusions. In addition, future perspectives and directions of research are summarized.

Besides the work presented in the five papers forming the heart of this thesis, the PhD candidate was also involved in several other investigations that resulted in two other papers in peer-reviewed journals and in one paper in conference proceedings. First of the two articles is presented in this work as Appendix A. The list of the candidate's publications at the moment of the thesis submission is summarized in Table 1.1. Among the outcomes of this work are also 11 oral and poster presentations at various international conferences and symposia, listed in Table 1.2.

Table 1.1 List of the candidate's publications at the moment of defending the thesis. The papers that form an integral part of the thesis are denoted by a roman number.

	Papers in peer-reviewed journals
I	M. Hála, O. Zabeida, B. Baloukas, J.E. Klemberg-Sapieha, L. Martinu, "Time- and species-resolved plasma imaging as a new diagnostic approach for HiPIMS discharge characterization", *IEEE Trans. Plasma Sci.*, vol. 38, no. 11, pp. 3035 - 3039, Nov. 2010.
II	M. Hála, N. Viau, O. Zabeida, J. E. Klemberg-Sapieha, and L. Martinu, "Dynamics of reactive high-power impulse magnetron sputtering discharge studied by time- and space-resolved optical emission spectroscopy and fast imaging, *J. Appl. Phys.*, vol. 107, p. 043305, Feb. 2010.
III	M. Hála, O. Zabeida, J.E. Klemberg-Sapieha, and L. Martinu, "Dynamics of HiPIMS discharge operated in oxygen", *IEEE Trans. Plasma Sci.*, vol. 39, no. 11, pp. 2582 -2583, Nov. 2011.
IV	M. Hála, J. Čapek, O. Zabeida, J.E. Klemberg-Sapieha, and L. Martinu, "Pulse management in high power pulsed magnetron sputtering of niobium", *Surf. Coat. Technol.* – submitted, Dec. 2011.
V	M. Hála, J. Čapek, O. Zabeida, J.E. Klemberg-Sapieha, and L. Martinu, "Hysteresis-free deposition of niobium oxide films by HiPIMS using different pulse management strategies", *J. Phys. D: Appl. Phys.* – accepted, Dec. 2011.
•	J. Čapek, M. Hála, O. Zabeida, J.E. Klemberg-Sapieha, and L. Martinu, "Steady state HiPIMS discharge optimization through the control of the magnetic field", *J. Appl. Phys.*, vol. 111, p. 023301, Jan. 2012.
•	A. Anders, J. Čapek, M. Hála, and L. Martinu, "The "recycling trap": A generalized explanation of discharge runaway in high power impulse magnetron sputtering", *J. Phys. D: Appl. Phys.*, vol. 45, no. 1, p. 012003, Jan. 2012.
	Papers in conference proceedings
•	M. Hála, N. Viau, O. Zabeida, J.E. Klemberg-Sapieha, and L. Martinu, "Time- and Space-Resolved Optical Emission Spectroscopy Study of Reactive HiPIMS Discharges", *Proc. of the 43th Ann. Tech. Conf. of Society of Vacuum Coaters (SVC)*, Santa Clara, CA, USA, May 2009.

Table 1.2 List of the candidate's oral presentations at the moment of defending the thesis.

Contributed oral presentations

- M. Hála, N. Viau, O. Zabeida, J.E. Klemberg-Sapieha, and L. Martinu, "Time-resolved optical emission spectroscopy in argon-nitrogen gas mixtures", *HPPMS/HiPIMS Workshop*, Golden, CO, USA, 2009.
- M. Hála, N. Viau, O. Zabeida, J.E. Klemberg-Sapieha, and L. Martinu, "Time- and Space-Resolved Optical Emission Spectroscopy Study of Reactive HiPIMS Discharges", *52nd Society of Vacuum Coaters (SVC) Annual Technical Conference*, Santa Clara, CA, USA, 2009.
- M. Hála, N. Viau, O. Zabeida, J.E. Klemberg-Sapieha, L. Martinu, "Analyse résolue dans le temps et dans l'espace de décharges HiPIMS réactives par spectroscopie d'émission optique", *Colloque de Plasma-Québec; Les plasmas: Outils du 21ème siècle*, Montréal, Canada, 2009.
- M. Hála, N. Viau, O. Zabeida, J.E. Klemberg-Sapieha, and L. Martinu, "Dynamics of Reactive HiPIMS Discharge Studied by Time- and Space-Resolved Optical Emission Spectroscopy and Fast Imaging", *53rd Society of Vacuum Coaters (SVC) Annual Technical Conference*, Orlando, FL, USA, 2010.
- M. Hála, J. Čapek, O. Zabeida, J. E. Klemberg-Sapieha, and L. Martinu, "Comparative study of HiPIMS discharges with different pulsing characteristics using time-resolved electrical and optical diagnostics, *53rd Society of Vacuum Coaters (SVC) Annual Technical Conference*, Orlando, FL, USA, 2010.
- M. Hála, J. Čapek, O. Zabeida, J. E. Klemberg-Sapieha, and L. Martinu, "Time-resolved characteristics of reactive HiPIMS plasmas, *37th International Conference on Metallurgical Coatings and Thin Films (ICMCTF)*, San Diego, CA, USA, 2010.
- M. Hála, O. Zabeida, J. E. Klemberg-Sapieha, and L. Martinu, "Dynamics of HiPIMS Discharges Studied by Time- and Species-resolved Plasma Imaging and Emission Spectroscopy, *1st International Conference on High Power Impulse Magnetron Sputtering (HiPIMS)*, Sheffield, UK, 2010.
- M. Hála, J. Čapek, O. Zabeida, J. E. Klemberg-Sapieha, and L. Martinu, "Comparative Study of Nb and Nb_2O_5 Coatings Prepared by High Power Pulsed Discharges Using Different Pulse Shape Characteristics, *54th Society of Vacuum Coaters (SVC) Annual Technical Conference*, Chicago, IL, USA, 2011.
- M. Hála, J. Čapek, O. Zabeida, J. E. Klemberg-Sapieha, and L. Martinu, "Hysteresis suppression in reactive HiPIMS discharges, *Colloque de Plasma-Québec; Les plasmas: science, applications, industrie*, Montréal, Canada, 2011.
- M. Hála, J. Čapek, O. Zabeida, J. E. Klemberg-Sapieha, and L. Martinu, "Hysteresis suppression and elevated deposition rate of Nb_2O_5 optical films prepared by reactive HiPIMS discharges, *6th Symposium on Functional Coatings and Surface Engineering (FCSE)*, Montréal, Canada, 2011.

Poster presentations

- M. Hála, N. Viau, O. Zabeida, J.E. Klemberg-Sapieha, L. Martinu, "Time-and Space-Resolved Optical Emission Spectroscopy Study of Reactive High Power Impulse Magnetron Sputtering (HiPIMS) Discharges", *Annual meeting of Regroupement québécois sur les matériaux de pionte (RQMP)*, Montréal, Canada, 2009.

CHAPTER 2

Theoretical background

In this chapter, the essential theoretical basis for the presented work will be offered. In the first part, the fundamentals of plasma discharges suitable for materials processing will be outlined, with a special focus on the magnetron discharges. In the second part, the principal concepts of sputtering, reactive sputtering and thin film deposition will be discussed. Finally, a brief summary of the present knowledge on the HiPIMS technique will be presented, supported by several relevant experimental results taken from the literature.

2.1 Plasmas for materials processing

2.1.1 Plasma discharge fundamentals

Among the common examples of plasma – sometimes called a fourth state of matter – are solar corona, aurora borealis, flame and fluorescent lights. In fact, most of the known universe is in the plasma phase. When a solid substance is in thermal equilibrium, it can pass into a liquid state with increasing temperature, and further into a gas. Then, at a sufficiently high temperature, a significant amount of gas atoms or molecules release some of their least-bonded electrons. These are then free to move independently, as well as the rest of the original neutral atoms/molecules that are left with a positive charge. Thus, plasma consists of freely moving positively- and negatively-charged particles and of the surrounding atoms/molecules. In common processing plasma (*glow discharge*), only a few percent of the working gas species are ionized and the rest stays neutral. In contrast, high temperature plasma, such as that used in nuclear reactors, may be composed of only ionized species.

There are generally two principal properties of plasma that can be used for its elementary characterization:

1. It is a quasineutral medium; The overall density of electrons together with negative ions is equal to the density of positively charged ions. Localized imbalance between the

two may exist but only within a very limited distance that is a function of the plasma characteristics.

2. It exhibits a collective behavior; The charged particles in the plasma interact with one another not only by collisions, but also by long-range electric and magnetic fields that are themselves created by these particles.

In order to illustrate these points, we can imagine a situation where a disproportion exists in the density of negatively and positively charged species. In such a case, the electric field created by such charge imbalance will create Coulomb forces that will cause charge rearrangement. Hence, plasma acts as an electrically neutral medium on macroscopic scale.

The characteristic distance at which a significant charge separation may exist is called *Debye length*, λ_{D}. It can be expressed as:

$$\lambda_{\mathrm{D}} = \left(\frac{\epsilon_0 \, \mathrm{k} T_{\mathrm{e}}}{e n_{\mathrm{e}}} \right)^{1/2}, \tag{2.1}$$

where ϵ_0 is the permittivity of vacuum, k [eV K^{-1}] is the Boltzmann constant, T_{e} [eV] is the electron temperature, e is the elemental electron charge, and n_{e} is the electron density.

Fig. 2.1 shows a schematic representation of the plasma discharge that is commonly employed in materials processing. It illustrates the quasineutral discharge space filled with electrons and ionized, neutral and excited working gas species (for example, Ar). In addition, it shows a typical process geometry, including a driving electric circuit composed of a voltage source and two electrodes: a negatively charged cathode and a grounded anode.

The majority of discharges used for materials processing and thin film fabrication are operated in low pressure gas environment. The generated plasma is far from thermal equilibrium (*non-thermal plasma*) since the applied electric fields preferentially heat light electrons (of mass m_{e}) as opposed to heavy ions (of mass m_{i}), and since the frequency of their mutual collisions is low. Mobile electrons can hence accumulate a sufficient kinetic energy to excite or ionize the surrounding heavy particles upon collisions. In contrast, ions exchange their energy mostly by collisions with the working gas, which is in thermal equilibrium with the surrounding environment at the ambient temperature, T_0. Consequently, T_{e} is much higher than the ion temperature, T_{i}. The ionization degree, which represents the fraction of the

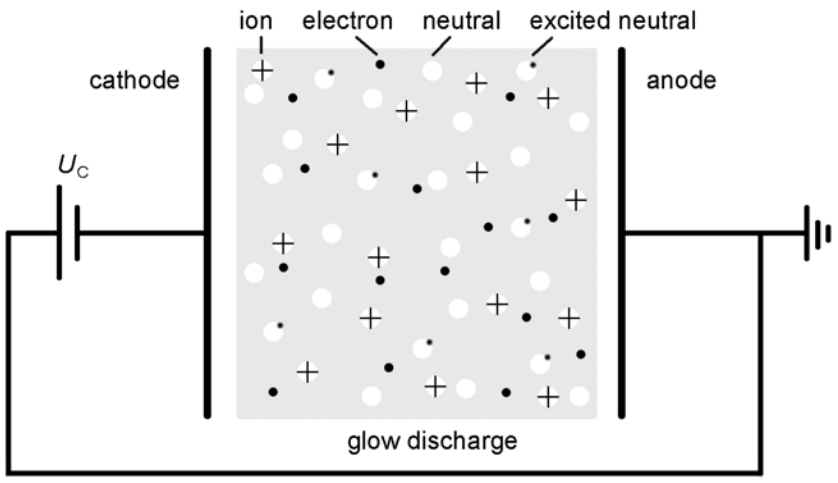

Figure 2.1 Schematics of the glow discharge and the driving electric circuit. Neutral, excited neutral and ionized atoms, as well as free electrons, are depicted within the quasineutral bulk plasma. U_C stands for the voltage applied to the cathode by the power supply.

original neutral gas species which have become ionized, is hence an important parameter of a plasma discharge. In a weakly ionized plasmas, sometimes referred to as *low temperature* or *cold* plasmas, the temperature of neutrals – that largely outnumber ions – determines the ion temperature; $T_i \approx T_0$.

2.1.2 Excitation and ionization processes

Collisional products of the electron-atom impacts – ionized and excited species – and their interactions with exposed surfaces are of great importance in plasma processing of materials. For instance, the exothermic reactions of both ions and excited species upon their collisions with the other species significantly contribute to the chemistry of the discharge and to the reactions on the treated surfaces/growing films. In addition, the ionized species can deliver additional energy to the treated surfaces/growing films since they can be accelerated by the difference between the plasma potential and the surface potential. The importance of such energy transfer will be discussed in section 2.2.4.

Collisions between individual species can be divided into elastic and inelastic, depending on whether the internal energy of the colliding species is preserved or not. An *elastic collision* is characterized by the kinetic energy interchange, where momentum and kinetic energy of translational motion are conserved. This is the most common interaction in electron-

electron and even electron-ion collisions in low temperature glow discharges. During an *inelastic collision* the momentum is preserved, but the kinetic energy is not. The difference in total kinetic energy of the interacting particles before and after the collision then equals the gain/loss in their overall potential energy that is reflected by excitation or ionization processes. In the following paragraphs, the most important inelastic interactions in common discharges used in materials processing will be listed. An electron will be denoted by letter e and the atoms by capital letters A or B. An overview of these reactions with the corresponding examples is also offered in Ref. [1]

Electron impact excitation, $\mathrm{e} + \mathrm{A} \longrightarrow \mathrm{A}^* + \mathrm{e}$, is a process where an outer-shell electron of the atom A is elevated (*excited*) to a higher energy level, if the energy transfer from the impacting free electron equals to respective excitation energy threshold, E_k. Whole atom (neutral or ion) is then referred to as excited and denoted as A*. Usually, the lifetime of the excited state is very short (e.g., $10^{-7}\,\mathrm{s}$ - $10^{-8}\,\mathrm{s}$) and the outer-shell electron returns spontaneously by electric dipole radiation to its original ground state, $\mathrm{A}^* \longrightarrow \mathrm{A} + \mathrm{h}\nu$, or to another lower-lying energy level. Here, $\mathrm{h}\nu$ stands for the energy of the specific emitted photon. The deexcitation emission spectrum of each of the plasma-excited species (neutral or ion, atom or neutral), formed by the emitted photons, is unique and can be used for plasma diagnostics, such as will be discussed in section 3.2 (Chapter 3).

It should be noted that there are some energy levels from which the spontaneous electron transition to the ground state is forbidden. In these cases, the lifetime of the excited atom may be $10^{-3}\,\mathrm{s}$ or even longer, and the principal deexcitation mechanism can become the energy exchange with another atom/molecule via inelastic collision. Such long-lived excited atom is referred to as metastable atom or simply a *metastable*. Metastables are often found in the low-pressure discharges commonly employed in material processing.

Electron impact ionization, $\mathrm{e} + \mathrm{A} \longrightarrow \mathrm{A}^+ + 2\mathrm{e}$, is a process, where positive ion and additional electron are formed by the collision of an energetic electron and a preliminary neutral atom. The ionization usually occurs when the energy conveyed to one of the outer-most valence electrons exceeds the ionization energy threshold, E_i ($E_\mathrm{i} > E_\mathrm{k}$). This process is of primary importance for sustaining the low temperature discharges, where high energy electrons exist but where the excitation of neutrals is moderate [64].

The rate for the two above-mentioned electron impact phenomena is given by:

$$\frac{\partial n_{\mathrm{x}}}{\partial t} = K_{\mathrm{ea}} n_0 n_{\mathrm{e}}, \tag{2.2}$$

where n_{x} stands for the excited atom density, n^*, or ion density, n_{i}, n_0 stands for the neutral atom density, and K_{ea} is the respective excitation/ionization rate coefficient defined as:

$$K_{\mathrm{ea}} = \int \sigma_{\mathrm{ea}}(E) f_{\mathrm{e}}(E) E^{1/2} \mathrm{d}E. \tag{2.3}$$

Here, E is the electron energy, $f_{\mathrm{e}}(E)$ is the electron energy distribution function (EEDF), and $\sigma_{\mathrm{ea}}(E)$ is the material-dependent effective excitation/ionization cross section. The latter variable quantifies the respective interaction probability with the impacting electron and is usually described as a function of E. σ_{ea} increases rapidly above the threshold energy for excitation (E_{k}) or ionization (E_{i}) of the impacted species. The value of σ_{ea} then peaks and decreases for $E > 50 - 100\,\mathrm{eV}$, as a consequence of the shortening interaction time of the bypassing electron [65]. It should be noted, that metals have significantly lower E_{k} and E_{i} thresholds in comparison with working gas atoms, such as Ar. An example can be found in Table 5.1, where E_{k} and E_{i} values for Cr, Cr^+, Ar and Ar^+ are listed.

Another important process is *charge transfer*, $\mathrm{A}^+ + \mathrm{B} \longrightarrow \mathrm{A} + \mathrm{B}^+$, where A and B can be identical species. It can occur when an energetic ion passes close to a thermal neutral. This process is an important loss mechanism for energetic ions in the sheath region of a discharge [64].

A collision of metastable A* with ground state neutral B can cause the excitation/ionization of the latter species, if the excitation energy of A* is greater than the excitation/ionization energy of B. These processes, called *Penning excitation*, $\mathrm{A}^* + \mathrm{B} \longrightarrow \mathrm{A} + \mathrm{B}^*$, and *Penning ionization*, $\mathrm{A}^* + \mathrm{B} \longrightarrow \mathrm{A} + \mathrm{B}^+ + \mathrm{e}$, can significantly contribute to the excitation and ionization rates in plasma [66].

The common inverse processes, where electrons and ions are lost by mutual recombination, are the following: *three body recombination*, $\mathrm{A}^+ + 2\mathrm{e} \longrightarrow \mathrm{A} + \mathrm{e}$, where two electrons are necessary to conserve momentum, and *radiative recombination* $\mathrm{A}^+ + \mathrm{e} \longrightarrow \mathrm{A} + \mathrm{h}\nu$, where energy and momentum differences are balanced by the emission of a photon. However, the

most important loss mechanism for both electrons and ions in the low pressure discharges is diffusion towards the walls, which serve as a sink for the charge species.

If the neutral species A has a high electron affinity (e.g., F), the *electron capture* process results in the generation of a negative ion, $\mathrm{A} + \mathrm{e} \longrightarrow \mathrm{A}^-$.

When a discharge is operated in a reactive atmosphere, the excitation or ionization of the reactive molecules significantly affect the discharge parameters. Molecules have numerous accessible rotational and vibrational energy states that require much less energy in order to be excited than single atoms. Consequently, there are much greater electron energy losses in comparison with non-reactive discharges.

When an electron collides with a molecule AB, a number of gas-phase processes may occur, such as:

Dissociation, $\mathrm{e} + \mathrm{AB} \longrightarrow \mathrm{A} + \mathrm{B} + \mathrm{e}$, and *ionizing dissociation*, $\mathrm{e} + \mathrm{AB} \longrightarrow \mathrm{A}^+ + \mathrm{B} + 2\mathrm{e}$, are electron impact fragmentations of molecules which result in the formation of neutrals, charged chemically reactive radicals, or smaller atomic or molecular fragments.

Dissociative attachment, $\mathrm{e} + \mathrm{AB} \longrightarrow \mathrm{A}^- + \mathrm{B}$, is a dissociation of the molecule, where the products are a negative radical and a neutral molecular fragment. The reverse process is called *associative detachment*.

Associative recombination, $\mathrm{e} + \mathrm{A}^+ + \mathrm{B} \longrightarrow \mathrm{AB}$, is an inverse process in which a molecule is formed from the constituent radicals after the collision with an electron.

It should be pointed out that the fragments of reactive molecules are generally much more chemically active than the parent gas molecules. They can accelerate gas-phase reactions and can readily react with the exposed surfaces. This is the reason why plasma discharges are often employed in fabrication of functional coatings based on nitrides, oxides, and other chemistries. At the same time, high gas reactivity may represent a serious issue in reactive sputtering, as it will be discussed in section 2.2.2.

2.1.3 Plasma sheath and secondary electron emission

The thermal velocity of electrons, v_e, significantly differs from that of ions, v_i, within low temperature plasma discharges. This is partly due to their large mass difference, and due to their different thermal energies given by $\mathrm{k}T_\mathrm{e}$ and $\mathrm{k}T_\mathrm{i}$, respectively, according to:

$$v_{\mathrm{e}} = \left(\frac{\mathrm{k}T_{\mathrm{e}}}{m_{\mathrm{e}}}\right)^{1/2}, \text{ and} \tag{2.4}$$

$$v_{\mathrm{i}} = \left(\frac{\mathrm{k}T_{\mathrm{i}}}{m_{\mathrm{i}}}\right)^{1/2}. \tag{2.5}$$

Since $\mathrm{k}T_{\mathrm{e}} \gg \mathrm{k}T_{\mathrm{i}}$ and $m_{\mathrm{e}} \ll m_{\mathrm{i}}$, it is clear that $v_{\mathrm{e}} \gg v_{\mathrm{i}}$. This disparity is responsible for the formation of the boundary layer at the plasma edge known as *plasma sheath*. In fact, the flux of the mobile electrons towards the surrounding surface exceeds the flux of slower ions. If this surface is non-conductive or is an isolated conductor, it will promptly charge negatively with respect to the surrounding quasineutral plasma bulk. This results in a depletion of electrons in the adjacent *sheath* layer and hence in a net positive charge, i.e. $n_{\mathrm{i}} > n_{\mathrm{e}}$. The created charge imbalance will generate an electric field that will slow down the electron flux. Conversely, the flux of ions will be enhanced by the negative wall potential until it equals that of the electrons. The potential of such an isolated surface immersed in plasma is called

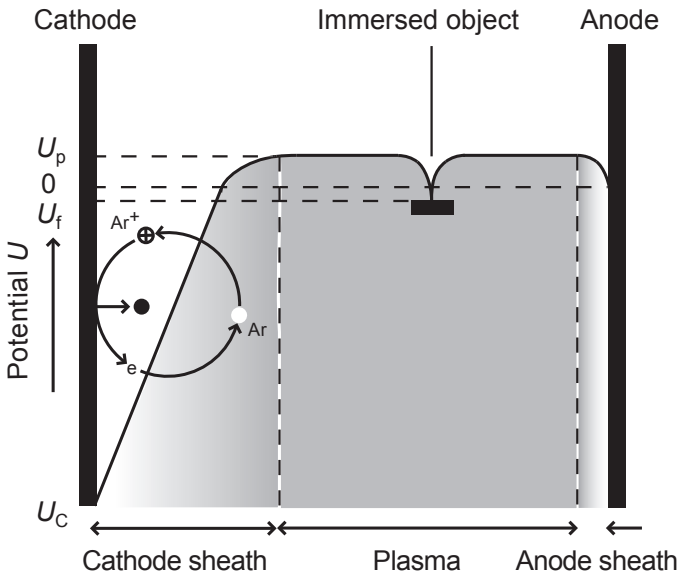

Figure 2.2 Potential distribution of the glow discharge between the cathode and the anode (e.g., chamber wall) of the driving electric circuit. U_{C} stands for the cathode voltage, U_{f} for the floating potential and U_{p} for the plasma potential. Working gas neutral (Ar) and ion (Ar^+), a sputtered target atom (black circle) and a secondary electron (e) released from the target surface are schematically depicted within the cathode sheath region.

floating potential, U_{f}. In case of a grounded conductive surface (such as the chamber wall), the self-established *plasma potential*, U_{p}, will be positive in order to repel the electrons and to accelerate the ions, as illustrated on the right side of Fig. 2.2. The usual value of U_{p} is a few T_{e}/e and the typical sheath thickness, s, is of the order of the Debye length [66].

In a typical glow discharge configuration, one of the plasma-exposed surfaces is negatively charged with respect to the rest of the chamber, and serves as a cathode of the driving electric circuit (left side of Fig. 2.2). The cathode voltage, U_{C}, is usually in the range of $100 - 1000\,\mathrm{V}$. The adjacent plasma sheath then exhibits a high potential drop equal to $|U_{\mathrm{p}} - U_{\mathrm{C}}| \approx |U_{\mathrm{C}}|$ (since $U_{\mathrm{C}} \gg U_{\mathrm{p}}$). The corresponding current density, J_{C}, across the high voltage sheath is limited by the space charge. If s is significantly smaller than the ion mean free path ($\lambda_{\mathrm{i}} = 1/\sigma_{\mathrm{n}} n_{\mathrm{n}}$, where σ_{n} is a collisional cross section), J_{C} can be expressed by the non-collisional Child-Langmuir law [66]:

$$J_{\mathrm{C}} = \frac{4}{9}\epsilon_0 \left(\frac{2e}{m_{\mathrm{i}}}\right)^{1/2} \frac{{U_{\mathrm{C}}}^{3/2}}{s^2}. \tag{2.6}$$

It is well known, that the total ion current leaving the plasma sheath is given by:

$$J = e n_{\mathrm{e}} \mathrm{v}_{\mathrm{B}}, \tag{2.7}$$

where v_{B} is the Bohm velocity [66]:

$$\mathrm{v}_{\mathrm{B}} = \left(\frac{kT_{\mathrm{e}}}{m_{\mathrm{i}}}\right)^{1/2}. \tag{2.8}$$

By setting equal the right sides from Equations 2.6 and 2.7, one can estimate the self-established non-collisional sheath thickness from the known values of U_{C}, T_{e} and λ_{D}:

$$s = \frac{\sqrt{2}}{9}\lambda_{\mathrm{D}} \left(\frac{2e\,U_{\mathrm{C}}}{kT_{\mathrm{e}}}\right)^{3/4}. \tag{2.9}$$

It should be stressed that the high potential fall is necessary for keeping the glow discharge running; Firstly, it accelerates the heavy gas ions, entering the plasma sheath region due to their thermal movement, towards the cathode surface. Their energetic impacts then cause (i) cathode erosion – the phenomenon used in the sputtering process employed in the coating

deposition – and (ii) emission of secondary electrons (SE). Secondly, SE accelerated by the potential difference between U_C and U_p gain energy from the electric field, provided by the external electric circuit, and transfer it to other particles through collisions. In fact, highly energetic SE are of crucial importance for the generation of a number of new ion-electron pairs due to inelastic collisions and also for the heating of other bulk electrons via elastic collisions, which in turn can cause further (primary) electron production by gas ionization process. Without SE, the direct current (DC) discharge would extinguish as a consequence of the charged particle losses towards the surrounding chamber walls and via recombination collisions described in the previous section.

For the relatively low kinetic energies used in a common DC magnetron sputtering process ($U_C < 700\,V$), the SE emission yield, γ_{SE}, is solely a function of the potential energy of the impacting ions (such as their ionization and/or excitation state) and of the work function of the bombarded material, ϕ. This can be illustrated in Fig. 2.3, where γ_{SE} is constant for Ar ions ($E_i \approx 15.8\,eV$) impacting the "clean" metal target surface ($4\,eV < \phi < 6\,eV$) with kinetic

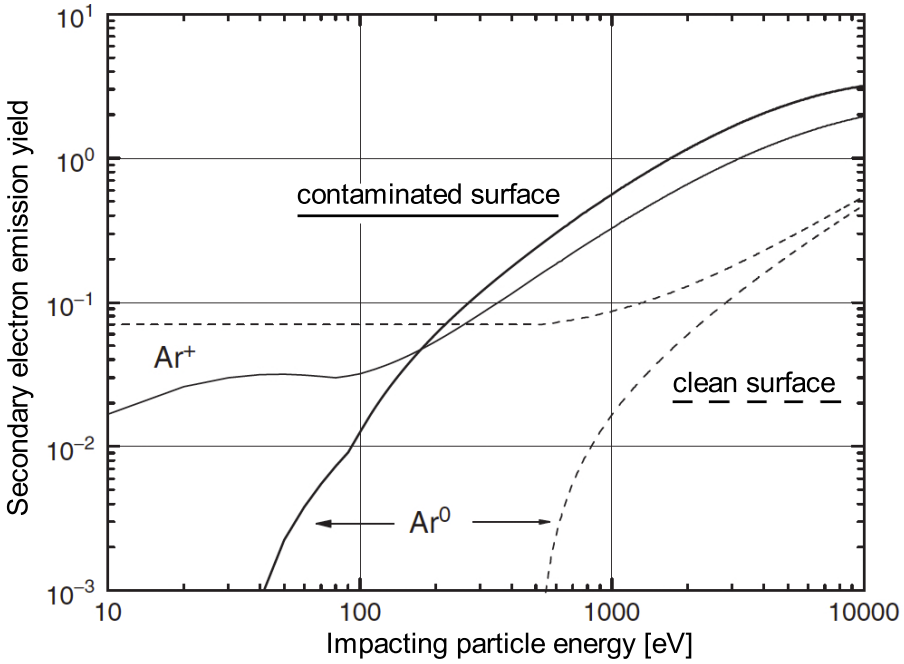

Figure 2.3 Electron emission yield for Ar ions and Ar neutrals incident on clean (dashed curves) and "contaminated" (e.g., oxidized or nitrided) (solid curves) metal surface versus impacting particle energy (proportional to U_C). Modified from [67].

energies up to 700 V. The respective mechanism responsible for *potential electron emission* is the two-electron Auger process [67]. At higher energies, γ_{SE} increases due to the contribution of *kinetic electron emission* caused by Coulomb interactions of the impacting ions with the target atoms [67].

In addition, γ_{SE} is largely affected, among other parameters, by the chemical composition of the target surface; "Contaminated" metal target - e.g., due to surface oxidation or nitridation - can exhibit lower or higher γ_{SE} than the "clean" metallic target, depending on the energy of the impacting Ar ions and neutrals [68], such as illustrated in Fig. 2.3.

Overlooking the last figure, one could conclude that the discharge operation above the contaminated target at $U_C > 300$ V will result in an increased γ_{SE} value, and hence in a higher plasma density (I_C). However, the situation is further complicated since some of the compound materials (e.g., TiO_2 or Nb_2O_5) are reduced under the intense ion bombardment [69]. Consequently, the composition of the upper-most layer of the bombarded surface may significantly differ from both underlying compound and metal (e.g., suboxide may be formed). The value of γ_{SE} for some materials can thus decrease when the surface is exposed to the contaminant, even for $U_C > 300$ V. This is also a common experience in reactive magnetron discharges (operated typically at $300\,V < U_C < 600\,V$) above Nb, Ti and numerous other target materials [69]. It should be also noted, that SE emission may be enhanced by the impacting energetic metastables and photons.

2.1.4 Ambipolar diffusion

In the previous paragraphs the plasma sheath regions close to the chamber walls and electrodes were discussed, while assuming that the remaining plasma volume is a homogeneous environment. In fact, the latter has a nonuniform distribution of ions and electrons with a density gradient due to the existence of a source of charged particles, localized in the proximity of the cathode. Consequent density gradients are the origin of diffusion processes within plasma bulk. In contrast to classical particle diffusion that can be described by Fick's laws, ions and electrons within plasma cannot diffuse independently of each other, owing to their mutual electromagnetic interactions which will counteract the charge separation. As a result, both species diffuse simultaneously, albeit much higher thermal velocity of electrons.

This type of diffusion, common for processing plasmas, is called *ambipolar diffusion*.

Plasma diffusion within the chamber can be affected by the magnetic fields penetrating the plasma region. This is due to the Lorentz force acting on any charged particle that is crossing the magnetic field lines, given by:

$$\vec{F} = q\vec{v} \times \vec{B}. \tag{2.10}$$

The particle trajectory will hence be diverted from its original direction and it will be forced to gyrate in the plane perpendicular to $\vec{B}$, such as illustrated in Fig. 2.4(a). Its gyration, or *Larmor* radius, r_{L}, is then given by:

$$r_{\mathrm{L}} = \frac{mv_{\perp}}{|q|B}, \tag{2.11}$$

where m is a mass and q is a charge of the particle, $v_{\perp}$ is the particle velocity in the plane perpendicular to $\vec{B}$, and B is the intensity of the magnetic field.

Larmor radius of electrons is usually small compared with the curvature of the magnetic field. Consequently, the electrons readily follow the magnetic field lines. In contrast, r_{L}

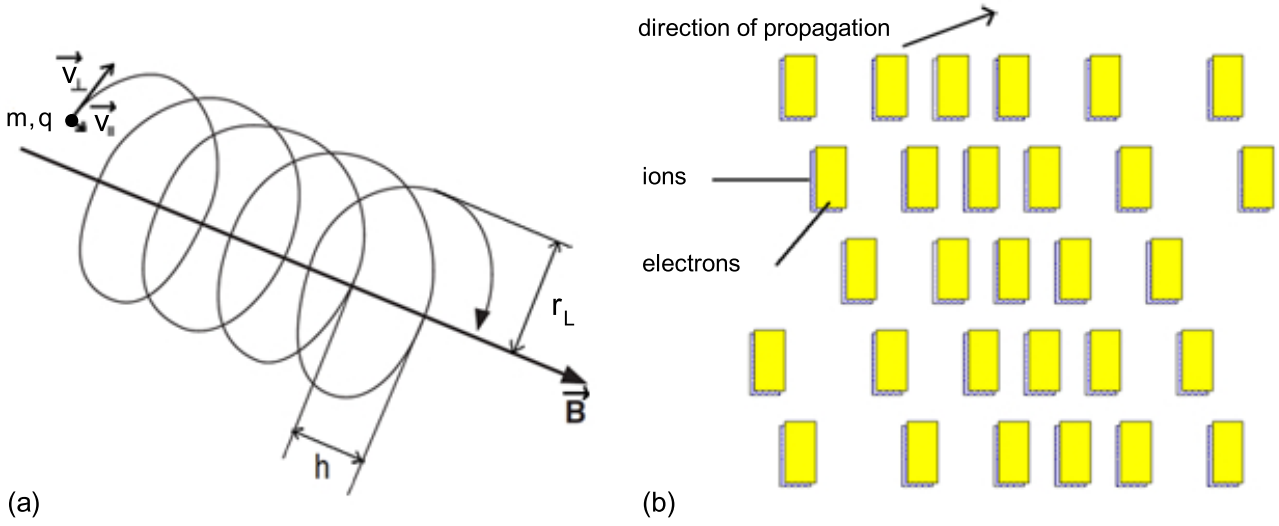

Figure 2.4 Schematic representation of (a) the gyration of a charged particle in a homogeneous magnetic field, and of (b) the ion acoustic wave, a compressional wave of ions and electrons, propagating through the plasma. Modified from [65].

of ions is much larger due to their substantially higher mass ($m_\mathrm{i} \gg m_\mathrm{e}$). Therefore, only electrons can be entrapped in the magnetic field while the ions can more or less freely move across the magnetic field lines. Nevertheless, the motion of ions will be bounded to that of the electrons through the ambipolar diffusion.

It is to be mentioned that plasma environment can support several types of waves, such as electromagnetic and ion-acoustic waves. The ion-acoustic waves are a longitudinal propagation of a disturbance in the ion density, which is swiftly followed by the electron density [66], such as schematically shown in Fig 2.4(b). A specific type of these waves, the ion-acoustic solitary waves that propagate with a fixed velocity and with a preserved shape, can be observed in the HiPIMS discharge during the plasma expansion outwards from the cathode [70, 13]. The observation of such waves is also reported, for instance, in Chapter 5.

2.1.5 Magnetron discharge

Magnetron discharge is a variation of the glow discharge which permits one to reach higher plasma densities at lower pressures (e.g., smaller than 1 Pa, instead of units and tens of Pa) and at lower cathode voltages (e.g., $U_\mathrm{C} \approx 300\,\mathrm{V}$) than the densities achievable with a conventional glow discharge configuration. This is of great significance for the sputtering process efficiency in terms of the coating's growth rate and quality.

The principal difference from the conventional glow discharge configuration consists of the introduction of a set of magnets behind the cathode. The generated magnetic field, that enters and leaves through the cathode plate, is designed to be mostly parallel to the cathode surface and perpendicular to the electric field, such as illustrated in the example of a flat circular magnetron in Fig. 2.5(a). Such a combination of the two fields restraints the movement of the electrons (especially SE) to the vicinity of the target surface.

SE, ejected from the cathode by the impacting ions, gain energy due to the acceleration caused by the voltage gradient within the plasma sheath. The Lorentz force acting on these electrons will force them to gyrate in a cycloidal-like motion with a drift in a direction perpendicular to both electric and magnetic field lines. The resulting movement of the gyrating electrons creates an azimuthal electron current (called *Hall current*) within the toroidal re-

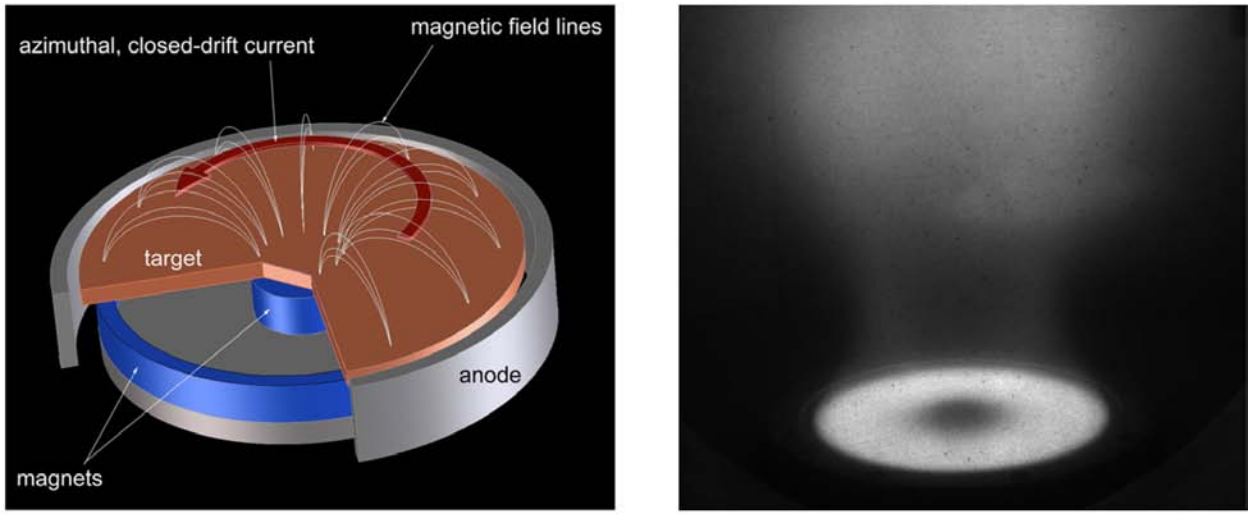

Figure 2.5 (a) Structure of a planar circular magnetron similar to the one used in the presented work, showing the cathode (target), the anode and the set of magnets. Magnetic field lines are illustrated by the white thin lines and the azimuthal drift current due to the confined electrons by the thick arrow. The racetrack region will be created directly under this magnetized zone. Reproduced from [71]. (b) Photograph of the emission from a discharge in pure N_2 atmosphere above a magnetron powered by HiPIMS PS at $U_C \approx 800$ V. The bright emissive toroidal region above the cathode surface marks the region of the strongest electron confinement.

gion above the cathode surface, defined by crossed magnetic and electric fields. Trapped electrons are sometimes referred to as *magnetized* since they are not able to leave the torus without collisions or plasma instabilities that would modify their gyration trajectory [66].

In general, the electron residence time within the target proximity is substantially prolonged and the losses to the chamber walls (anode of the external circuit) are minimized. Consequently, the number of ionization and excitation collisions that each electron may undergo with the surrounding gas neutrals (not confined by any field) is increased and the plasma density rises. As an illustration, a bright emission originating from the region with the highest density of magnetized electrons and excited atoms is visible in Fig. 2.5(b). Here, it should be noted that generated ions can pass freely through the magnetized region since their gyration radius is too large, usually on the same scale as the plasma processing chamber. They can be accelerated by a large potential fall towards the cathode and, consequently, cause its erosion. The resulting ring-shaped erosion zone that develops with time on the target surface is called *racetrack*.

Fig. 2.6 shows the two principal types of the magnetron design: balanced and unbalanced. In the former case, magnetic field lines form closed loops above the target surface, while in the latter case some of the lines expand into the chamber due to the different strength of the inner and outer magnetron magnets. The balanced magnetic field configuration does not permit the plasma to expand far from the cathode surface due to the effective electron confinement described above, and thus only a few ions can leave the dense plasma region. In contrast, unbalancing the magnetic field of the magnetron increases the escape probability of the electrons that may follow the open magnetic field lines, accompanied by the ions due to the diffusion process described previously. Plasma hence spreads further from the target (as visible on the example of the strongly unbalanced magnetron in Fig. 2.5(b)), and the ion fluxes towards the substrates are significantly enhanced. This may be advantageous, for instance, in the preparation of the dense coatings as discussed in section 2.2.4.

In some specific applications, the magnetron discharge is operated in the pulsed DC mode, also known as pulsed magnetron sputtering (PMS) discharge. If the PMS repetition frequency, f, is lower than several kHz, the discharge fully extinguishes in between the individual pulses. At higher frequencies, some of the long living plasma particles survive untill the following pulse onset. Therefore, the discharge is not quenched during the "off" period but it pulses in between the high and low density states. Frequency, pulse width, and also pulse polarity can then be used as variables for customizing the plasma parameters and

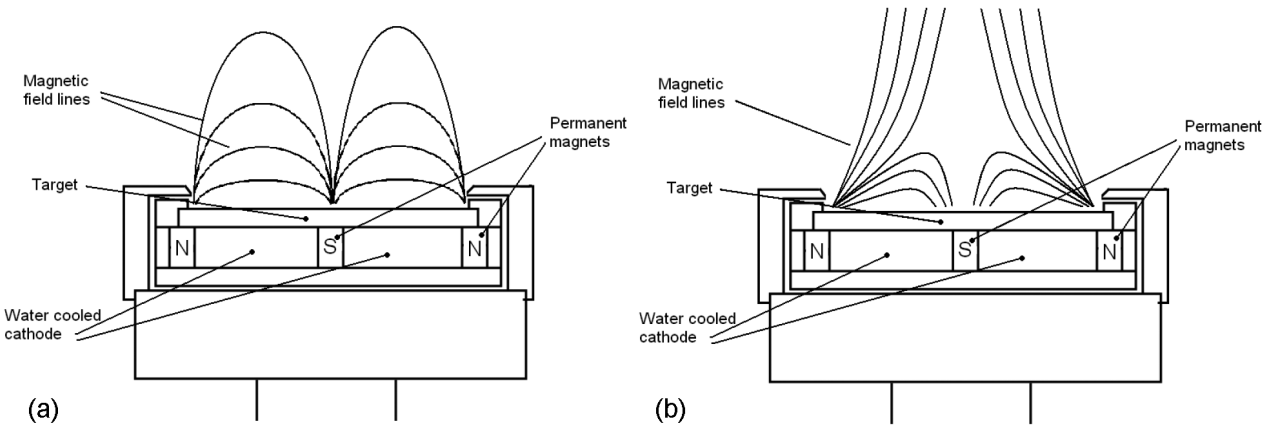

Figure 2.6 Schematic drawing of the cross-section of the balanced (a) and unbalanced (b) types of magnetrons. Modified from [66].

target conditions. For instance, the possibility to apply bipolar pulses is beneficial in the reactive sputtering where a non-conductive compound may be formed on the target surface; Positive bias attracts the plasma electrons to neutralize any charge build-up produced during the negative portion of the cycle. In this way, the arc formation probability is significantly reduced or eliminated [7, 72]. This type of discharge, operated usually in the frequency range $10\,\mathrm{kHz} < f < 200\,\mathrm{kHz}$ (called mid-frequency (MF) range), is hence very popular in the coating industry.

Another common type of magnetron discharge employs alternating current (AC) RF power instead of DC. The usual pulsing frequency is $f = 13.56\,\mathrm{MHz}$. At this frequency, the ions cannot follow the potential fluctuations near the target/chamber walls due to their high mass, and flow out of the plasma with approximately constant flux. In contrast, the electrons can reflect these fluctuations, while maintaining the Maxwellian distribution [65]. Furthermore, the electrons can gain energy from the expanding and receding plasma sheath, which significantly increases the high-energy tail of the EEDF [66]. The ionization probability is thus enhanced (and subsequently the plasma density), and the discharge can be operated at lower working pressures than DCMS or PMS. This may be advantageous if the incorporation of impurities (inherent to any background atmosphere) in the deposited film is to be minimized.

Due to the large difference in the electron and ion mobilities, the average self-established target potential will be negative during the majority of the RF cycle, and positive during a short extent of time [66]. The latter period will prevent any charge built-up on the target surface, such as in the bipolar DC pulsing. Therefore, the RF discharge can be used for sputtering of the insulating targets. Moreover, due to the significantly higher f than that used in MF discharges, the RF technique can effectively couple sufficient power for sputtering to even thick insulating targets (e.g., 0.1-1 cm) [72]. This is also why RF magnetron sputtering (RFMS) is commonly applied in the preparation of oxide films, mainly in the semiconductor industry. A drawback of this technique is the need for the specialized RF generator and impedance matching network, which are more costly than DC PS, and more difficult to scale up. In addition, the obtained deposition rates are usually substantially lower than those of DCMS and PMS.

2.2 Sputtering and thin film deposition

2.2.1 Fundamentals of sputtering

Sputtering is the target material vaporization by momentum transfer from bombarding atomic-sized particles. In principal, it is a statistical process which occurs as a result of a collisional cascade initiated at the target surface by incident energetic projectile particles. In magnetron sputtering, these particles are usually gas ions that are accelerated by the strong electric field of the plasma sheath adjacent to the cathode.

The incident ion first impacts the surface or near-surface atoms of the solid and conveys some of its energy to the surrounding atoms. If this energy is high enough to break the atomic bonds and to dislodge some of the impacted atoms, one or more of these atoms may be removed from the solid. Sputtering mechanisms can be divided into three principal categories, depending on the kinetic energy of the impinging ion. These are (Fig. 2.7): (a) single knock-on events where the impacting ion removes one of the target atoms from its lattice position, which itself may then transfer its energy to the other atoms by another knock-on event, (b) linear collisional cascades, which involve numerous subsequent knock-on events, and finally (c) spikes, in which the bombarding particle sets in motion simultaneously many neighboring

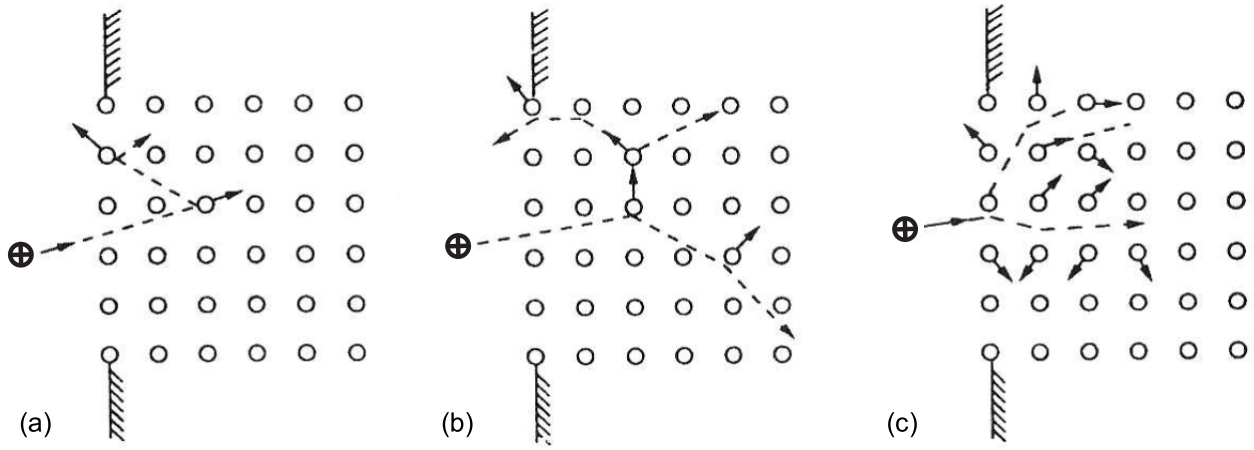

Figure 2.7 Schematics of the three principal regimes of sputtering: (a) single knock-on (low energy), (b) linear collisional cascade and (c) spike (high energy). The impacting working gas ions are marked by open circles with an inscribed plus sign and target atoms by empty open circles. Particle trajectories are highlighted. Modified from [3].

atoms alongside its trajectory in the impacted area due to locally increased temperature. In principle, the higher is the impacting ion energy, the higher is the amount of the dislocated and sputtered atoms (for energies up to approx. 10^4 eV).

The energy distribution of the sputtered atoms, $F(\epsilon)$, originating in the collision cascade initiated by the heavy ion impacting the target under normal incidence can be approximated by Thompson formula, that can be simplified as: [73]

$$F(\epsilon) \approx \frac{E_\mathrm{b}}{(\epsilon + E_\mathrm{b})^3}, \tag{2.12}$$

where ϵ is the sputtered atom energy, and E_b is the binding energy of the target atoms.

The sputtering efficiency is determined by the sputtering yield, Y, which is defined as the ratio of the number of emitted target atoms per incident particle. Y depends on the elemental composition of target – particularly on its mass, density, and lattice and surface binding energy – and on the mass, energy and angle of incidence of the bombarding projectile. In contrast to the emission of SE, which depends mainly on the potential energy of the impacting particle, both ions and neutrals can be used for sputtering even at low impacting ion energies (lower than 1000 eV).

Y is usually higher when the mass of bombarding particles is of the same order of magnitude or larger than that of target atoms. Hence, a selection of suitable working gas for the plasma discharge is essential. Typically, argon (Ar) is commonly used for sputtering because of its inertness, relatively high mass (40 amu) and low cost. Mixtures of argon with reactive gases are commonly used for the preparation of compound materials.

The value of Y for the common metallic target materials bombarded by Ar, and for the range of the accelerating U_C used in sputter-deposition, is typically near unity and varies within one order of magnitude. This can be illustrated by plotting Y as a function of the impacting ion energy for several elements bombarded by Ar ions (Fig. 2.8). In contrast, Y reaches significantly lower values if the target surface is composed of non-metallic compounds, such as oxides or nitrides, which can be formed during the sputtering in reactive gas mixture. It should be noted that Fig. 2.8 does not show the energetic threshold of the sputtered material, given by its surface binding energy, which usually ranges in between 10 eV and 30 eV for metals [74].

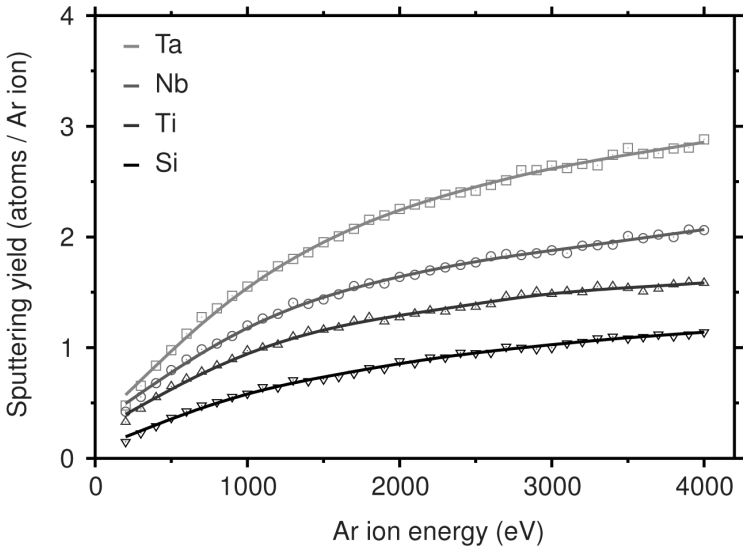

Figure 2.8 Sputtering yield for several target materials as a function of the energy of the bombarding Ar^+ ions, calculated using software TRIM [34]. Courtesy of J. Čapek.

Sputtering process is accompanied by numerous other phenomena, such as surface topography alteration and target heating [7]. Specifically, the latter effect can represent a serious issue which may cause target overheating and melting. Therefore, the sputtered target needs to be effectively cooled. Target cooling also minimizes the amount of radiant heat in a sputtering system which may be important if the treated/coated substrates are temperature-sensitive.

2.2.2 Reactive sputtering and hysteresis

DCMS and PMS techniques are commonly used to deposit thin films of compound materials by two principal ways: by sputtering either from a compound target or from an elemental target in the reactive gas mixture. While the former approach is mainly limited to conducting compounds, practically any material can be synthesized when sputtering the elemental target in a partial pressure of reactive gas. Therefore, diverse compounds based on oxides, nitrides, oxynitrides, carbides or sulphides are commonly prepared in reactive sputtering employing mixtures of Ar with N_2, O_2, C_2H_2, H_2S or their mutual mixtures.

The principal advantage of the use of reactive gases is their high chemical activity which is further enhanced in various inelastic collisions within plasma discharge (section 2.1.2).

Majority of the reactions occur on the exposed surfaces, where the reactive gas binds with the sputtered material and forms a compound. These reactions are vital for the formation of the desired coatings. On the other hand, the compounds are also formed on the cathode surface, which may be facilitated by the higher temperature of the latter due to massive ion bombardment. If the compound layer formation rate exceeds the sputtering rate, the target is referred to as *poisoned*. This phenomenon, commonly encountered in the reactive DCMS, is the origin of several issues.

Firstly, Y of the formed compound drops by about an order of magnitude compared to Y of the metallic target surface, which substantially reduces the film deposition rate, r. This effect can be illustrated by the abrupt drop in r of Nb films prepared by reactive DCMS discharge operated above a Nb target in the O_2/Ar mixture presented in Chapter 8. Secondly, the compound layer formed on the target surface may result in positive charge accumulation due to impacting ions, since most of the formed compounds are dielectric. Charge accumulation may give rise to arcing and the subsequent formation of droplets. These can deteriorate the coating in preparation. It should be highlighted that the compound may also be formed on the sides or in the center of the cathode at lower reactive gas flows than necessary for its complete poisoning, since these areas experience lower ion bombardment than the racetrack area. Hence, charge build-up and the subsequent arcing may be encountered at lower reactive gas concentrations than is the threshold necessary for target poisoning.

Fig. 2.9 illustrates an example of the evolution of U_C and p with the varying oxygen flow, $\Phi(O_2)$, during a reactive DCMS discharge operated above an Al target in the O_2/Ar mixture. At $\Phi(O_2) < 2.3$ sccm, both p and U_C are approximately stable, even though $\Phi(O_2)$ rises. The reactive gas is being absorbed (gettered) on the substrate surface and on the chamber walls where it reacts with sputtered Al and forms under-stoichiometric AlO_x oxide. These suboxides are also formed on the target surface but are effectively removed by the bombarding Ar ions.

If $\Phi(O_2)$ is further increased and stoichiometric Al_2O_3 is formed, no more of the reactive gas can be absorbed on the substrate and on the chamber walls. Subsequently, the compound formation rate on the target rises and Y decreases. As a result, the partial pressure of the unused reactive vapors in the chamber (and hence the total pressure p) increases since the

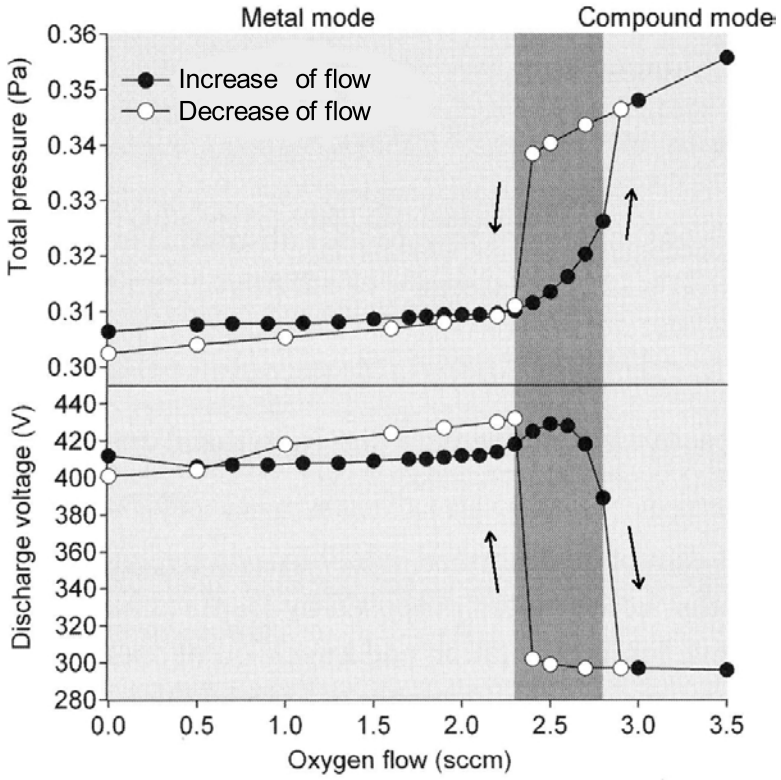

Figure 2.9 Hysteresis curves for the reactive sputtering discharge above Al cathode in O_2/Ar mixture. The argon pressure and the discharge current were kept constant at 0.3 Pa and at 0.3 A, respectively. Transition region between the metallic and poisoned target is highlighted. Reproduced from [7].

supply of Al, that otherwise serves as getter of the oxygen, is reduced. This further intensifies Al_2O_3 formation rate on the cathode until its full coverage. The transition in the target composition from the metallic to the poisoned regime is also reflected by an abrupt drop in the U_C, due to the rise in γ_{SE} as discussed in section 2.1.3. Further rise in $\Phi(O_2)$ is followed by a linear growth of p while U_C stays constant.

Conversion of the target back from the poisoned to the metallic state occurs at a lower value of $\Phi(O_2)$, as a consequence of the lower Y for the formed oxide layer. Thus, both curves for U_C and p follow different pathways with the increasing and decreasing $\Phi(O_2)$ (Fig. 2.9). This phenomenon is known as *hysteresis* and presents a real challenge for the deposition of compound coatings by DCMS. In order to prepare a stoichiometric film at a viable deposition rate, one has to operate the discharge at a certain critical value of the reactive gas flow that is at the edge of the transition towards the poisoned target state. However, stabilization of

this critical flow is not an easy task since any process instability or perturbation result in an irreversible fall to the poisoned mode.

The outcome of the reactive process can be predicted using the so-called *Berg's model* [76]. This model successfully describes the basic hysteresis behavior in sputtering discharges, even though it is based on a simplified approximation of reactive processes on the cathode surface; It assumes formation of a single chemisorbed compound monolayer on the target. More recently, it has been reported that other processes, such as reactive ion implantation and knock-on events of previously chemisorbed atoms into the target, can play an essential role in the target poisoning since they increase its oxidation rate [77, 78, 79, 80]. For instance, Amassian *et al.* have investigated ion-surface interactions at the RF-powered electrode during O_2 surface treatment in a PECVD environment [79] and during reactive sputtering [80] by *in situ* real-time spectroscopic ellipsometry monitoring of the target surface, complemented by Monte Carlo simulations. The authors have identified oxygen subplantation as responsible mechanism for damage layer formation and target oxidation. Consequently, it has been argued that subsurface oxidation should be taken into account even in analytical modelling of the reactive sputtering process, in agreement with the latest findings summarized in Ref. [7].

2.2.3 Reactive sputtering control

A common way of stabilizing the deposition conditions in the transition zone of the hysteresis is to implement a feedback control of the reactive gas flow, based on the monitoring of the cathode voltage, reactive gas partial pressure, or optical emission from the discharge [81]. There are also several means to reduce or even eliminate hysteresis; One approach is to significantly increase the pumping speed, which decreases the amount of the unused reactive gas in the chamber [82]. Other approach is to substantially decrease the size of the cathode surface [83]. However, both of these solutions are rarely employed in industrial-sized coaters since the price of the necessary equipment may be extremely costly.

Another approach is to use bipolar MF pulsing (PMS) in which the target is alternatively sputtered and neutralized, as previously discussed in section 2.1.5. The pulse frequency needs to be adjusted according to the sputtered compound composition, and more specifically, according to its breakdown voltage threshold; The lower the threshold, the higher the frequency

must be in order to prevent the positive charge accumulation that could result in arcing [72]. Furthermore, the pulse duty cycle should be lower than 65% if a long duration arc-free process is to be reached, as reported in Ref. [84].

In some applications, such as architectural and automotive glass production, the AC MF sputtering is performed in a dual cathode configuration; Here, one of the magnetrons serves as a cathode and the second one as an anode for a half of the cycle. Afterwards, their polarity is reversed. In this way, one of the targets is always sputter-eroded from the compounds while the other one is neutralized. This significantly reduces the probability of arcing and stabilizes the transition into the fully contaminated cathodes [81]. In addition, the "disappearing anode" effect is effectively suppressed, since there is always at least one clean anode surface, even though the chamber walls are being coated with an insulating film.

Hysteresis-free and arc-free reactive process can be reached by replacing DC by RF power, since even thick insulating compounds (including bulk compound targets) may be sputtered by RFMS. Reactive RFMS is thus widely employed, for instance, in the semiconductor industry. However, the principal drawback of reactive RFMS is the low deposition rate-to-consumed power ratio in comparison to feedback-controlled DCMS or PMS. Consequently, RFMS is not suitable for coating applications where the resulting film thickness and the respective power consumption are both crucial parameters (e.g., protective coating fabrication). Most interestingly, the hysteresis-free sputtering may also be achieved in HiPIMS, using low repetition frequency and low duty cycle unipolar pulses of high voltage (e.g, $U_{\mathrm{C}} > 600\,\mathrm{V}$), as demonstrated in the example of reactive NbO_x deposition in Chapter 8.

2.2.4 Energy requirements in thin film growth

The microstructure and morphology of sputter-deposited films are determined by the elementary processes of surface diffusion of condensing atoms (*adatoms*) and by the subsequent film formation phenomena, such as nucleation and crystal growth. These atomistic processes are directly affected by the energy and time available to the adatoms to move around on the substrate before they bond to the surrounding atoms. If the supplied energy and/or the time of diffusion are insufficient, adatoms cannot find the binding positions with the lowest possible energy on the underlying crystalline lattice. The resultant films frequently possess

porous columnar microstructure and tensile stress [85].

The most straightforward way how to increase the energy flux towards the forming film is to heat the substrates during the deposition process. In addition to the enhanced surface diffusion, the volume diffusion and the consequent recrystallization of the formed film microstructure may contribute to the desired film densification. However, film preparation at elevated substrate temperatures is often undesirable. Therefore, deposition processes are usually performed at much lower temperatures than the melting point of the prepared material.

Another way to enhance the mobility of the film-forming adatoms is to convey the required energy locally, on an atomic scale. Some energy can be delivered directly by the condensing species; In the sputtering deposition, the kinetic energy of vaporized target particles is typically between 2 and 7 eV [3]. However, the energy of sputtered atoms travelling in between the target and the substrates may be substantially lowered due to collisions with surrounding gas species, specifically at higher working gas pressures. Such a process is callled *thermalization*. In order to avoid the thermalization and also the unwanted losses of sputtered particles due to the scattering towards the chamber walls, the common deposition discharge is operated at relatively low pressures, in the range of $0.1 < p < 1$ Pa. Nevertheless, the energy left to the condensing atoms is usually not sufficient for the desired film densification and an additional source of energy is necessary [10, 85]. This can be arranged by assisting bombardment of the growing film by the energetic working gas ions (e.g., Ar^+). Another way is to ionize a fraction of the condensing target atoms, whose energy (and direction) can be tuned by the substrate bias, such as previously outlined in section 1.4 (Chapter 1).

The effect of ion bombardment can be characterized by two principal parameters; The first one is the arriving ion's kinetic energy, E_{kin}, which is an additive of the ion energy leaving the plasma, E_0, and its acceleration within the plasma sheath given by:

$$E_{\mathrm{kin}} = E_0 + Qe|U_{\mathrm{p}} - U_{\mathrm{C}}|, \tag{2.13}$$

where Q is the ion charge state. The second parameter is the "ion-to-neutral" ratio, $\frac{\Phi_{\mathrm{i}}}{\Phi_{\mathrm{n}}}$, where Φ_{i} stands for the ion flux bombarding the growing film, and Φ_{n} stands for the condensing film atoms (comprising also the neutralized condensing film ions).

Another parameter of interest is the energy per deposited particle, E_{P}, that can be ap-

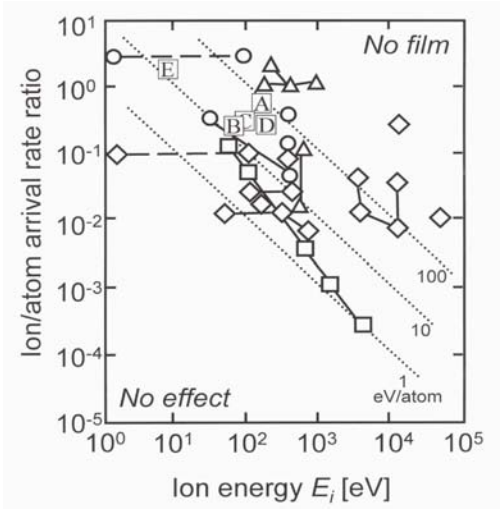

Figure 2.10 Plot of critical ion/condensing particle arrival rate ratio $\frac{\Phi_i}{\Phi_n}$ over critical ion energy E_i, required for film structural modification (particularly densification) of: (A) $SiN_{1.3}$:H, (B) SiO_2:H, (C) a-C:H, (D) and (E) TiO_2 obtained from dual MW/RF plasma. Other data points stand for different materials obtained by various PVD techniques: in circles SiO_2, in triangles other dielectrics, in squares metals, in diamonds semiconductors. Several values of E_P are highlighted by dashed lines. Reprinted from [86].

proximated in the simplest case of non-reactive deposition process as a multiplication of the two above-defined variables:

$$E_P \approx E_{kin} \cdot \frac{\Phi_i}{\Phi_n}. \tag{2.14}$$

Fig. 2.10 shows the plot of the experimentally obtained critical $\frac{\Phi_i}{\Phi_n}$ vs. critical E_{kin} values that are required for film structural modification for several IPVD and PECVD deposition techniques. It should be noted that energetic conditions leading to dense films exhibiting low internal stress and good environmental stability were usually reached for E_P within the range $1 < E_P < 100$ eV [86, 87]. This illustrates that a single parameter can be used for characterization of the energetic requirements for the film structural modification due to ion bombardment. Nevertheless, it has been demonstrated that E_P is not an universal parameter for describing effects of ion irradiation on the film microstructure. Instead, varying E_i and $\frac{\Phi_i}{\Phi_n}$ lead to diverse microstructures [10, 11, 88]. It has been shown that it is desirable to keep the ion energy at low ($10 - 50$ eV) or intermediate levels (≤ 100 eV) while keeping high ion fluxes, if dense good-quality films are to be fabricated [1, 10]. In this way, the atomic mixing

at the growing surface and the consequent working gas entrapment (resulting in an increased lattice strain) are minimized.

Unfortunately, the ion energy and ion fluxes cannot be decoupled in the majority of deposition techniques, as is the case for MS. In order to permit an independent variation in E_i and $\frac{\Phi_\mathrm{i}}{\Phi_\mathrm{n}}$, numerous approaches have been developed; Among many others, pulsing the discharge (PMS or pulsed PECVD), substrate biasing (DC, pulsed DC, AC RF), and application of assisting ion beams (DIBS) are commonly used solutions [1, 7, 17]. It is also believed, that HiPIMS technique – only recently introduced to the coating industry – has a potential to produce high ion fluxes with low mean ion energy, as will be discussed in section 2.3.2.

2.2.5 The film microstructure and structure zone model

The self-organized structural evolution of polycrystalline films, deposited by PVD techniques at various growth conditions, have been systematically characterized during the last five decades. The obtained model types of film microstructure were correlated to the individual deposition parameters and categorized in the so-called structure zone model (SZM) [89, 90, 91, 92, 93, 94, 95]. SZM can be considered as a "roadmap" which is conceived to facilitate prediction of the structure and morphology of fabricated films, knowing solely the parameters of the deposition.

A first version of SZM for evaporated films was introduced in 1969 by Movchan and Demchishin [89]. It featured three types of possible microstructure, depending on the one single parameter, a homologous temperature, T_h, which represented the ratio of the substrate temperature, T_s, over the melting point of the deposited material, T_m:

$$T_\mathrm{h} = \frac{T_\mathrm{s}}{T_\mathrm{m}}. \tag{2.15}$$

The SZM model has been further expanded to better describe the film microstructure of sputter-deposited films by Thornton [90], Messier *et al.* [91], and Kelly and Arnell [93]. In the work of Thornton, the film microstructure was depicted as a function of T_h and working gas pressure, p, which represented the amplitude of the condensing particles' energy (the higher is p, the higher is the thermalization of the gas species). Instead, Messier *et al.* introduced

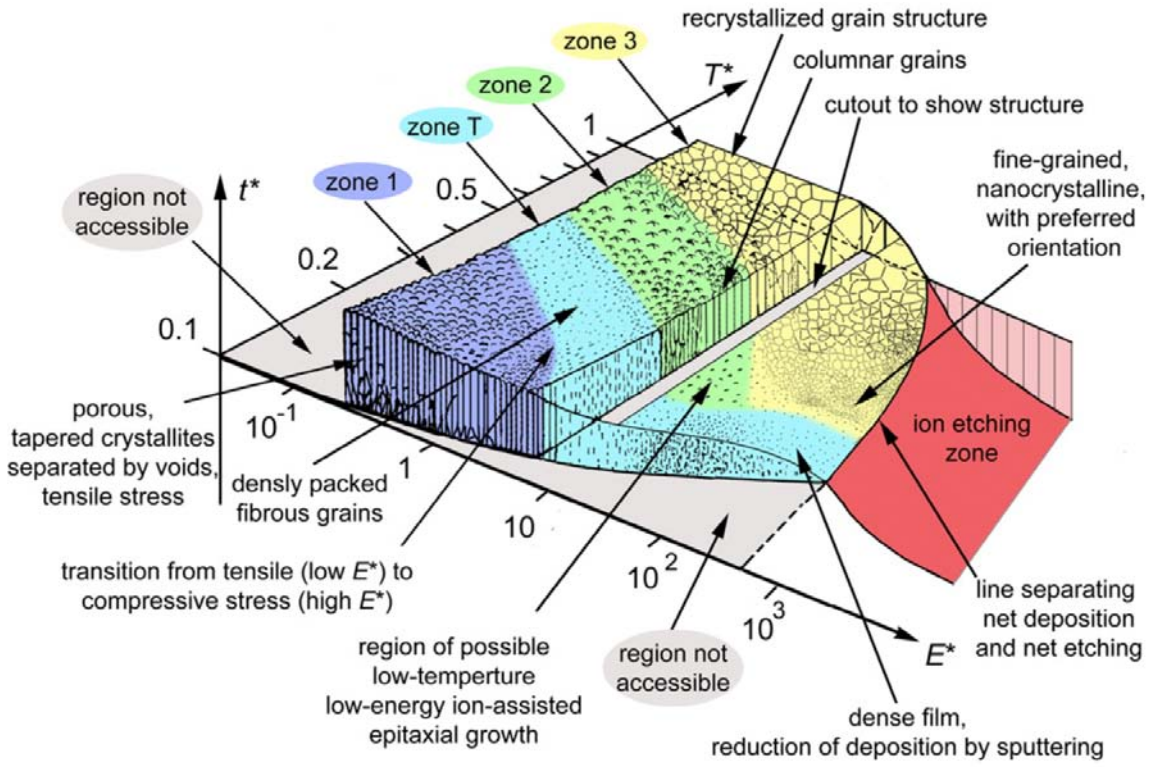

Figure 2.11 Representation of the structure zone model (SZM) showing a cross-sectional view of the types of the possible polycrystalline film microstructure. Borders between the individual zones, as well as all numerical values, are only illustrative. E^* and T^* scales are logarithmic. Reproduced from [95].

the bias potential, U_b, as a second parameter to T_h, which can quantify the energy of the bombarding particles. Furthermore, Kelly and Arnell [93] included the influence of ion fluxes by adding the $\frac{\Phi_\mathrm{i}}{\Phi_\mathrm{n}}$ parameter to the SZM specifically suggested for unbalanced MS. The impact of the co-deposited impurities or additive species on the resulting film microstructure was demonstrated and interpreted in the contribution of Barna and Adamik [92].

Fig. 2.11 represents the latest modification to SZM, recently introduced by A. Anders, that is suitable for energetic plasma-based deposition processes, such as are different variations of IPVD and PECVD techniques, including HiPIMS [95]. Here, the microstructure of the film is depicted in a three-dimensional space. The horizontal axes represent two thermodynamical variables: the normalized energy flux delivered by the bombarding particles, E^*, and the generalized substrate temperature, T^*. The third vertical axis gives an approximative idea of the resulting thickness of the prepared film.

E^* can be expressed by the arriving particles' kinetic energy defined in Eq. 2.13, normalized by the deposited material's cohesive energy, E_C, and multiplied with the ratio of mass of the arriving particles, m_α, to mass of the surface atoms, m_s:

$$E^* = \sum_\alpha \frac{E_{\mathrm{kin},\alpha}}{E_\mathrm{C}} \frac{m_\alpha}{m_\mathrm{s}} J_\alpha \Big/ \sum_\alpha J_\alpha. \tag{2.16}$$

Here, J_α is the flux of particles α (e.g., film neutrals, film ions, assisting working gas ions).

T^* stands for all the thermal effects, which comprise T_h introduced earlier, and a thermal contribution from the ion's potential energy, E_pot, that was transferred to the surrounding atoms upon its impact:

$$T^* = T_\mathrm{h} + \frac{1}{\mathrm{k}} \sum_\alpha \frac{E_{\mathrm{pot},\alpha}}{N_\mathrm{dis}} J_\alpha \Big/ \sum_\alpha J_\alpha, \tag{2.17}$$

where N_dis is the number of the displaced atoms to which the heat was released due to ion neutralization, and E_pot is defined as:

$$E_\mathrm{pot} = E_\mathrm{b} + (E_\mathrm{i} - \phi). \tag{2.18}$$

Overlooking Fig. 2.11, one can recognize several zones which differ in the type of the film microstructure and surface texture. The following paragraphs offer a brief description of the individual film microstructures respective to each zone, classified according to the film growth kinetics

Zone 1 Statistical roughening and self-shadowing effects are observed due to the very limited adatom mobility [94]. The resulting film is composed of fine crystallites or textured fibers of a small diameter, and has a high density of defects and imperfections. Films possessing this type of microstructure are usually in tensile stress due to the relaxation of the open grain boundaries [96].

Zone T Adatoms are able to diffuse on underlying crystallites (grains) they impinged to. The film microstructure is typically formed by V-shaped columns that can overgrow each other only by shadowing effects [94]. Intercolumnar porosity may still be observed.

Zone 2 Condensing atoms can diffuse on the underlying surface. Film structure thus develops by competitive growth of differently oriented neighboring crystals [94]. The film microstructure is dense and composed of columnar grains which can span throughout the whole film thickness. The surface may be faceted.

Zone 3 If the energy supply is sufficiently high, the bulk atoms can participate in diffusion processes within the film volume. Hence, the grain boundaries become mobile, resulting in gradual coalescence and grain coarsening [94]. Final grains can thus be homogeneous and the surface flat. The size of the grains increases with temperature [92].

Ion etching zone With the rising value of E^*, the net thickness of the deposited film decreases. This is due to the increasing sputtering yield of the bombarding ions. Finally, for a certain material-dependent energy threshold situated in between 400 and 1400 eV, the ion sputtering rate equals the film formation rate [95]. For even higher energies, the substrates are not coated but etched.

It should be noted that the substrate etching by energetic ions is commonly used as the pre-treatment procedure in order to sputter-clean the surface oxides and other impurities prior to film deposition. In this way, one can achieve exceptionally smooth substrate-film interface, such as previously illustrated in Fig. 1.3(b) (Chapter 1).

2.3 HiPIMS

2.3.1 Principal parameters

HiPIMS discharge is a type of high-current glow discharge above a magnetron cathode characterized by a high voltage value, typically above 500 V. The consequent power densities can exceed by up to two orders of magnitude those used in DCMS [97, 98]. Most of the power is dissipated in the form of heat, which can cause extensive target heating and/or melting of the magnets within the magnetron. Thus, high power has to be applied in pulses with low repetition frequency, f (usually 50-1000 Hz), and a low duty cycle, D (0.5-5%), in order to enable efficient cathode cooling during the off-time. Since the thermal load of the target is limited by the average power rather than the peak power, the latter can reach very high values (up to several megawatt). Schematic representation of the power delivery in HiPIMS and in MPPMS, in comparison to DCMS, is illustrated in Fig. 1.2 (Chapter 1).

A typical HiPIMS pulse has a square shape and is 50-400 μs long [Fig. 2.12(a)]. In contrast, an MPPMS pulse is much longer (400-3000 μs) and can have a adjustable shape [Fig. 2.12(b)]. Usually, it consists of two or more segments characterized by different voltage and current levels, which are generally lower than in the HiPIMS pulse. Further discussion on the pulse management in both HiPIMS and MPPMS will follow in section 3.1. Common ranges of discharge parameters in HiPIMS, MPPMS and DCMS, together with the reported plasma density values and maximum sputtered-material ionization, are shown in Table 2.1.

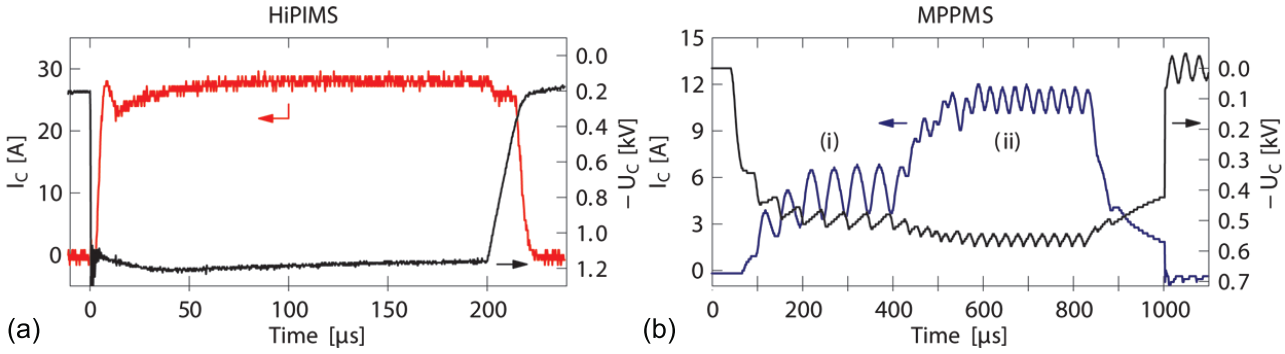

Figure 2.12 Discharge current and voltage waveforms of the HiPIMS and MPPMS pulses operated at $f = 50$ Hz above a Nb target in Ar at 1 Pa. Reprinted from Paper V (Chapter 8).

Table 2.1 Ranges of the typical discharge parameters and selected plasma characteristics during the HiPIMS and MPPMS pulses, and during DCMS. The examples of the maximum reported percentage of the ionized species in the sputtered flux (denoted as ionization ratio) is also listed.

	Cathode voltage	Peak current density	Peak power density	Plasma electron density	Ionization ratio
HiPIMS	500 - 2000 V	1 - 10 A·cm^{-2}	0.5 - 6 kW·cm^{-2}	10^{12}-10^{13} cm^{-3}	over 90%
MPPMS	300 - 800 V	0.1 - 1 A·cm^{-2}	100 - 500 W·cm^{-2}	10^{11}-10^{12} cm^{-3}	N/A
DCMS	300 - 500 V	10 - 100 mA·cm^{-2}	10-100 W·cm^{-2}	10^{9} -10^{11} cm^{-3}	up to 3%

2.3.2 Plasma characteristics

In this section, several selected plasma characteristics of the HiPIMS discharges operated above a metallic target will be summarized. Since there is yet a limited amount of work done on the characterization of the custom-shaped MPPMS pulses, the examples presented below are related solely to the simpler square-shaped HiPIMS pulses. An investigation of the effects of the different power management in HiPIMS and MPPMS on the resulting discharge behavior can be found in Chapter 7 (non-reactive conditions) and Chapter 8 (reactive conditions).

In the HiPIMS discharge, the high power applied to the cathode during each pulse generates dense plasma expanding from the magnetron's racetrack, as illustrated by the time- and space-resolved plasma density monitoring in Ref. [23]. The maximum plasma density can reach up to $n_e \cong 10^{12} - 10^{13}$ cm^{-3} [22, 23, 24, 25, 26, 27], which is up to 3 orders of magnitude higher than in the usual DCMS. The examples of the time evolution of the EEDF and of the respective T_e acquired by Langmuir probe analysis for HiPIMS discharges above a Cr target, are plotted in Fig. 2.13 (a) and (b), respectively. T_e peaks at similar values as in a conventional DC magnetron discharge (up to few eV, according to the pressure, applied power and target material) and it then decreases to much lower values ($T_e \approx 1.0$ eV). Such a drop can be explained by the significant cooling of the electrons in the impact excitation and ionization processes with the sputtered metal atoms that have significantly lower energy thresholds than Ar. Therefore, the measured EEDF at the end of the pulse has typically a Maxwellian-like form, exhibiting lower peak energy than commonly observed in DCMS discharges, and a depleted high energy tail due to the inelastic collisions with sputtered metal [25, 24, 27].

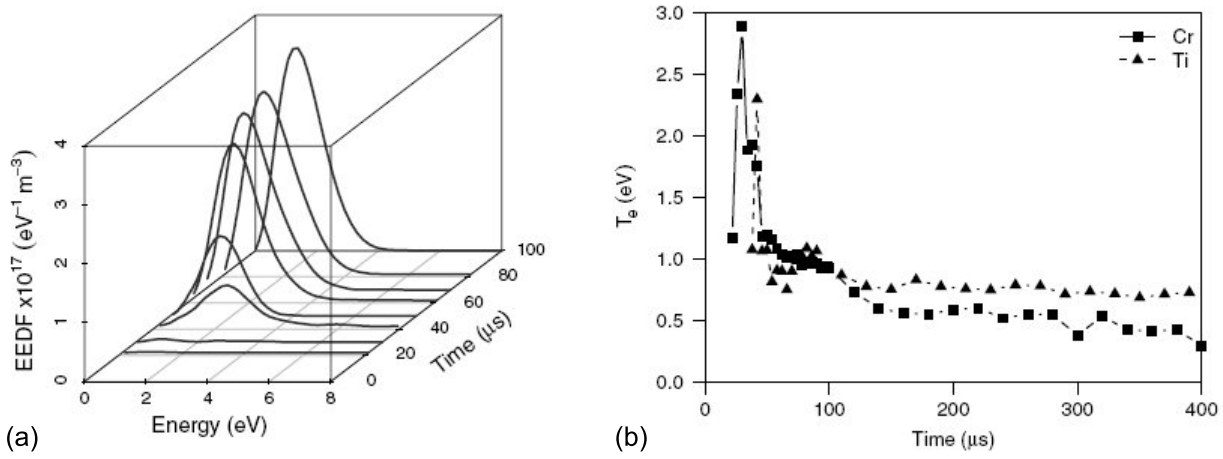

Figure 2.13 Evolution of the EEDF (a) and of the T_e (b) as a function of time measured by the Langmuir probe positioned at $d = 10\,\text{cm}$ from the Cr [and Ti (b)] target in a HiPIMS discharge operated in Ar at 0.28 Pa with $f = 100\,\text{Hz}$. $U_C = -750\,\text{V}$ was applied to the target during the first 70 μs. Modified from [25].

High plasma densities encountered in HiPIMS increase significantly the ionization probability of the sputtered material from the target when compared to conventional DCMS; Firstly, the ionization mean free path decreases substantially down to several cm, which is the scale of the high density plasma region above the target [99]. Secondly, a high quantity of sputtered metal neutrals can accumulate during the pulse in front of the cathode [100], as will be discussed in the following section. This results in their higher thermalization and, consequently, in higher residence time within the most dense plasma region. Indeed, high ionization fraction of the sputtered material reaching up to 30% for Cr [28], 60% for Cu [29] and above 90% for Ti, has been reported [30, 31], as well as significant presence of multiply charged metal ions [34, 32, 33]. Under special conditions, double ionized atoms can even become predominant in the total ion flux on the substrates [33]. High sputtered material ionization was also predicted by modelling [101, 102, 103, 104]. Gudmundsson [101] has shown that the energetic electron impact ionization is the principal mechanism of the metal ion generation during the energetic HiPIMS pulses, while the charge exchange is the dominant process in the post-discharge.

An example of IEDF obtained using plasma sampling mass spectrometry for both working gas and sputtered metal for a HiPIMS discharge above a Cr target is illustrated in Fig. 2.14(a).

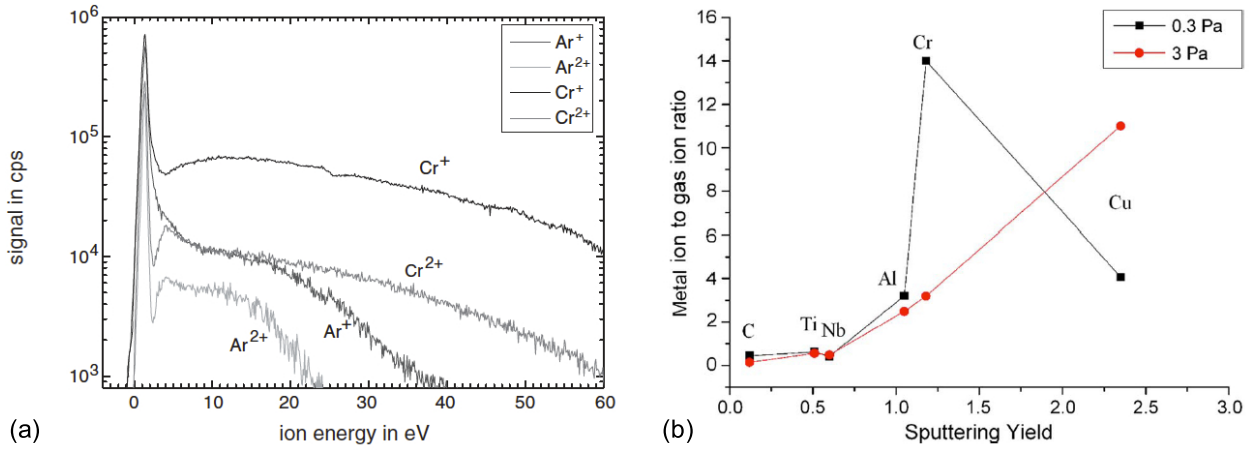

Figure 2.14 (a) IEDFs of ionized Ar and Cr species recorded by mass spectrometry during the 100 μs long HiPIMS pulses ($U_C = 1500$ V) operated at $f = 50$ Hz in Ar at 0.13 Pa. The probe was positioned at $d = 5.5$ cm and at 10 cm from the magnetron's center axis. Reproduced from [105]. (b) Metal-to-gas ion ratio estimated by mass spectrometry at $d = 17$ cm for several elements sputtered by 70 μs long HiPIMS pulses at $f = 50$ Hz and at the same peak current density ($J_C = 1\,\mathrm{A\,cm^{-2}}$). The disparity in the ratio value for Cr and Cu at 3 Pa is a consequence of the large variation in power during the respective discharges. Reproduced from [34].

IEDFs for Cr^+ and Cr^{2+} exhibit a low energy peak that is due to completely thermalized ions, and a significant high energy tail that originates from the Thompson kinetic energy distribution of the sputtered Cr atoms [106, 107, 108]. At certain conditions, more than 50% of ions can have energies higher than 20 eV and the respective IEDF may expand up to 100 eV, as shown by Bohlmark *et al.* for an HiPIMS discharge above a Ti target [106]. It has been also observed that the high energy tail of IEDF grows with the rising cathode current [106, 107, 109, 33], while it decreases with higher pressure and with increasing distance from the target as a result of the metal thermalization in collisions with the working gas [110, 111, 112].

Time-resolved measurements revealed that the high energy tail of metal ion IEDF decreases in both amplitude and extent with the elapsed time from the pulse onset while, at the same time, the intensity of the low energy peak rises [110, 113]. Simultaneously, the tail of the Ar ion IEDF increases, which gives the origin to the important high energy tail of the averaged IEDF for both Ar^+ and Ar^{2+} depicted in Fig. 2.14(a). These observations indicate the collisional energy transfer from the energetic metal ions.

It should be stressed that the mean metal ion energies (e.g., $0.3 - 5$ eV for sputtered Cr ions [107, 110, 112]) reach relatively low values, if compared to those reported with CA, which is another deposition technique capable to generate highly ionized metal plasma (see section 1.4 in Chapter 1). In addition, the metal ions can significantly outnumber the working gas ions, specifically for the high-yield elements, such as shown in Fig 2.14(b). The combination of the low ion energy and of the substantial metal ion fluxes is highly beneficial for the growth of dense films without the unwanted defect generation [10, 17, 86]. This makes HiPIMS a very attractive technique for the fabrication of the functional coatings. Moreover, high metal ion content within the condensing material flux facilitates the coating of the complex-shaped substrates, such as demonstrated in Refs. [13, 15]. A parametric steady-state model for target material fluxes in HiPIMS discharge, originally introduced by D.J. Christie [114], has recently been extended by Vlček and Burcalová [104].

2.3.3 Gas rarefaction and self-sputtering

In the following paragraphs, two distinct dynamic phenomena commonly observed in HiPIMS discharges will be introduced. Fig. 2.14(b) shows that the metal-to-gas ion ratio grows with the sputtering yield (Y) of the metal. This is the fingerprint of the working *gas rarefaction* (gas replacement by sputtered species) originating in the momentum transfer from the energetic sputtered atoms accompanied by the *collisional gas heating*. The latter of the two effects was recently documented by Vitelaru *et al.* [115] who reported that the working gas temperature can rise 4 times (from 300 to 1200 K) during the HiPIMS pulse. The amplitude of the gas rarefaction is a function of the instantaneous amount of sputtered material (determined by Y) and of its mass, such as discussed in the model presented by S.M. Rossnagel [116], and as illustrated for several HiPIMS-sputtered elements in Appendix A.

The gas rarefaction by sputtered metal increases progressively during the individual HiPIMS pulses, while the reverse process (gas refill) takes place in between them. This was demonstrated by the modelling of the volume density of the sputtered and background neutrals by S. Kadlec [100] (Fig. 2.15), and by the experimental analysis of the plasma density distribution by Horwat and Anders [117]. In fact, the current "hump" that is usually observed during HiPIMS pulses operated at low power levels – such as that observed for

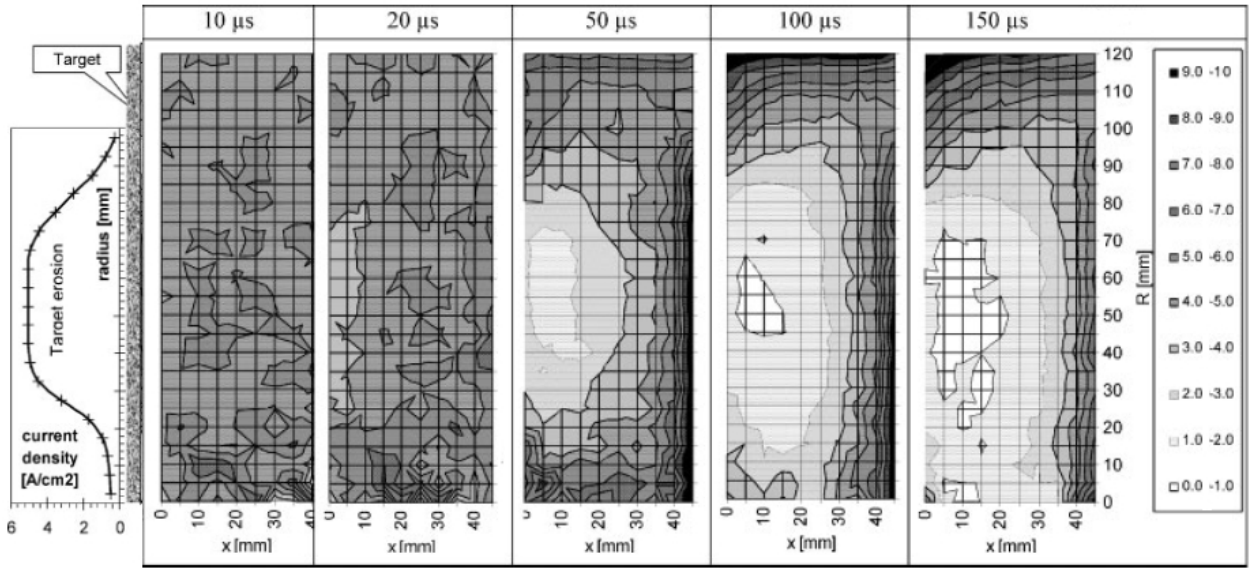

Figure 2.15 Simulated time evolution of Ar gas density during the 200 μs long HiPIMS pulse above a half of the Ti cathode (positioned on the left). The scale on the right is in $10^{13}\,\mathrm{cm}^{-3}$. The average density of Ar prior to the pulse initiation was $4.83 \cdot 10^{13}\,\mathrm{cm}^{-3}$ (equivalent of $p = 0.2\,\mathrm{Pa}$). Modified from [100].

HiPIMS pulses at $U_\mathrm{C} < 535\,\mathrm{V}$ in Fig. 2.16(a) is in fact a sign of the reduction in the gas density since the gas ion production also drops .

An important consequence of significant metal-gas collisions is the feedback that the thermalized sputtered atoms can provide: they themselves can become part of the background gas that subsequently slows down sputtered atoms. Hence, accumulation of the sputtered material in front of the target results also in its higher residence time within the region of the highest plasma density. This increases the probability of its ionization, which is basically the main objective of the high power pulsing. A part of the ionized fraction of the sputtered species may then be attracted back to the cathode ("recycled") and participate in the sputtering process, which is then referred to as *self-sputtering*.

In certain conditions, even self-sustained gasless sputtering can be achieved, such as earlier demonstrated for DCMS [118] and recently also for sufficiently long HiPIMS pulses [119]. The condition for sustained self-sputtering was defined by Hosokawa *et al.* as [118]:

$$\alpha\beta Y_\mathrm{S} \geq 1, \tag{2.19}$$

where α is the probability that the sputtered metal atoms become ionized, β is the probability that the ionized atoms return to the target, and Y_S is the material self-sputtering yield. As $\alpha < 1$ and $\beta < 1$, the condition $Y_S > 1$ is necessary, but not sufficient, for sustained self-sputtering. In particular, the secondary electron emission yield (γ_{SE}) is of crucial importance for keeping the plasma density and hence the vaporized material ionization high [120, 121, 104].

The transition from the gas-dominated sputtering towards the self-sputtering is usually accompanied by a significant rise in current (and power) density, such as illustrated by the current waveforms for HiPIMS discharges operated with $U_C > 530\,V$ in Fig. 2.16(a). Such current "runaway" into a high power discharge can be observed for materials exhibiting Y_S values closely above or under unity, such as Ta, Cr, Al, Ti or Nb, and even for materials for which Y_S is substantially below unity, such as Si and C. This indicates that both target and gas ions may contribute to the target sputtering during the high density discharge, as discussed in Appendix A. The respective generalized runaway criterion is offered in the recently submitted paper by A. Anders *et al.* [122].

Fig. 2.16(b) illustrates that the discharge operation well above the runaway threshold into a high density discharge ($U_C > 530\,V$) results in an important rise in the ion current collected at the substrates. This observation indicates excessive ion production which may

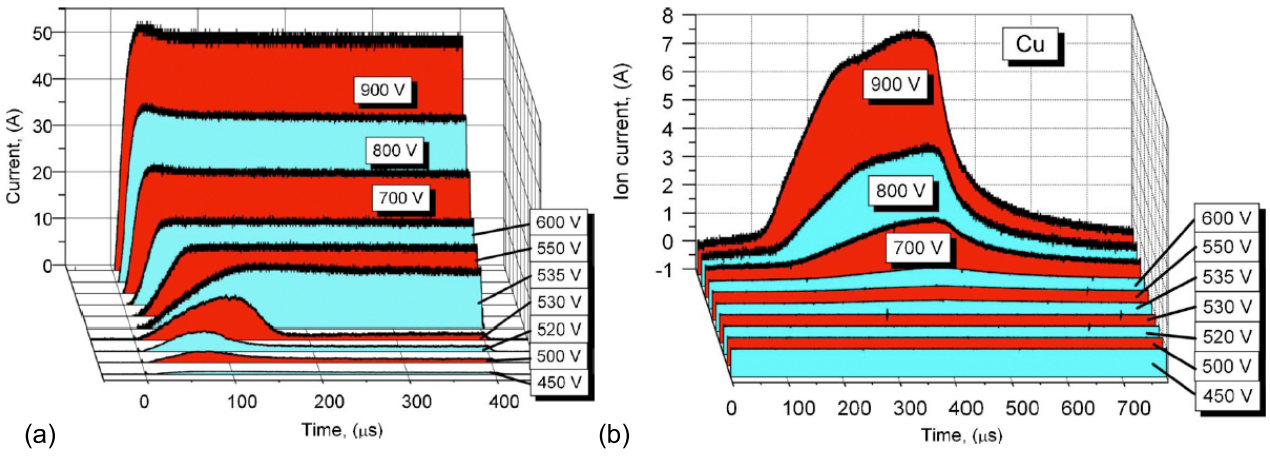

Figure 2.16 Discharge current on the cathode (a) and the ion current at the substrate at $d = 20\,cm$ (b) as a function of U_C during 400 μs long HiPIMS pulses operated at $p = 1.8\,Pa$. Reproduced from [120].

break the "recycling trap" of self-sputtering. Subsequently, a large quantity of the generated ions may escape from the target's pre-sheath region, such as demonstrated experimentally by Andersson and Anders [123] and confirmed by modelling by Vlček and Burcalová [104]. More details about the discharge dynamics related to the transition from the gas-dominated towards the metal-dominated discharge can be found in Chapter 5.

2.3.4 Deposition rate

Deposition rate of the prepared films is of great concern in the coating fabrication, alongside with their microstructure and their properties, since it affects the economics of the production. One of the issues commonly encountered in the non-reactive HiPIMS process is its lower deposition rate in comparison to DCMS, as illustrated for several target materials in Fig. 2.17. The observed deposition rate reduction originates from various physical reasons. The most important ones are: (i) less-than-linear dependence of the sputtering yield on the energy of bombarding ions [124, 125], (ii) loss of the sputtered material via ionization and subsequent back-attraction towards the target [104, 125], and (iii) modified target-substrate transport geometry [104, 126]. The following paragraphs summarize the main reasons:

Effect (i): The deposition rate at the substrate is proportional to the sputtering yield at the target. The latter quantity has a less-than-linear dependence on the impacting ion energy, such as previously depicted on the plot of Y in Fig. 2.8. This non-linear rise of Y (and equally of Y_S) with U_C is an inevitable cause of the deposition rate reduction [124, 125]; Since HiPIMS employs substantially higher values of U_C than DCMS, the consequent deposition rate reduction is also necessarily higher, even if both discharges are operated at the same power load.

Effect (ii): A direct consequence of the self-sputtering phenomenon introduced in the previous section is the loss of the ionized target atoms back to the target. A fraction of sputtered material thus cannot participate in the film formation, but is recycled instead. This recycling (determined by coefficient β from Eq. 2.19) is most significant at U_C values close above the self-sputtering runaway threshold [104, 123]. Target material recycling and the subsequent self-sputtering also result in moderately diminished overall sputtering yield (due to both working gas and target ions), since $Y_S < Y$ [74].

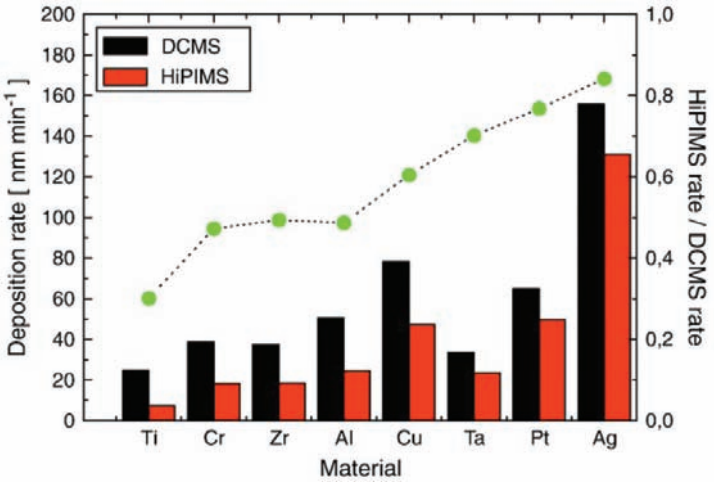

Figure 2.17 Deposition rate for several elemental target materials prepared by DCMS and HiPIMS operated at the same conditions ($P = 125\,\mathrm{W}$, $p = 0.67\,\mathrm{Pa}$, $d = 6.5\,\mathrm{cm}$). The ratio of HiPIMS and DCMS deposition rate is plotted as scattered points. Reproduced from [103].

Effect (iii): In a typical HiPIMS discharge, a large fraction of the sputtered material flux is ionized. Since the movement of the charged species is subject to magnetic fields, the transport of the ionized fraction of the sputtered material is largely affected by the magnetic field configuration of the deposition system; For instance, Bohlmark *et al.* [127] have demonstrated that the deposition rate of HiPIMS-deposited Al in front of the planar target can be increased by 80% by modifying the magnetic field between the target and substrates. Vlček *et al.* [29] have reported the rise in the power-normalized deposition rate of Cu by 31% when increasing the magnetic field strength of the unbalanced magnetron. In addition, recent investigations by Lundin *et al.* [126] and Brenning *et al.* [128] showed that the propagation of ionized species can be largely affected by plasma instabilities, as in the case of anomalous ion transport across the magnetic field lines. This behavior results in an azimuthal ion transport towards the sides of the deposition chamber, and hence in a lower deposition rate on the substrates facing the target.

In contrast to non-reactive conditions, HiPIMS operated in reactive gas mixtures may exhibit a higher deposition rate than common DCMS operated at the same current [12, 49] or power [129]. These observations were interpreted by additional phenomena that affect the deposition process, such as reduced or eliminated hysteresis, and elevated erosion rate. Further discussion on the subject of reactive HiPIMS discharges is offered in Chapter 8.

CHAPTER 3

Experimental methodology

This chapter describes the two types of HiPIMS generators used in this work, as well as the experimental methods and approaches for optical plasma monitoring and material characterization of the fabricated films. The first part elaborates on generation of square-shaped and modulated voltage pulses by HiPIMS and MPPMS PS, and it offers the schematics of the respective electrical circuits. The second part introduces the principles of the Optical emission spectroscopy (OES) technique, and it lists some of its applications for the plasma characterization and process monitoring. In addition, details of the experimental apparatus necessary for OES and fast plasma imaging is offered. The last part is devoted to the description of the diagnostic techniques applied for the evaluation of Nb and NbO_x coatings' properties.

3.1 Characteristics of HiPIMS power supplies

Growing interest in the HiPIMS technique stimulated the development of suitable PS. At the present moment, there is a variety of PS from different producers that provide different pulse shapes and various levels of control over the voltage and current characteristics [53, 54, 55, 56, 57]. The majority of PS on the market can be divided into two principal categories, according to the form of the high power pulses that they produce. These are: (i) square voltage pulse generators (HiPIMS generators), and (ii) modulated pulse power (MPP) generators (MPPMS generators) producing longer, custom-shaped voltage pulses.

The main difference between the voltage delivery and the resulting pulse shapes for the two types of generators used in this work is depicted in Fig. 3.1; While the HiPIMS generator (HÜTTINGER Electronic HMP2/1) produces single unipolar high-voltage pulses (usual length $2\,\mu$s - $200\,\mu$s), the MPPMS generator (ZPulser Axia 180) applies to the target sequences ($500\,\mu$ - $3000\,\mu$s long) of shorter pulses of fixed amplitude. These "micropulses" of adjustable length ($6\,\mu$ - $18\,\mu$s) and duty cycle (several tens of %) generate a "macropulse" of modulated form on the cathode (hence *modulated pulse power*), as systematically illustrated

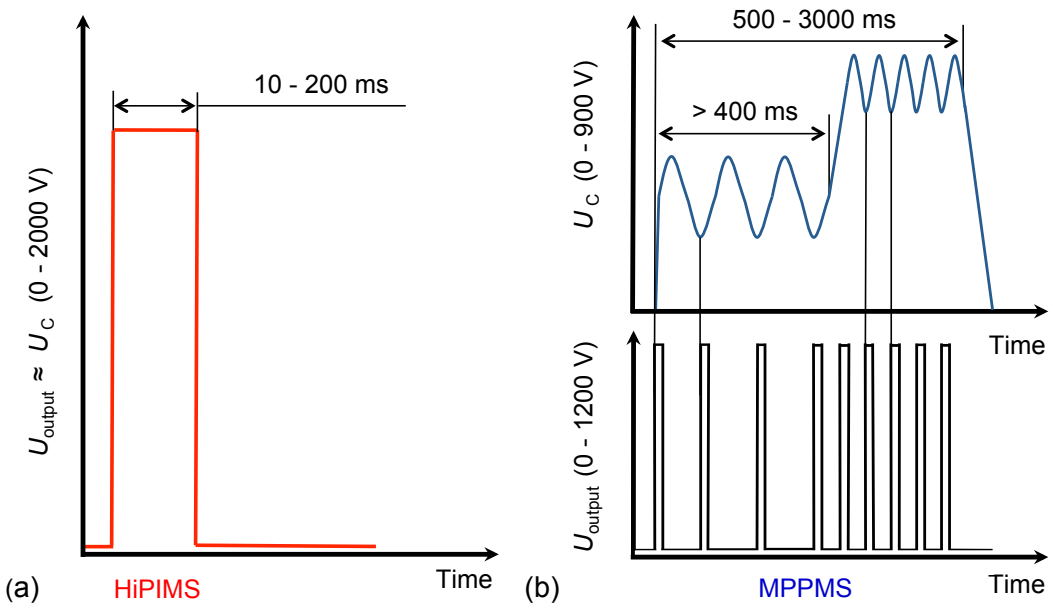

Figure 3.1 Schematic representation of the typical voltage pulses generated by HiPIMS (a) and MPPMS (b) power supplies. Please note that the voltage on the generator output, U_{output}, and the resulting cathode voltage, U_{C}, are equal in HiPIMS. In MPPMS, the pulse shape of U_{C} is formed by a sequence of U_{output} micropulses.

in Ref. [130]. An example of the experimentally obtained voltage and current waveforms for typical HiPIMS and MPPMS pulses is shown in Fig. 2.12 (Chapter 2), and the schematics of the resulting power delivery is depicted in Fig. 1.2 (Chapter 1).

It is to be noted that further details on the power management of the HiPIMS and MPPMS generators used during the herein presented work, together with their specifications, can be found in Chapter 7. In the following subsections, a brief description of the simplified electric circuits and of the related pulse generation in both types of PS is offered.

3.1.1 Square voltage pulse generator (HiPIMS)

Square voltage pulse generator, used by Kouznetsov et *al.* [21] in their pioneer work, is presently the most common type of HiPIMS PS on the market. It usually consists of three units: a DC unit, which can be a specific charging circuit or a common DCMS generator, a pulse unit that is responsible for generation of voltage pulses of defined length and stable amplitude, and a matching unit. A simplified circuit diagram is shown in Fig. 3.2.

The heart of the HiPIMS PS is the pulse unit. It consists of the capacitor bank C of a large capacitance (e.g., 1 μF - 50 μF [131, 132, 17]) that is charged by the DC unit through a thyristor switch. The accumulated charge is then discharged towards the external load (cathode, anode and plasma) through an inductor L within the matching unit, once the semiconductor switch S is closed. Thus, the length of the resulting HiPIMS pulse is set by the period during which the switch S closes the circuit. The inductance coil of the matching unit helps to shape the output current pulse; The higher is its inductance, the slower is the current rise and fall.

The generated cathode voltage is in hundreds V to 2000 V (HÜTTINGER Electronic HMP2/1). Its value should be stable during the entire pulse length (usually 50 μs - 200 μs). However, if the pulse is long and the current is high (e.g., due to the large cathode surface), the voltage amplitude can drop significantly during the pulse duration due to the diminishing charge of the capacitor bank. This effect is depicted in Chapter 5, and also discussed in Appendix A. The current density on the cathode reaches high values (several A cm^{-2}), which in turn increases the probability of arc development. In order to prevent arcing, a current sensor is integrated within the pulse unit; If the current rises above a certain user-defined threshold, the pulse unit is disconnected from the external circuit. Another approach in how to detect arcing is the monitoring of an abrupt drop in the voltage amplitude. Some power supplies can also dissipate the energy accumulated within the cables connecting the PS and the electrodes, as a part of the arc suppression mechanism [53].

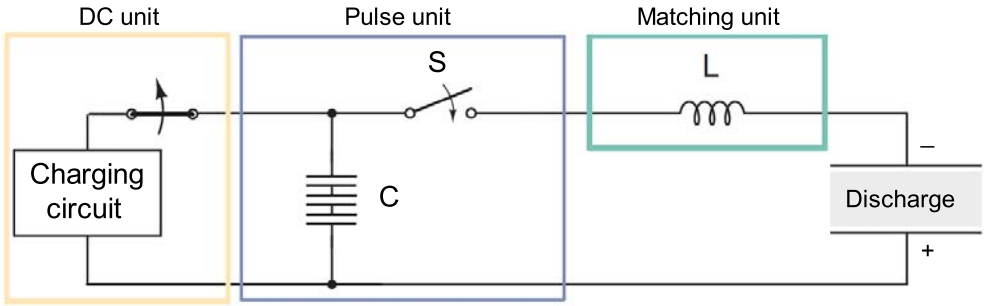

Figure 3.2 Schematics of the electrical circuit of the HiPIMS square voltage pulse generator connected to the discharge load.

3.1.2 Modulated pulse power generator (MPPMS)

MPP generator is a recent modification of the HiPIMS PS, first introduced by Chistyakov and Abraham [133, 134, 130]. The basic schematics of the circuitry is shown in Fig. 3.3(a). DC unit of the MPP generator charges the capacitor bank C1 to a certain voltage level (*voltage load*), usually up to 600 V in amplitude (ZPulser Axia 180). The solid state switch S1 then converts the DC input towards the sequence of bipolar micropulses of defined duty cycle and repetition frequency set by the control circuit. Subsequently, the amplitude of these micropulses is doubled by the transformer T. The form of the micropulses on the primary and secondary coil of the transformer is depicted in Fig. 3.3(b)(1-2). Finally, the unipolar sequence of micropulses [Fig. 3.3(b)(3)] is formed by the LC circuit that consists of inductors L and capacitor C2, and other circuits. MPP PS also features integrated arc control that functions in a similar way as in HiPIMS PS. The duty cycle of the generated micropulses ranges from 5 to 75%, and the micropulse frequency ranges from 8.4 to 62.5 kHz (ZPulser Axia 180). The macropulse duty cycle is limited by 28%.

In contrast to HiPIMS PS, the cathode voltage (U_C) does not equal the voltage on the PS output, U_{output}, such as schematically illustrated in Fig. 3.3(b). Instead, U_C oscillates around a certain value that is set by the cathode charging and discharging rates. In addition, MPP generator permits the use of different "micropulse recipes" (defined by the constant f and D

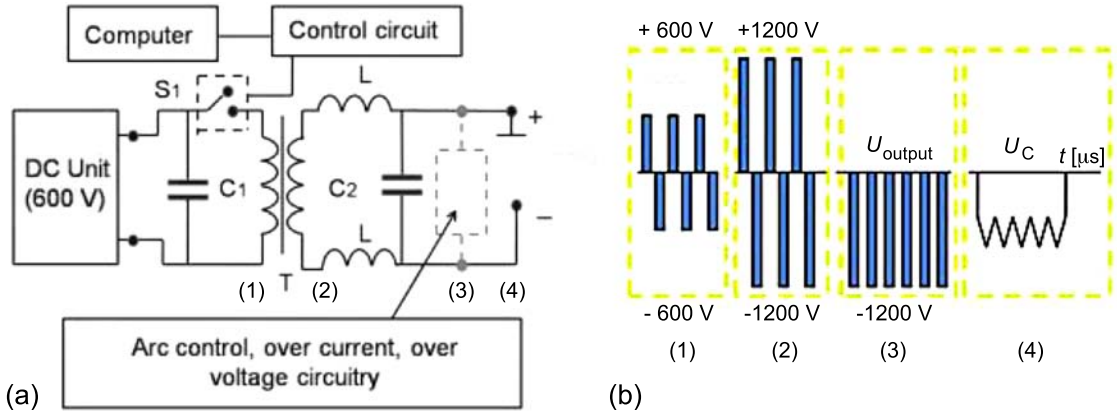

Figure 3.3 Schematics of the electrical circuit of the modulated pulse power generator connected to the discharge load (a), and form of the voltage pulse sequence on different components (1-4) of the power supply (b). Modified from [130].

values) during a single macropulse (500 μs - 3000 μs), which gives the option to further modulate the resulting pulse shape. A typical MPPMS pulse can thus exhibit two or more stages characterized by different voltage and power levels, according to the number of micropulse recipes. An example of the two-stage MPPMS (macro-)pulse can be found in Fig. 3.1(b) or in Fig. 2.12(b) (Chapter 2). Usually, a low power stage is used for discharge ignition and cathode conditioning, and the high power stage is used for effective sputtering of the target material [130, 135]. Further discussion on the power management of the MPPMS PS operated in both non-reactive and reactive conditions, accompanied with examples of numerous experimentally obtained current waveforms, is presented in Chapters 7 and 8.

3.2 Optical emission spectroscopy

OES is a popular non-intrusive diagnostic technique suitable for analysis and monitoring of physical and chemical processes within plasma. It is mostly used for the identification or quantification of various gas-phase species present in the plasma. However, its judicious use permits the estimation of T_e, n_e, vibrational and rotational temperatures of the molecular species, and of other important plasma parameters. The basic advantage of OES when compared with other plasma diagnostic techniques (e.g., mass spectrometry, Langmuir probes, ion energy analysis) is its non-perturbing character, high reliability and relative simplicity in implementation in both laboratory and manufacturing environments. It allows fast and easy qualitative discharge monitoring, which can be performed in both time- and space-resolved mode. However, OES is limited only to the light-emitting (excited) species. Furthermore, the interpretation of the quantitative information can be difficult, due to the indirect relation between the excited species' concentration and the detected radiation intensity, and due to the complex convolution of the measured optical signal.

3.2.1 Basics of OES

OES technique is based on the detection of the radiation originating from the de-excitation transitions of bound electrons in atoms, ions, molecules or molecular ions; Each spontaneous electron transition in between the higher-lying (E_k) and lower-lying (E_l) energy levels results

in the emission of a photon of wavelength, λ_{kl}, given by:

$$\lambda_{kl} = \frac{hc}{E_k - E_l}, \tag{3.1}$$

where h stands for the Plank's constant and c for the speed of light. It should be noted that E_l may or may not be the ground state from which the electron was originally excited. The typical lifetime of the excited state is in the range 10^{-7} to 10^{-8} s (proportional to the Einstein coefficient, A_{kl}), which is a much shorter period than the usual time in between the atomic/molecular collisions (e.g., $\sim 10^{-4}$ s in Ar atmosphere at $p = 1$ Pa) and than the collisions with electrons ($\sim 10^{-6}$ s). Therefore, the majority of the de-excitation electron transitions in low-pressure discharges is radiative. This means that the optical emission may be used for the TR monitoring of the excited species' position within the discharge.

Fig. 3.4 shows several radiative electron transitions in between various energy levels of the excited Ar atom, with the respective emitted light wavelengths/wavelength ranges. Each time

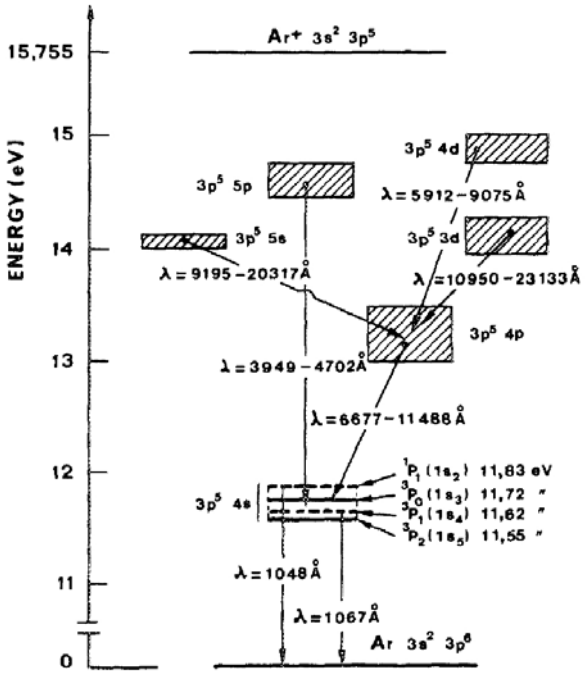

Figure 3.4 Schematic diagram of energy levels of Ar atom with several radiative transition paths highlighted, together with the respective emitted photons' wavelength/wavelength ranges (1 Å= 0.1 nm). Resonance $^1P_1$ and $^3P_1$ energy levels are marked in dashed lines and metastable (non-radiative) $^3P_0$ and $^3P_2$ levels in solid lines. Reproduced from [136].

an excited electron spontaneously descends to a lower-lying energy level, it causes an emission of a photon with a well defined energy (wavelength) equivalent to the energy difference of the higher-lying and lower-lying energy level, according to Eq. 3.1. A large number of such emitted photons can be detected as an emission peak, or *emission line*. The set of emission lines emitted by the individual excited species (such as Ar) is unique, and thus can be used for the identification of the radiating species; One needs to compare the experimentally obtained spectral lines with the tabulated values in literature. In addition, intensities of emission lines due to the electronic transitions originating from energy levels of various E_k may be used for the estimation of T_e [137, 138].

An example of the emission spectra from HiPIMS discharges operated with Cr target in Ar, N_2/Ar mixture, and N_2 is plotted in Fig. 3.5. It is shown that the non-reactive emission spectrum is composed of numerous Cr and Ar emission lines, which can be distinguished with a common low resolution spectrometer [Fig. 3.5(a)]. In addition to the atomic emission lines, both reactive spectra also exhibit the *emission bands* in red and near-infrared ranges ($\lambda > 500\,\mathrm{nm}$), where strong emission from molecular N_2 is situated [Fig. 3.5(b,c)]. In fact, the observed bands are composed of a large number of emission lines which originate from numerous electronic transitions in between various vibrational and rotational energy levels that are superimposed to the molecular electronic states. The small energy differences between these vibrational ($\Delta E = 1 - 5\,\mathrm{eV}$) and rotational ($\Delta E = 0.001 - 0.1\,\mathrm{eV}$) states, and the broadening of emission energies caused by the movement of emitting molecules along with their mutual collisions, lead to an overlap of the emission lines which subsequently form bands rather than sharp emission peaks. However, high resolution spectrometers permit distinguishing these emission lines, which can be used for the evaluation of the vibrational and rotational energies of the particular molecular gas [139, 140].

3.2.2 Plasma characterization

A quantitative determination of the plasma species' densities, based solely on the measured emission intensity, is a difficult and complex task. The number of photons collected from the investigated plasma volume is not only a function of the monitored species' concentration, n_A, but also of the ability of plasma to excite the ground state species A into the electroni-

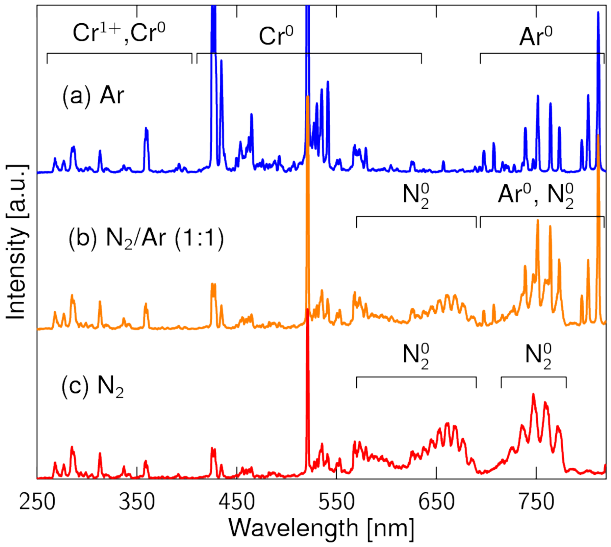

Figure 3.5 Averaged emission spectra recorded at $d = 10\,\mathrm{cm}$ from the target powered by HiPIMS operated in Ar (a), N_2/Ar (1:1) mixture (b) and N_2 (c) at 1.3 Pa. The condition of the experiments can be found in Paper II (Chapter 5). The dominant regions of atomic Cr and Ar emission lines and molecular N_2 emission bands are indicated.

cally excited emitting species A*, and of their subsequent de-excitation. For the specific case of high density discharges ($n_e > 10^{11}\,\mathrm{cm}^{-3}$), such as those generated by HiPIMS pulses, the electron-impact excitation is the dominant excitation mechanism [141, 101]. The relation in between the resulting radiation intensity originating from the unit volume, I_A, and n_A can then be expressed simply by:

$$I_A = \alpha_{eA} n_A, \tag{3.2}$$

where α_{eA} is the proportionality constant for the electron excitation depending on the plasma density, electron energy distribution, pressure, and other conditions:

$$\alpha_{eA} = K_d(E)\, n_e \int_0^\infty Q_e(p, n_e)\sigma_{eA}(E) f_e(E) E^{1/2} \mathrm{d}E. \tag{3.3}$$

Here, $K_d(E)$ is an energy-dependent response constant of the detector or the entire detection system, $Q_e(p, n_e)$ is the quantum yield for the photon emission from the respective excited state for given pressure and electron density of the plasma, and $\sigma_{eA}(E)$ is the energy-dependent cross section for excitation of A by electron impact. It should be highlighted, that

Eq. 3.2 is valid only for spontaneous radiative de-excitation from the energy levels populated directly from the ground state with no contribution from other excitation path, e.g., stepwise excitation via underlying metastable energy levels. However, these conditions are commonly encountered in non-equilibrium plasmas employed in materials processing. It is also assumed that there is no absorption of the emitted light on its way towards the detector (*optically thin* plasma).

Given the complexity of the relation between the measured emission intensity and the concentration of radiating species, it is evident that an additional analysis using another plasma diagnostic technique may be necessary for proper determination of the latter quantity. For instance, Langmuir probe measurements permit estimation of the average n_e within the monitored plasma volume and of the respective electron energy distribution. Nevertheless, characterization of the electron energy distribution at higher energies, which is pertinent to the excitation of the plasma species, is problematic even when using Langmuir probe [137].

An efficient approach how to avoid the necessity for a complicated evaluation of the coefficient α_{eA} is to compare the emission intensity of the species of interest with the intensity of the other radiative species of known concentration. The latter species, also called actinometers or "tracers", are usually rare gases (e.g., Ne, Ar, Kr) introduced into the gas mixture in a controlled amount, that is small enough in order not to perturb the discharge (e.g., $\sim 1\%$ of the total gas content). It is important to ensure that both emission lines (of species A and of actinometer B) possess comparable excitation thresholds (E_k), and that $\sigma_{eA}(E)$ and $\sigma_{eB}(E)$ have similar shapes in the monitored energy range. In this way, the differences in the energy-dependent excitation conditions are minimized, and the ratio of the emission intensities can be simplified as:

$$\frac{I_A}{I_B} = \frac{\alpha_{eA} n_A}{\alpha_{eB} n_B} \approx K \frac{n_A}{n_B}, \tag{3.4}$$

where n_B is the known concentration of the actinometer and K is a constant independent of the discharge parameters. This approach, originally introduced by Coburn and Chen [142] for the analysis of plasma-etching discharges, is called *actinometry*. The addition of rare gases of trace amounts into the discharge – approach called trace rare gases OES (TRG-OES) – can be also used for the evaluation of T_e and the electron energy distribution, such as recently reviewed by Donnelly in Ref. [137].

It should be stressed that the knowledge of the exact concentrations of the gas-phase species is often unnecessary. Even though the excitation conditions are strongly affected by the specific plasma conditions, the emission line intensities provide a qualitative indication of the species' concentration in the discharge. Therefore, optical emission monitoring can be applied for the detection of small variations in discharge operation, for instance, due to the dissociation of the reactive gas, contamination, or vacuum leaks. OES diagnostics are thus commonly used for judicious control of plasma processing of materials.

The most common example of the optical emission-based process monitoring is the end-point detection in plasma etching [143, 144]; Typically, a strong emission line of the monitored material is selected, and its intensity is empirically related to the modification in the surface composition etched by the plasma. The removal of the etched material induces a significant variation in plasma composition, which substantially affects the monitored emission line intensity that serves as a triggering signal for the termination of the etching process. Another common use of plasma emission monitoring (PEM) is in the process stabilization during reactive DCMS [145]. In the latter case, the emission of the sputtered metal is used for the feedback control of the reactive gas flow, as briefly discussed in section 2.2.3 (Chapter 2).

The radiation intensities from the two species of interest may also be used for the estimation of their relative concentration ratio, according to Eq. 3.4, under the condition that the respective spectral lines are positioned close to one another, and that their σ_{eA} are comparable. As an illustration, the emission intensity ratio of the selected ionized and neutral Nb emission lines was used for the relative comparison of the sputtered Nb ionization in different types of discharges and various discharge conditions in Chapter 7.

The above-listed examples demonstrate that the OES technique is a simple and powerful tool for qualitative monitoring of the gas-phase processes within the investigated discharge. However, an identification of all the emitting species may be compromised by several issues. The first one is the convolution of radiation originating from different excited species that span over the same spectral region. For instance, the majority of Ar^0 emission lines, clearly distinguished in the emission spectra of HiPIMS discharge in pure Ar [Fig. 3.5(a)], are convoluted with N_2 molecular bands if the HiPIMS discharge is operated in the reactive mixture of Ar and N_2 [Fig. 3.5(b)]. Similarly, some of the Cr^0 lines are convoluted with N_2^0 bands.

Enhancing the spectral resolution of the spectrometer may be a possible solution, with a drawback of a higher cost of the equipment. Nevertheless, a de-convolution of the emission signal originating from different gas-phase elements can be difficult, particularly if the discharge is operated in the reactive gas mixture containing complex chemical compounds.

Another important issue may be the reabsorption of the emitted radiation, which is commonly encountered in the *optically thick* plasmas, such as in high pressure discharges exhibiting high plasma densities [66]. In such a case, the measured emission line intensity may be significantly lowered, especially if the respective de-excitation transition is to the heavily populated ground energy level. Strong reabsorption may be, however, identified from the characteristic shape of the monitored emission lines.

Both of the above-listed shortcomings are emphasized by the fact that the emission signal is acquired along the line of sight of the probe. Consequently, the spatial information in that particular direction is lost. Thus, only 2D spectroscopic diagnostics of the plasma volume is possible, in the perpendicular plane to the viewing direction. However, if the acquired images are axially symmetric, it is possible to calculate the original emission distribution by the reverse Abel transformation applied on these images [146].

3.2.3 Experimental apparatus

A typical apparatus for OES diagnostics is formed by several components, as illustrated in the example of the experimental setup used in the present work in Fig. 3.6(a). Firstly, the emitted light has to be collected by an optical probe, that is often introduced within the deposition chamber in order to permit the space-resolved discharge analysis. For that reason, the probe can be positioned on the movable feedthrough, rod or other mechanism. The collected light is then transmitted by the fiber optic cable into the monochromator, where it is dispersed. Finally, the obtained spectrum, or its selected portion, is recorded by a photomultiplier, an optical multichannel analyzer or a camera. The detection element may also be implemented together with the monochromator within one spectrometer body. This is the case of the portable spectrometer (Ocean Optics USB2000) that was employed for the low-resolution time-averaged discharge monitoring presented in Chapters 7 and 8.

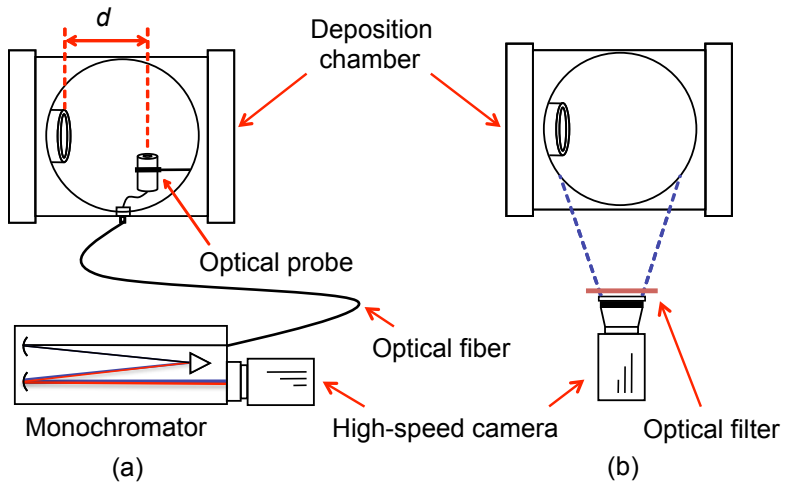

Figure 3.6 A schematic diagram of the two experimental arrangements used in this work: (a) OES setup using the monochromator with rotable triple grating turret and with the camera mounted on its ouput, and (b) Imaging setup using the camera with an objective overlooking the content of the deposition chamber through a transparent window, with a position of the optional optical filter highlighted.

High-resolution monochromator

A typical high-resolution monochromator designed for plasma spectroscopy contains a collimating mirror that reflects the incoming light into a parallel beam, which is then diffracted on the reflection grating, and focused by another mirror towards the exit slit with an adjustable thickness. The resulting spectral resolution (ability to distinguish two emission lines) is determined by the monochromator's focal length and by the density of the diffraction grating; The higher the focal length and/or groove density is, the better is the achieved resolution on the monochromator's focal plane, where the detector is situated. However, the increase in the resolution results also in the smaller spectral range that can be projected at once.

The monochromator used in this work (PI Acton SpectraPro 2750) has a focal length of 750 mm and three holographic gratings of different groove densities, mounted on a rotable triangular turret. In this way, the user has an option to choose which grating he wants to use, and thus an option to select the monochromator's spectral resolution and the wavelength range that can pass through the exit slit. These three gratings have 150 grooves mm^{-1}, 1200 grooves mm^{-1} and 2400 grooves mm^{-1}, respectively. For the most dense 2400 grooves mm^{-1} grating, the spectral resolution is better than 0.1 nm and the width of the spectral range

detectable at the exit slit lies within 2 nm - 20 nm, depending on the central wavelength. An example of the high-resolution spectra recorded by the fast camera at different times from the initiation of the investigated HiPIMS pulse is presented in Fig. 5.2 (Chapter 5).

Light detector

The light detector serves to measure the incoming radiation intensity, typically limited to the visible and near ultraviolet (UV) spectral range. Light can be recorded in a narrow range of wavelength by the photomultiplier tube or photomultiplier tube arrays, providing extreme sensitivity and speed of detection (<1 ns). However, the most common detector used in nowadays plasma spectroscopy is the charge coupled device (CCD), comprising numerous pixels arranged in a linear or 2D array (chip). In the latter configuration, all the vertical pixels are usually binned in order to obtain spectral intensity versus wavelength. The advantage of CCD to the photomultiplier tube is its capacity to accumulate the information over a period of time and over a large range of wavelengths (e.g., 200 nm - 900 nm). Even though a common CCD has its sensitivity depending on the incoming light wavelength (energy), this does not represent a substantial problem for qualitative discharge monitoring. Furthermore, recent development of *intensified* CCD (ICCD) greatly enhanced the sensitivity of such devices, while enabling fast and electronically-controlled triggering suitable for TR analysis. The 2D configuration of CCD chips also permits convenient and fast 2D imaging, as illustrated in Chapters 4, 5 and 6.

A schematic representation of the ICCD used in this work (Princeton Instruments PI-MAX2 camera), together with the example of the typical light path, are shown in Fig. 3.7. The number of incoming photons is first multiplied by an electronic amplifier composed of a photocathode, a micro-channel plate (MCP) and a fluorescent screen [147]. At first, the incident photons strike the photocathode surface that releases electrons. These are then accelerated by the adjustable potential difference between the two charged plates in the front and at the back of the MCP; The higher the positive potential on the output of the MCP is (600 V - 900 V in Fig. 3.7), the higher the *gain* of additional electrons will be. Subsequently, the electrons leaving the MCP are further accelerated towards the fluorescent screen which – due to the electron gain – emits more photons compared with their original number at the

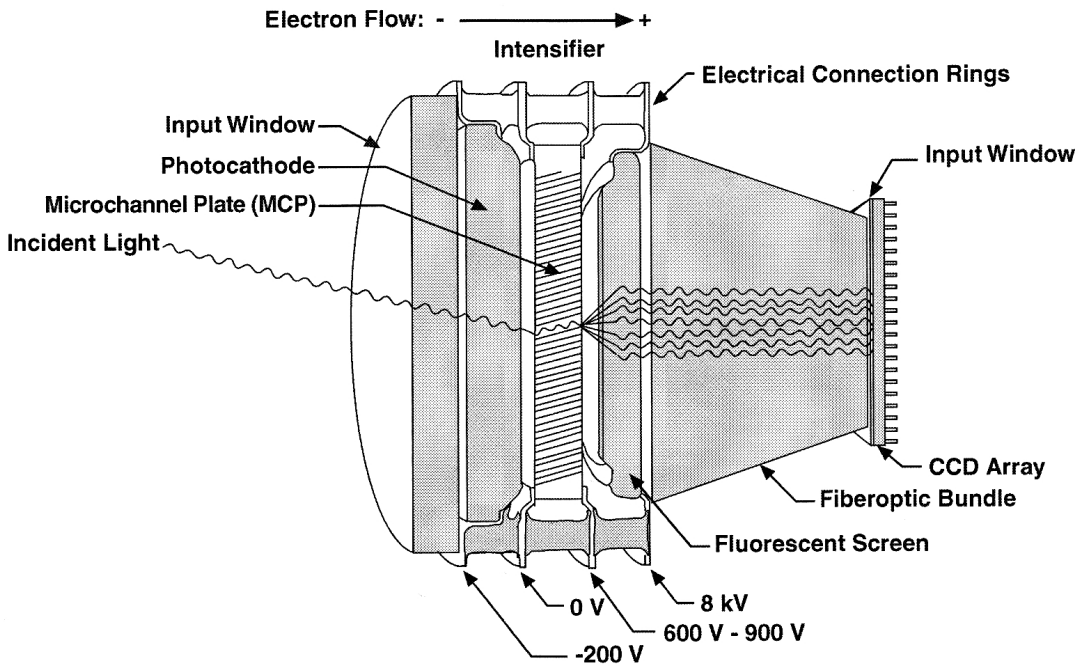

Figure 3.7 Schematics of the internal components of the ICCD intensifier of the PI Acton SpectraPro 2750 high-speed camera used in this work. Reproduced from [147].

photocathode. These photons are finally transferred by the fiber optic bundle towards the 1024×1024 pixels CCD chip (Kodak KAI-1003). The resulting charge, generated on each of the CCD pixels due to the accumulation of the incoming photons, will then undergo a 16-bit digitization process.

Gating and synchronization

The intensifier of the high speed camera can act as a shutter to the incoming light. In comparison to mechanical shutters, *gating* is performed electronically by modifying the potential that is applied to the photocathode; If the photocathode has its potential negative with respect to the MCP input (as depicted in the example given in Fig. 3.7), the generated electrons are attracted to enter the MCP, and consequently, the CCD chip receives light. On the contrary, the positive potential on the photocathode inhibits the electrons to enter the MCP and the CCD chip to detect light. The process of turning the intensifier electronically "on" and "off', in a processs called *gating*, can be repeated very quickly, and with extremely precise timing (on a ns timescale) [147]. Moreover, the gating can be synchronized with

an internal or external source of pulsing, such as a pulsed power generator. Details of such synchronization, applied for the TR analysis of the gas-phase processes during HiPIMS pulses, can be found in section 5.2 (Chapter 5).

It should be noted, that the light accumulated on the CCD during a typical HiPIMS pulse or during its portion of interest (e.g., period 0 - 5 μs from the pulse initiation) may not be sufficient for obtaining a strong enough signal for further data analysis. In such a case, an accumulation of the light originating from several pulses (typically 5 to 100) is necessary for enhancing the signal-to-noise ratio. Once the desired number of repetitions is reached, the accumulated charge on the CCD is "read" by the camera electronics, and the whole process may be repeated for another integration interval (e.g., 5 - 10 μs period). However, reading and digitizing of this charge can take up to 250 ms, before the CCD and the related circuits are ready for a new acquisition [147]. Therefore, it is possible that a significant number of pulses can pass before another measurement is made. Thus, the TR spectra are never acquired from a single pulse or from several consecutive pulses. Instead, a typical set of TR measurements, such as that presented in Fig. 5.2 (Chapter 5), represents the discharge emission from selected periods of the pulse, averaged over a predetermined number of pulses.

3.2.4 Plasma imaging

Cameras equipped with a sensitive CCD chip are convenient non-perturbing tools for 2D discharge mapping, which – in combination with a set of suitable optical filters – can replace lengthy space-resolved analyses by OES. The gating capacity of modern ICCD cameras also enabled the analysis of the evolution of the investigated discharges, with a time-resolution down to tens of ns [148]. *Fast imaging* thus became a valuable tool for plasma diagnostics, as demonstrated in a number of studies related to different types of discharges (for instance, Refs. [149, 150, 151, 152, 153]). Moreover, fast imaging performed through custom-made optical interference filters allows the monitoring of the time- and space-evolution of the selected plasma-excited species. This can be advantageous for the observation of various plasma effects, specifically during the highly dynamic pulsed discharges. An example of such investigation can be found in Fig. 3.8. Characterization of the HiPIMS discharge dynamics will be discussed in Chapters 4, 5 and 6.

The experimental setup for fast plasma imaging employed in this work is shown in Fig. 3.6(b) (Chapter 5). The camera is positioned on a tripod, with its line of sight perpendicular to the plane of the transparent feedthrough window of the plasma-containing reactor. It may either overlook the discharge through a pinhole [152], or it may be equipped with a focusing lens [149] or a commercial camera objective [150] (the latter being used in the present work). An optical interference filter, usually positioned in between the focusing element and the source of radiation, can be a highpass, a lowpass or a bandpass filter, depending on the monitored spectral range. In some specific cases – if the spectral region, where the selected emission lines of interest are situated, has also abundant emission originating from other plasma-excited species – a narrow bandpass filter may be necessary to efficiently filter all parasitic radiations. However, a longer integration period may then be required to accumulate a sufficient number of photons. More details on the filter design, suitable for monitoring of different working gas and sputtered metal species within the HiPIMS discharges, together with the demonstration of such diagnostics, can be found in Chapter 4.

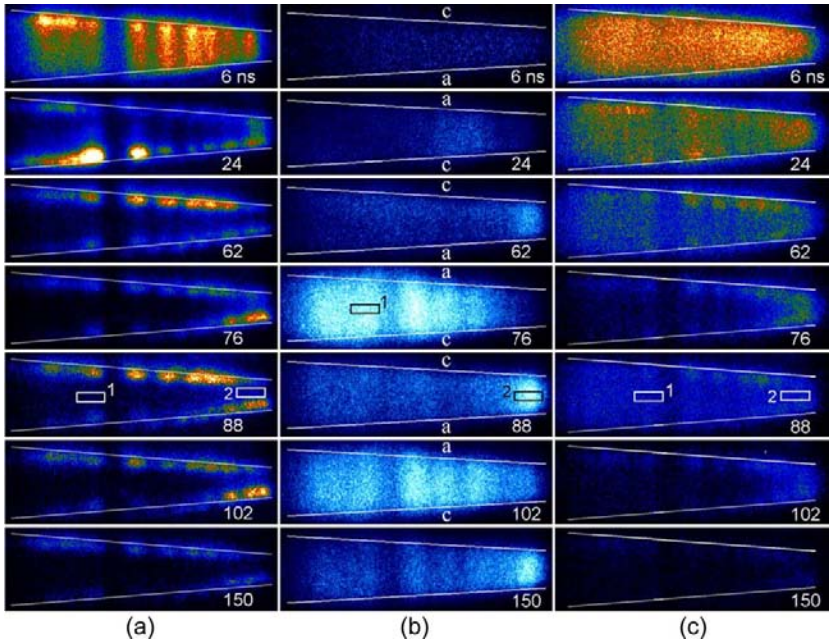

Figure 3.8 Example of ultrafast imaging of the first 150 ns of a pulsed high-pressure (400 Pa) discharge in between two plane electrodes highlighted by the white lines. The images are acquired from the UV-visible continuum without any filter (a), and with a set of filters suitable for monitoring of the UV excimer Ar^*_2 molecular emission at 126 nm (b) and for Ar* emission in the red part of the spectrum (c). Reproduced from [152].

3.3 Film characterization techniques

3.3.1 Stylus profilometry

The thickness of the fabricated coating is an important parameter since some of the film properties may depend on its amplitude (e.g., internal stress level). The most common way to determine film thickness is the stylus profilometry, which is highly suitable for the measurement of the step height from the substrate to the film surface and for the evaluation of the surface topography. This technique consists in measuring the mechanical movement of a stylus in a vertical direction as it is moved horizontally (scanned) on the sample's surface. The position of the stylus, terminated by a diamond needle with a tip radius of several μm, is monitored by the piezoelectric sensor.

The stylus profilometer used in this work (Veeco Dektak 3030ST) is equipped with a conical diamond stylus. Its instrumental horizontal and vertical position resolution is less than $0.2\,\mu$m and less than 1 nm, specifically. Nevertheless, the precision of the measurement is additionally affected by the step geometry and other parameters, such as roughness and curvature of the substrate or background vibrations. The length of a scan can be adjusted according to the lateral size of the measured feature.

3.3.2 Internal stress evaluation

The evaluation of the residual internal stress level of the prepared coating is of crucial importance for the characterization of the coating environmental stability and of its adhesion to the underlying substrate. The total internal stress is a sum of the thermally-induced stress due to the difference in thermal expansion coefficients between the substrate and the film, and of the intrinsic microstructural stress originating in growth defects (e.g., interstitial atoms or voids) and other phenomena. Stress may also be induced by the phase transformation, recrystallization or other processes following the film deposition, namely when the latter was performed at elevated temperatures.

Total stress, σ, can be evaluated from the measured film thickness, t_f, and the substrate curvature caused by the deposition of a stressed thin film, R, if the specific properties of the substrate are known, such as its thickness, t_s, Young's modulus, E_s, and Poisson's ratio, ν_s.

The internal stress value of the deposited film is then obtained from the Stoney equation [154]:

$$\sigma = \frac{E_\mathrm{s}}{1-\nu_\mathrm{s}} \frac{{t_\mathrm{s}}^2}{6t_\mathrm{f}} \frac{1}{R}. \tag{3.5}$$

R can be determined experimentally by measuring the curvature of the substrate before and after the film deposition. In the present work, these curvatures were evaluated by laser scanning (Tencor FLX-2900 instrument) while using rectangular Si stripes with approximative dimensions of $10 \times 50 \times 0.43\,\mathrm{mm}^3$ as substrates. The evaluation precision is usually related to the systematic measurement errors (such as those originating from uneven positioning of the substrates on the laser scanning apparatus), but also to the thickness uniformity of prepared films. A typical measurement uncertainty was in the range $\Delta\sigma = 30 - 50\,\mathrm{MPa}$.

3.3.3 X-ray diffraction

X-ray diffraction (XRD) is a sensitive non-destructive technique commonly applied for material characterization of thin films with a thickness as little as few atomic planes. It is based on the analysis of the X-ray radiation reflected from the investigated sample under a defined incidence angle. If the atoms are arranged in a periodic fashion, as in a crystalline lattice, the diffracted X-rays will generate sharp interference maxima which reflect the symmetry of the lattice atoms, as predicted from the Bragg's law. Thus, the analysis of the obtained diffraction pattern can be used for a deduction of the atomic distribution within the studied material, from which the crystalline structure, the lattice spacing and the residual stress level can be determined. In addition, diffraction line broadening can be used for the estimation of the crystallite (grain) size and of the lattice strain. Grazing incidence XRD measurements permit the evaluation of the thickness, roughness, and density of the film.

In the present work, the XRD diagnostic was performed in the θ–2θ configuration using Cu Kα ($\lambda = 0.15406\,\mathrm{nm}$) radiation in a Philips X'PERT instrument. Specifically, XRD was employed to analyze the out-of-plane lattice spacing of the fabricated Nb films (Chapter 7).

3.3.4 Scanning electron microscopy

Scanning electron microscopy (SEM) is a popular technique for the film's surface and/or substrate-film interface imaging that can reach nanometer resolution. Typically, a specimen to be investigated is rastered by a beam of highly energetic electrons (e.g., energy of units to tens kV) created by an electron gun. This electron beam is focused on the sample by a system of electromagnetic lenses, which also serve for its deflection necessary for rastering. The electrons bombarding the specimen are partly recoiled and partly absorbed within the subsurface region. In addition, their impacts cause the emission of SE that carry information about the topography and composition of the surface. The emitted SE and/or backscattered electrons are then collected by the respective detectors positioned in the sample vicinity. Hereby generated signal is used for the intensity modulation of the other electron beam of the cathode ray tube (CRT) – projecting the magnified surface under examination – that has its movement synchronized with the beam that probes the sample. The magnification of the resulting image is determined by the ratio of the CRT screen size to the size of the investigated area rastered by the electron beam. The images of Nb films' microstructure presented in Chapter 7 were obtained by Hitachi FB2000A SEM.

3.3.5 Depth-sensing nanoindentation

Depth-sensing nanoindentation is a dynamic test that allows one to evaluate the mechanical properties of thin films, such as hardness, H, and reduced Young's modulus, E_{r}. It is based on the measurement of the vertical position of the indenting stylus during its displacement into and from the examined sample, caused by the variable load applied upon. The values of H and E_{r} of the indented specimen can then be calculated analytically from the obtained load vs. displacement curve, according to the Oliver-Pharr method [155]. This approach was applied during the characterization of H and E_{r} of the NbO_x films, while using the data generated by a Hysitron TI 900 triboindenter equipped with a Berkovich pyramidal tip (presented in Chapter 8).

It should be noted that there are several important issues related to the determination of the hardness value when examining a thin film. For instance, the size of the indenter, as well as its penetration depth, strongly affect the measured value of H [156]. It is also of

great importance for the accuracy of the measurement that the stylus has a precisely defined geometry (i.e., it is not worn by an excessive use), and that the nanoindentation apparatus is well calibrated before each experiment. Furthermore, the evaluation of the indentation of thin films deposited on the soft substrates may be difficult or even impossible if the deformation of the latter cannot be avoided. Therefore, a proper use and interpretation of the depth-sensing nanoindentation analysis requires a particular caution and expertise.

3.3.6 Ellipsometry

Ellipsometry is a non-intrusive diagnostic technique that allows the determination of optoelectronic properties of metallic and dielectric materials, such as their dielectric or optical constants. The principal advantages are high speed and precision of the measurement, and the ability to evaluate even ultrathin films of several atomic layers in thickness. Moreover, the ellipsometry can be performed *in situ* during the film deposition or plasma processing, as illustrated in Ref. [79].

The examination of the sample is based on the evaluation of the changes in light polarization between the incoming light beam and the beam reflected from the sample surface. Due to the light-material interaction on the sample, the reflected light beam will possess different polarization state than before the impact; This change can be characterized by the two ellipsometric angles Ψ and Δ, which are related to the amplitude and the phase of the polarized light, respectively. The examined film quantities, such as the film thickness and the optical constants may then be deduced from the values of Ψ and Δ by a model analysis [157]. However, the development of the model that accurately describes the entire coating + substrate system can be a lengthy and difficult task. The precision of the obtained values strongly depends on the accuracy of such model.

The optical properties of the NbO_x films were examined by a J. A. Woollam RC2-DI multi-functional variable-angle spectroscopic ellipsometer, and their optical characteristics were modelled using the CompleteEASE software (J. A. Woollam), as specified in Chapter 8.

CHAPTER 4

Paper I: Time- and species-resolved plasma imaging as a new diagnostic approach for HiPIMS discharge characterization

Authors: M. Hála, O. Zabeida, B. Baloukas, J.E. Klemberg-Sapieha, L. Martinu

Article published: IEEE Transactions on plasma science, vol. 38, no. 11, pp. 3035 - 3039, Nov. 2010.

Comment: This paper is a part of the special issue: HIPIMS and High Power Glow Discharges

Abstract: We present a novel approach in fast imaging of HiPIMS discharges in which band-pass optical interference filters are used to isolate the optical emission signal originating from different species populating the plasma. In this work, we describe the methodology of the proposed diagnostics and discuss its application. In particular, we demonstrate the use of this technique for the time-resolved analysis of HiPIMS discharges operated with a chromium cathode in argon at 4 Pa. Two optical filters were designed and fabricated: (i) one for neutral chromium emission lines (400 to 540 nm), and (ii) the other one for neutral working gas emission lines and bands (above 750 nm). The introduction of such filters is used to distinguish different phases of the discharge, and to reveal numerous plasma effects including background gas excitations during the discharge ignition, gas shock waves, and expansion of metal-rich plasmas.

4.1 Introduction

High-power impulse magnetron sputtering (HiPIMS) is a rapidly developing deposition technique based on pulsed DC magnetron sputtering: High-power unipolar pulses are applied to a target with a low (usually 0.5% – 5%) duty cycle. In this way, high-density plasmas with peak power densities in the kW cm^{-2} range and a high degree of ionization of the sputtered material are obtained [22, 28, 108]. These characteristics have been shown to be beneficial in deposition of high-density films with low surface roughness [40, 158] and homogeneous coating of complex-shaped substrates [159, 15]. Moreover, HiPIMS has been demonstrated as a powerful tool for adhesion pre-treatment in protective coating preparation due to the high metal-ion fluxes available at the substrate [14].

Understanding the plasma processes within a HiPIMS discharge is necessary in order to develop and optimize the deposition process. HiPIMS pulses can be characterized by several diagnostic techniques, such as mass spectrometry that permit monitoring of the ion flux composition [160] and of ion energies [110, 109], and by Langmuir probe diagnostics suitable for electron density and temperature determination [27]. Another diagnostic approach is to study the optical emission originating from the discharge in order to extract valuable information about the plasma composition [161] and/or about the excited species' spatial distribution and dynamics [162]. A comprehensive summary of HiPIMS discharge dynamics is given in reference [98].

In this work, we demonstrate the application of time- and species-resolved plasma imaging using optical interference filters specifically fabricated for the monitoring of different excited species. First, we discuss the design of the suitable band-pass filters. Second, we show how the time evolution of different plasma processes within the HiPIMS pulse can be characterized and how the transport of the sputtered material can be visualized. Finally, we discuss a possible application of this diagnostic approach for the optimization of the deposition process.

4.2 Experimental details

The experiments were carried out using a magnetron with a 5 cm diameter Cr cathode in pure Ar and in reactive gas mixtures of Ar with N_2. HiPIMS pulses with a peak cathode

voltage of $U_C = -2000$ V and a duration of 200 μs were applied to the target with a repetition rate of 50 Hz. The substrate holder facing the target at a distance of 10 cm was biased by an RF power supply with a -100 V DC voltage in between the pulses in order to maintain background plasma for faster HiPIMS discharge ignition. This bias voltage dropped during each HiPIMS pulse to values around -10 V.

The voltage and current waveforms were recorded using a Tektronix TDS2014B digital oscilloscope equipped with a Tektronix P6015A voltage probe and a Pearson 301X current probe. The optical emission of the discharges was monitored by optical emission spectroscopy (OES) using an optical fiber probe mounted within the deposition chamber, a SpectraPro 2750 spectrometer (PI Acton) with a holographic grating (150 grooves mm^{-1}) and a high-speed PI-MAX2 camera (Princeton Instruments).

During time-resolved imaging of the discharge the high-speed camera was placed outside of the deposition chamber, recording a series of images through the viewing port. The camera was gated using a pulse synchronized with the onset of the HiPIMS voltage pulse. Each image was recorded during a 5 μs period following a pre-set delay from the initiation of the voltage pulse, and summed over 10 pulses. More details about our experimental system and the data acquisition can be found in [162].

4.3 Filter design and characterization

In order to distinguish the optical signal originating from excited sputtered material and working gas species during the plasma imaging, a set of band-pass optical filters is required. These filters should be designed to maximize the transmission within a specific spectral range in which the emission of the selected species to be monitored is high. Simultaneously, the filter transmission outside of the selected range of wavelengths should be minimized.

The first step in the design of suitable optical filters is to determine the wavelength ranges in which the emissions from different excited species do not overlap. Fig. 4.1 shows the optical emission spectra of the HiPIMS discharges recorded above the Cr target sputtered in (a) pure Ar and in (b) N_2/Ar (1:1) reactive mixture at 4 Pa. It can be observed that specific regions in which the emission from the sputtered metal and the working gases are isolated can be identified for both non-reactive and reactive discharges. These are the regions of interest

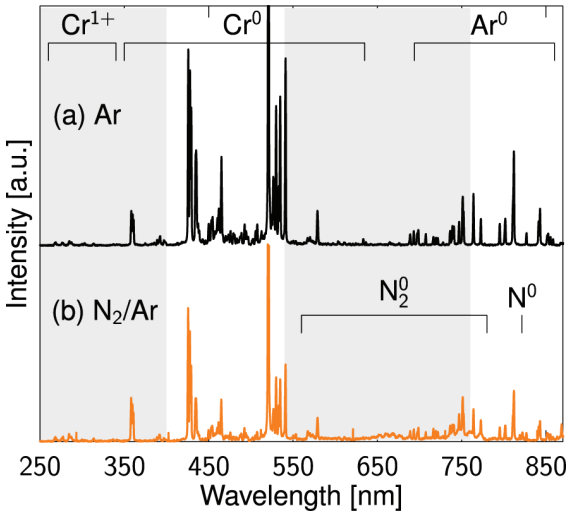

Figure 4.1 Emission spectra of the HiPIMS discharges operated with a Cr cathode in (a) Ar and (b) N_2/Ar (1:1) reactive mixture at 4 Pa, recorded at a target-probe distance of $d = 6$ cm. The spectral regions specific for the emission originating from individual excited species are indicated, as well as the spectral regions of the intended interference filters applied in this work (white area). Note that the Cr^0 emission line at 520 nm is saturated.

for which two band-pass filters have been considered in this work (the regions highlighted in white with respect to the grey background).

The filters used in this study were designed using the OpenFilters sofware [163] and optimized for the wavelength range from 350 nm (camera objective glass cut-off) to 900 nm (sensitivity maximum of the camera's CCD). Filter A consists of 56 alternating layers of SiO_2 ($n = 1.49$ @ 550 nm) and Nb_2O_5 ($n = 2.28$ @ 550 nm) with a total thickness of 4.7 μm, and filter B consists of 40 alternating layers of SiO_2 and Ta_2O_5 ($n = 2.14$ @ 550 nm) with a total thickness of 3.4 μm. The latter filter also includes an antireflective coating on the backside of the substrate.

Both filters were deposited on B270 glass in a pilot dual ion beam sputtering (DIBS) system (Spector II by Veeco-Ion Tech) equipped with two Kaufman gridded ion sources. The primary 16 cm diameter beam was used to sputter Nb, Ta or SiO_2 targets while the second ion beam served for film densification and additional oxidation.

The optical transmission spectra of the fabricated filters are plotted in Fig. 4.2. The first filter (A) has a transmission band between 400 and 540 nm, and is suitable for monitoring the neutral emission lines originating from excited atoms of transition metals, such as chromium.

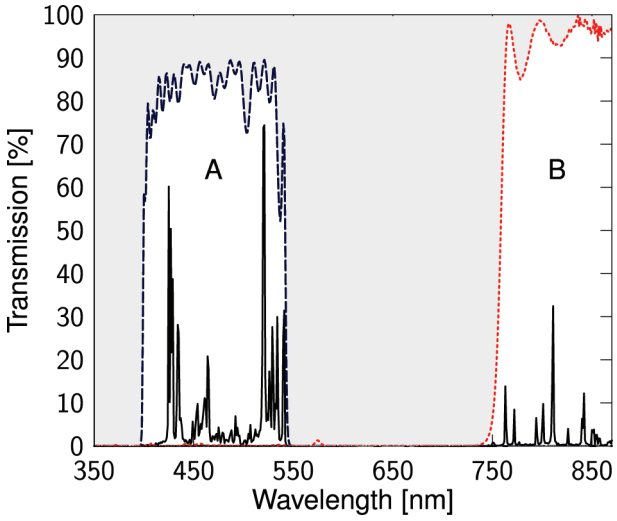

Figure 4.2 Transmission functions of band-pass interference filters designed for observation of neutral Cr emission lines (dashed curve - stack of filters A) and neutral working gas emission lines such as Ar^0 (dotted curve - stack of filters B). The emission spectrum of the HiPIMS discharge operated with a Cr cathode in Ar at 4 Pa convoluted with the transmission functions of these filters is plotted in solid black (arbitrary units scale).

The average transmission outside of this region is below 0.4%. In all our experiments, a pair of filters A were stacked in order to futher eliminate this parasitic transmission. The second filter (B) is a high-pass filter with a cut-off wavelength at approximately 750 nm, allowing observation of the emission lines and bands from excited working gases, such as Ar, N_2 or dissociated O_2. Its transmission outside the high-transmission region was in average below 2.7%. Once again, a pair of filters B were stacked in all experiments, and the resulting average parasitic transmission was below 0.1%.

It is important to note that an appropriate set of filters can be prepared for any combination of sputtered material and working gas with a necessary condition that the emission regions from the sputtered metal and working gas stay well separated within the spectral sensitivity range of the imaging system. Furthermore, specific filters can be designed to distinguish the emission from neutral and ionized metal atoms. However, one should bear in mind that the ionized transition-metal emission lines, such as Cr^{1+} in Fig. 4.1, are often situated in the near UV. Unfortunately, their monitoring may be inhibited by the limitations imposed by the individual imaging components. For instance, the absorption threshold of the camera objective glass used in our experiments limits detection to wavelengths above 350 nm.

4.4 Results and discussion

In this section, we will demonstrate the application of the set of fabricated optical filters for the diagnostics of the HiPIMS discharge operated in pure Ar at 4 Pa. The current and voltage waveforms of the examined 200-μs HiPIMS pulses are illustrated in Fig. 4.3. After the discharge ignition, following the application of the voltage pulse, a stable high-current discharge is reached, indicating the metal-dominated phase of the discharge as previously discussed in [162].

Please note that a movie depicting the discharge evolution during the first 400 μs from the voltage pulse application can be downloaded at http://ieeexplore.ieee.org. The movie is composed of two series of images, each recorded using one of the two band-pass filters.

Three series of images obtained during the first 75 μs of the HiPIMS pulse are shown in Fig. 5.8. Each row represents the instantaneous discharge emission recorded at different times after the initiation of the voltage pulse (indicated in grey in Fig. 4.3). The unfiltered discharge emission is illustrated in the first column, while the second and the third columns depict the experiments with the two band-pass filters A and B described above. In the following, we will analyze and interpret these images.

The first row of images depicts the ignition phase during which fast secondary electrons excite the working gas. This is illustrated by the absence of the emission recorded with the "Cr" filter A, while the bright light detected without any filter and with the "Ar" filter B is

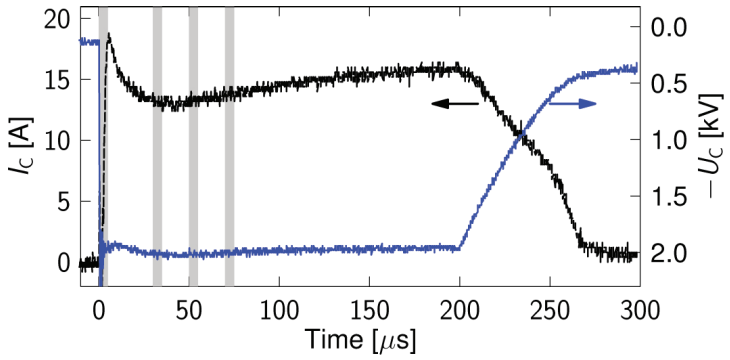

Figure 4.3 Current and voltage waveforms recorded during a 200-μs HiPIMS pulse operated with a Cr cathode in Ar at 4 Pa. Four time intervals, during which the discharge emission depicted in Fig. 5.8 was recorded, are indicated in grey. The peak power density on the target was 2 kW cm^{-2}.

essentially the same. This observation provides evidence of the working gas excitation by high-energy electrons originating from the cathode and escaping the magnetic confinment of the unbalanced magnetron. Similar observations made by OES and Langmuir probe diagnostics were reported in ref. [22]. The form and the emission intensity distribution from the excited gas partly follow the magnetron's magnetic field lines. The small fraction of light originating from excited metal, confined to the closest target proximity, is the manifestation of the onset of the target sputtering.

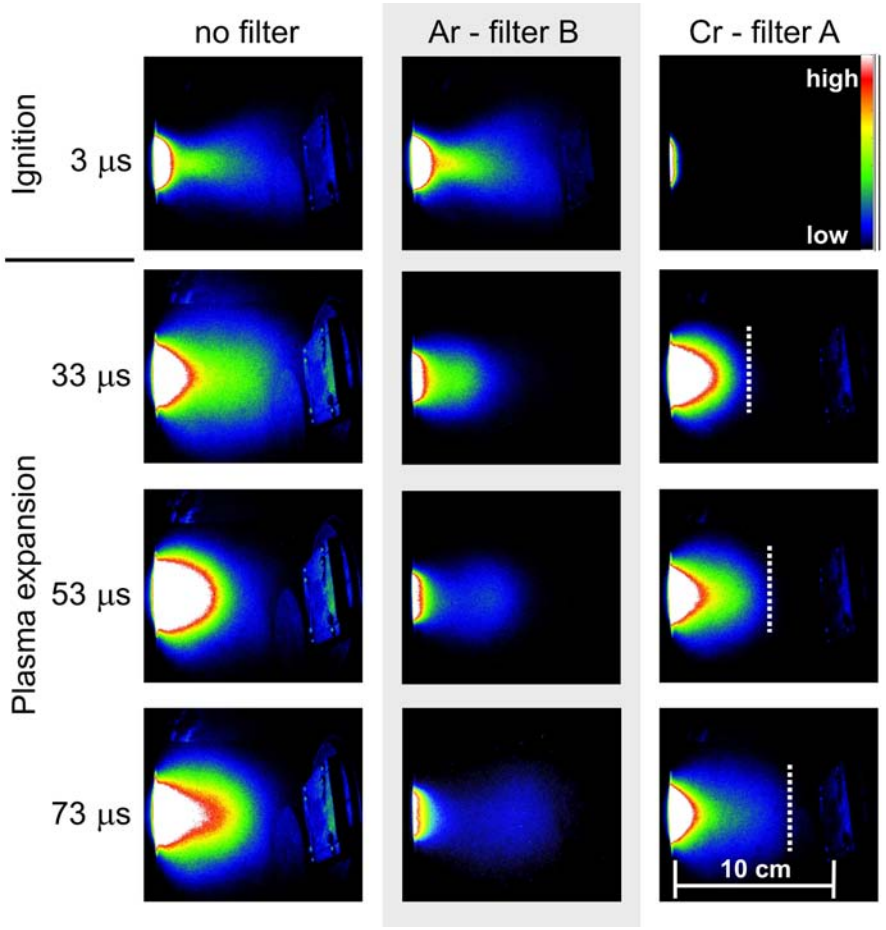

Figure 4.4 Images taken during 200-μs HiPIMS discharge pulses in pure Ar at 4 Pa with no filter on the camera objective (left column), and with an optical band-pass filter specific for emission from neutral Ar (middle column - filter B), and from neutral Cr (right column - filter A). The images were recorded at different times after the pulse initiation as indicated in Fig. 4.3. For clarity purposes, different colors are assigned to different emission intensities, according to the scale depicted in the upper right image. The position of the Cr emission wavefront is highlighted by a dashed line.

The three other rows of images illustrate the development of a dense-plasma region close to the target during the metal-dominated high-current phase of the HiPIMS discharge. In contrast to the ignition phase, the light distribution in the images recorded without any filter and with filter A is similar. The emission intensity from the excited Cr prevails over that of the working gas with increasing time. Simultaneously, its wavefront, of a hemispherical shape, visibly propagates outwards from the target at a constant speed ($v_{\mathrm{Cr}} \approx 0.8\,\mathrm{km\,s^{-1}}$), as highlighted by the dashed line in Fig. 5.8. On the contrary, the working gas emission continuously diminishes in both intensity and spatial extent, until it is confined to the proximity of the sputtered cathode. Furthermore, a discrete emissive region visibly detaches from the target vicinity and travels towards the substrate holder at a speed which is conformal to that of the excited-metal emission wavefront.

Based on these observations, several conclusions can be made. The advancing emission wavefront from neutral Cr indicates the expansion of a dense plasma rich in sputtered metal. This assumption is supported by our previous findings of the simultaneous propagation of both neutral and ionized Cr emission peaks [162]. The plasma wavefront travels towards the deposition chamber at a constant speed with a hemispherical shape, confirming the existence of the ion-acoustic solitary wave expanding away from a HiPIMS-powered cathode [70]. Take note that the travelling speed of this wave, calculated from the propagation of the ionized Cr emission signal, is pressure- and gas-dependent [162].

The drop in light intensity from the excited working gas with rising discharge current suggests two effects: (1) Working gas rarefaction due to the increasing amount of sputtered metal, and (2) electron energy quenching due to lower excitation and ionization tresholds of the metal atoms in comparison to those of the working gas [27]. The fact that the intensity of excited Ar remains high close to the magnetron is due to the high-energy electron accumulation in the magnetized region above its racetrack.

Another important observation is the apparent working gas emission region travelling outwards from the target synchronized with the propagation of the metal emission wavefront (for clarity, refer to the colored electronic version of Fig. 4). This is most probably an envelope of excited Ar that precedes the expanding metal-rich plasma as a consequence of momentum transfer from the energetic sputtered metal to the much colder working gas atoms. This

visual observation seems to confirm the existence of the working gas shock wave originally reported by Kadlec [100].

It should be underlined that the current plasma diagnostics approach presented here can be performed with the same set of filters in different gases or working gas mixtures such as N_2/Ar and O_2/Ar. Related discharge dynamics, not shown in this paper, in the case of N_2 and Ar mixtures was reported earlier [162].

The ability to provide direct information about the gas and metal transport within the deposition chamber makes time- and species-resolved plasma imaging an attractive technique for optimization of the deposition process. For example, it could be used to minimize undesired working gas incorporation into the growing film. In fact, inert Ar atoms may occupy interstitial positions within the film lattice which can lead to a higher internal stress that can compromise coating's durability. Furthermore, incorporation of Ar atoms within the substrate-coating interface can weaken adhesion due to increased lattice strain [14].

In combination with pulsed substrate biasing, the information about the discharge evolution would enable the operator to selectively choose the kind of ionized species to be incorporated within the growing film. This could be performed by the application of a negative bias during the time period when the metal species reach the substrate. A positive bias, preventing incorporation of the working gas ions into the substrate, such as during the ignition phase, could also be applied. The bias power supply could then be triggered by the onset of the applied cathode voltage with a set delay selected by the operator.

4.5 Conclusion

Time- and species-resolved plasma imaging permits the visualization of different plasma processes within the HiPIMS pulse evolution. These processes include background gas fast-electron excitations during the discharge ignition, gas shock waves, and metal-rich plasma expansion in the form of ion-sound waves. Such diagnostics can be performed in both non-reactive and reactive discharges. The principal advantage of this non-intrusive diagnostic approach is its ability to provide direct information about the sputtered material spatial distribution and about its transport between the target and the substrate. This can be particularly helpful if combined with pulsed substrate biasing synchronized with the HiPIMS pulse.

Acknowledgment

The authors wish to thank Mr. M. Biron for his assistance in designing the interference filters and Dr. J.-M. Lamarre for helpful discussions.

CHAPTER 5

Paper II: Dynamics of reactive high-power impulse magnetron sputtering discharge studied by time- and space-resolved optical emission spectroscopy and fast imaging

Authors: M. Hala, N. Viau, O. Zabeida, J.E. Klemberg-Sapieha, L. Martinu

Article published: Journal of Applied Physics, vol. 107, p. 043305, Feb. 2010.

Abstract: Time- and space-resolved optical emission spectroscopy (OES) and fast imaging were used for the investigation of the plasma dynamics of high-power impulse magnetron sputtering (HiPIMS) discharges. 200-μs pulses with a 50-Hz repetition frequency were applied to a Cr target in Ar, N_2 and N_2/Ar mixtures and in a pressure range from 0.7 to 2.66 Pa. The power density peaked at 1.2-4 kW cm^{-2}. Evidence of dominating self-sputtering was found for all investigated conditions. Up to four different discharge phases within each pulse were identified: (i) the ignition phase, (ii) the high-current metal-dominated phase, (iii) the transient phase, and (iv) the low-current gas-dominated phase. The emission of working gas excited by fast electrons penetrating the space in-between the electrodes during the ignition phase spread far outwards from the target at a speed of 24 km s^{-1} in 1.3 Pa of Ar and at 7.5 km s^{-1} in 1.3 Pa of N_2. The dense metal plasma created next to the target propagated in the reactor at a speed ranging from 0.7 to 3.5 km s^{-1}, depending on the working gas composition and the pressure. In fact, it increased with higher N_2 concentration and lower pressure. The form of the propagating plasma wave changed from a hemispherical shape in Ar, to a drop-like shape extending far from the target in N_2. An important N_2 emission rise in the latter case was detected during the transition at the end of the metal-dominated phase.

5.1 Introduction

High-power impulse magnetron sputtering (HiPIMS) is a deposition technique capable of creating very dense metal plasmas by means of high-power unipolar pulses applied to a magnetron target. This enables a significant degree of ionization of the sputtered material. A high ionization fraction of the sputtered material reaching up to 30% for Cr, 60% for Cu and 60% for Ti has been reported [28, 29, 30], as well as the detection of multiply (up to four-fold [32]) charged metal ions. A high number of metal ions in the deposition flux was found to be beneficial, for instance, in the substrate pre-treatment for adhesion improvement [14], and in the fabrication of dense, defect-free coatings with low surface roughness [40]. In order to understand the properties of the HiPIMS discharge and to optimize the deposition process, numerous systematic studies of discharge dynamics have been conducted in the last several years [28, 22, 100, 164, 161, 160, 165, 25, 120, 166, 126, 167, 13, 70, 168, 169, 170, 26]. In the following, we summarize some of the major findings.

During the discharge ignition, a significant amount of fast electrons accelerated outwards from the target penetrate the space in-between the electrodes and causes a significant excitation and ionization of the working gas [22]. The amount of sputtered metal atoms in the region close to the target increases with rising current. Consequently, the working gas in front of the target is rarefacted due to the energy transfer from the increasing amount of sputtered metal neutrals as in the case of conventional direct current magnetron sputtering (DCMS) discharges [116]. Since the current and the flux of sputtered atoms are higher in HiPIMS than in DCMS, the rarefaction effect is more pronounced. This phenomena has been supported by Monte Carlo simulations of the neutral particle flows in HiPIMS [100] and demonstrated, for instance, in the case of HiPIMS discharges using a Cu cathode in Ar [164]. The gradual change in the discharge composition due to the injection of the sputtered metal was observed by optical emission spectroscopy (OES) [22, 28, 161] and time-of-flight mass spectrometry [160]. The subsequent drop of the electron temperature measured by Langmuir probes [165, 25] can be interpreted as being electron cooling in collisions with metal atoms replacing the working gas. This is due to the fact that metals have their first ionization and excitation threshold energies below that of non-reactive working gas atoms (such as Ar).

As metal atoms gradually replace the working gas near the target, a growing amount of the sputtered metal neutrals is thermalized and ionized in the established plasma. If the plasma density (power density) is high enough, a significant fraction of the target current is consequently due to metal ions which are attracted back to the target (self-sputtering, SS). SS can even become self-sustained, without the participation of the working gas ions, as was demonstrated by Andersson and Anders[119]. The sustainability of SS depends on numerous parameters, such as the self-sputtering yield of the target material, the secondary electron emission yield [121], the applied cathode voltage [120], the magnetic field strength of the magnetron, and the working gas used [160]. In general, this phase of the discharge may be defined as metal-dominated since the gas ions are still expected to contribute to target sputtering, combined with the metal ions; Such behavior is expected for transition metal targets (like Cr), with low self-sputtering yields. The transition in composition for different HiPIMS discharges has been reported, for instance, in [28, 120, 166, 126, 167]. However, information about the development of reactive discharges in nitrogen, commonly used in the preparation of hard and protective coatings, is still missing.

Sputtered target atoms represent a particle supply, creating a density gradient and a directional momentum which forces both neutral and ionized metal to diffuse away from the target. Moreover, the high-density plasma close to the target generates a high local plasma pressure. It was shown that metal ions may propagate in the ballistic regime [161] or via ambipolar diffusion [165], in dependence on the working pressure and phase of the discharge. In addition, some authors have reported on ion acoustic solitary waves reflecting off the chamber walls [13, 70].

Since the propagation of ions is bound to electrons in order to maintain the quasi-neutrality, the strength and the shape of the magnetron's magnetic field confining the movement of the electrons play an important role in plasma transport towards the substrate [29]. To further complicate the matter, this magnetic field is altered by large azimuthal currents close to the racetrack region as demonstrated in [168]. In fact, the plasma propagation and sputtered material transport towards the substrate are complex problems that are not yet well understood. Furthermore, open questions remain regarding the propagation of both ionized and neutral species in reactive gases, in which the complexity of plasma phenomena increases.

In this work, we apply time- and space-resolved high-resolution OES to analyze the evolution of both non-reactive and reactive HiPIMS discharges, in pure Ar, pure N_2, and the N_2/Ar (1:1) mixture. In addition, time-resolved discharge imaging was performed to better understand the propagation of individual excited species within the deposition chamber. Specifically, we identify several development stages of HiPIMS pulses. Furthermore, we show the development of the dense metal plasma close to the target and its expansion into the reactor. Finally, we determine the relationship between the plasma propagation, the working gas composition and pressure.

5.2 Experimental details

An unbalanced magnetron with a 100-mm diameter Cr target was powered by an HMP2/1 power supply (HUTTINGER Electronics) with a peak power capability of 2 MW. The initial cathode voltage, U_C, was set to -900 V. However, the actual U_C decreased during the individual pulses owing to high currents drawn by the discharge under investigation and to power supply limitations. The HiPIMS discharges were ignited at a frequency of 50 Hz and a duty cycle of 1%. The voltage and current waveforms were measured by a Tektronix P6015A voltage probe and a Pearson 301X current monitor, respectively, and recorded by a Tektronix TDS2014B digital oscilloscope. The base pressure in the deposition chamber prior to experiments was less than $5\,10^{-4}$ Pa. The HiPIMS discharges were operated in three different working gas compositions, namely in pure Ar, N_2/Ar mixture with a 1:1 partial pressure ratio, and in pure N_2, using a total pressure of 0.7, 1.3 and 2.66 Pa. The peak power density on the target ranged from 1.2 to 4 kW cm^{-2}, depending on the gas composition and working pressure.

Time-averaged and time-resolved (TR) OES of the discharge plasma were performed using a system comprising a SpectraPro 2750 spectrometer (PI Acton) with a holographic grating (2400 grooves mm^{-1}) connected to a high-speed PI-MAX2 camera (Princeton Instruments). In time-resolved measurements, an optical signal was recorded during a 5-μs period, after a set delay from the initiation of the voltage pulse (see Fig. 5.1(a)). The signal was averaged over 5 to 50 pulses, depending on its intensity. Subsequently, the process was repeated for the following 5-μs interval, corresponding to the next data point. Exceptionally, 1-μs long

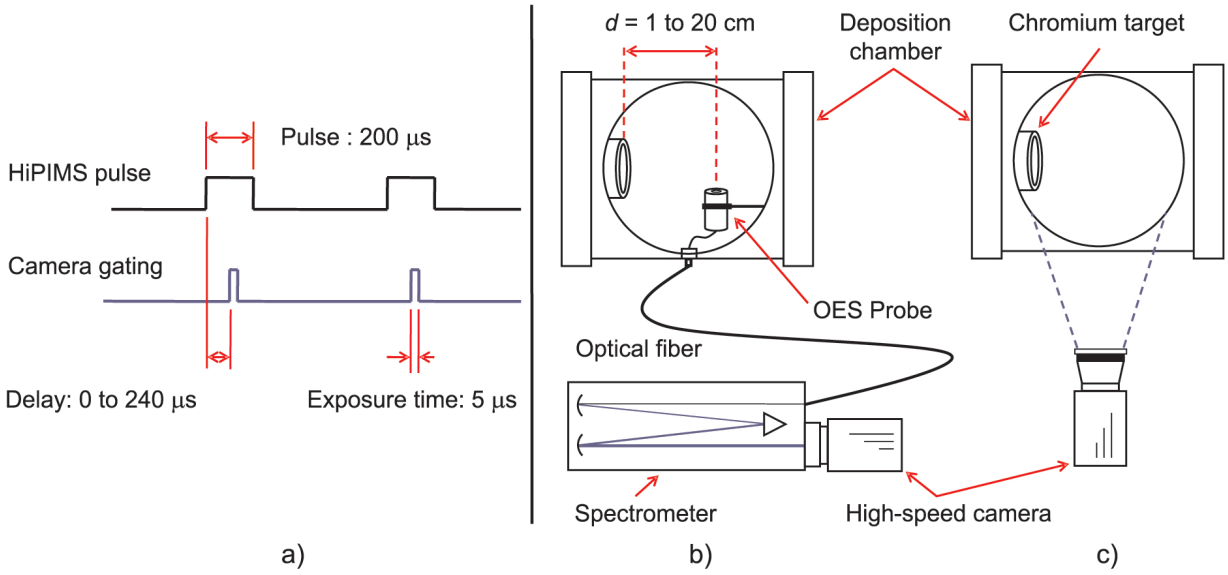

Figure 5.1 The principle of time-resolved (TR) gating for data acquisition (a) and two modes of TR measurements: spectroscopy (b) and imaging (c).

intervals were used in order to increase the precision of the speed estimation of the excited neutral Ar during the ignition phase.

TR mesurements were performed in two modes: spectroscopy and imaging. In the first case, the camera was mounted in front of the spectrometer output aperture, as illustrated in Fig. 5.1(b), to record high-resolution (better than 0.1 nm) spectra. The light emitted by the plasma was collected using a probe mounted within the deposition chamber at different distances from the target, d, ranging from 1 to 20 cm. The line of sight of the probe was parallel to the target surface and the diameter of the light cone from which the light was collected did not exceed 1 cm. In the imaging mode, the camera was placed outside of the deposition chamber, and it recorded sets of images through the viewing port as depicted in Fig. 5.1(c).

For a given set of discharge conditions, emission lines of the same species (in wavelengths ranging from 230 to 820 nm) followed similar time-resolved development. This is illustrated in the TR emission spectra in Fig. 5.2 in which the time variation of the two Ar^{1+} emission lines is the same, while the Cr^0 emission lines behave differently. Furthermore, the latter lines also have similar time development. The specific lines chosen for this study may therefore be considered to be general representatives of the excited species' behavior.

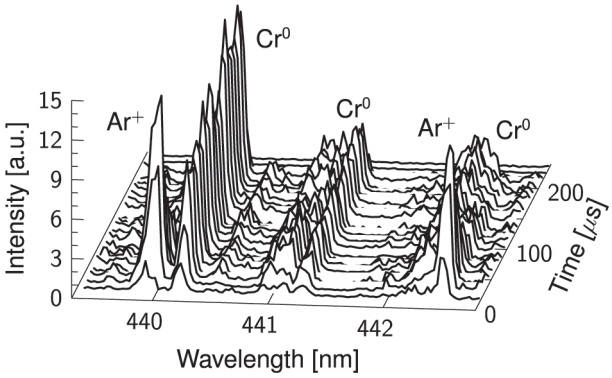

Figure 5.2 Time-evolution of optical emission spectra within a pulse period at a target-probe distance of $d = 1$ cm. Discharge was operated in Ar at 1.3 Pa. Several emission lines of Ar^+ and Cr^0 are indicated.

The list of the monitored emission lines for different neutral and ionized species with the corresponding excitation energies, E_k, and ionization energies, E_i, is given in Table. 5.1. The N_2^0 is represented by the $(B^3\Pi_g \rightarrow A^3\Sigma_u^+)$(6-2) band of the first positive system, and the N_2^{1+} by the $(B^2\Sigma_u^+ \rightarrow X^2\Sigma_g^+)$(0-0) band of the first negative system. Neither of the selected Cr emission lines are due to radiative de-excitation to the energy ground level, hence the self-absorption effect can be considered as negligible. Also, all of these lines have a transition probability higher than $4{\cdot}10^{-7}$ s^{-1}. Since corresponding de-excitation times are much shorter than the time scale of the plasma propagation, the emission of these species indicates their presence at specific target-probe distances.

Table 5.1 List of the monitored OES lines with corresponding wavelengths, λ, excitation energies of the upper excited states, E_k, and of ionization energies, E_i. The values of E_k for ionized species are for electron excitations from the ion ground state. The values of E_k and E_i for molecular nitrogen are only approximative since the exact values depend on the actual vibrational state.

OES line	Cr^0	Cr^{1+}	Cr^{2+}	Ar^0	Ar^{1+}	N_2^0	N_2^{1+}
λ [nm]	492.22	267.72	231.91	800.62	442.6	660.3	391.44
E_k [eV]	5.62	6.18	12.38	13.17	19.55	7.3	3.3
E_i [eV]	6.77	16.50	–	15.76	–	15.58	–

5.3 Results and discussion

5.3.1 Current monitoring

In the first section we present the evolution of HiPIMS pulses in dependence on nitrogen concentration in the N_2/Ar mixture at 1.3 Pa analyzed by TR current monitoring. One of the major differences between the reactive and non-reactive discharges is the rise of the discharge current during each pulse as illustrated in Fig. 5.3. For instance, the maximum current increases by a factor of three in the case of discharges in pure N_2 (I_C = 320 A) compared to that in pure Ar (I_C = 100 A). In fact, this rise is gradual with the addition of N_2 into the working atmosphere. This increase may be explained by a higher compound electron-impact ionization cross section for N_2 and dissociated N when compared with that of Ar, for high-energy electrons. In such a case, the overall amount of working gas ions would increase together with nitrogen concentration in the gas mixture, assuming abundant electrons with energies higher than, for instance, 100 eV in the magnetized region as suggested in [169]. However, at this moment it is difficult to obtain reliable cross section values for both gases in order to compare both cases.

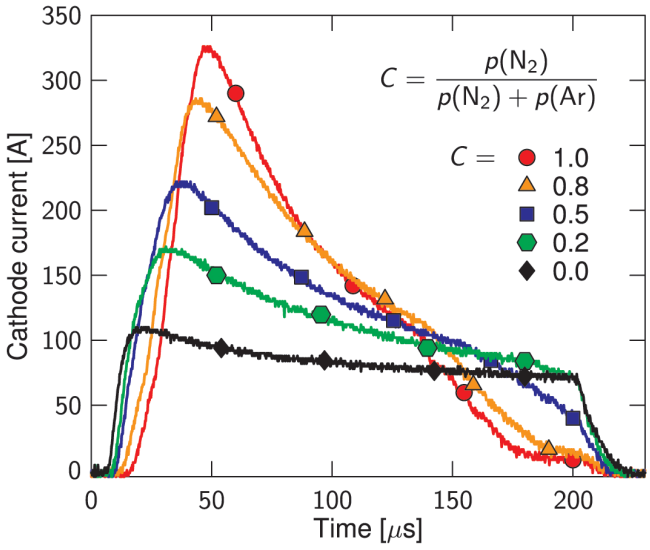

Figure 5.3 Time-resolved current pulse waveforms produced by HIPIMS using a Cr target at different nitrogen concentrations C in the N_2/Ar mixture at 1.3 Pa.

It is to be noted that the current during each pulse is not stable in any of the studied discharges. High currents (peaking at $I_C = 320$ A in N_2) result in an important reduction of the charge stored in the pulse unit capacitors of the HiPIMS power supply. This causes a drop of the cathode voltage and, consequently, further fall of the current. The origin of a significant current fall at the end of the pulse at higher N_2 concentrations will be discussed in the following section.

The time lag between the voltage pulse application and the rise of the discharge current grows with higher nitrogen content. In addition, the initial current increases more slowly than in pure Ar (Fig. 5.3). The latter two effects are indication of delayed gas breakdown due to the energy loss of fast electrons to the excitation of N_2 molecules. When compared to atomic Ar, molecular nitrogen has numerous vibrational and rotational excitation levels accessible for energy absorption. Moreover, the electron energy can also be lost in N_2 dissociation ($E_{dis} = 24.3$ eV). For instance, a significant presence of atomic N^{1+} was detected in HiPIMS discharges in pure N_2 close to the Cr cathode by time-of-flight spectrometry in [160]. However, we could not detect any atomic nitrogen emission lines due to strong chromium emission within the accessible wavelength range.

5.3.2 Discharge evolution close to the target

An important part of this work was to analyze the magnetized plasma region by TR OES at a target-probe distance of $d = 1$ cm. The waveforms of the time-resolved current and voltage and of emission line intensities of both metal and gas species in Ar, N_2/Ar (1:1) mixture and N_2 are presented in figures 5.4, 5.5 and 5.6, respectively. It was observed that the emission intensity waveforms measured at 0.7 Pa and 2.66 Pa exhibited only minor differences from those at 1.3 Pa presented here. For instance, both current and individual emission line intensities increased faster and achieved higher values when using higher working pressure.

Based on the analysis of the current and the emission intensity waveforms, we have divided the investigated HiPIMS pulses into several subsequent stages. In general, the discharges develop through the ignition phase (I), followed by the high-current metal-dominated phase (M). Moreover, a transient phase (T) towards a high-voltage DCMS-like gas-dominated discharge (G) characterized by a significant drop in current and discharge emission was detected

in reactive discharges. These phases can be described in more detail below.

Ignition phase (I): The first detected emission is that from neutral working gas excited by quickly diffusing fast electrons which could be divided into two categories depending on their origin. The first ones are the electrons created by electron impact with gas molecules in the collisional cascades due to the high potential difference between the magnetron and the chamber walls during the gas breakdown. The second kind of energetic electrons are secondary electrons produced on the target by impacting ions and accelerated in the developing sheath. A few microseconds after the Ar^0 and/or N_2^0 emission rise, the emission intensity of Ar^{1+} and/or N_2^{1+} increases as working gas atoms are ionized in collisions with these energetic electrons. Simultaneously, the rising emission intensities of Cr^0, Cr^{1+} and Cr^{2+} indicate the

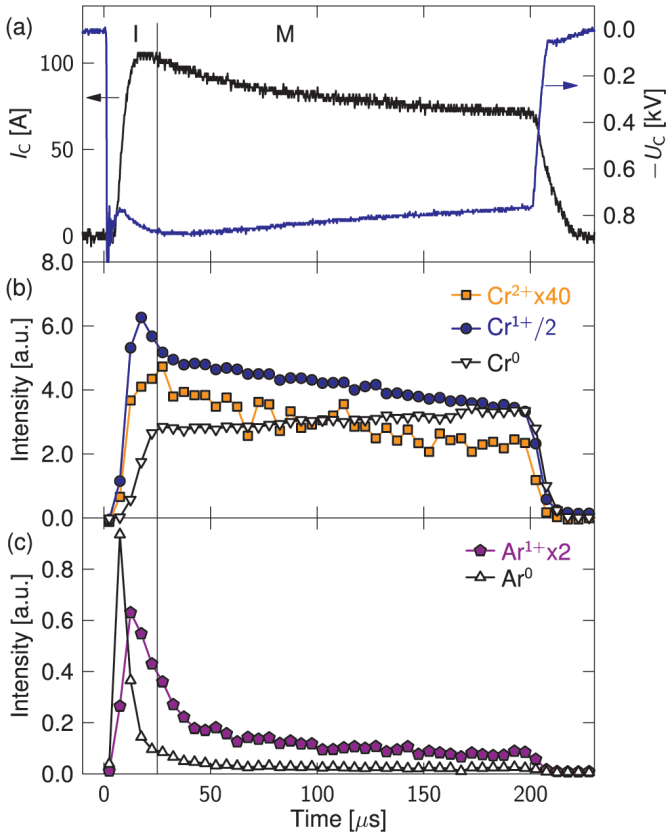

Figure 5.4 Time evolution of the target current, I_C, and the target negative voltage, U_C, (a) and of OES line intensities of metal species (b) and of working gas species (c) during a HiPIMS pulse using a Cr target and the initial cathode voltage $U_C = -900$ V. The discharge was operated in Ar at 1.3 Pa. The ignition phase (I) and the metal-dominated phase (M) are indicated.

injection of metal into the discharge after having been sputtered by working gas ions. The subsequent decrease of Ar^0, Ar^{1+} and N_2^{1+} emission intensity is a sign of electron cooling in electron-metal collisions and of local working gas rarefaction. However, in reactive discharges, the N_2^0 line intensity follows the current waveform. This may be explained by its relatively low excitation energy threshold ($E_{k,N2} = 7.3$ eV) and, perhaps, higher electron temperature.

Metal-dominated phase (M): The intense emission from neutral and ionized metal dominates the discharge emission. The intensity waveforms of Cr^{1+} and Cr^{2+} emission lines approximately follow the evolution of the current amplitude during the whole pulse, while ionized working gas emission is significantly diminished after the termination of the ignition phase. This indicates that Cr^{1+} ions are actually the principal component of the discharge current. Furthermore, the relatively strong emission of Cr^{2+} points to a possibility of sustainable SS process [121].

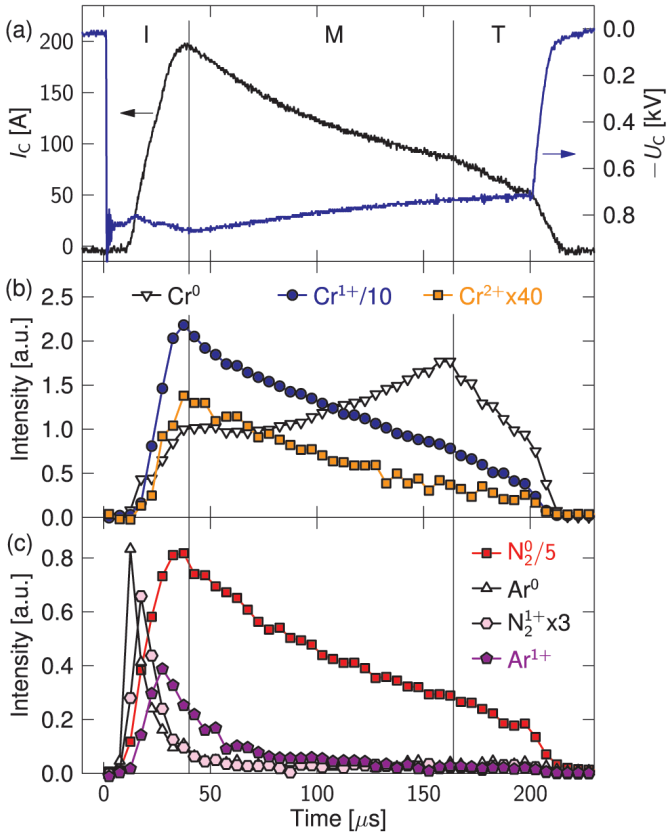

Figure 5.5 Time evolution of the HiPIMS pulse as described in Fig. 5.4. The discharge was operated in N_2/Ar (1:1) mixture at 1.3 Pa. The ignition phase (I), the metal-dominated phase (M) and the transient phase (T) are indicated.

The current during Phase M is not stable in any of the discharges as would be expected for a sustained SS process [120]. This is an artefact due to the power supply limitations as discussed in section 5.3.1. In addition, the current might also be diminishing due to decreasing contribution of working gas ions to the sputtering process. In fact, the high pressure-independent currents during this phase of the discharge and the similarity of the HiPIMS pulse spectroscopic development in figures 5.4, 5.5 and 5.6 suggest that the SS process with a possible gas-ion contribution can be initiated and sustained (up to 185 μs for 200-μs pulses) in both non-reactive and reactive atmospheres, including pure nitrogen. This seems to be in disagreement with the recently published claim that sustaining the high-voltage, high-current HiPIMS regime using a Cr cathode is not possible over a longer period of time (e.g. higher than 100 μs), and that the transition to DCMS-like discharge is inevitable due to depletion of the sputtering gas [171]. We believe, that the authors were limited in

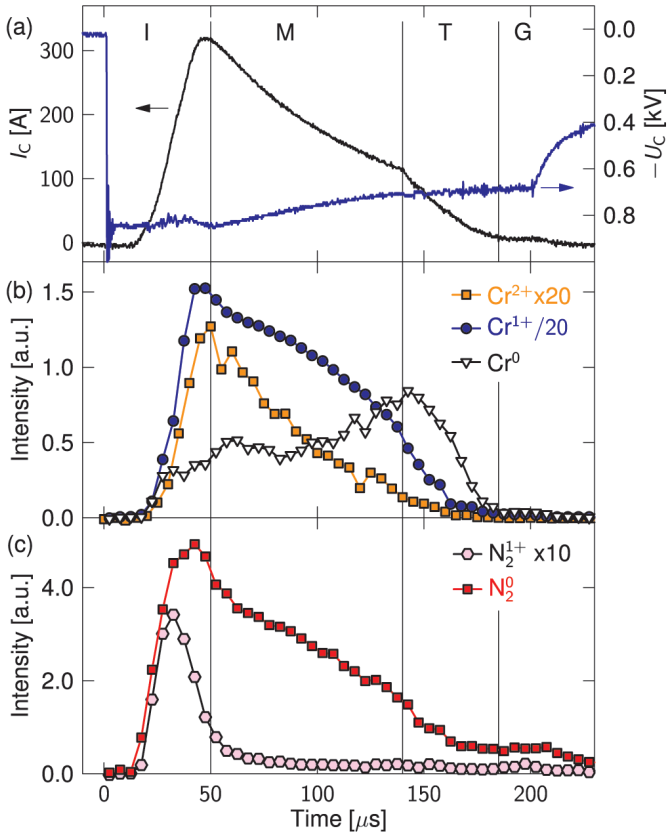

Figure 5.6 Time evolution of the HiPIMS pulse as described in Fig. 5.4. The discharge was operated in N_2 at 1.3 Pa. The ignition phase (I), the metal-dominated phase (M), the transient phase (T) and the gas-dominated DCMS-like phase (G) are indicated.

their study by the cathode voltage (U_C = 700 V), which was most probably lower than the required threshold for sustained SS.

It may be noted that neutral Cr emission generally rises during phase M even though the current drops. This rise is more pronounced with lower working pressure. This phenomenon was observed previously [22, 28, 161] but no satisfactory explanation has been offered so far. For instance, Vasina *et al.* [161] proposed that the rise in neutral metal emission may be caused by an increase of metal density in the case of 10-μs long HiPIMS pulses using a Cu cathode in pressures ranging from 0.7 to 9 Pa. In this case, the Cr^0 emission signal growing throughout the Phase M would imply the accumulation of Cr atoms close to the target.

Another possible explanation is that the surface temperature of the ion-heated target grows during the pulse duration. Substantial heating of the cathode surface could enhance the ion-induced sublimation, as suggested by Vlcek *et al.* [172]. In their work, the HiPIMS deposition rate increased dramatically when the target cooling was reduced. However, our preliminary numerical simulations suggested that the target cooling, which is most efficient between HiPIMS pulses, is sufficient to maintain the temperature of the cathode surface stable. More investigations are necessary in order to explain this phenomenon.

Transient phase (T): When the cathode voltage drops under a certain threshold ($U_C \approx 720$ V in N_2 discharges), the system undergoes a transition from a high-voltage, high-current metal-dominated HiPIMS discharge to a high-voltage, low-current DCMS-like discharge dominated by gas-ion sputtering since the SS process is no more the principal sputtering process. The onset of this transition can be identified by a kink in the decreasing region of the current amplitude and a sudden fall of the emission signal of all metal species including the neutral Cr (Fig. 5.5 and 5.6) This kind of transition was also observed in HiPIMS discharges in Ar and different N_2/Ar mixtures if the voltage dropped under a certain value, which diminishes with decreasing N_2 content in the working gas.

Gas-dominated discharge (G): The subsequent high-voltage DCMS-like discharge may be characterized by pressure-dependent, low current levels ($I_C \approx 10$ A) and significantly diminished plasma emission. Also, Cr^{2+} emission decreases under the detection limit and neutral Cr with neutral working gas emission lines dominate the discharge emission, as in the conventional DCMS.

5.3.3 Discharge spatial evolution

In this section, we focus on the spatial evolution of the plasma during the HiPIMS pulse. Fig. 5.7 shows the time-resolved space distributions of emitted light by the three types of HiPIMS discharges as recorded by a high-speed camera. The upper three images of each discharge illustrate the instantaneous discharge emission during the ignition phase (I), and the lower three images depict the metal-dominated phase (M). In addition, movies composed of the images representing a 5-μs intervals for the three investigated discharges can be downloaded on the journal's webpage at http://dx.doi.org/10.1063/1.3305319 (movies 5.8, 5.9 and 5.10).

During the ignition phase, neutral working gas emission dominates the developing discharge due to collisional excitations by fast electrons emitted from the cathode. However, the spatial emission distribution and the time scale differ depending on the working gas composition. In Ar discharges, a "blast" of light appears to develop rapidly during the first microseconds after the plasma breakdown, spreading far from the cathode into the reactor (Fig. 5.7 and movie 5.8). This strong emission due to excited working gas indicates the fast electrons released from the target by impacting ions and accelerated in the developing sheath to energies high enough to escape the magnetic confinement of the unbalanced magnetron. As the discharge current grows, plasma density rises, and an increasing amount of these electrons is trapped in the vicinity of the target as a consequence of numerous collisions with other electrons and ions. This phenomenon agrees with time- and space-resolved Langmuir probe measurements in a HiPIMS discharge using a $Ti_{0.5}Al_{0.5}$ cathode and Ar atmosphere [22]. The authors reported on fast-propagating ion-current peak due to ionized Ar accompanied by neutral Ar emission, preceding the metal ions propagating outwards from the target later during the pulse.

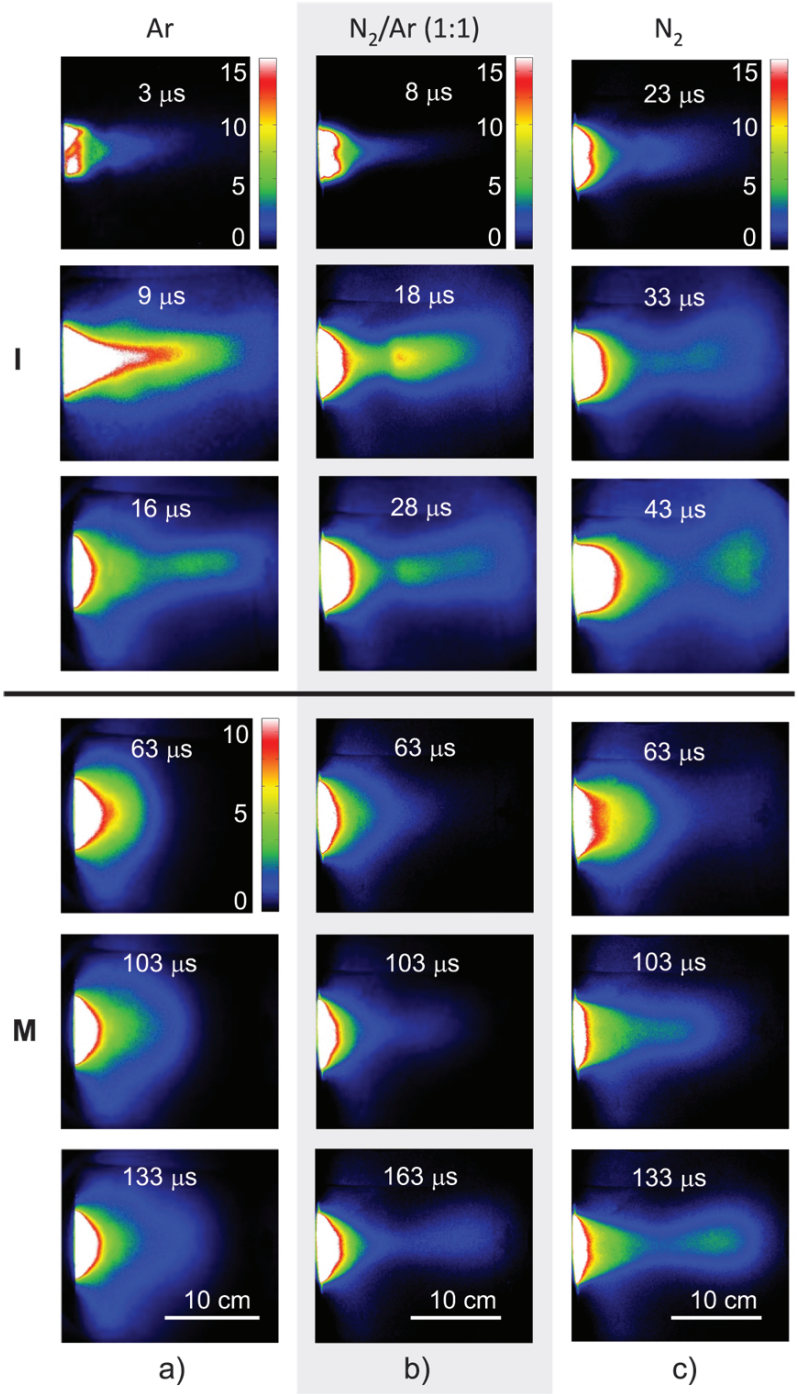

Figure 5.7 Images taken during the 200-μs HiPIMS discharge pulses in Ar (a), N_2/Ar (1:1) mixture (b) and N_2 (c) at 1.3 Pa at different times of the pulse. The three upper rows of images show the ignition phase (I) and the three lower rows show the metal-dominated phase (M). For the sake of clarity, different colors are assigned to different emission intensities (arbitrary units) as indicated in the upper picture of each column. The intensity scales of the lower three images of Ar discharge during the Phase M are shifted in order to make the advancing plasma emission more visible.

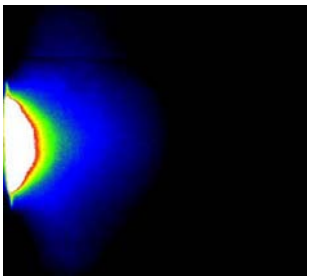

Figure 5.8 Movie depicting the emission evolution of the 200-μs HiPIMS pulse recorded through the viewing port by a high-speed camera (enhanced online). The discharge was operated at 1.3 Pa of Ar.

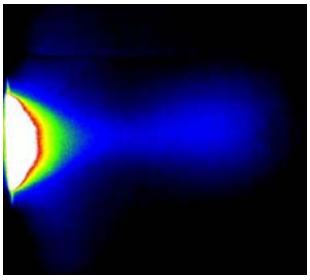

Figure 5.9 Movie depicting the emission evolution of the 200-μs HiPIMS pulse recorded through the viewing port by a high-speed camera (enhanced online). The discharge was operated at 1.3 Pa of the N_2/Ar (1:1) mixture.

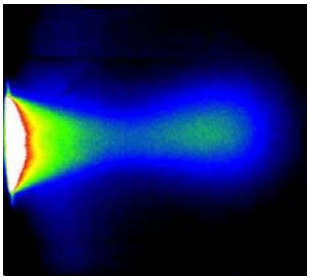

Figure 5.10 Movie depicting the emission evolution ofthe 200-μs HiPIMS pulse recorded through the viewing port by a high-speed camera (enhanced online). The discharge was operated at 1.3 Pa of N_2.

With the introduction of nitrogen into the working gas mixture, the time needed for the establishment of a stable discharge is extended, and so is the time of fast electron-induced gas excitations (movies 5.9 and 5.10). Furthermore, the working gas emission drifts at a significantly lower speed than in Ar discharges. This is illustrated by a position-time plot in Fig. 5.11 in which the target-probe distances of the emission maximum for the different monitored species were plotted as a function of their detection time from the pulse initiation. For instance, the N_2^0 emission peak propagates at a speed of $v_{N2} \approx 7.5\ \mathrm{km\,s^{-1}}$ in N_2 at 1.3 Pa, while the speed of the Ar^0 emission peak reach $v_{Ar} \approx 25\ \mathrm{km\,s^{-1}}$ in Ar at 1.3 Pa. In general, the speed of the advancing electron-induced gas excitation wave decreases with higher nitrogen content, as it does with increasing working gas pressure. This feature can possibly be attributed to the aforementioned losses of electron energy in a larger number of inelastic collisions with molecular N_2. In addition, the shape of the working gas emission spreading away from the target modifies from a conical shape in Ar into an emissive "blob" in N_2. The intensity of this emission rises with increasing working pressure and current.

Interestingly, a zone of diminished emission intensity in the high-emission region can be observed in most of the images during the ignition phase (Fig. 5.7, movies 5.9 and 5.10). This low-emission zone might be a region of near-zero-magnetic-field that might have been displaced from its original position at $d = 3.5$ cm along the magnetron's axis due to the superimposed magnetic field induced by the strong azimuthal current above the cathode. It is well known that the azimuthal current in magnetron discharges is higher than the discharge current. The magnetic induction of this strong current may modify the magnetic field far from the target as shown by Bohlmark *et al.* [168]. The authors have experimentally demonstrated that these modifications are on the order of units of milliteslas even at large distances from the target, where the magnetron's magnetic field is of the same order of magnitude. Changes in magnetic confinement may alter the number of inelastic collisions, hence the emission intensity from the excited background gas. Further analysis by complementary techniques, such as Langmuir probe, should be performed in order to understand this feature.

In the metal-dominated phase, the dense plasma region generated close to the target diffuses outwards from the target zone as shown in the three lower rows of Fig. 5.7. Plasma expansion is constant with time and its speed increases with decreasing gas pressure as listed

Table 5.2 Speed of metal plasma wavefront, v_{Cr+}, calculated from the advancing Cr^{1+} line emission wavefront for nine different working conditions.

	Pressure [Pa]	0.7	1.3	2.66
v_{Cr+} [km/s]	Ar	1.3	1.1	0.7
	N_2/Ar (1:1)	2.0	1.4	1.1
	N_2	3.5	1.9	1.7

in Table 5.2. The speed of the metal plasma wavefront was estimated by recording the Cr^{1+} emission intensity resolved in time at different target-probe distances as illustrated in Fig. 5.12 for discharges in Ar and N_2. The propagation of the Cr^{1+} peak was then plotted in the position-time dependence in Fig. 5.11. The speed of the ionized Cr emission peak in pure Ar at 1.3 Pa is $v_{Cr+} \approx 1.1\ \mathrm{km\,s^{-1}}$. This value is close to the speed of Ti ions in an Ar discharge at 1.3 Pa ($v_{Ti+} \approx 1.15\ \mathrm{km\,s^{-1}}$ [170]) and to the speeds of ion-acoustic waves reported for HiPIMS discharges in Ar at 2.66 Pa using a Ta cathode ($v_{Ta+} \approx 1.1\ \mathrm{km\,s^{-1}}$ [13]) or a Ti cathode ($v_{Ti+} \approx 1.1\ \mathrm{km\,s^{-1}}$ [70]). Table 5.2 illustrates that the Cr-ion propagation speed increases with higher nitrogen content. For example, it reaches $v_{Cr+} \approx 1.9\ \mathrm{km\,s^{-1}}$ at 1.3 Pa in N_2. Such a significant rise may be possibly related to a higher plasma density which may facilitate the transport of charged particles within the reactor in a similar way as if using additional plasma [170]. Since the current amplitude grows with the introduction of nitrogen in the discharge, the plasma density predictably increases. In support of this claim we have reported a rise in chromium ion-to-neutral OES ratios with increasing nitrogen concentrations in different N_2/Ar mixtures using the same discharge conditions (e.g. the same initial cathode voltage) [173].

In Ar discharges, the emission intensity peaks of Cr^0 and Ar^{1+} propagate at the same speed as that of diffusing Cr^{1+} (Fig. 5.11(a)). Also, the Cr^0 emission waveforms (not shown) follow those of Cr^{1+}, suggesting that the diffusion of Cr neutrals follows the Cr plasma. In contrast, Ar^{1+} emission reaches its maximum ahead of the metal plasma wavefront and subsequently drops. Similar observations for the propagating Ar^0 emission peak were made by fast plasma imaging with the use of custom-made optical filters, which will be discussed in a separate study. This confirms the existence of a gas shock wave closely preceding the

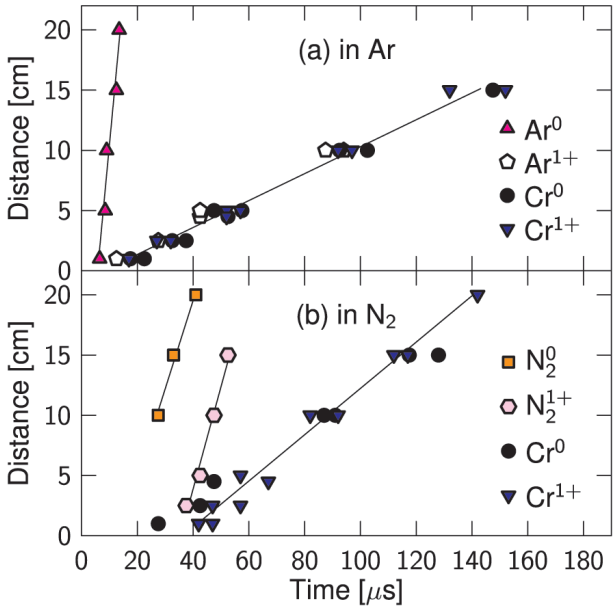

Figure 5.11 Distance from the target of the emission intensity peak versus time from pulse initiation for different emitting species in Ar (a) and N_2 (b) discharges at 1.3 Pa. The solid lines represent the linear regressions for Cr^{1+}, Ar^0, N_2^0 and N_2^{1+} emission intensity peaks used for the estimation of the propagation speed .

expanding metal plasma as previously simulated by the Monte Carlo method by Kadlec [100]. Ar atoms traveling in front of the expanding metal plasma may then be ionized and excited by energetic electrons leaving its wavefront. However, the emission from excited N_2^{1+} follows the N_2^0 emission in the N_2/Ar mixtures, propagating at a speed close to that of N_2^0 ($v_{N2+} \approx 8.5$ km s^{-1} in N_2 at 1.3 Pa). This is illustrated in Fig. 5.13, in which the TR N_2^0 and N_2^{1+} emission intensities are plotted for different values of distance d.

The wavefront of expanding plasma propagates along the magnetron's axis outward from the target due to electron confinement by the magnetic field of the unbalanced magnetron. Interestingly, the introduction of nitrogen into the working gas modifies, in addition to the different propagation speed, the apparent form of the propagating plasma. In Ar discharges, the emission of the propagating plasma had a hemispherical shape and was confined to the vicinity of the target. In reactive mixtures, the plasma wavefront changed during the pulse from hemispherical to conical and finally to a drop-like shape extending far into the reactor.

The plasma emission separates into two distinct emission regions at the end of the metal-dominated phase and during the transient phase in reactive discharges. For example, the

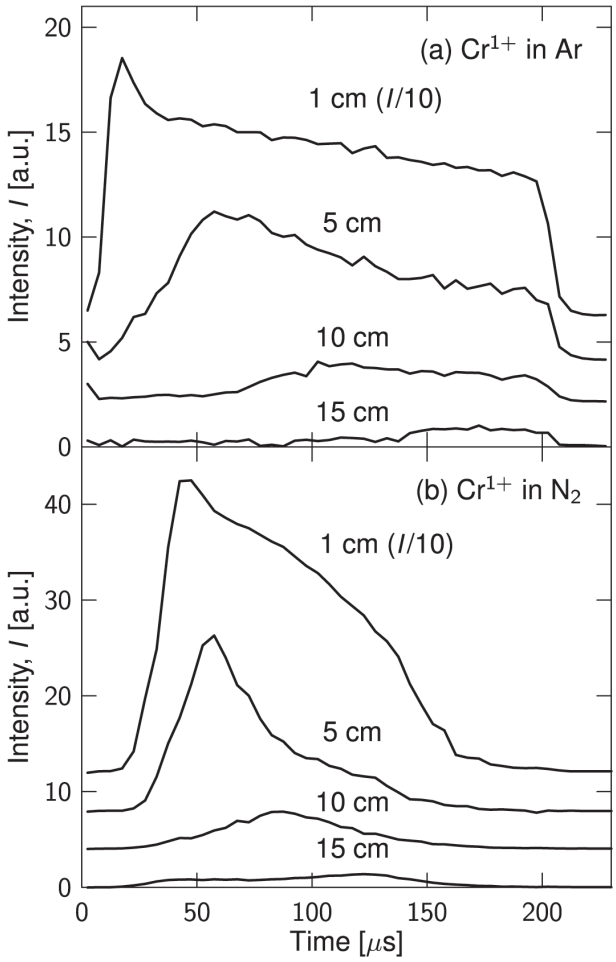

Figure 5.12 Time evolution of the Cr^{1+} line emission intensity for 4 different target-probe distances d in a HiPIMS pulse in Ar (a) and N_2 (b) at 1.3 Pa. Intensities at $d = 1$ cm were divided by a factor of 10. The early emission rise (succeeding the pulse initiation) in N_2 atmosphere at $d \geq 10$ cm is an artifact due to the reflection of the very bright Cr^{1+} emission close to the target.

bottom images of Fig. 5.7(b,c) show these two regions which may be described as follows: The discharge close to the target is dominated by Cr^{1+} emission while the drop-like-shaped plasma shines predominantly due to excited N_2^0. The latter emission region is depicted in Fig. 5.13(a) as a pronounced secondary peak at $d = 15$ cm. The strong emission originating from $N_2(B^3\Pi_g)$ excited states may result from the transfer of the internal energy from metastable $N_2(A^3\Sigma_u^+)$ states during the collisions in-between nitrogen molecules. This energy transfer is a dominant excitation mechanism in post-discharges, where the electron-induced excitation mechanism is negligible.

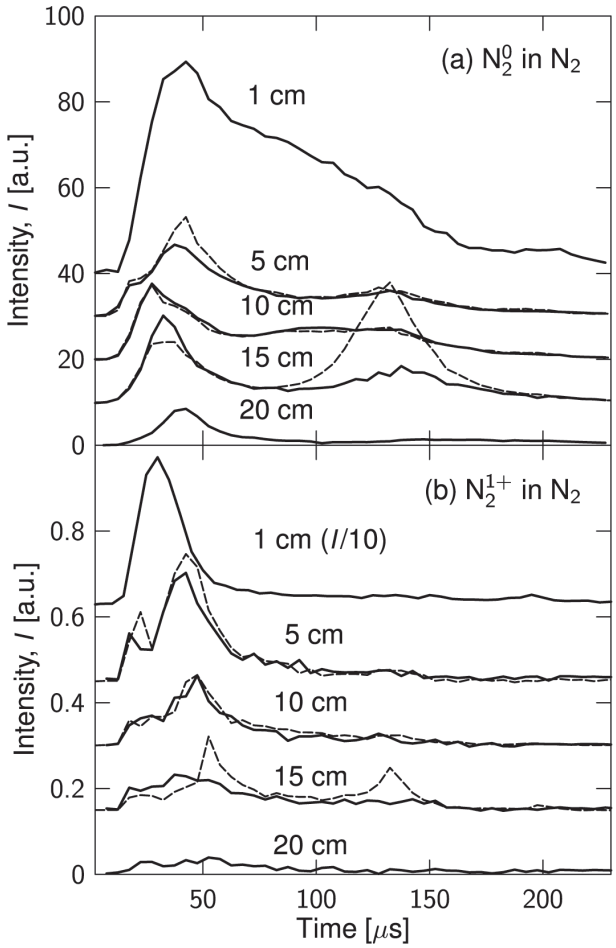

Figure 5.13 Time evolution of the N_2^0 (a) and N_2^{1+} (b) line emission intensities for 5 different target-probe distances d in a HiPIMS pulse in N_2 at 1.3 Pa. The intensity for the N_2^{1+} emission line at $d = 1$ cm was divided by a factor of 10. The dashed lines represent the data from experiments with a circular gas distributor mounted at $d = 11$ cm and a grounded substrate holder facing the target at $d = 16$ cm .

The N_2^0 emission at the end of Phase M was stronger when a circular gas distributor located at $d = 11$ cm and a grounded substrate holder at $d = 16$ cm were mounted within the reactor facing the cathode. In such a configuration, the N_2^0 peak was also accompanied by an important N_2^{1+} emission peak (Fig. 5.13(b), in dashed line). It is also worth noting that the intensities of both the N_2^0 and N_2^{1+} secondary peaks rose significantly when higher discharge currents were used. This was achieved by using a magnetron with a stronger magnetic field or by increasing the working gas pressure. The working gas is efficiently rarefacted by the large amount of sputtered Cr, proportional to the cathode current, in the region in front of

the target. In contrast, N_2 density may locally rise in the proximity of the gas distributor and specifically in-between the distributor and the substrate holder. For instance, the localized increase in the working gas density at the substrate holder was previously discussed in the case of a HiPIMS discharge in Ar [100]. A higher amount of working gas might then be excited (ionized) by energetic electrons travelling outwards from the target alongside the magnetic lines of the unbalanced magnetron.

The nitrogen-emission region located far from the target, depicted in Fig. 5(b,c), extinguishes during the transient period. In the subsequent gas-dominated phase, the discharge emission, dominated by Cr^0 and N_2^0, is confined close to the target ($d < 7$ cm) in the same way as in DCMS discharges (see movie 5.10).

It is important to highlight that the OES technique and imaging are both limited by the excitations conditions of emitting species. Hence, we were only able to study the discharge dynamics within the pulse period during which the energetic electrons are produced. However, long-lived plasma comprising mostly thermalized metal ions was reported in HiPIMS post-discharges using TR optical absorption spectroscopy [165], mass spectroscopy and Langmuir probe diagnostics [174].

5.4 Conclusions

Non-reactive and reactive HIPIMS discharges operated in Ar, N_2/Ar (1:1) mixtures and N_2 were systematically investigated by a combination of time- and space-resolved OES and fast imaging. This approach represents a powerful tool for discharge dynamics analysis in complement with other analytical techniques, such as Langmuir probe diagnostics and mass spectrometry.

The individual phases of discharge evolution were identified: (i) The ignition phase, characteristized by bright working gas emission and the development of a dense-plasma region close to the target, followed by (ii) the metal-dominated high-current phase, characterized by the self-sputtering process with a possible gas-ion sputtering contribution, during which the metal plasma expands outwards from the target. Furthermore, (iii) the transient period and subsequent (iv) high-voltage DCMS-like gas-dominated phase, characterized by a significantly lower current and plasma emission intensity, was detected at the end of the reactive HiPIMS

pulses as a consequence of the voltage drop caused by limitations of the power supply.

The effects observed during individual HiPIMS pulses significantly differed depending on the working atmosphere used. During the discharge ignition, the light emitted by excited gas due to fast electrons penetrating the space in between the electrodes changed from a conical shape, propagating at a speed of 24 $\mathrm{km\,s^{-1}}$ in 1.3 Pa of Ar, to an emissive blob, traveling at a much lower speed of 7.5 $\mathrm{km\,s^{-1}}$ in 1.3 Pa of N_2. A region of remarkably decreased working gas emission intensity was observed during the ignition period in all investigated discharges.

The speed of plasma propagation during the metal-dominated phase ranged from 0.7 to 3.5 $\mathrm{km\,s^{-1}}$. It was found that this speed rose with increasing N_2 concentration and decreasing working gas pressure. Moreover, the form and the emission intensity of the expanding plasma were modified with nitrogen introduction into the working atmosphere. In Ar discharges, the propagating plasma wave visible due to strong emission from Cr^0 and Cr^{1+} had a hemispherical shape, with ionized and excited working gas on its wavefront. In reactive mixtures, the plasma wavefront changed during the pulse from hemispherical through conical to a drop-like shape, extending far into the reactor, and visibly detaching from the dense plasma region close to the target during the transition into the low-current DCMS-like discharge. The discharge in the proximity of the target was still dominated by Cr^0 and Cr^{1+} emissions while the drop-like-shaped plasma at higher target-probe distances ($d = 15 - 20$ cm) shined predominantly due to strong emission from excited N_2^0. An important rise in nitrogen emission in the latter region was detected at the end of the metal-dominated phase, especially when the gas distributor and the substrate holder faced the target and when higher discharge currents were used. Many of the observed phenomena confirm previous findings made by both modeling and other analytical techniques.

Acknowledgments

The authors would like to thank Mr. Maxime Biron for his assistance in the experimental and data-processing work. Also, fruitful discussions with Dr. Andre Ricard are gratefully acknowledged.This work was financially supported by NanoQuebec, NSERC and CRIAQ within the CRDPJ 328038-05 project.

CHAPTER 6

Paper III: Dynamics of HiPIMS discharge operated in oxygen

Authors: M. Hála, O. Zabeida, J.E. Klemberg-Sapieha, L. Martinu

Article published: IEEE Transactions on plasma science, vol. 39, no. 11, p. 2582, Nov. 2011

Comment: This paper is a part of the 6th triennial special issue: Images in plasma science

Abstract: We report on time- and species-resolved plasma imaging analysis of high-power impulse magnetron sputtering discharge operated above a Cr target in pure oxygen. It was found, that the discharge emission is dominated by oxygen species. No metal-dominated sputtering has been detected, in contrast to the discharges in Ar, N_2 and N_2/Ar mixtures investigated previously.

6.1 Published paper

High-power impulse magnetron sputtering (HiPIMS) is a novel PVD deposition technique in which a high-density plasma (densities in the $\mathrm{kW\,cm^{-2}}$ range) is reached by applying short high-voltage unipolar pulses (600 to 2000 V) to a target using a low duty cycle (usually 0.5% – 5%). In this way, high fluxes of ionized sputtered material are available for coating deposition [98].

HiPIMS technology has been applied for the fabrication of hard coatings, and more recently of optical coatings [98]. In addition to our earlier work on the discharges using Ar and N_2 [175, 162], the latter application stimulated our interest to understand the HiPIMS dynamics in O_2/Ar mixtures. In this context, a time-resolved optical investigation of the discharge above a Cr target was performed in pure O_2, in order to gain a better insight into individual plasma-phase processes within the reactive plasmas.

The experiments were carried out in O_2 at 1.7 Pa, using a magnetron with a 5 cm diameter Cr target powered by an HMP2/1 power supply (HUTTINGER Electronik). The substrate holder, mounted at a distance of 10 cm, was biased to -100 V by a RF power supply in order to facilitate the discharge ignition. HiPIMS pulses with a peak voltage of $U_C = -700\,\mathrm{V}$ and a duration of 200 μs were applied to the target with a repetition rate of 50 Hz. The discharge current density, I_d, peaked at $t = 25\,\mathrm{s}$, and then stabilized at $I_d \approx 6\,\mathrm{A\,cm^{-2}}$, compared to $I_d \approx 0.5\,\mathrm{A\,cm^{-2}}$ in pure Ar at the same voltage and pressure. Such a high current density is caused by the high secondary electron emission yield of the oxidized target surface at high voltages [68].

Time- and species-resolved plasma imaging diagnostics [175] of the discharge was performed using a high-speed PI-MAX2 camera (Princeton Instruments) overlooking the deposition chamber through a viewing port. Each image was recorded during 5 μs after a set delay from the initiation of the voltage pulse, and summed over 5 pulses. In order to select the optical signal originating from different excited species, a set of band-pass optical interference filters were placed in front of the camera. More information about the experimental apparatus and a detailed discussion of the design of the suitable band-pass filters can be found in Ref. [175].

The emission spectra of the HiPIMS discharge were also recorded by a USB2000 spectrometer (Ocean Optics) at various target-probe distances (not shown). Close to the target, the spectra were dominated by the emission lines originating from atomic oxygen, while only few chromium emission lines could be identified. This is in contrast to the HiPIMS discharges operated in Ar, N_2/Ar mixtures, and even pure N_2, where the emission from sputtered Cr was predominant [175, 162]. In fact, only a limited amount of Cr appears to be released from the target in the pure O_2 atmosphere, mainly due to the fact that there are no heavy ions available for sputtering (such as Ar^+), and that the target surface is covered by Cr-O compounds exhibiting a low ion-impact sputtering yield.

Fig. 6.1 shows instantaneous images of the discharge at different times from the initiation of the HiPIMS pulse, as recorded by the high-speed camera through two different filters A and B. Filter A is a pass-band filter with a high-transmission region between 400 and 540 nm. In this spectral range the strongest emission originates from the O^+ lines at the proximity of the target, while at distances higher to 5 cm from the target the emission intensity from the O_2^+ lines (first negative system) prevails. The lack of molecular oxygen emission closer to the target indicates a high rate of oxygen dissociation by energetic electrons. Filter B is a high-pass filter with a cut-off wavelength of approx. 750 nm, permitting the monitoring of the two O^0 emission triplets centered at 777.4 and 844.6 nm.

Early after the plasma breakdown ($t = 3$ s) the fast electrons penetrate the space in front of the cathode, giving rise to the neutral dissociated oxygen emission visible with filter B. The establishment of a dense plasma region in the target proximity can be observed within a short delay ($t = 8$ s) due to the emission from O^+ (filter A). Images taken at $t = 13$ to 33 s illustrate a developing discharge during the current peak. Note that a travelling emissive region of excited O^0 indicates plasma expansion outwards from the target racetrack. Images at $t = 83$ s represent a stabilized discharge at $50\,\mathrm{s} < t < 170\,\mathrm{s}$.

The apparently reduced O^0 emission in the proximity of the target may be explained by the high degree of oxygen ionization within the magnetized plasma region. Indeed, the area of the strongest magnetic field confinement is filled with bright O^+ emission. A similar observation was recently reported for Ar and Ar^+ emissions in the case of HiPIMS discharges operated in argon above an Al-doped Zn target [176].

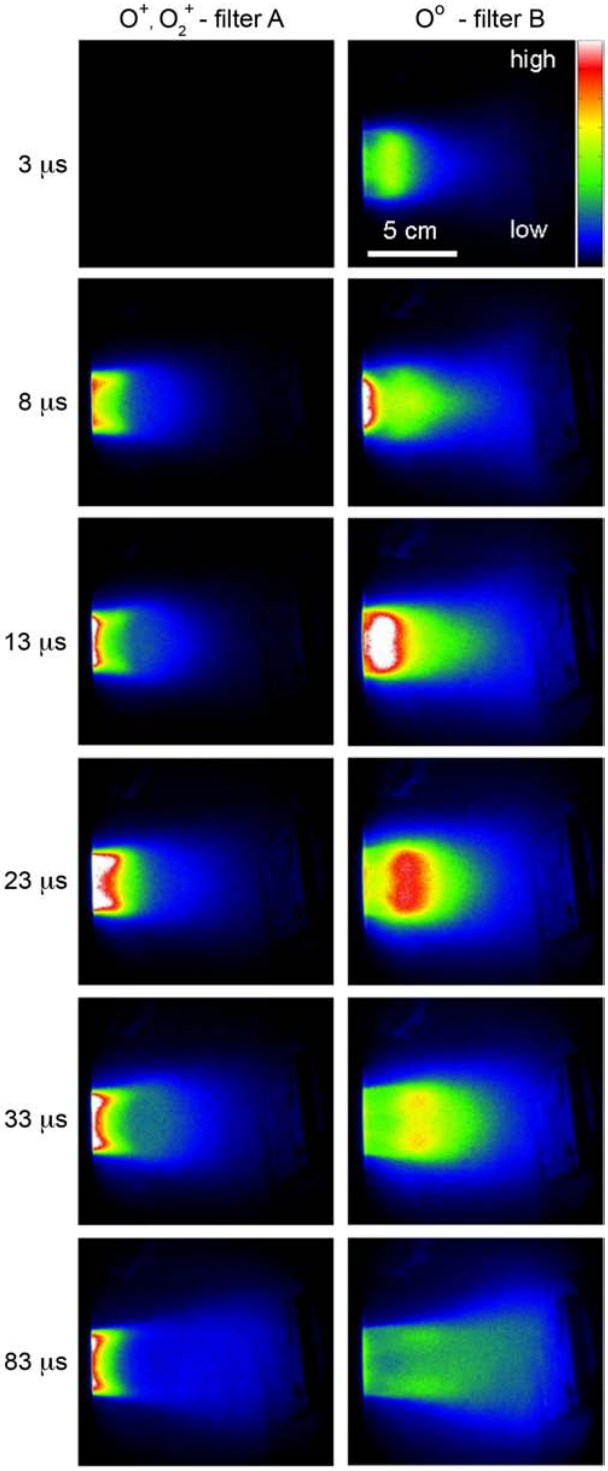

Figure 6.1 High-speed camera images taken during 200-μs HiPIMS pulses in O_2 at 1.7 Pa above a Cr target with an optical bandpass filter specific for emission from ionized oxygen (left column, filter A), and from neutral oxygen lines (right column, filter B). The images were taken at different times from the pulse initiation as displayed on the left side of each row. Different colors are assigned to different emission intensities, according to the linear scale depicted in the upper-most right image.

The oxygen discharge dynamics significantly differs from those in Ar, N_2 and N_2/Ar mixtures operated in the metal-dominated sputtering mode. In the latter case, the discharge development is largely affected by the sputtered metal accumulating close to the target and expanding outwards [162]. The emission from excited Cr then gives the discharge an apparent hemispherical shape, such as illustrated in Fig. 6.2(a). In contrast, very little metal is sputterred from the poisoned target in O_2. The optical emission is thus dominated by dissociated ionized oxygen concentrated above the magnetron racetrack region, copying the form of the magnetic field configuration of the magnetron (Fig. 6.2(b)).

In conclusion, we found that the HiPIMS discharge operated in pure O_2 is dominated by oxygen species, and that no metal-dominated sputtering period has been detected. This can help to better understand the HiPIMS deposition process of metal oxide optical films in O_2/Ar mixtures.

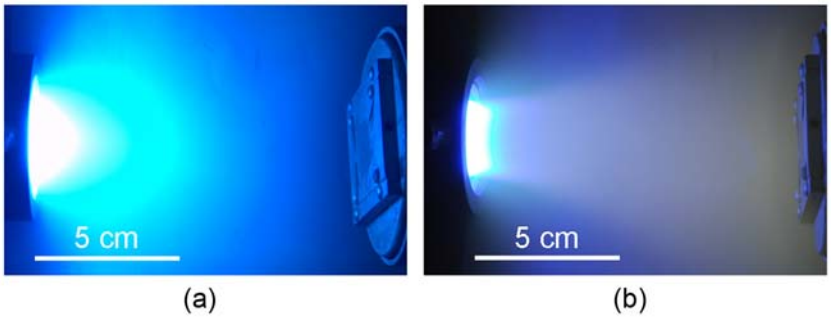

Figure 6.2 Photographs of the HiPIMS discharges operated at an average power of $P = 1\,\mathrm{kW}$ above a Cr target in pure Ar (a) and in pure O_2 (b), recorded by a conventional digital camera over many pulses. Please note that the yellow color in the proximity of the RF-powered substrate holder on the right of the image (b) originates from excited O_2^+.

6.2 Waveforms and emission spectra pertaining to the O_2 discharge

The published paper presented above had a limited length imposed by the publisher. However, the following results further complete the time-resolved measurements, and they are shown here for completeness.

Fig. 6.3 shows the averaged discharge current and voltage waveforms during the 200-μs HiPIMS pulses applied to a Cr target in O_2 at 1.7 Pa. Please note the elevated average value of I_C to which the high frequency oscillations are superimposed. The respective optical emission spectra, depicted in Fig. 6.4, illustrate that the emitted light is dominated by the working gas ions, specifically in the nearest proximity of the target. This contrasts with the spectrum of the non-reactive HiPIMS discharge operated at the comparable conditions in pure Ar (Fig. 4.1 in Chapter 4 [175]). The two latter observations (high pulse currents accompanied by an important emission from ionized working gas) suggest a steady-state high density discharge in which not the metal ions but the working gas ions are the dominant sputtering species, as discussed in Appendix A [177] and detailed in Ref. [122].

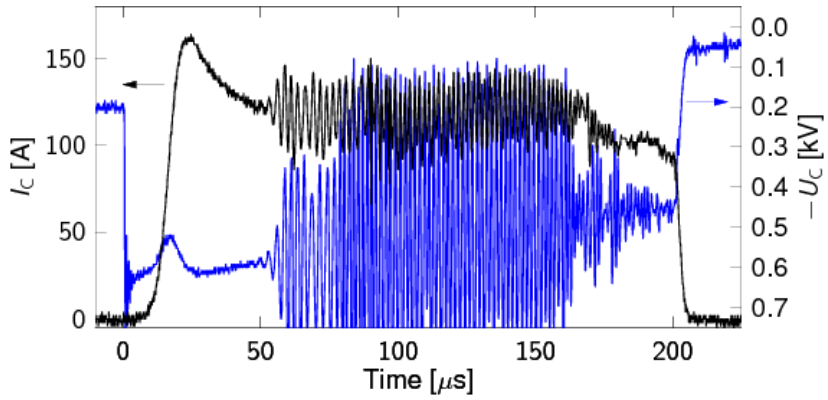

Figure 6.3 Current and voltage waveforms recorded during a 200-μs HiPIMS pulse operated with a Cr cathode in O_2 at 1.7 Pa. Both waveforms were averaged over 64 pulses.

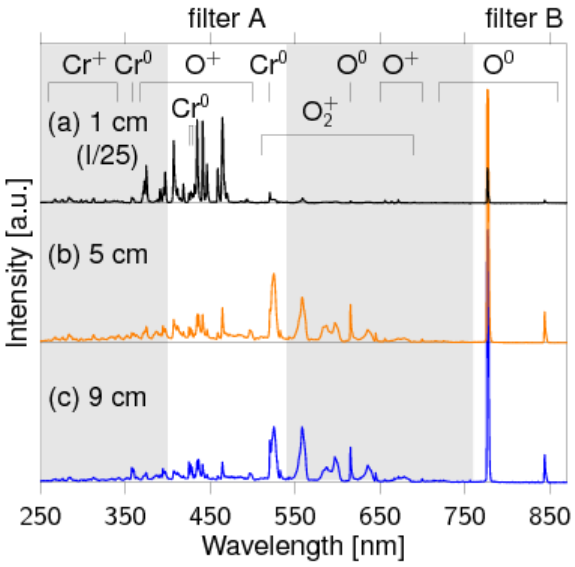

Figure 6.4 The emission spectra of the HiPIMS discharges operated above the Cr target in O_2 at 1.7 Pa recorded at three target-probe distances $d = 1$ (a), 5 (b) and 9 cm (c). Spectral intensities at $d = 1$ cm were divided by a factor of 25. The spectral regions specific for the emission originating from individual excited species are indicated, as well as the high-transmission regions of the two band-pass interference filters (white area). It is to be noted that the O^0 emission line at 777.5 nm is saturated at $d = 5$ and 9 cm.

CHAPTER 7

Paper IV: Pulse management in high power pulsed magnetron sputtering of niobium

Authors: M. Hála, J. Čapek, O. Zabeida, J.E. Klemberg-Sapieha, L. Martinu

Article submitted: Surf. Coat. Technol. (Dec. 2011)

Abstract: High power pulsed magnetron sputtering is being extensively explored as a very promising approach for the fabrication of functional coatings with enhanced performance. However, a direct comparison of the results obtained in different systems is complicated given the variety of pulse power supplies with different pulse shape, voltage and current characteristics. In this study, we systematically investigate and compare sputtering processes above a model niobium target operated in the same reactor using two commercially available power supplies: (i) a shorter ($200\,\mu$s) square voltage pulse generator permitting higher cathode voltage values, and (ii) a modulated pulse power generator with longer ($800 - 3000\,\mu$s) custom-shaped pulses. In addition, target sputtering using a conventional DC power supply is also analyzed for comparison purposes. The pulsed discharges are characterized by time-resolved current and voltage probes and optical emission spectroscopy. The deposition rate, the microstructure, and the mechanical stress of the fabricated Nb coatings are evaluated and compared. Finally, the effect of the power delivery management is discussed in terms of discharge characteristics and coatings properties.

7.1 Introduction

Recent developments in the field of physical vapour deposition has generated a great interest in processes that provide high ionization of the sputtered material. One of the most promising techniques, recently introduced to both academia and industry, combines magnetron sputtering and pulsed power technology. The application of short duration high power pulses to a metallic target mounted on a magnetron head can generate high density plasma (up to $10^{13}\,\mathrm{cm}^{-3}$) and high fluxes of sputtered metal ions available for the deposition process [21, 98, 104].

It was demonstrated that such a technique, called "high power pulsed magnetron sputtering" (HPPMS) or "high power impulse magnetron sputtering" (HiPIMS), can be beneficial in coating and interface engineering [158, 14], in coating of complex-shaped substrates [21, 15], and in tailoring the film properties [97, 98]. The transfer of this technology from academia and R&D departments towards industrial applications has already started and several companies have now implemented it into production [178, 179, 180].

The growth in attention related to high power pulsed sputtering also stimulated the development of suitable power supplies (PS) with different pulse shape, voltage and current characteristics, offered from a variety of producers. Therefore, there is a need for a rigorous comparison of the available PS capacities and limitations in order to facilitate the manufacturer's choice for a specific deposition process. Furthermore, a detailed comparison with standard DC magnetron sputtering (DCMS) is required as well.

Commercially available PS can be divided into two principal categories according to the type of the high power magnetron discharge they can produce: (i) square voltage pulse generators allowing one to reach high cathode voltage values, which we will label in this study as HiPIMS PS, and (ii) custom-shaped voltage generators producing longer pulses of lower amplitude, applied for "modulated pulse power magnetron sputtering" (MPPMS). The shapes of the pulses generated by the two types of PS, compared to DCMS power delivery, are illustrated in figure 7.1.

In this work, we systematically investigate HiPIMS and MPPMS discharges using a Nb target sputtered in Ar, and compare them with conventional DCMS discharges. Nb is a

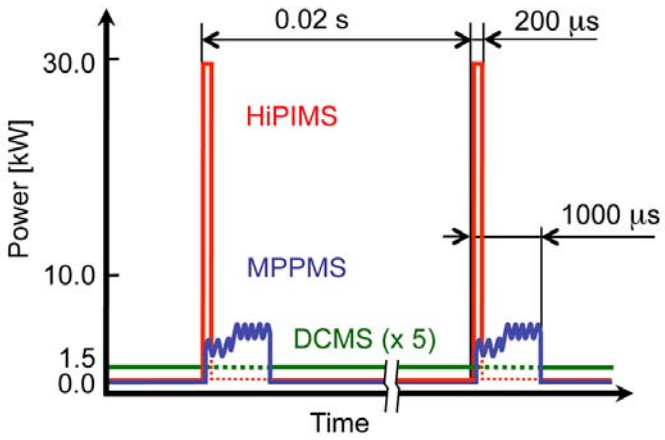

Figure 7.1 Schematic representation of the power delivery during the pulsed discharges above a magnetron powered by HiPIMS, MPPMS and DCMS power supply operated at the same average power $P = 300\,\mathrm{W}$.

highly interesting transition metal that exhibits superconducting properties and that forms an attractive high refractive index oxide when sputtered in reactive oxygen-containing gas mixtures. Firstly, we discuss the effect of the different power management strategies on discharge current waveforms, plasma characteristics, and on sputtered material ionization evaluated by optical emission spectroscopy (OES). Subsequently, we rigorously characterize the deposition rate, the microstructure and the internal mechanical stress of Nb coatings prepared by HiPIMS, MPPMS and DCMS at various discharge powers, and at two different Ar pressures.

7.2 Experimental details

The experiments were performed in the system shown in figure 7.2, consisting of a turbomolecularly pumped stainless steel chamber, an unbalanced magnetron and a substrate holder. The magnetron with a 5 cm diameter Nb target was powered by either (i) HÜTTINGER Electronic HMP2/1 HiPIMS PS, (ii) ZPulser Axia 180 MPPMS PS, or (iii) Advanced Energy MDX 1K DCMS PS. The specifications of these PS are summarized in table 7.1. The duration of the HiPIMS and MPPMS pulses was fixed at 200 μs and 1500 μs respectively, unless otherwise specified. The pulse repetition frequency was fixed at $f = 50\,\mathrm{Hz}$ in both cases.

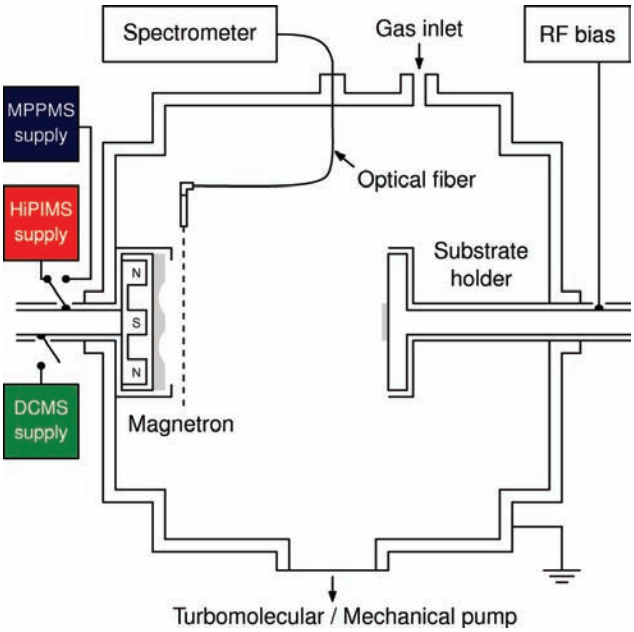

Figure 7.2 Schematic diagram of the experimental setup. A 5 cm diameter magnetron with a Nb target can be powered by either a HiPIMS, MPPMS or DCMS power supply. The substrate holder, positioned at a distance of 10 cm from the target, is biased by an RF generator. The optical fiber has its line of sight parallel to the target surface at a distance $d \approx 1\,\mathrm{cm}$.

Waveforms of the cathode voltage, U_C, and of the cathode current, I_C, were measured by a Tektronix P6015A voltage probe and a Pearson 301X current monitor, respectively, and recorded by a Tektronix TDS2014B digital oscilloscope. The average discharge power, P, was then calculated as:

$$P = f \int_0^\mathrm{T} U_\mathrm{C}(t) I_\mathrm{C}(t)\,\mathrm{d}t, \tag{7.1}$$

where t stands for time and T for the pulse duration during which the cathode current has a non-zero value.

The optical emission from the discharge was recorded by an optical fiber with its line of sight parallel with the target surface at a distance $d \approx 1\,\mathrm{cm}$. Time-averaged measurements were analyzed by an Ocean Optics USB2000 spectrometer. For the time-resolved (TR) diagnostics, and for the estimation of the metal ion-to-neutral intensity ratio, a PI Acton SpectraPro 2750 monochromator with a holographic grating (2400 grooves mm^{-1}) was used in combination with a high speed Princeton Instruments PI-MAX2 camera. The list

Table 7.1 Specifications of the HiPIMS, MPPMS and DCMS power supplies used in this study.

	HiPIMS	MPPMS	DCMS
Power regulation by	Voltage	Capacitors' charge	Voltage
		Micropulse duty cycle	Current
	Pulse length	Pulse length	Power
Pulse shape programming	no	yes	—
Maximum mean power	2 kW	5 kW	1 kW
Maximum peak power	2000 kW	330 kW	1 kW
Maximum cathode voltage	2000 V	900 V	1000 V
Maximum current	1000 A	550 A	1 A
Maximum pulse length	200 μs	3000 μs	—
Maximum frequency	500 Hz	400 Hz	—
Maximum duty cycle	10 %	28 %	—

of the monitored emission lines representing different neutral and ionized species with their corresponding higher and lower excitation energy levels is given in table 7.2.

In TR OES analysis, each optical signal was recorded during a $5\,\mu$s period, following a preset delay from the initiation of the voltage pulse. The signal was averaged over 10 to 50 pulses, depending on its intensity. Subsequently, the acquisition and averaging was repeated for the following $5\,\mu$s interval. Such a process was iterated until the pulsed discharge extinction.

The experiments were carried out in pure Ar at two working gas pressures, $p = 1\,\mathrm{Pa}$ and $p = 2\,\mathrm{Pa}$. The Ar flow rate was kept constant at 44 sccm, and the total pressure was adjusted by the throttling valve. Nb coatings were prepared on Si(100) substrates kept at ambient temperature, positioned at a distance $d = 10\,\mathrm{cm}$ from the target. The substrate holder was biased to $-20\,\mathrm{V}$ by an Advanced Energy RF 600 PS in order to facilitate the discharge ignition.

Table 7.2 List of the monitored OES lines with corresponding wavelengths, λ, excitation energies of the upper excited states, E_k, and of the lower excited states, E_l. The emission lines used for the estimation of the metal ion-to-neutral ratio are highlighted by an asterisk ($\star$). The values of E_k and E_l for Nb and O are taken from [181], and for Ar from [182].

	Nb^0	$Nb^0\star$	$Nb^+\star$	Nb^{2+}	Ar^0	Ar^+
λ [nm]	466.38	466.62	313.08	245.70	811.53	442.60
E_k [eV]	2.85	4.05	4.40	—	13.08	19.55
E_l [eV]	0.20	1.39	0.44	—	11.55	16.75

The thickness of the fabricated films was determined by a Veeco Dektak 3030ST Profilometer equipped with a conical diamond stylus. The internal stress of the films was evaluated before and after film deposition by measuring the curvature of rectangular Si stripe ($10\,\mathrm{x}\,50\,\mathrm{mm}^2$) using a Tencor FLX-2900 stress measurement instrument. The value of the internal stress was then calculated from the Stoney relation [154]. The crystal structure was studied by X-ray diffractometry (XRD) in $\theta - 2\theta$ configuration using Cu Kα ($\lambda = 0.15406\,\mathrm{nm}$) radiation in a Philips X'PERT instrument. The film microstructure was characterized by field emission gun scanning electron microscopy (FEG SEM) using a Hitachi FB2000A.

7.3 Results and discussion

7.3.1 Characterization of HiPIMS and MPPMS discharges

In this section, we describe the power management of the two pulsed PS and analyze their respective discharge characteristics by OES diagnostics.

Power management

The effect of the different power adjustments in HiPIMS and MPPMS generators on the discharge current waveforms recorded at various power loads is shown in figure 7.3. The HiPIMS PS is a constant voltage generator that produces single square-shaped voltage pulses of adjustable length (10–200 μs) and amplitude. Hence, one has a direct control over U_C that may reach, in our case, values up to 2000 V in amplitude. Maintaining U_C above a certain threshold during a sufficiently long period results in a transition from gas-ion dominated sputtering towards metal-ion dominated sputtering in which the sputtered material ions contribute to the target sputtering process. The presence of the latter process can be distinguished by a steady high current level, that is independent of the working gas pressure [120, 71]. Such a transition from a low current "DC"-like discharge towards a steady high current "metal-dominated" discharge is indeed observed in figure 7.3(a), when the voltage amplitude is higher than $U_\mathrm{C} \approx 650\,\mathrm{V}$.

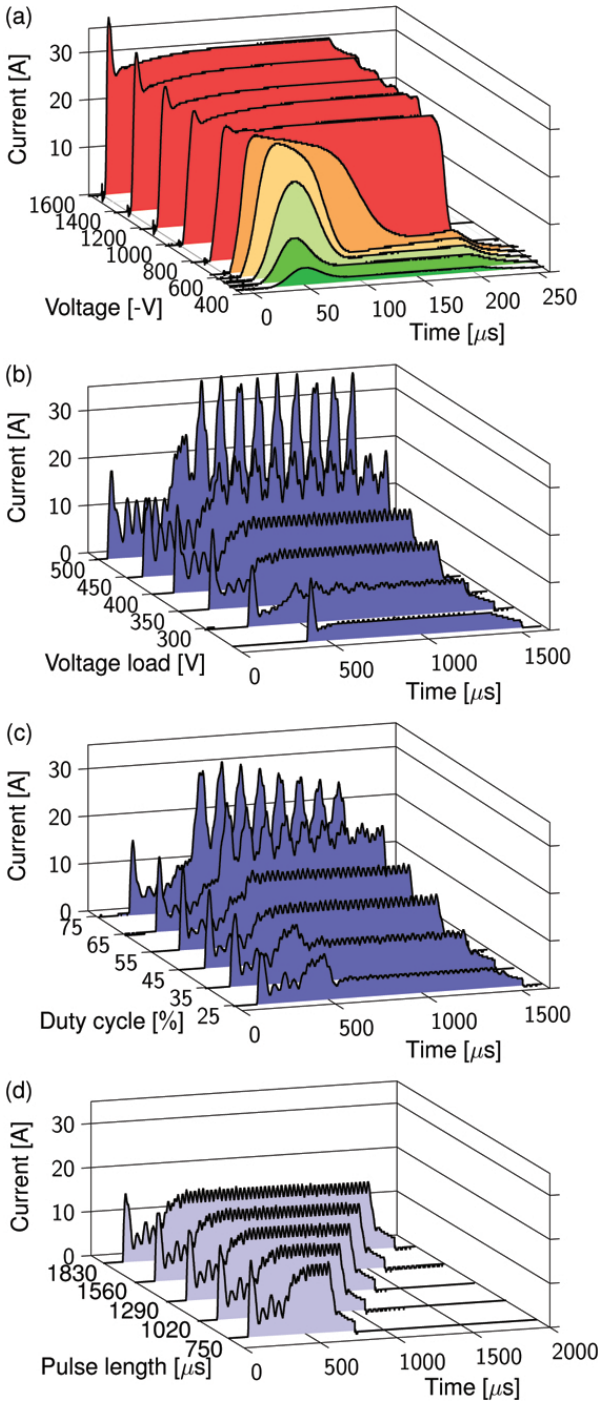

Figure 7.3 Effect of the increasing power load on the current waveforms for HiPIMS (a) and MPPMS (b)-(d) pulses operated with a Nb cathode in Ar at $p = 1\,\mathrm{Pa}$. The applied power was modified either by varying the HiPIMS cathode voltage (a), the voltage load of the MPPMS capacitors (b), the duty cycle of the micropulses during the high power stage of the MPPMS pulse (c), or by adjusting the MPPMS pulse length (d). The pulse frequency was kept constant at $f = 50\,\mathrm{Hz}$. All waveforms were averaged over 64 pulses. Note the modification in the current waveforms of the HiPIMS discharges when the cathode voltage approaches the threshold for metal-dominated sputtering, indicated by the colour change in (a).

In contrast to the square-shaped HiPIMS pulses, the MPPMS PS generates a sequence of short duration voltage micropulses (length of several μs to several tens of μs). Its application to the cathode results in an oscillating U_{C}, such as shown in figure 8.1(d). The amplitude of these voltage oscillations can be controlled by (i) the "voltage load" of the PS capacitors, and (ii) the combination of the micropulse recipes using variable on and off times (hence "duty cycle", D) [130, 135]. A typical MPPMS pulse (length up to a few ms) is much longer than any HiPIMS pulse (length of tens or hundreds of μs) and consists of two or more segments characterized by its specific micropulse recipe, resulting in a different power output. In the present experiments, the on/off time of the applied micropulses is modified after the first 400 μs from 10 μs/40 μs ($D = 20\,\%$, used during the low power ignition stage) to 12 μs/45 μs ($D = 45\,\%$, used during the high power stage producing a high density plasma).

The effect of the varying voltage load on the resulting discharge current waveforms is illustrated in figure 7.3(b). At elevated voltage load values, both amplitude and period of the current oscillations increase. However, a steady metal-dominated sputtering regime cannot be achieved even at an applied power which is twice as high as that used in the HiPIMS discharge operated at a maximum voltage ($U_{\mathrm{C}} = 2000\,\mathrm{V}$).

Figure 7.3(c) shows the current waveforms representing MPPMS pulses with various micropulse duty cycles during the high power stage of the MPPMS pulse. One can see, that the resulting effect on the current waveform is similar to that of the varying voltage load. For this reason, the duty cycle during the high power stage was fixed at 45 % in all other experiments, and the voltage load was used as the principal variable for discharge power modification. Figure 7.3(d) illustrates MPPMS pulses composed of the same micropulse recipes but with a different length of the high power segment.

Figures 8.1(a) and 7.3(d) illustrate the TR evolution of the discharge current and voltage of typical HiPIMS and MPPMS pulses respectively. It is shown that the HiPIMS PS applies a maximum U_{C} instantly at the beginning of the pulse, followed by a high current rise. The combination of the high instantaneous voltage and current values increases the probability of arcing, which in turn can limit the deposition process. In contrast, both U_{C} and I_{C} increase gradually at the beginning of the MPPMS pulse, and reach substantially lower values than in the case of HiPIMS (when operated at the same P). This behaviour significantly reduces

the probability of arc development [14]. Furthermore, if no current is drawn (discharge not ignited), MPPMS PS progressively increases U_C until discharge breakdown conditions (or the maximum U_C value) are met. This feature is illustrated by an example of an MPPMS discharge operated in a O_2/Ar mixture [figure 4(d) in [184]]. The resulting long pre-ignition period can be beneficial at low pressures or under reactive conditions in which the time-lag of the current onset behind the voltage application may be larger than the duration of the pulse itself (e.g. 200 μs in HiPIMS). Therefore, the use of MPPMS pulses of long duration allows one to operate a discharge in conditions in which a HiPIMS discharge would be difficult to ignite or would be prone to arcing.

Optical diagnostics

In order to gain information about pulsed discharge dynamics, plasma composition and sputtered material ionization, the OES diagnostics was performed in both time-averaged and time-resolved modes. The evolution of the optical emission intensity from selected metallic and working gas excited species during typical HiPIMS and MPPMS pulses is shown in figures 8.1(b-c) and 8.1(e-f), respectively. We first discuss the evolution of the HiPIMS pulse, and then we follow up with an analysis of the MPPMS pulse.

HiPIMS discharge breakdown is characterized by an appearance of the emission peak of Ar^0 excited by the energetic electrons. Onset of the target sputtering is marked by a rise of Ar^+ and of both neutral and ionized Nb emissions [figures 8.1(c) and 8.1(b)]. A large number of sputtered metal atoms then enter in collision with the working gas and causes its localized heating and rarefaction [116, 100, 117]. Furthermore, the injection of the sputtered metal into the plasma zone results in significant electron cooling due to inelastic electron-metal collisions. The latter effect is the principal origin of the drop in the emission intensities of Ar^+ and also of the metallic emission lines, following their peak at $t = 20\,\mu$s. The observed delay between the current peak and the emission intensity maxima of Ar^+ and of the metallic species may be ascribed to the travelling time of the expanding high density plasma towards the probe position [162].

For the rest of the pulse, $t > 75\,\mu$s, the emission intensities of all Nb lines are approximately steady, such as U_C and I_C values are. The peaking Ar^0 emission following the end

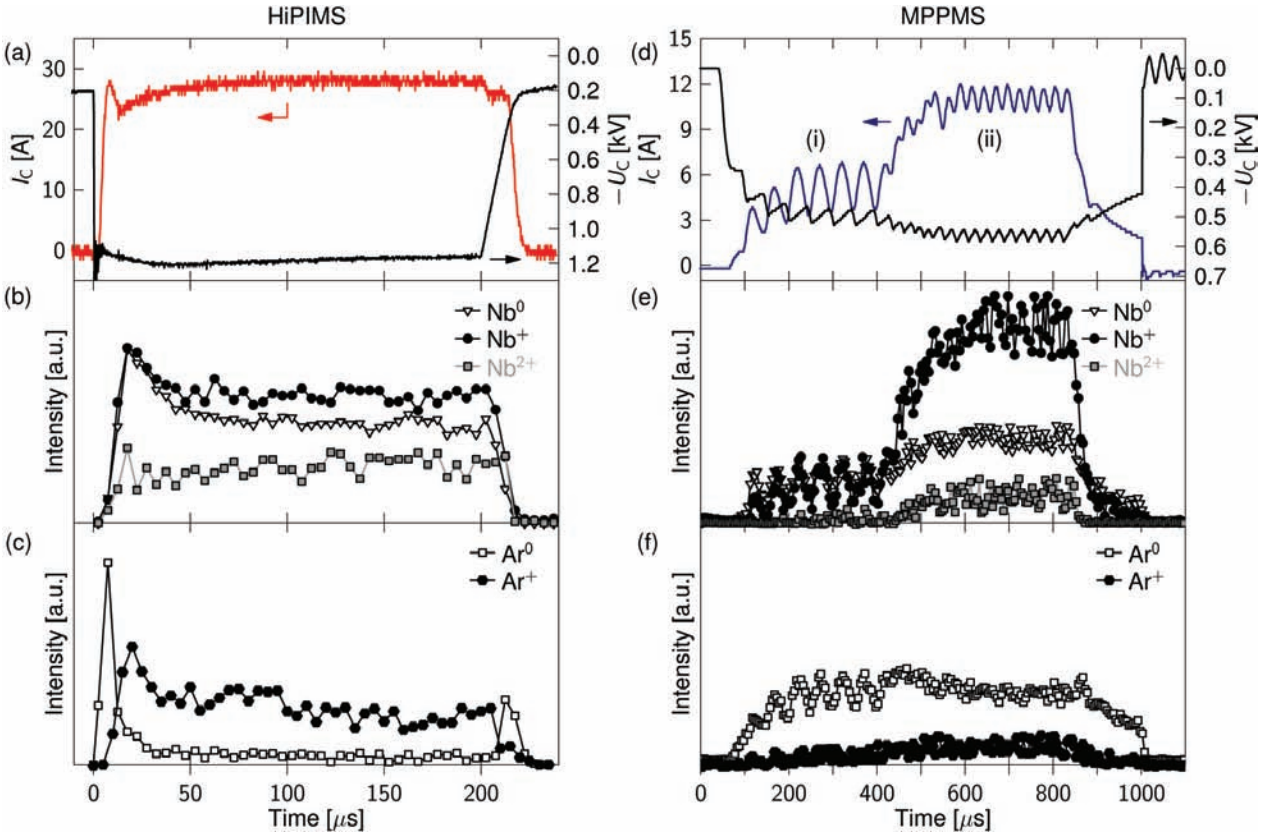

Figure 7.4 Time evolution of the discharge current I_C and the cathode voltage U_C (a,d), and of the optical emission intensities originating from the excited metal species (b,e) and working gas species (c,f), recorded during a 200 μs HiPIMS pulse (a,b,c) and a 1000 μs MPPMS pulse (d,e,f). Both discharges were operated in Ar at $p = 1$ Pa. The low power (i) and the high power (ii) segments of the MPPMS pulse are highlighted in (d). The acquisition time for different monitored species was not normalized.

of the pulse suggests a presence of high energy electrons escaping the magnetic confinement close to the cathode due to the abrupt drop in the discharge current [26]. More detailed information about the relevant discharge dynamics can be found in [71] and [162].

In the MPPMS discharge, both U_C and I_C oscillate with a period equal to that of the driving voltage micropulses [130]. Figures 8.1(d) and 8.1(f) show that the emission intensities of all the monitored emission lines also reflect these oscillations due to the varied current amplitude, and hence the plasma density [185].

The transition into the high power stage of the MPPMS pulse (after the first 400 μs from the pulse onset) is followed by a significant rise in the metal emission intensity. In contrast,

Ar^0 emission stabilizes at an intensity level comparable to the one during the low power pulse stage. The only possible explanation of this observation is the gas rarefaction by the large amount of the sputtered metal injected into the monitored plasma region, such as previously reported for other high density discharges [100, 117]. It is to be noted that the emission intensity from both Nb^+ and Nb^{2+} increased several times during this transition, while the Nb^0 signal only doubled. Such an observation suggests a significant rise in metal ionization. However, the average ion-to-neutral ratio in MPPMS discharges is lower than in the HiPIMS discharges operated at the same average power, as will be shown below.

The averaged optical emission spectra of HiPIMS, MPPMS and DCMS discharges obtained at $P = 300\,\mathrm{W}$ are displayed in figure 7.5. It should be stressed that all the three spectra were normalized to the same acquisition time. The HiPIMS spectrum is dominated by an intense emission from Nb^+. Furthermore, strong Nb^0 and even Nb^{2+} emission lines can be identified. The high emission from the ionized Nb species can serve as an indication that the HiPIMS discharge is operated in the metal-dominated sputtering regime, such as previously shown in [177]. The MPPMS spectrum shows an important emission from Nb^+, but the strongest emission originates from Nb^0. This observation suggests a lower ionization of the sputtered metal in MPPMS than in HiPIMS discharges operated at the same power

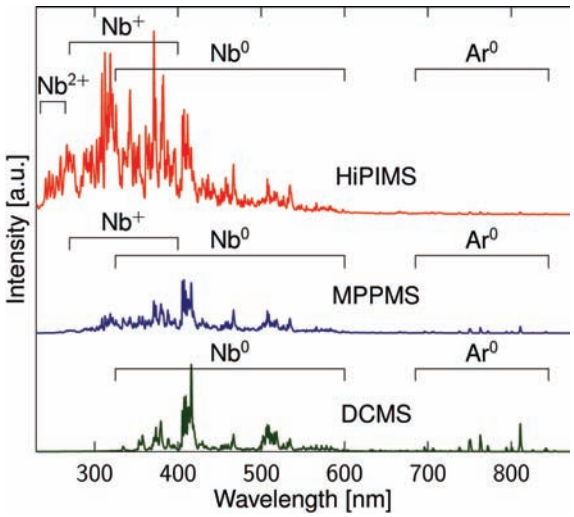

Figure 7.5 Normalized optical emission spectra recorded at $d = 1\,\mathrm{cm}$ from the Nb target powered by HiPIMS, MPPMS and DCMS in Ar at $p = 1\,\mathrm{Pa}$ and at the average power $P = 300\,\mathrm{W}$.

load. In contrast to both pulsed discharges, only neutral Nb lines can be identified in the DCMS spectra. In addition, Ar^0 emission lines in DCMS have a notably stronger intensity than in HiPIMS and MPPMS. This may be another indication of working gas rarefaction by the sputtered Nb and of subsequent electron cooling in both pulsed discharges.

Figure 7.6 shows the power-dependence of the emission intensity ratio, $I(Nb^+)/I(Nb^0)$, of two selected Nb^+ and Nb^0 lines listed in table 7.2. These particular emission lines were chosen because they are both formed by transitions for which the upper level energies are similar. Assuming that both of these emitting species are only populated by electron impact excitation from the ground state, and only depleted by a pure radiative process, their emission line intensity ratio can be used as a qualitative measure of the ion-to-neutral density ratio.

The $I(Nb^+)/I(Nb^0)$ ratio appears much higher in both high power pulsed discharges in comparison with DCMS. For instance, at $P = 300\,W$ its amplitude was 19 times higher in HiPIMS and 7 times higher in MPPMS. This observation indicates that both high power pulsed discharges produce plasmas with a significantly higher metal ionization than the

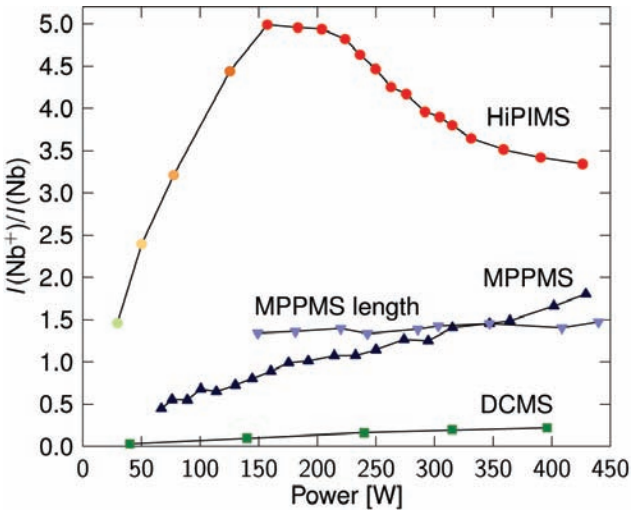

Figure 7.6 Optical emission intensity ratio $I(Nb^+)/I(Nb^0)$ measured at $d = 1\,cm$, as a function of the power load P on the target. The power was modified by changing the cathode voltage in DCMS, HiPIMS, and in MPPMS by either adjusting the voltage load (MPPMS) or the length of the pulse (MPPMS length). All discharges were operated in Ar at $p = 1\,Pa$. The maximum in the HiPIMS emission intensity ratio represents a transition from a gas-dominated to a metal-dominated discharge.

DCMS discharge operated at the same power. Moreover, it identifies HiPIMS as the most suitable technique for deposition processes where maximum metal ionization is required.

It is also to be mentioned that the $I(\mathrm{Nb}^+)/I(\mathrm{Nb}^0)$ ratio exhibits a turning point in HiPIMS, while it constantly increases with P in DCMS and MPPMS. For $P < 150\,\mathrm{W}$, the ratio for HiPIMS rises, while for $P > 150\,\mathrm{W}$, it drops. This is a consequence of the transition into the metal-dominated sputtering in HiPIMS at $P \approx 125\,\mathrm{W}$ (when $U_\mathrm{C} \approx 650\,\mathrm{V}$). In fact, it is the substantial rise in the emission intensity from Nb^0 for $P > 125\,\mathrm{W}$ that is the cause of the diminishing $I(\mathrm{Nb}^+)/I(\mathrm{Nb}^0)$ ratio at higher powers. We have previously observed a similar development of ion-to-neutral intensity ratio in optical diagnostics of the HiPIMS discharges operated with a Cr target (unpublished results). The decreasing ion-to-neutral density ratio may indicate that an increasing portion of the metal ions escapes the magnetized plasma region, such as reported by Andersson and Anders [123] and confirmed by modelling by Vlček and Burcalová [104]. The latter effect can be due to the existence of the potential gradient within the bulk HiPIMS plasma suggested by Brenning *et al.* [128] and experimentally validated by Horwat and Anders [186].

7.3.2 Characterization of Nb coatings

In the previous section, the effect of the power management on the high power pulsed discharge behaviour and characteristics was discussed. In this section, we explore the properties of the fabricated Nb coatings.

Nb films were deposited at two Ar pressures (1 and 2 Pa) under the following four power regulation conditions:

(i) HiPIMS discharges using different cathode voltage amplitudes during the pulse [such as shown in figure 7.3(a)],

(ii) MPPMS discharges using different voltage loads of the PS capacitors [figure 7.3(b)],

(iii) MPPMS discharges using different lengths of the high power pulse segment ("MPPMS length") [figure 7.3(d)], and

(iv) DCMS discharges using different cathode voltage levels.

Table 7.3 specifies the ranges of the average U_C values during the pulses (or during the high power stage of the MPPMS pulses), and of the used pulse duration, together with the respective average powers and peak power densities. All of the deposited Nb films were 700 to 900 nm thick.

Table 7.3 Type of power regulation and ranges of the discharge parameters used in the preparation of four series of Nb coatings. In order to permit the power density evaluation, the effective sputtering area of the target was estimated from the racetrack surface measurement as $S = 12.5\,\mathrm{cm}^2$.

	HiPIMS	MPPMS	MPPMS length	DCMS
Type of power regulation	Cathode voltage	Voltage load	Pulse length	Cathode voltage
Cathode voltage [V]	550 – 1600	470 – 670	650 (1 Pa) / 500 (2 Pa)	290 – 390
Pulse duration [μs]	200	1500	880 – 1830	—
Average power [W]	45 – 345	100 – 345	105 – 320	38 – 310
Peak power density [W/cm^2]	700 – 3200	140 – 540	400	3 – 25

Deposition rate

The dependence of the Nb deposition rate, r, on the average discharge power is shown in figure 7.7(a). It demonstrates that for all pulsed discharges r is lower than for DCMS discharge. For instance, r for HiPIMS and MPPMS is about 55% of r_{DCMS} at $P = 300\,\mathrm{W}$. Moreover, the difference between r_{HiPIMS} ($p = 1\,\mathrm{Pa}$), r_{MPPMS} and r_{DCMS} further increases with rising power. This phenomenon is also illustrated by the power-normalized deposition rate, r_{n}, plotted in figure 7.7(b). One can see that $r_{\mathrm{n,\,MPPMS}}$ and $r_{\mathrm{n,\,HiPIMS}}$ ($p = 1\,\mathrm{Pa}$) drop considerably with growing power, while $r_{\mathrm{n,\,DCMS}}$ and $r_{\mathrm{n,\,MPPMS\,length}}$ are almost constant.

There are several effects that may be responsible for the observed deposition rate reduction in high power pulsed discharges. The most important ones are: (i) less-than-linear dependence of the sputtering yield on the energy of bombarding ions [124, 125], (ii) loss of the sputtered material via ionization and subsequent back-attraction towards the target [104, 125], and (iii) modified target-substrate transport geometry [126, 104]. As will be illustrated below, the effect (i) can be recognized as the principal origin of the power-dependent deposition rate reduction in the investigated experiments.

It is well known that the sputtering yield, Y, does not scale proportionally with the energy of bombarding ions ($\sim U_C$) within the here-discussed energy range (300 - 1600 eV). Instead,

it can be approximated by [187, 125, 124]:

$$Y \approx U_{\mathrm{C}}^{0.5}. \tag{7.2}$$

Because of this less-than-linear dependence of Y on U_{C}, discharges operated at a same average power, but with a different combination of U_{C} and I_{C}, cannot reach an identical deposition rate. Thus, high power pulsed discharges that use higher U_{C} than DC discharges have to exhibit lower r in comparison with DCMS, unless other phenomena than sputtering (e.g. evaporation) are considered.

Anders [125] has shown that the theoretical deposition rate achievable by HiPIMS, $r_{\,\mathrm{HiPIMS}}$, can be related to that of DCMS operated at a same P, $r_{\,\mathrm{DCMS}}$, and to their respective U_{C} ratio through a simple relation:

$$\frac{r^{\star}_{\mathrm{HiPIMS}}}{r_{\,\mathrm{DCMS}}} \approx \left(\frac{U_{\mathrm{C,\,HiPIMS}}}{U_{\mathrm{C,\,DCMS}}} \right)^{-0.5}. \tag{7.3}$$

Figure 7.7(a) shows an estimation of the maximum HiPIMS deposition rate defined by equation 7.3, $r^{\star}_{\mathrm{HiPIMS}}$, calculated with the experimental voltage values $U_{\mathrm{C,\,HiPIMS}}$ and $U_{\mathrm{C,\,DCMS}}$, and with the measured $r_{\,\mathrm{DCMS}}$. One can see that $r^{\star}_{\mathrm{HiPIMS}}$ approximately coincides with the measured $r_{\,\mathrm{HiPIMS}}$. Such finding suggests that the effect (i) is a crucial phenomenon that could explain the observed deposition rate reduction.

It should be stressed that the herein presented results were obtained in experiments with a relatively little eroded Nb target. A further drop in the deposition rate of Nb films prepared by HiPIMS was observed with the increasing target erosion (not shown here). More specifically, the progressing depth of the target erosion zone, and consequently the increased magnetic field strength above its surface, resulted in significantly higher discharge currents and in further reduction of $r_{\mathrm{n,\,HiPIMS}}$ in comparison with $r_{\mathrm{n,\,DCMS}}$. This observation indicates the influence of other effects, such as the metal back-attraction (ii) and modified material transport (iii). In-depth analysis of the importance of these phenomena on the deposition rate reduction will be presented elsewhere.

The evaluation of the theoretical deposition rate reduction for MPPMS is rather complicated because U_{C} varies greatly during individual MPPMS pulses. Since U_{C} is generally

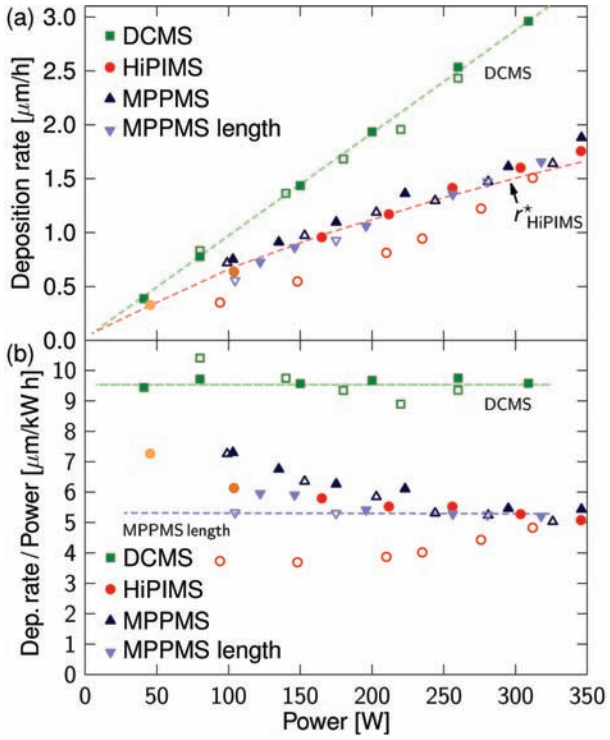

Figure 7.7 Deposition rate r (a) and deposition rate normalized to power r_{n} (b) for Nb coatings prepared at two Ar pressures, $p = 1\,\mathrm{Pa}$ (full symbols) and $2\,\mathrm{Pa}$ (open symbols), as a function of the average applied power P. The coatings were deposited by DCMS, HiPIMS, and MPPMS at different cathode voltages and by MPPMS using different pulse lengths (see table 7.3). The linear approximations of r_{DCMS}, $r_{\mathrm{n,\,DCMS}}$, $r_{\mathrm{n,\,MPPMS\ length}}$ and the theoretical deposition rate limitation for HiPIMS, $r^{\star}_{\mathrm{HiPIMS}}$, are highlighted by dashed lines.

lower in MPPMS than in HiPIMS operated at a same P, $r_{\mathrm{n,\,MPPMS}}$ can reach higher values than $r_{\mathrm{n,\,HiPIMS}}$, as also confirmed in figure 7.7(b).

It is to be noted that $r_{\mathrm{n,\,MPPMS\,length}}$ is smaller than $r_{\mathrm{n,\,DCMS}}$ at all investigated powers, such as highlighted by the two dashed lines in figure 7.7(b). This contradicts with the findings reported by Lin *et al.* [188] who observed that r_{MPPMS} for Cr films had exceeded r_{DCMS} at target power densities higher than $15\,\mathrm{W\,cm^{-2}}$, which are comparable to the values used in the present study (for $P > 190\,\mathrm{W}$). Their results might indicate an enhanced sputter-assisted evaporation/sublimation caused by the increased target surface temperature due to insufficient cathode cooling, such as reported by Vlček *et al.* [172].

Figure 7.7(b) also illustrates that $r_{\mathrm{n,\,DCMS}}$ and $r_{\mathrm{n,\,MPPMS}}$ are comparable at both Ar pressures. In contrast, $r_{\mathrm{n,\,HiPIMS}}$ at $p = 2\,\mathrm{Pa}$ is significantly lower than at $p = 1\,\mathrm{Pa}$ for $P < 350\,\mathrm{W}$.

This effect might originate from the rapid change in the material transport between the target and the sample holder during and immediately after short (200 μs) HiPIMS pulses. Metal atoms released from the target within a short sputtering period have to first make their way through the zone of background gas atoms, which may deflect them from their original direction towards the substrate. As opposed to DCMS, the instantaneous quantity of these atoms and the related amount of metal-gas collisions are substantially higher in the HiPIMS process. Furthermore, it has been documented that the consequent gas rarefaction takes place on a time scale comparable to the HiPIMS pulse duration, and that the speed of the expanding sputtered metal wavefront decreases with rising gas pressure [162, 117]. Therefore, the background gas rarefaction by sputtered material during a HiPIMS pulse can indeed play a significant role in the transport of sputtered species within the deposition chamber, such as recently demonstrated in [112].

Film characteristics

In section 7.3.1, we have witnessed significant differences in the discharge behaviour and plasma emission related to pulse and power management. It is therefore expected that the plasma characteristics, especially the plasma density, and the ion flux and ion energy would affect the growth of Nb films and their properties. In the following study, we particularly focus on the evolution of the residual stress and its relation to the corresponding microstructural features.

The analysis of the residual mechanical stress, σ, of coatings deposited at $p = 1\,\mathrm{Pa}$ and $2\,\mathrm{Pa}$ is presented in figures 7.8(a) and (b), respectively. HiPIMS- and MPPMS-deposited coatings prepared at $p = 2\,\mathrm{Pa}$ exhibit a low compressive stress, while the films prepared by DCMS are in tension. All Nb coatings prepared at $p = 1\,\mathrm{Pa}$ are in compression, including DCMS-deposited films ($\sigma \approx -0.6\,\mathrm{GPa}$). The compressive stress of pulsed discharge-deposited samples increased by $\Delta\sigma = 0.3 - 0.8\,\mathrm{GPa}$ in comparison with the respective stress values at $p = 2\,\mathrm{Pa}$. The highest compressive stress was detected in HiPIMS-deposited films, while the lowest one was found in the DCMS-prepared coatings.

XRD investigation revealed that all Nb films have a strongly textured body centered cubic (bcc) structure, suggested by the significant (110) and (220) reflections. The position of the

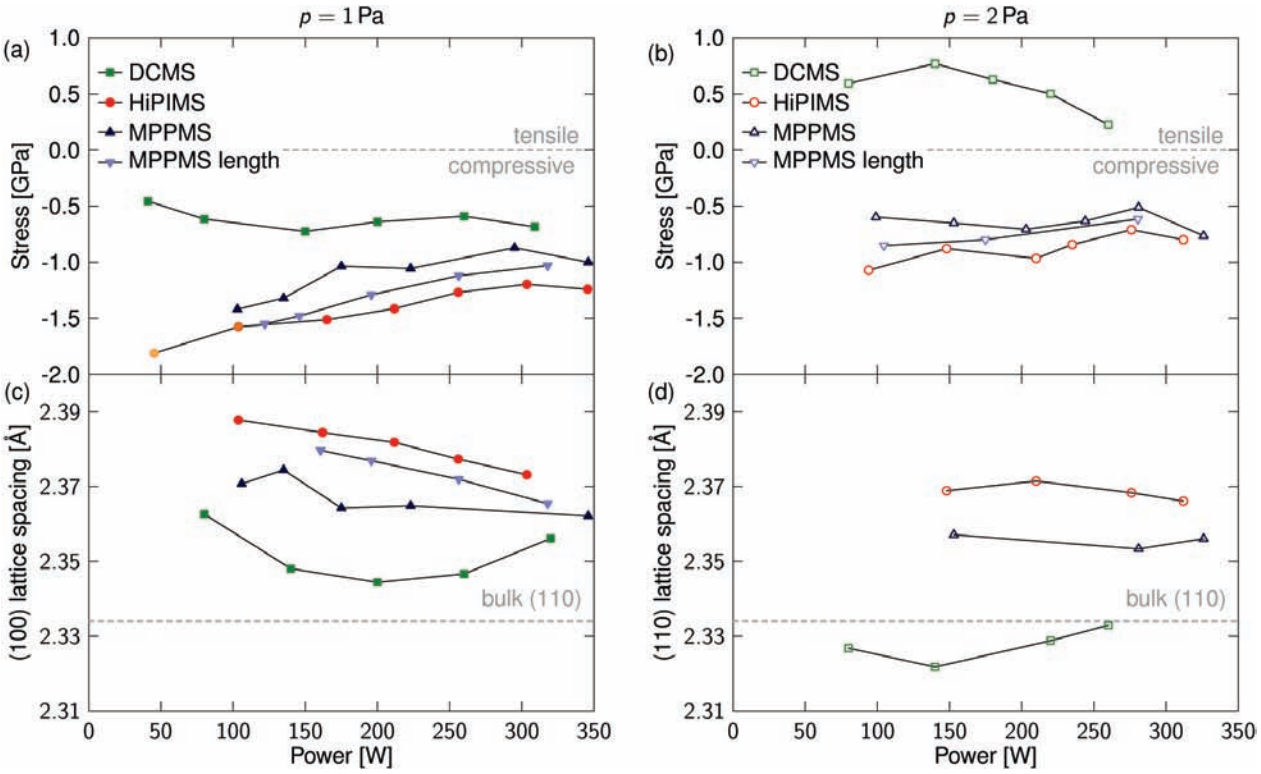

Figure 7.8 Residual mechanical stress σ of Nb coatings (a,b) and the calculated (110) lattice spacing in perpendicular direction to the coating plane $d_{(110)}$ (c,d) as a function of the average applied power P. The investigated coatings were prepared in Ar at $p = 1\,\mathrm{Pa}$ (a,c) and at $p = 2\,\mathrm{Pa}$ (b,d) by DCMS, HiPIMS, and MPPMS at different cathode voltages and by MPPMS using different pulse lengths (see table 7.3). The zero stress level and the tabulated value of $d_{(110)}$ for Nb bulk are indicated by a dashed line.

Nb (110) diffraction peak was used for the evaluation of the out-of-plane lattice spacing, $d_{(110)}$, that is presented in figures 7.8(c) and (d). We observe that all coatings prepared at $p = 1\,\mathrm{Pa}$ possess larger $d_{(110)}$ than its tabulated bulk value. HiPIMS coatings show the largest $d_{(110)}$ value, while DCMS coatings exhibit the smallest one. Films deposited at $p = 2\,\mathrm{Pa}$ have a smaller $d_{(110)}$ in comparison with $p = 1\,\mathrm{Pa}$, and DCMS films have even lower values of $d_{(110)}$ than Nb bulk.

It should be noted that the results presented in figure 7.8 suggest a close correlation between the in-plane mechanical stress and the out-of-plane lattice spacing. In fact, the compression/enlargement of the crystalline lattice due to the residual in-plane stress results

in a lattice extension/contraction in a perpendicular direction to the coating plane, such as described by the Poisson effect.

XRD results help to explain the stress characteristics such as those obtained at $p = 2\,\mathrm{Pa}$ (σ is compressive for HiPIMS and MPPMS, while it is tensile for DCMS). Specifically, the out-of-plane lattice spacing for the pulsed plasma-deposited Nb films is higher than its bulk value, in contrast to DCMS. These findings suggest film densification due to interstitial lattice atoms originating from the ion bombardment-induced knock-on events. Indeed, the optical emission diagnostics discussed in section 7.3.1 revealed high metal ion production in both pulsed discharges, suggesting elevated Nb^+ fluxes available for the deposition process. In support of such an interpretation, significant ion fluxes at the substrate level were previously reported for both HiPIMS [108, 111] and MPPMS [135, 188].

The observation of the highest compressive stress and of the largest $d_{(110)}$ parameter in films deposited by HiPIMS at both Ar pressures indicates the largest amount of interstitial Nb due to the energetic condensation. This supports the finding of higher ion generation by HiPIMS in comparison with MPPMS (and DCMS) presented in section 7.3.1.

The analyses of the lattice spacing and of the in-plane residual stress are further supported by FEG SEM examinations of selected Nb films. Figure 7.9 shows the cross-sectional images of coatings prepared at the same power ($P = 300\,\mathrm{W}$) by HiPIMS, MPPMS and DCMS, and at the two Ar pressures of $p = 1\,\mathrm{Pa}$ and $p = 2\,\mathrm{Pa}$. Films deposited by both high power pulsed techniques have a columnar structure with a smooth surface. No visible defects, such as voids or incorporated macroparticles, can be identified. Identical film morphology can also be found in the case of Nb films prepared by DCMS at $p = 1\,\mathrm{Pa}$. In contrast, the DCMS-deposited coating prepared at a higher pressure, $p = 2\,\mathrm{Pa}$, exhibits a rough columnar morphology with visible intercolumnar voids and with columns terminated by considerable pointed tops. It is the film porosity that is the origin of the observed tensile stress and out-of-plane lattice contraction.

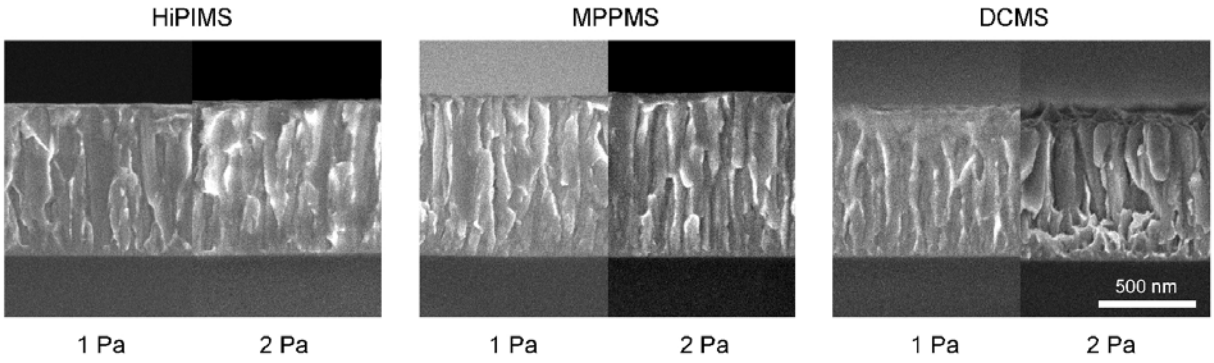

Figure 7.9 FEG SEM micrographs of Nb coatings prepared by HiPIMS, MPPMS and DCMS in Ar at $p = 1\,\text{Pa}$ and $2\,\text{Pa}$, using an average power $P = 300\,\text{W}$.

7.4 Conclusions

We studied different power management approaches in HiPIMS and MPPMS, operated above a Nb target, and their effects on the pulsed discharge evolution, plasma composition, and metal ionization estimated by OES. It was shown that HiPIMS is the only technique that enables the discharge operation in self-sputtering mode within the investigated range of applied powers, resulting in a significantly higher ionization of the sputtered metal than that reached with MPPMS. In contrast to HiPIMS, MPPMS provides a higher versatility in adjusting the pulse shape and pulse length. This feature can be particularly beneficial, for instance, in the discharge ignition.

Nb coatings prepared by HiPIMS and MPPMS have very similar deposition rates that are lower than in DCMS, e.g. by about 45% at $p = 1\,\text{Pa}$ and at $P = 300\,\text{W}$. The disparity in the deposition rate between DCMS and pulsed discharges was found to increase with rising power due to the non-linear dependence of the sputtering yield on the impacting ion energy and due to other phenomena. All films prepared at $p = 1\,\text{Pa}$ possess a dense columnar structure. Coatings deposited by the two high power pulsed discharges exhibit higher compressive stress and larger out-of-plane lattice spacing than those prepared by DC sputtering under comparable conditions. At higher pressure, $p = 2\,\text{Pa}$, DCMS-grown films show a tensile stress due to a porous microstructure, while films prepared by HiPIMS and MPPMS are dense and in compression, most probably due to the higher ion bombardment.

Acknowledgments

The authors wish to thank Mr. Francis Turcot and Mr. Sébastien Chenard for their expert technical assistance. The financial support by NSERC of Canada within the CRDPJ 380174-08 project is gratefully acknowledged.

CHAPTER 8

Paper V: Hysteresis-free deposition of niobium oxide films by HiPIMS using different pulse management strategies

Authors: M. Hála, J. Čapek, O. Zabeida, J.E. Klemberg-Sapieha, L. Martinu

Article accepted: Journal of Physics D: Applied Physics (Dec. 2011)

Abstract:

We systematically investigate reactive behaviour of two types of high power pulsed magnetron discharges above a Nb target using either square voltage pulses (denoted as HiPIMS) or custom-shaped pulses (denoted MPPMS), and compare it to that of a DC magnetron sputtering (DCMS) discharge. We demonstrate that the surface metal oxides can be effectively sputter-eroded from the target during both HiPIMS and MPPMS pulses operated in reactive O_2/Ar gas mixtures, and that sputtering from a partially oxide-free target is possible even at high oxygen concentrations. This results in a hysteresis-free deposition process which allows one to prepare optically transparent high refractive index Nb_2O_5 coatings exhibiting an elevated deposition rate without the need of feedback control commonly used in reactive DCMS. The cathode voltage was identified as the principal parameter that affects the reactive discharge behaviour.

8.1 Introduction

High power impulse magnetron sputtering (HiPIMS) represents the state-of-the-art surface engineering and functional coating fabrication technology, as recently summarized in [98]. For illustration, HiPIMS discharges were shown to be beneficial in the deposition of single-layer, multilayer and nanocomposite protective coatings [40, 189, 15], and in substrate pre-treatment for adhesion enhancement [14]. More recently, HiPIMS has also been applied in the preparation of various transparent metal oxides, e.g. TiO_2 [46, 12, 190, 47, 48], ZrO_2 [49, 33] and HfO_2 [50], and of transparent conductive oxides (TCO), such as indium tin oxide, Al-doped ZnO [51, 52], and RuO_2 [167]. It has been reported that higher film density, higher index of refraction, and lower surface roughness can be obtained for the optical coatings deposited by HiPIMS in comparison with those prepared by DCMS [46, 12]. Other studies have also shown a lower resistivity of the HiPIMS-deposited TCO films than that of their DCMS-counterparts [51, 52].

These promising results stimulated the development of power supplies (PS) suitable for the HiPIMS deposition process. Presently, there are numerous PS on the market that provide different pulse shapes and various levels of control over the voltage and current characteristics [53, 54, 55, 56, 57]. The majority of these PS can be divided into two principal categories according to the form of the high power pulses that they produce. These are: (i) shorter ($10 - 200\,\mu$s) square voltage pulse generators allowing one to reach higher cathode voltage values, which we label in this study as HiPIMS PS, and (ii) modulated pulse power (MPP) generators producing longer ($800 - 3000\,\mu$s), custom-shaped voltage pulses. The application of the latter type of PS for the "modulated pulse power magnetron sputtering" (MPPMS) has been demonstrated, for instance, in the fabrication of protective coatings based on transition metal nitrides; CrN films deposited by MPPMS were shown to possess a denser microstructure, a lower surface roughness, and improved mechanical and tribological properties as compared to films prepared by DCMS or pulsed DCMS [191].

Despite the demonstrated capacity of both HiPIMS and MPPMS discharges to prepare high-quality coatings based on nitrides and oxides, numerous open questions remain regarding the stability and control of the reactive deposition process. Specifically, there are ambiguous

reports concerning the hysteresis effect in HiPIMS discharges ignited in reactive mixtures of Ar and O_2. Some authors highlight the need for feedback control in order to circumvent hysteresis [81, 192], while some others report on hysteresis reduction [49, 193], and even its suppression [129, 167, 194]. Moreover, only limited information concerning the hysteresis behaviour in reactive MPPMS exists at the present time [135]. Therefore, there is a need for a rigorous analysis of both high power pulsed discharges in reactive conditions.

In the present work, HiPIMS and MPPMS discharges operated in reactive O_2/Ar mixtures above a niobium target are systematically characterized and compared to the standard DCMS process. The choice of the target material was made for the following two reasons: Firstly, Nb is a highly reactive metal when exposed to oxygen and hence can serve as a model target material that commonly exhibits a hysteresis effect if sputtered in reactive gas mixtures. Secondly, the fabricated Nb_2O_5 is an attractive high refractive index oxide suitable for the fabrication of optical interference filters. This also motivated us to analyze the characteristics of the prepared NbO_x coatings.

In the first part, we employ current and voltage waveform monitoring to study the discharge behaviour in different O_2/Ar gas mixtures. Simultaneously, thin NbO_x films are prepared and their deposition rate is evaluated. In the second part, the plasma is monitored by optical emission spectroscopy (OES) in order to gain further understanding of the discharge time evolution within individual pulses and to estimate the plasma composition. The origins of the effective target cleaning from the surface oxides, observed in both HiPIMS and MPPMS, are then summarized, and the principal parameters affecting the hysteresis behaviour are defined. Finally, the optical and mechanical properties of the deposited transparent Nb_2O_5 coatings prepared by HiPIMS, MPPMS and DCMS are presented and discussed.

8.2 Experimental details

The experiments were performed in a system consisting of a turbomolecularly pumped stainless steel chamber, an unbalanced magnetron and a substrate holder. The magnetron with a 5 cm diameter Nb target was powered by one of the following power supplies (PS): (1) HÜTTINGER Electronic HMP2/1 HiPIMS PS, (ii) ZPulser Axia 180 MPPMS PS, or (iii) Advanced Energy MDX 1K DCMS PS.

HiPIMS PS used in this study produces single square-shaped voltage pulses of adjustable length (10–200 μs) and amplitude (0–2000 V). Hence, one had a direct control over the cathode voltage, U_C. For illustration, the experimentally obtained voltage and current waveforms of a HiPIMS pulse operated in pure Ar at an average power $P = 320$ W are depicted in figure 8.1(a). In contrast to single HiPIMS pulses, MPPMS PS generates a sequence of short duration voltage micropulses (length of several μs to several tens of μs). Their application on the target results in an oscillating U_C, such as shown in figure 8.1(b). The amplitude of these voltage oscillations can be controlled by the "voltage load" (0–600 V) of the PS capacitors, and by the combination of the micropulse recipes using variable on and off times (hence duty cycle) [130, 135]. A typical MPPMS pulse (length of several hundreds of μs up to few ms) is much longer than any HiPIMS pulse (length of tens or hundreds of μs) and it consists of two or more segments characterized by its specific micropulse recipe, leading to a different instantaneous power output.

In the present experiments, the voltage load of the MPPMS PS capacitors was kept at 400 V while the duty cycle, D, of the applied micropulses was modified after the first 400 μs from $D = 20\,\%$ (on/off time 10 μs/40 μs, used during the low power (L) ignition segment) to $D = 45\,\%$ (on/off time 12 μs/15 μs, used during the high power (H) segment). The resulting U_C, depicted in figure 8.1(b), oscillated within $450\,\text{V} < U_C < 530\,\text{V}$ during the (L) segment, and within $550\,\text{V} < U_C < 600\,\text{V}$ during the (H) segment of the MPPMS pulses operated in Ar.

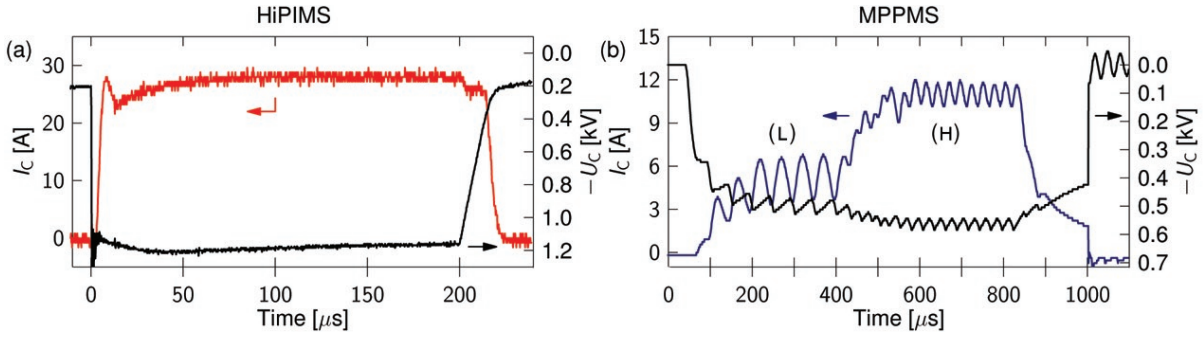

Figure 8.1 Time evolution of the discharge current I_C and the cathode voltage U_C recorded during a 200 μs HiPIMS pulse (a) and a 1000 μs MPPMS pulse (b). Both discharges were operated in Ar at $p = 1$ Pa. The low power (L) and the high power (H) segments of the MPPMS pulse are highlighted in (b).

The length of theses macropulses was fixed to 1000 μs for the time-resolved OES diagnostics, and to 1500 μs in other experiments. The pulse repetition frequency, f, was fixed to 50 Hz for both HiPIMS and MPPMS, unless otherwise specified. It should be noted that HiPIMS and DCMS PS were used as constant voltage generators. The value of U_{C} was set to either 1200 V, during 200 μs HiPIMS pulses, or to 360 V in DCMS. This set of experimental parameters was chosen to assure the same average power delivery by the three generators when operating in pure Ar atmosphere ($P = 320$ W), and in order to avoid magnetron overheating in the reactive gas mixtures when the power may rise notably, as discussed in the following sections.

The Ar flow rate, $\Phi(\mathrm{Ar})$, was fixed at 44 sccm during all experiments in order to obtain a working pressure, p, of 1 Pa. The O_2 flow rate, $\Phi(O_2)$, was then varied between 0 sccm and 15 sccm, resulting in a maximum pressure of 1.25 Pa. The substrate holder, mounted at a distance $d = 10$ cm, was biased to -100 V by an additional RF power supply in order to maintain the background plasma which facilitates the ignition of the high power pulsed discharges. Nevertheless, the instantaneous bias value, U_{b}, rapidly decreased during HiPIMS and MPPMS pulses ($50\,\mathrm{V} > |U_{\mathrm{b}}| > 10\,\mathrm{V}$) due to rapid changes in the plasma impedance.

Waveforms of U_{C} and of the cathode current, I_{C}, were measured by a Tektronix P6015A voltage probe and a Pearson 301X current monitor, respectively, and recorded by a Tektronix TDS2014B digital oscilloscope. The average discharge power, P, was then calculated as:

$$P = f \int_0^{\mathrm{T}} U_{\mathrm{C}}(t) I_{\mathrm{C}}(t)\,\mathrm{d}t, \tag{8.1}$$

where t stands for time and T stands for the pulse duration during which I_{C} has a non-zero value.

Table 8.1 List of the monitored OES lines with corresponding wavelengths, λ, excitation energies of the upper excited states, E_{k}, and of the lower excited states, E_{l}. The values of E_{k} and E_{l} for Nb and O are taken from [181] and for Ar from [182], respectively.

	Nb^0	Nb^+	Nb^{2+}	Ar^0	Ar^+	O^0
λ [nm]	466.38	313.08	245.70	811.53	442.60	777.54
E_{k} [eV]	2.85	4.40	—	13.08	19.55	10.74
E_{l} [eV]	0.20	0.44	—	11.55	16.75	9.15

The discharge emission was sampled by an optical fiber mounted within the deposition chamber with its line of sight parallel with the target surface at a distance $d \approx 1\,\mathrm{cm}$. Time-averaged measurements were analyzed by an Ocean Optics USB2000 spectrometer. For the time-resolved (TR) diagnostics, a PI Acton SpectraPro 2750 monochromator with a holographic grating (2400 grooves mm^{-1}) was used in combination with a high speed Princeton Instruments PI-MAX2 camera. The list of the monitored emission lines representing different neutral and ionized species with their corresponding higher and lower excitation energy levels is given in table 8.1.

In TR OES analysis, each optical signal was recorded during a $5\,\mu$s period, following a preset delay from the initiation of the voltage pulse. The signal was averaged over 10 to 50 pulses, depending on its intensity. Subsequently, the acquisition and averaging was repeated for the following $5\,\mu$s interval. Such a process was iterated until the pulsed discharge extinction.

NbO_x films were deposited at ambient temperature on Si(100) and on BK7 glass substrates for mechanical and optical characterization, respectively. The thickness of the fabricated films was determined by a Veeco DEKTAK profilometer equipped with a conical diamond stylus. The structure of the selected films was evaluated by X-ray diffractometry (XRD) in $\theta - 2\theta$ configuration using Cu Kα radiation in a Philips X'PERT instrument.

The optical properties of the NbO_x films were examined by a J. A. Woollam RC2-DI multifunctional variable-angle spectroscopic ellipsometer. The data acquired by the spectroscopic ellipsometer (Ψ and Δ, as well as the reflectivity) at four angles of incidence (45°, 55°, 65° and 75°) were combined with normal-incidence transmission analysis ($190\,\mathrm{nm} < \lambda < 1690\,\mathrm{nm}$) in order to enhance the measurement accuracy. The optical characteristics of the NbO_x films (E_g, n and k) were then obtained by CompleteEASE software using the Cody-Lorentz dispersion model.

The film's internal stress was estimated by measuring the curvature of a rectangular Si stripe (5 x $50\,\mathrm{mm}^2$) before and after film deposition using a Tencor Flexus FLX-2900 laser deflection system. The value of the internal stress was calculated from the Stoney formula [195]. The mechanical properties of the NbO_x films were determined by depth sensing nanoindentation using a Hysitron TI 900 triboindenter equipped with a Berkovich pyramidal tip. Selected samples were indented 25 times with a maximum load varying from 100 to 2000 mN. The

hardness and reduced Young's modulus were calculated by analyzing the load-displacement curve according to the Oliver-Pharr method [155].

8.3 Results and discussion

8.3.1 Characterization of the reactive sputtering process

In this section, we explore the reactive sputtering process behaviour in terms of the current amplitude and pulse shape, the dissipated average power, the hysteresis effect and the deposition rate of the prepared NbO_x films.

Figures 8.2(a) and 8.2(b) illustrate the effect of an increasing oxygen flow on the pulse current waveforms of typical 200 μs HiPIMS pulses and 1500 μs MPPMS pulses. The cathode current significantly rises in HiPIMS discharges. For instance, the I_C maximum grows from 27 to 77 A when $\Phi(O_2)$ is increased from 0 to 15 sccm. MPPMS discharges in O_2/Ar mixtures exhibit a different behaviour; I_C increases only at the beginning of the high power pulse segment when large amplitude oscillations start to develop. These are then damped and succeeded by low amplitude oscillations of the same frequency as the I_C oscillations during the MPPMS discharge in pure Ar.

The observed current rise in both high power pulsed techniques can be related to either target surface phenomena, or gas-phase phenomena. In order to better distinguish the effect of these two, we performed experiments at different repetition frequencies while keeping the gas composition fixed [$\Phi(Ar) = 44$ sccm, $\Phi(O_2) = 5$ sccm]. Figures 8.2(c) and 8.2(d) illustrate the resulting current waveforms. It can be noticed that the peak current values in HiPIMS, as well as the number of periods and the duration of large amplitude current oscillations in MPPMS, increase with the decreasing f (longer pulse off-time) in a similar way as with the rising $\Phi(Ar)$. Here, it should be highlighted that the modification in I_C with varying f cannot be ascribed to the gas rarefaction and gas refill phenomena illustrated in references [193, 71]; The time scale of the latter effects is in the hundreds of μs (order of magnitude estimation), while the delay in between the pulses in the present experiments is in the tens of ms. Hence, the observation of a similar pulse current evolution due to the variation in $\Phi(O_2)$ and f excludes the gas-phase "volume" processes as a primary origin of

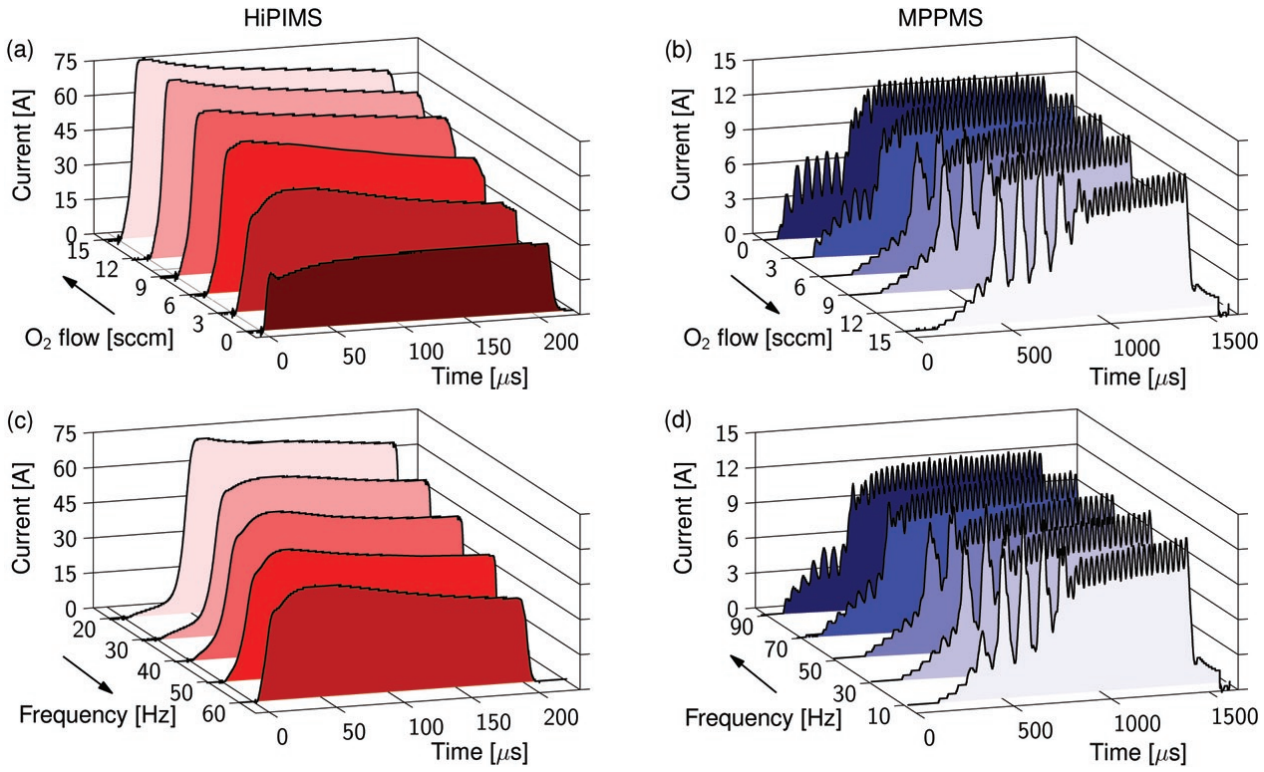

Figure 8.2 Effect of the oxygen flow $\Phi(O_2)$ in O_2/Ar mixture ($f = 50\,\text{Hz}$, $\Phi(O_2)$ varied) (a,b) and of the pulse repetition frequency f (f varied, $\Phi(O_2) = 5\,\text{sccm}$) (c,d) on the pulse current waveforms of the HiPIMS (a,c) and MPPMS (b,d) discharges. All the waveforms were averaged over 64 pulses.

the observed current growth.

Besides the pressure and nature of the gas, the target surface composition is an important parameter affecting the current level in reactive discharges. As it will be discussed below, the current rise can be related to an increase of the ion-induced secondary electron emission (ISEE) due to target surface oxidation. The current amplitude dependence on f is a proof that this surface oxidation takes place not only during the high power pulses but mostly in between them: The longer periods between the individual pulses are, the longer is the time available for target oxidation.

Phelps and Petrovic [68] have shown that the ISEE of the target surface increases with the energy of the impacting Ar ions. Moreover, the ISEE of an oxidized target surface rises at a higher pace than the ISEE of a clean metal surface for energies higher than approximately

300 eV [68]. This means that the ISEE of the compound target may be higher or lower than that of the elemental target material, depending on the instantaneous value of U_C. Therefore, U_C is an important parameter in the secondary electron production, and consequently, in the resulting plasma density and I_C.

The HiPIMS PS delivers square-shaped voltage pulses with $U_C \approx 1200\,\mathrm{V}$. When the target surface biased by such a high voltage is oxidized, the ISEE significantly increases and hence does I_C [figure 8.2(a)]. Another important effect is the transition from the metal-dominated to the gas-dominated sputtering regime which accompanies the progressing target oxidation, as will be discussed in section 8.3.2. It should be stressed that similar behaviour [rising I_C during the pulse with the increasing $\Phi(O_2)$] was also observed for HiPIMS discharges above 5 cm and 10 cm diameter Cr, Ta and V targets sputtered in O_2/Ar mixtures (unpublished results), as well as for HiPIMS discharge above a 10 cm Cr target sputtered in N_2/Ar mixtures [162].

During the MPPMS pulse, U_C is not steady but it oscillates between $450 < U_C < 600\,\mathrm{V}$ [figure 8.1(b)]. The ISEE for this range of voltages is lower than in HiPIMS, but also higher than in DCMS. The resulting current rise is visible at the beginning of the MPPMS pulse high power stage ($t \approx 500\,\mu\mathrm{s}$), as documented by the peaks of the several first I_C oscillations [see figures 8.2(b) and (d)]. It is most probable, that the current increase would be higher if the micro-pulse power management of the MPPMS PS was capable to maintain a steady voltage and power delivery. The large amplitude current oscillations observed at the beginning of the MPPMS pulses are later replaced by the low amplitude oscillations reaching lower peak values. Such a current evolution cannot be easily interpreted without considering the target surface composition variation during the MPPMS pulses. Further discussion of this phenomenon will follow in section 8.3.2.

The evolution of the average discharge power with the increasing or decreasing oxygen content within the O_2/Ar mixture is shown in figure 8.3(a). Before oxygen is introduced to the reactor, the discharge power was set to $P = 320\,\mathrm{W}$ (at $\Phi(O_2) = 0\,\mathrm{sccm}$). It should be noted that an important reduction in P, observed for DCMS discharges at $\Phi(O_2) \approx 5\,\mathrm{sccm}$, indicates a critical O_2 flow at which the target gets fully covered by surface metal oxide ("target poisoning"). This sudden power drop is caused by a diminished ISEE of the surface compounds sputtered at low U_C [196]. In addition, the evolution of P follows different path-

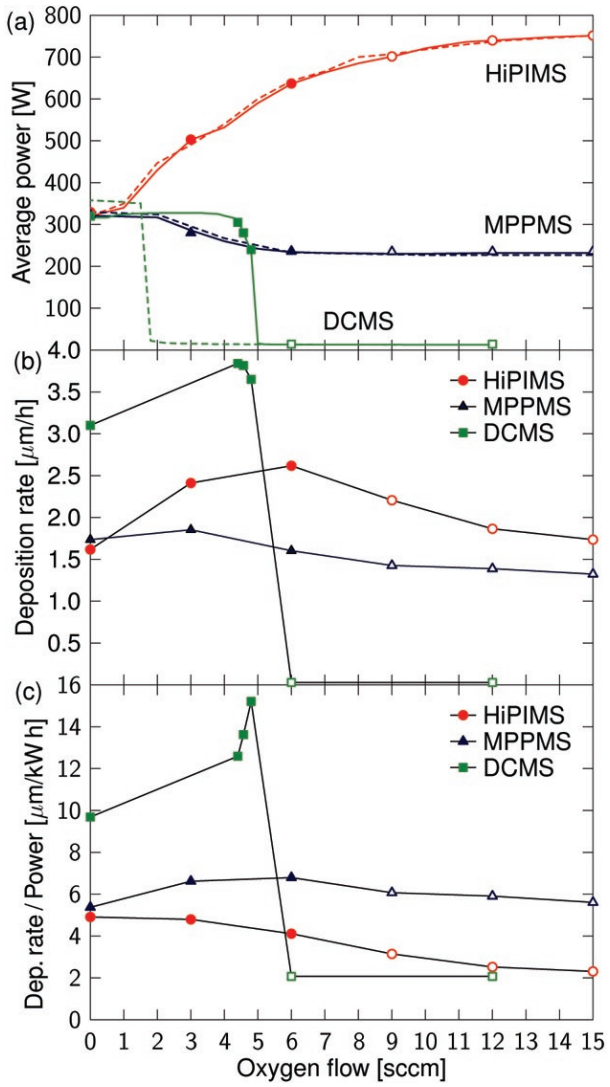

Figure 8.3 Average discharge power P (a), deposition rate r (b), and power-normalized deposition rate r_n (c) for NbO_x coatings prepared by DCMS, HiPIMS, and MPPMS, as a function of oxygen flow $\Phi(O_2)$ in the O_2/Ar mixture ($f = 50\,\text{Hz}$, $\Phi(O_2)$ varied). The solid and dashed lines in (a) stand for experiments with increasing and decreasing oxygen flows, respectively. Data for absorbing coatings are marked by full symbols and for transparent coatings by open symbols.

ways with the increasing and decreasing $\Phi(O_2)$. This shows the well-known hysteresis effect, which is a consequence of the significantly lower sputtering yield of the surface compounds, as opposed to the elemental target material [82].

Contrary to DCMS, HiPIMS and MPPMS discharges exhibit a gradual power variation following an overlapping pathway with both increasing and decreasing $\Phi(O_2)$. Furthermore,

the two discharges reach a steady operation at high oxygen flows. These observations indicate that the abrupt transition to the poisoned target state (at $\Phi(O_2) \approx 5\,\text{sccm}$) is inhibited and the subsequent hysteresis is suppressed. In fact, MPPMS discharge characteristics were stable even at $\Phi(O_2) = 50\,\text{sccm}$ ($O_2/Ar \approx 1/1$, not shown). In contrast, HiPIMS discharges exhibited instabilities and arcing at $\Phi(O_2) > 15\,\text{sccm}$. However, the onset of these instabilities has been shifted to higher $\Phi(O_2)$ with increasing target erosion (racetrack surface).

In order to verify the deposition process efficiency of the investigated reactive discharges, NbO_x coatings were prepared at different $\Phi(O_2)$, ranging from 0 sccm to 15 sccm with a step $\Delta\Phi(O_2) = 3\,\text{sccm}$. The obtained deposition rate, r, and the deposition rate normalized to the average power at $\Phi(O_2) = 0\,\text{sccm}$ ($P = 320\,\text{W}$), r_n, are plotted as a function of $\Phi(O_2)$ in figures 8.3(b) and 8.3(c), respectively. It is to be noted that r for Nb films prepared by both pulsed techniques in pure Ar ($\Phi(O_2) = 0\,\text{sccm}$) equal only 55% of r_n obtained by DCMS.

Figure 8.3(b) shows a notable drop in r for DCMS at $\Phi(O_2) = 5\,\text{sccm}$, which is a consequence of target poisoning and discharge operation at very low powers. Such a transition was not observed for coatings prepared by the two pulsed processes. Instead, r remained high even for optically transparent NbO_x films ($\Phi(O_2) > 9\,\text{sccm}$). In fact, r of NbO_x coatings prepared by HiPIMS reached even higher values than r of pure Nb, albeit at elevated powers. A moderate drop in r was observed for MPPMS-deposited films as a consequence of the diminished powers. It should be mentioned that a very similar observation of the hysteresis-free deposition process of AlO_x coatings by HiPIMS was also reported by Wallin and Helmersson [129].

Figure 8.3(c) displays the values of r_n, which may be used as an indicator of the deposition process efficiency. For all transparent NbO_x films prepared by HiPIMS and MPPMS, r_n reaches notably higher values in comparison with DCMS operated above a poisoned target. Furthermore, r_n for optically transparent NbO_x prepared by MPPMS exhibits up to 2.5 times higher values than r_n of the HiPIMS-deposited films. These results demonstrate that optically transparent NbO_x films with technologically interesting r and r_n values can be reached by the two pulsed techniques within a broad range of $\Phi(O_2)$. Hence, the need for a reactive gas control employing a sophisticated feedback system based on, for instance, the reactive gas partial pressure [81] or optical plasma emission monitoring [197], can be avoided.

8.3.2 Plasma emission diagnostics

The main goal of this section is to interpret the reactive high power pulsed discharge development during the individual pulses and to evaluate the plasma composition with respect to the state of the target surface and to the dominant sputtering regime. In the following, we apply TR current-voltage and spectroscopic monitoring of the different emission lines to study the evolution of 200 μs long HiPIMS pulses and 1000 μs long MPPMS pulses operated in an O_2/Ar mixture with an oxygen flow corresponding to the DCMS target poisoning threshold, $\Phi(O_2) = 5$ sccm.

Figure 8.4(a) shows an example of the current and voltage waveforms recorded during the HiPIMS pulses. I_C rises shortly after the high voltage application, saturates at $t = 35\,\mu$s after the pulse onset, and gradually decreases with time. The respective evolution of selected optical emission lines from excited sputtered metal and gas species is presented in figures 8.4(b) and (c), respectively. Peaking emission from excited Ar^0 marks the discharge breakdown, succeeded by the establishment of a dense plasma indicated by the rising emission intensity from ionized Ar, dissociated atomic O, and both neutral and ionized Nb. Following the initial intensity maximum, all the emission signals decrease significantly for $25\,\mu\text{s} < t < 50\,\mu$s, despite little variation in I_C during this period.

For the rest of the pulse, $t > 50\,\mu$s, the emission intensities of all the excited species diminish, in accordance with the falling I_C. The only exception is the emission from the neutral Nb atoms that grows in intensity, despite a decreasing plasma density (I_C). Similar behaviour was also found for several other monitored Nb^0 emission lines with different excitation energy thresholds, underlining the fact that it cannot be explained by the modified excitation conditions for each particular line. Instead, it may indicate a growing concentration of Nb atoms within the monitored plasma region in front of the target. It should be stressed that the Nb^0 emission line exhibited a steady intensity level during the HiPIMS pulses operated in pure Ar (not shown here), such as did the discharge current amplitude [figure 8.1(a)]. In the subsequent text, a possible interpretation of the related reactive discharge dynamics will be offered, based on the presented optical emission analysis summarized above, and on the findings of the HiPIMS discharge diagnostics discussed in [162].

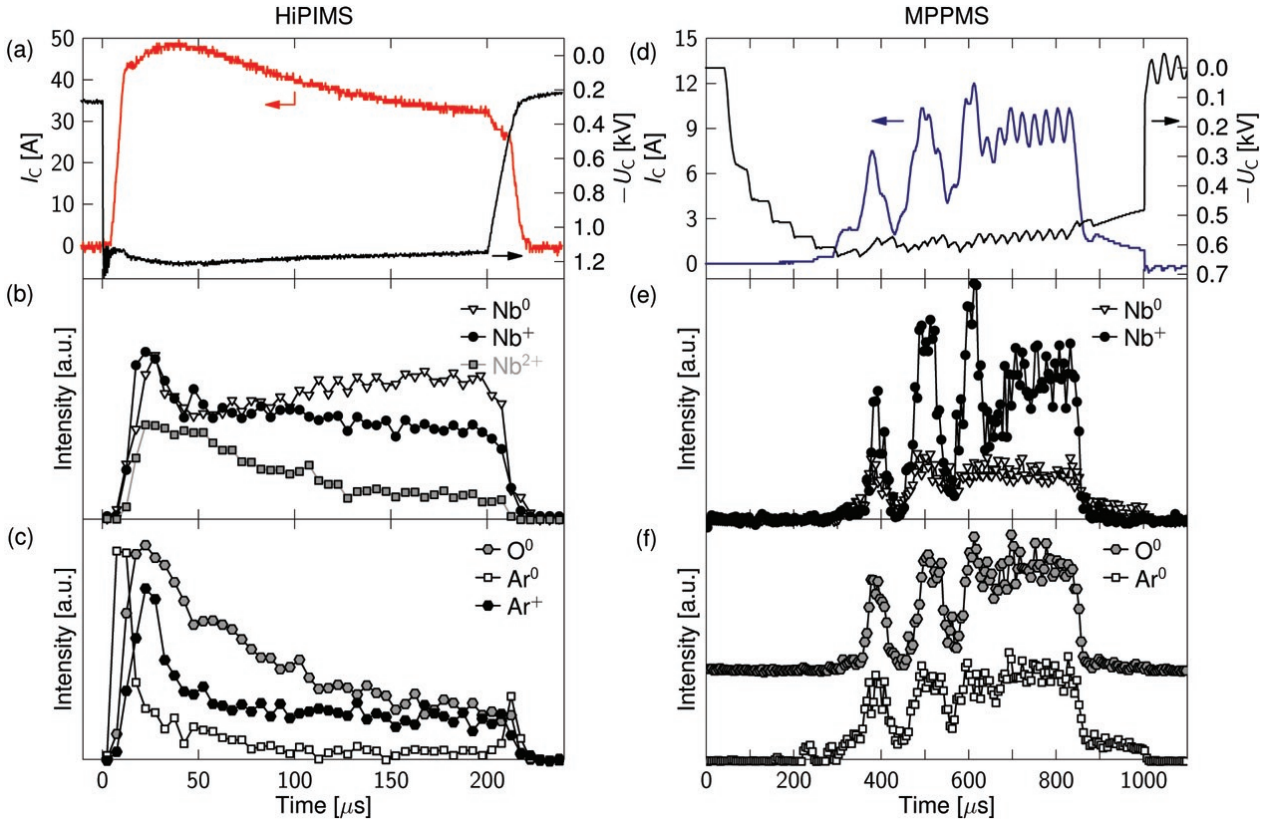

Figure 8.4 Time evolution of the discharge current I_C and of the cathode voltage U_C (a,d), and of the optical emission intensities originating from the excited metal species (b,e) and working gas species (c,f), recorded during a 200 μs HiPIMS pulse (a,b,c) and a 1000 μs MPPMS pulse (d,e,f). Both discharges were operated in the O_2/Ar mixture with $\Phi(O_2) = 5$ sccm. The acquisition time for different monitored species was not normalized. Nb^{2+} and Ar^+ emission lines were not monitored in the case of the MPPMS discharge because of their weak intensity.

Following the HiPIMS discharge ignition, both argon and oxygen ions start to bombard the oxidized target surface. If target sputter-erosion prevails over surface oxidation and over sub-surface oxygen implantation, the compound layer is progressively removed from the target. Consequently, the target sputtering yield rises, since the pure metal has a lower binding energy than the surface compounds. This is indicated by the growing emission intensity from all Nb species for $5\,\mu s < t < 25\,\mu s$. The injection of the sputtered metal into the examined plasma region then lowers the mean electron energy, due to the lower excitation and ionization energy thresholds of Nb in comparison with Ar. Furthermore, the growing amount of sputtered metal causes working gas rarefaction in front of the target [100, 117].

For these two reasons, all emission signals decrease substantially, in spite of the stable I_C at $25\,\mu s < t < 50\,\mu s$. Due to the highest current density, the region expected to be first "cleaned" is the center of the target's racetrack that is defined by the magnetron's magnetic field configuration.

The decreasing I_C value and the rising Nb^0 emission intensity for $t > 50\,\mu s$ suggest a gradual modification of the target surface composition from predominantly oxidized towards more metallic during the individual HiPIMS pulses; The ISEE from the oxide-free area decreases, which lowers the plasma density and hence the current amplitude, as supported by the results discussed in section 8.3.1. On the contrary, the Nb sputtering yield from the larger metallic surface increases, which should result in a higher metal concentration in the discharge. This is a rather preliminary conclusion which would require a proper TR analysis of the racetrack surface composition, or perhaps TR absorption spectroscopic monitoring of Nb that would allow one to estimate the sputtered material density. Nevertheless, the elevated r and r_n of NbO_x films presented in figure 8.3 support this interpretation.

Figures 8.4(d), (e) and (f) present the characteristics of the reactive MPPMS discharge. The TR optical emission analysis shows that all the monitored emission lines follow the development of I_C. The MPPMS discharge breakdown is significantly delayed behind the onset of the voltage pulse in comparison with HiPIMS. This is due to the successive rise of U_C as a consequence of the MPPMS PS power management [130, 198]. Following the discharge ignition, notable I_C oscillations develop that are characterized by a large amplitude and a period equal to several micro-pulse cycles. However, these oscillations cease after only several periods at $t \approx 700\,\mu s$. The subsequent I_C oscillations exhibit a much smaller amplitude and period equal to that of the driving voltage micro-pulses, such as the current oscillations observed in the non-reactive MPPMS pulses [figure 8.1(b)]. Moreover, figure 8.2(b) shows that the average value of I_C at the end of the reactive MPPMS pulses approaches the I_C level of the non-reactive MPPMS. Such an observation indicates that the discharge may be operated above a metallic target racetrack that is cleaned from the metal oxide compounds. In such a case, the transition from the high amplitude to the low amplitude current oscillations would mark the moment when a significant part of the racetrack surface becomes metallic.

In support of the above hypothesis, it is observed that the proportion of the large ampli-

tude and of the low amplitude oscillations depends on $\Phi(O_2)$ or f [figures 8.2(b) or 8.2(d)]. In other words, this behaviour is a function of the surface compound thickness that increases with either the oxygen content in the O_2/Ar gas mixture, or with the time lag in between the pulses. Therefore, the duration of the high amplitude oscillations can be related to the time necessary for the racetrack cleaning from the oxides, and the duration of the low amplitude oscillations to the portion of the MPPMS pulse during which the sputtering from the metallic racetrack takes place. As a matter of fact, higher r_n values for NbO_x films compared to the other two investigated techniques [as indicated in figure 8.3(c)] can hardly be interpreted without considering the important rise in the Nb sputtering yield. Sputtering from the oxide-free surface for a portion of the MPPMS pulse can explain such an observation.

In order to gain additional information about the plasma composition in discharges operated in Ar and in O_2/Ar mixtures, the averaged emission spectra were also recorded and analyzed. Figures 8.5(a) and (b) illustrate the emission spectra from HiPIMS, MPPMS and DCMS discharges obtained at $\Phi(O_2) = 0$ sccm and at $\Phi(O_2) = 12$ sccm, respectively. It should be stressed that all the presented spectra were normalized to the same acquisition time and power ($P = 320$ W), even if the actual power was different in the reactive gas mixture.

The HiPIMS spectrum at $\Phi(O_2) = 0$ sccm is dominated by an intense emission from Nb^+. Furthermore, strong Nb^0 and even Nb^{2+} emission lines can be identified. The high emission from the ionized species may serve as an indication that the HiPIMS discharge is operated in the metal-dominated sputtering regime, in which the self-sputtering mechanism significantly contributes to target sputtering [177]. The MPPMS spectrum at $\Phi(O_2) = 0$ sccm shows an important emission from Nb^+, but the strongest emission originates from Nb^0. Such an observation indicates a lower ionization of the sputtered metal in MPPMS when compared to HiPIMS operated at the same power load. In fact, the form of this spectrum is very similar to that of the HiPIMS discharges using a comparable average voltage ($U_C \approx 500$ V, presented elsewhere [177]), which is lower than the threshold value for self-sputtering. One can hence conclude that the examined MPPMS discharge is operated in the gas-dominated sputtering mode since the cathode voltage is insufficient for the initiation of self-sputtering. Contrary to both pulsed discharges, only neutral Nb lines can be identified in the non-reactive DCMS spectra.

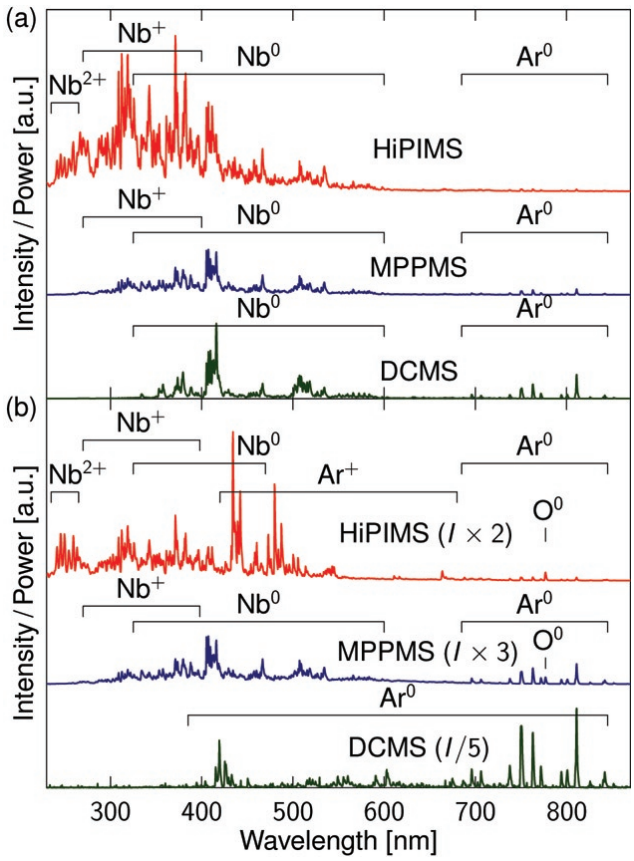

Figure 8.5 Optical emission intensities from discharges operated by HiPIMS, MPPMS and DCMS above a Nb target in pure Ar ($\Phi(O_2) = 0\,\text{sccm}$) (a) and in O_2/Ar mixture ($\Phi(O_2) = 12\,\text{sccm}$) (b), normalized to the same integration time and the same average power of $P = 320\,\text{W}$. For the sake of clarity, the intensities of reactive spectra were multiplied/divided by a specific factor, as indicated.

The spectra from the HiPIMS and MPPMS discharges at $\Phi(O_2) = 12\,\text{sccm}$ show intense metal emission lines, even though of a much lower intensity than those in pure Ar. This observation confirms significant metal sputtering at a high oxygen content in the O_2/Ar mixture. This sharply contrasts with the reactive DCMS spectrum which does not exhibit any Nb lines at $\Phi(O_2) = 12\,\text{sccm}$. In the latter case, the only detected emission lines are those of the excited working gas. Strong Ar emission indicates the elevated mean electron energy due to a negligible amount of Nb that may be sputtered from the target fully covered by metal oxide compounds.

The reactive HiPIMS spectrum [figure 8.5(b)] exhibits a substantially diminished emission from Nb^0 and Nb^+ lines (about 6 times in comparison to the Ar discharge) but nearly an unchanged emission intensity from Nb^{2+} lines. In addition, strong Ar^+ lines appear in the spectrum from the O_2/Ar mixture, accompanied by a moderate rise of Ar^0. In fact, Ar^+, Ar^0 and Nb^{2+} emission lines possess higher ionization and excitation energy thresholds in comparison with the other monitored species (Nb^0 and Nb^+). Thus, such an observation suggests an increase in the mean electron energy in the reactive discharges.

It is important to note that the HiPIMS discharge emission close to the cathode shows significant emission lines from ionized Ar, in contrast to the non-reactive discharge operated above a clean Nb surface. This, in fact, indicates a transition in the sputtering regime. In order to better understand the origin of such a change, one has to first consider a modification in the target surface composition in a reactive atmosphere; The oxidized portion of the target's surface has a higher binding energy than the pure metal. Consequently, the target oxidation (progressing with the increasing $\Phi(O_2)$ or decreasing f) inevitably results in a drop in the sputtering yield and hence in a smaller amount of sputtered metal that may be ionized and possibly back-attracted towards the cathode. Subsequently, the decreased metal concentration in front of the target leads to a lower background gas rarefaction, resulting in a higher Ar ion bombardment of the target. This in turn further enhances the secondary electron production (and I_C) along with target oxidation.

In conclusion, the high currents observed during HiPIMS discharges above a partially poisoned target cannot be simply attributed to self-sputtering (that is common for non-reactive discharge at elevated cathode voltages), but to gas sputtering. A similar observation of high pulse currents accompanied by an important emission from ionized Ar was reported by Čapek *et al.* [177] for HiPIMS discharges operated above target materials with a low sputtering yield, such as carbon. In the latter case, the occurence of the high currents was interpreted by a gas recycling mechanism [122], which may also play an important role in the reactive HiPIMS discharge studied in this work.

The general shape of the MPPMS spectra [figure 8.5(b)], containing the working gas and the metal vapour emission lines, appears to be fairly unaffected by the high oxygen flow, except for the substantially diminished emission intensity (about 3 times lower than

in pure Ar). The apparent similarity between the reactive and the non-reactive MPPMS spectra suggests that the sputtering regime, the plasma composition and the excitation conditions are comparable. This observation thus supports the previously made assumption that the (gas-dominated) sputtering from the oxide-free racetrack takes place during a considerable part of the MPPMS pulse, even at high oxygen flows.

8.3.3 Discussion on the origins of the high target cleaning efficiency

The above-presented TR optical diagnostics of the discharge evolution and of the reactive plasma composition confirms the high instantaneous sputter-erosion of the surface metal oxides during both HiPIMS and MPPMS pulses. This results in the stabilization of the deposition process, in the elimination of hysteresis, and in the elevated r and r_{n} values of the prepared NbO_x coatings reported in section 8.3.1. In this section, we will elaborate on the importance of U_{C} for such behaviour and also on the origins of the substantial difference in r_{n} of the optically transparent coatings prepared by HiPIMS and MPPMS.

High instantaneous value of U_{C} can be identified as the principal parameter that determines the superior target cleaning in high power pulsed discharges: Firstly, ISEE of the oxidized target surface substantially increases with the energy of the impacting ions [68], as discussed previously in section 8.3.1. High emission of secondary electrons then sustains the high plasma density. Secondly, the sputtering yield of the bombarded metallic or oxidized surface scales with the energy of the impacting ions [74, 199]. Consequently, the simultaneous effect of the elevated ion fluxes (due to the high plasma density) and of the increased sputtering yield (due to the higher impacting ion energy) results in an efficient sputter-erosion of niobium oxide compounds in both high power pulsed discharges, such as demonstrated by high r and r_{n} values in the presented experiments.

It should be noted that MPPMS exhibits a notably higher r_{n} in comparison with HiPIMS [figure 8.3(c)], albeit both U_{C} and P reach substantially lower instantaneous values. This observation indicates a higher target cleaning efficiency of the MPPMS technique. In the following paragraphs, three hypotheses on the origins of such a disparity are offered:

(i) Longer pulse duration; The application of longer pulses provides more time for surface compound removal. Therefore, the ability of the MPPMS PS to deliver pulses of long duration (e.g., up to 3000 μs) allows one to reach oxide-free racetrack area even at high $\Phi(O_2)$, as discussed in section 8.3.2. It is hence suggested that r_n may be further increased by the use of longer MPPMS or HiPIMS pulses if compared to the results presented here.

(ii) Lower ion implantation; There are generally two principal processes responsible for the oxidation of the sputtered target: chemisorption, resulting in the surface compound growth, and ion implantation, leading to the subsurface compound formation. It has been reported that the latter process plays an essential role in the target poisoning mechanism, which has been taken into account even in analytical modelling of the reactive sputtering process [77, 78]. As a matter of fact, several studies have demonstrated that the depth of the reactive ion subplantation within the target can exceed the thickness of the adsorbed compound layer [77, 78, 79]. Thus, it is obvious that the oxygen implantation and the subsequent sub-surface oxidation can substantially enhance the overall compound growth rate during the high power pulse. As a result, the compound removal efficiency by impacting working gas ions may be compromised.

An increased generation of reactive O ions ($E_i = 13.61$ eV) may be expected in the reactive HiPIMS discharges since the mean electron energy may be higher than in MPPMS, such as indicated in figure 8.5 by the elevated emission intensity from the ionized Ar ($E_i = 15.76$ eV) that has high excitation energy thresholds (e.g., $E_k = 19.55$ eV for the 442.6 nm emission line). Furthermore, U_C applied in HiPIMS reaches about twice as high values as in MPPMS. Hence, the penetration depth of the impacting O^+ is expected to be larger as well. For these two reasons, the overall compound formation rate can be significantly higher in HiPIMS in comparison with MPPMS.

(iii) Higher preferential sputtering of oxygen; Kubart *et al.* [200] have reported that the large mass difference between Nb and O atoms is responsible for the enhanced preferential sputtering of oxygen from the surface formed by NbO_x compounds bombarded by working gas ions, and hence for the surface oxide reduction. It was also shown that the preferential oxygen sputtering from the oxidized surface is more pronounced at lower energies of the

impacting Ar ions [200, 201]. In such a case, the use of lower cathode voltages ($U_C \approx 600\,V$ used in MPPMS as opposed to $U_C \approx 1200\,V$ in HiPIMS) should facilitate the oxygen removal from the top-most compound layer, hence allowing faster target cleaning.

It can be summarized that the combination of the longer pulse duration (providing more time for the gradual compound removal) and of the used range of U_C (resulting in the lower subsurface oxidation and/or the faster oxide sputtering) allows the MPPMS discharge to operate in the non-poisoned mode during a part of its pulse. It should be stressed that the here-presented hypotheses and conclusions are probably not exhaustive. Further investigations including different magnetron configurations, target materials and discharge conditions, as well as modelling, are needed to obtain a more detailed insight.

8.3.4 Nb_2O_5 coatings characterization

The NbO_x samples prepared at 9, 12 and 15 sccm were amorphous (as verified by XRD) and optically transparent. In this section, the comparison of the optical and mechanical properties of coatings prepared by HiPIMS, MPPMS and DCMS is then performed for the specific case of $\Phi(O_2) = 12\,sccm$.

Figure 8.6 shows the optical characteristics evaluated by spectroscopic ellipsometry combined with reflection and transmission analyses. The bandgap is found to be at 369 nm ($E_g = 4.37\,eV$), and the value of the extinction coefficient, k, is considered negligible ($k < 1 \times 10^{-4}$, which is the sensitivity of the measurement) in the entire visible and near infrared spectrum. This indicates a good transparency of the analyzed coatings. The obtained index of refraction, n, at 550 nm for the three coatings is also listed in Figure 8.6. It is to be noted that these values are comparable (DCMS, MPPMS) or even moderately higher (HiPIMS) to the values reported for the stoichiometric amorphous Nb_2O_5 prepared by the ion beam sputtering (IBS) [202] and by the dual ion beam sputtering techniques (DIBS) [203].

Slightly higher index of refraction of the HiPIMS-deposited Nb_2O_5 may be interpreted by an increased coating density induced by the intense ion bombardment during the film growth [10]. For instance, the elevated n of the HiPIMS-grown TiO_x coatings, in comparison with those deposited by DCMS, was associated with an increased coating density due to

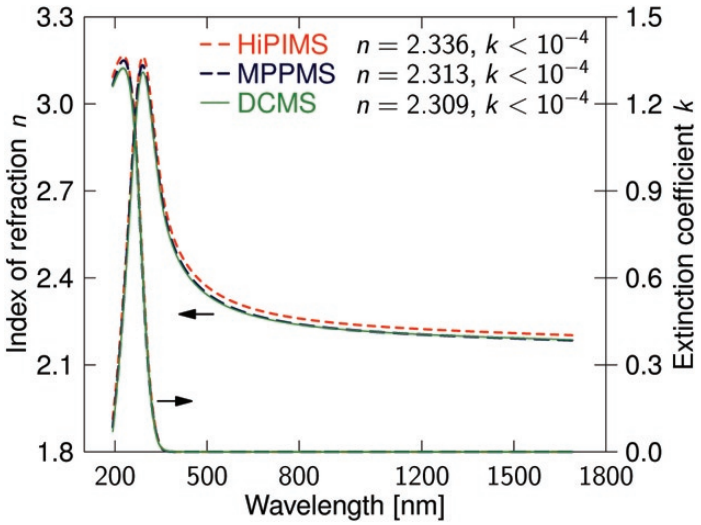

Figure 8.6 Spectral dependence of the index of refraction n and of the extinction coefficient k of the Nb_2O_5 coatings prepared by HiPIMS, MPPMS and DCMS at $\Phi(O_2) = 12\,\text{sccm}$ and $p = 1.2\,\text{Pa}$. The values of n and k for a wavelength $\lambda = 550\,\text{nm}$ are displayed.

the higher Ti^+ fluxes in [12]. In fact, high metal ion fluxes can be expected in the reactive HiPIMS discharges, as indicated by the notable emission from the excited Nb^+ detected at $\Phi(O_2) = 12\,\text{sccm}$ [figure 8.5(b)].

The surface roughness estimated using ellipsometry analysis was about 2 nm for the Nb_2O_5 coatings prepared by HiPIMS and MPPMS, and 4 nm for those prepared by DCMS. The results of internal stress evaluation, σ, and of the nanoindentation analysis are presented in table 8.2, together with measured thickness of the investigated films. HiPIMS and MPPMS-deposited coatings exhibited near-zero in-plane stress, in contrast to the moderate compressive stress of the DCMS coating. The reduction of the compressive stress level in high power pulsed discharges may be explained by the ion bombardment discussed previously. For instance, Çetinörgü *et al.* [203] observed the in-plane stress relaxation of the DIBS-prepared Nb_2O_5 films, from $\sigma = -240\,\text{MPa}$ (obtained without the ion bombardment) to $\sigma = -140\,\text{MPa}$, with the increasing energy of the assisting bombarding ions (up to 550 V). The theoretical interpretation for the coating stress relaxation due to the ion bombardment at moderately elevated ion energies (hundreds of eV) can be found in [204].

Table 8.2 Thickness, t_f, in-plane stress, σ, hardness, H, and reduced Young's modulus, E, of Nb_2O_5 coatings deposited by HiPIMS, MPPMS and DCMS at $\Phi(O_2) = 12\,\text{sccm}$ and at $p = 1.2\,\text{Pa}$. The film prepared by DCMS in the conditions of the poisoned target was very thin, which made the evaluation of σ difficult, and of H and E unreliable.

	t_f [nm]	σ [MPa]	$\Delta\sigma$ [MPa]	H [GPa]	ΔH [GPa]	E_r [GPa]	ΔE [GPa]
HiPIMS	755	50	50	6.2	0.2	140	5
MPPMS	960	-90	50	5.8	0.1	136	5
DCMS	77	-330	150	—	—	—	—

Hardness, H, and reduced Young's modulus, E_r, of the HiPIMS- and MPPMS-deposited coatings correspond to those reported by Çetinörgü *et al.* [203] for films obtained by DIBS. The authors demonstrated that H of the dense Nb_2O_5 coatings varied from 5.5 to 6.5 GPa and E_r from 118 to 130 GPa, in dependence on the flux and energy of the bombarding ions produced by the secondary ion source. It is to be stressed that in the current experiments no external ion beam assistance has been provided. Yet, a comparable H and a moderately higher E_r values are detected. The slightly higher hardness of the HiPIMS-deposited coating compared to that of the MPPMS-deposited coating is probably also a consequence of higher film density, such as suggested by the higher value of n.

The presented coating characterization shows that both pulsed techniques can produce dense optical films suitable for optical filter applications. The absence of a hysteresis and stabilization of the deposition process in both reactive HiPIMS and MPPMS discharges provide a great versatility of the deposition conditions at which optically transparent Nb_2O_5 coatings can be obtained. This opens a possibility to further tailor the deposition process, and hence, the coating properties.

8.4 Conclusions

The present study has demonstrated that the two investigated high power pulsed discharges above a Nb cathode in O_2/Ar mixtures can be operated in a hysteresis-free mode between the metallic and the poisoned target state. The current waveform monitoring and the TR optical emission diagnostics indicated that the surface oxide layer, created on the Nb target in between the pulses, was progressively sputter-eroded during both HiPIMS and

MPPMS pulses. This behaviour permits deposition of optically transparent Nb_2O_5 films exhibiting a technologically interesting deposition rate at a large range of the oxygen flows. Moreover, stable deposition conditions can be obtained by reactive gas flow control with no need of a feedback system, commonly used in reactive DCMS.

The differences between pulse power management in HiPIMS and MPPMS were found to significantly affect the sputtering regime and the reactive discharge behaviour. The cathode voltage was identified as the principal parameter defining the discharge current amplitude and the target cleaning efficiency, since ISEE, the sputtering yield, and the oxygen implantation depth are all functions of the impacting ion energy. The pulse duration is another important variable because it represents the time available for the gradual target cleaning.

Nb_2O_5 coatings prepared by both reactive high power pulsed discharges exhibited a high index of refraction, a low extinction coefficient, a near-zero internal stress, low surface roughness and high hardness and Young's modulus. These characteristics are compatible with optical coating technology requirements. The HiPIMS-deposited coatings showed the highest deposition rate. In comparison, MPPMS exhibited the highest power-normalized deposition rate among the three deposition techniques.

Acknowledgments

The authors wish to thank Mr. Etienne Bousser for the hardness and Young's modulus evaluation, Dr. Richard Vernhes for his assistance with the ellipsometry measurements and modelling, and Mr. Francis Turcot and Mr. Sébastien Chenard for their technical assistance. The financial support by NSERC of Canada within the CRDPJ 380174-08 project is gratefully acknowledged.

CHAPTER 9

General discussion, conclusions and perspectives

This chapter offers a brief recapitulation of the most important results obtained during the presented work and highlights the main contributions to the field. It should also serve as a confirmation that the objectives defined in Chapter 1 have been attained. At first, the principal findings of the optical diagnostics of HiPIMS discharges operated under both non-reactive and reactive conditions will be summarized, together with the description of the methodology developed during this work. Afterwards, the main conclusions resulting from the critical comparison of the two power management approaches in high power sputtering will be outlined. Finally, the perspectives and suggestions of the future work that should follow this work will be presented.

9.1 Diagnostics of HiPIMS discharge evolution

One of the primary objectives of this work was to gain an in-depth understanding of the physical processes within pulsed HiPIMS discharges operated under both non-reactive and reactive conditions. In order to achieve this goal, we have applied two methodological approaches based on the optical emission emanating from the plasma. The first one is the fast plasma imaging, employing the custom-made optical interference filters used to isolate the optical emission signal originating from different species populating the plasma. In Chapter 4, we have discussed the necessary steps for the design of appropriate filters, as well as their practical use for species-resolved plasma imaging suitable for the characterization of the spatial evolution of pulsed HiPIMS discharges. Subsequently, we have demonstrated the application of this diagnostic approach for the visualization of different plasma-phase processes, such as background gas excitations by energetic electrons appearing during the discharge ignition, and the expansion of the dense plasma region outwards from the target preceded by the gas shock wave. The understanding of these effects can be beneficial in the optimization of the coating deposition, specifically if combined with the generator-synchronized pulsed biasing

of the substrates that would permit to selectively choose the kind of ionized species to be incorporated within the growing film.

Species-resolved plasma imaging can be used for the monitoring of HiPIMS discharges operated in both non-reactive and reactive conditions, such as shown in the analyses of the 200 μs long square-shaped voltage pulses applied to a Cr target in pure Ar (Chapter 4) and in pure O_2 (Chapter 6). In the former case, the investigated discharge was operated in metal-dominated sputtering mode, while in the latter case, the discharge was operated above a fully poisoned (oxidized) Cr cathode from which only a minimum of the target material is sputtered.

In order to gain further information about the dynamics of HiPIMS discharges, we have carried out a systematic investigation of the 200 μs long square-shaped HiPIMS pulses operated in Ar, N_2 and N_2/Ar mixtures, and at various pressures ranging within $0.7\,\mathrm{Pa} < p < 2.66\,\mathrm{Pa}$ (Chapter 5). In this study, we have used the combination of fast plasma imaging and time- and space-resolved OES, together with the current waveform monitoring. This approach enabled characterization of the propagation velocity of the fast electron-induced gas excitations at the beginning of the pulse and of the metal-rich plasma generated during the metal-dominated phase of the discharge, as a function of the composition and pressure of the working gas. It was found, that the speed of the plasma wavefront varied in the range from 0.7 to $3.5\,\mathrm{km\,s^{-1}}$; It increased with higher nitrogen concentration within the reactive gas mixture and/or with decreasing pressure. The expanding plasma region had a hemispherical shape in pure Ar, predominantly due to the bright emission from the excited sputtered Cr. In the reactive atmosphere, the apparent form of the travelling plasma wavefront evolved from a hemispherical into a droplike shape extending far from the target, mostly due to the significant emission from molecular N_2.

We were able to identify up to four different phases during a single HiPIMS pulse, namely (i) the ignition phase, (ii) the high current metal-dominated phase, (iii) the transient phase, and (iv) the low current gas-dominated phase. The transition in between the metal-dominated and the gas-dominated discharge was found to depend on the cathode voltage amplitude, alongside with other parameters, such as the magnetron's magnetic field configuration. Here, it should be pointed out that the magnetic field strength can be optimized in such a way that

the high current discharge – also denoted as the high density discharge – can be stabilized during the entire duration of the HiPIMS pulse, as discussed and demonstrated in Appendix A.

The observation of the high density discharge – characterized by high amplitude pressure-independent currents – during HiPIMS pulses operated in N_2, and the similarity of the respective spectroscopic evolution to that of the non-reactive discharges, manifested the presence of self-sputtering mechanism in the reactive HiPIMS discharges. This finding was further supported by the observation of the high deposition rate of CrN coatings ($r = 2.5\,\mu\mathrm{m\,h^{-1}}$) prepared in pure N_2 at comparable conditions ($I_C \approx 1.1\,\mathrm{A}$, $p = 1.3\,\mathrm{Pa}$), using the same experimental setup [173].

9.2 Characterization of different pulse power management strategies in HiPIMS

From the understanding developed in Chapter 5, and using a similar methodology (time-averaged and time-resolved OES combined with current waveform monitoring), we extended our investigation to the characterization of pulsed discharge evolution, plasma composition and metal ionization during the high power pulsed discharges exhibiting different pulse shapes: square voltage pulses (HiPIMS) and modulated custom-shaped pulses (MPPMS). This was complemented by the critical analyses of the deposition rate, the microstructure and the internal mechanical stress of the prepared Nb coatings. Moreover, we explored the behavior of both HiPIMS and MPPMS discharges in reactive O_2/Ar gas mixtures and evaluated the material, mechanical and optical properties of the deposited NbO_x films. All the monitored discharge and coating characteristics were also compared to those obtained by the benchmark DCMS technique. Such a rigorous comparison study is of great importance for the coating manufacturers seeking an optimal approach for their specific deposition process.

In Chapter 7, we have characterized HiPIMS, MPPMS and DCMS discharges operated above a 5-cm Nb target at various powers (0 W - 450 W) and at two Ar pressures (1 and 2 Pa). Firstly, we have compared the different types of power regulation and evaluated the related discharge parameters. We have shown that the HiPIMS technique is the only one that enables the discharge operation in the metal-dominated sputtering mode within the investigated range of powers, resulting in a significantly higher ionization of the sputtered metal than that reached with MPPMS and DCMS. This identifies HiPIMS as the most suitable technique for

deposition processes where maximum metal ionization is required. However, the 200 μs long HiPIMS pulses were found to be difficult to ignite or were prone to arcing at low pressures and under reactive conditions. In these situations, the use of the MPPMS pulses of long duration (up to few ms) was found advantageous, particularly due to the gradual rise of the power applied by the MPPMS PS. Thus, the versatility that the modulated pulse power generator offers, together with the substantial metal ionization, makes MPPMS an attractive alternative to HiPIMS.

Both HiPIMS and MPPMS exhibited similar Nb deposition rates, which were lower than with DC sputtering, due to the non-linear dependence of the sputtering yield on the impacting ion energy and due to other phenomena. Coatings deposited by the two high power pulsed discharges at $p = 1\,\mathrm{Pa}$ were in higher compressive stress and had a larger out-of-plane lattice spacing than those prepared by DCMS, even though all the films possessed an apparently dense columnar structure. At higher pressure ($p = 2\,\mathrm{Pa}$), the DC-sputtered films showed a tensile stress and a porous microstructure, while films prepared by HiPIMS and MPPMS were dense and in compression. These observations were interpreted by a film densification due to the significant ion fluxes generated by both pulsed techniques.

Finally, in Chapter 8, we have shown that both HiPIMS and MPPMS discharges operated in the constant voltage-/voltage load mode above a Nb cathode in O_2/Ar mixtures can be operated in a hysteresis-free mode. It was suggested that the surface oxide layer, created on the Nb target in between the pulses, can be progressively sputter-eroded during the individual HiPIMS and MPPMS pulses. Consequently, the partially oxide-free target can be reached even at high oxygen concentrations (substantially higher than the threshold necessary for target poisoning in the DCMS discharge), which results in the stabilization of the deposition process and the hysteresis elimination. Therefore, stable deposition conditions can be obtained by reactive gas flow control with no need of a feedback system, commonly used in reactive DCMS. This behavior is particularly beneficial for the deposition of optically transparent films, such as demonstrated on the example of the prepared Nb_2O_5 exhibiting a technologically interesting deposition rate at a large range of the oxygen flows.

Nb_2O_5 coatings prepared by both high power pulsed discharges exhibited a high index of refraction, a low extinction coefficient, a near-zero internal stress, and high hardness and

Young's modulus. These characteristics are compatible with optical coating technology requirements. The observation of the highest index of refraction in the HiPIMS-deposited coatings was attributed to the higher film density. It should be noted that the highest power-normalized deposition rate among the three investigated deposition techniques was reached by reactive MPPMS. We have argued that the latter observation may be caused by the much longer period that is available for the gradual target cleaning during the MPPMS pulses (1500 μs), than during the much shorter HiPIMS pulses (200 μs). At the very end, we have offered an explanation for the high target cleaning efficiency during both HiPIMS and MPPMS pulses, and identified the cathode voltage as the key parameter for the resulting reactive discharge behavior.

9.3 Perspectives and future work

This thesis represents the first systematic work related to the investigation and implementation of the high power pulsed technology in the FCSEL laboratory. It is focused mainly on the optical and electrical characterization of the principal types of the HiPIMS discharges operated in the various working gas compositions and pressures. However, this work also reports on the fabrication and characterization of the model metal and metal oxide coatings in a great variety of conditions. Such a systematic study established a solid background for further directions of research that will be outlined in the following sections.

9.3.1 Discharge characterization

As it was clearly demonstrated in the present work, the optical emission from the plasma can be used as a powerful and versatile *diagnostic tool* for the characterization and hence optimization of the high power pulsed discharges. However, the emission signal from the plasma-excited species is unfortunately highly convoluted, since it also carries the information about n_e, T_e, etc. Therefore, this work should be complemented by the Langmuir probe measurements that would permit determination of these parameters in the studied discharges, specifically those operated in reactive gas mixtures. One could also employ actinometry in order to quantify the density of the selected species, as discussed in Chapter 3.

The species-resolved plasma imaging technique for HiPIMS discharge monitoring, addressed in Chapter 4, can be enhanced by a separate detection of the emission of spectral lines originating from either neutral or ionized plasma-excited species. For that purpose, one may use a set of narrow bandpass filters which would enable the monitoring of emission lines otherwise indistinguishable by the optical filters used in this work. An independent analysis of neutral and ionized fluxes would facilitate a proper understanding of the discharge dynamics and hence of the respective film growth conditions.

In order to improve the spatial resolution of the plasma imaging, it is recommended to process the acquired images by the reverse Abel transformation. This transformation is used for the calculation of axially symmetric emission distributions, given its projection to the

plane of observation (e.g., the image obtained by the fast camera) [146]. The combination of the species-resolved plasma imaging and the image processing by Abel inversion would provide a better accuracy in this diagnostic approach and an easier interpretation of the results. Such an analysis could also supply the data suitable for time-dependent modelling of neutral and ionized material fluxes in HiPIMS pulses, that could replace the current parametric steady-state models [114, 102, 104].

In the Appendix A, we discuss the application of the paramagnetic spacers in between the target and the magnetron head in order to decrease the magnetic field strength and hence to customize the resulting cathode current. It would be interesting to complement this study by the diagnostics of the discharge evolution using species-resolved plasma imaging at the different magnetic field configurations. Such an investigation would enable better understanding of the effect of the magnetic field on the pulsed discharge evolution, and more specifically, on the transport of the sputtered species. Furthermore, the presented approach is highly suitable for the in-depth analysis of the magnetic field perturbations – particularly visible due to the modified working gas emission during the discharge ignition, as depicted in Chapter 5 – that originate in the abrupt changes in the cathode current amplitude encountered during the HiPIMS pulses [168].

The hysteresis-free reactive sputtering in the O_2/Ar mixtures was demonstrated for the HiPIMS and MPPMS discharges operated above a Nb target (Chapter 8), but also above Ta and Cr targets. In contrast, both types of discharges did exhibit hysteresis when using a Ti target. In order to better understand this variable behavior, it is first necessary to determine the limiting conditions (e.g., cathode voltage amplitude, magnetic field strength, size of the cathode) at which the hysteresis is suppressed, for each of the target material of interest. Therefore, further investigation of the reactive HiPIMS and MPPMS discharges should follow under a variety of experimental conditions, and for different target materials.

The distinct feature of HiPIMS is a highly ionized flux of sputtered material towards the substrate. The monitoring of the metal plasma propagation (Chapter 5) and the estimation of the sputtered material ionization (Chapter 7), using solely the emission line intensities, should be supplemented by a rigorous characterization of the ion fluxes reaching the substrates

(e.g., flux intensity, flux composition, IEDF). FCSEL possesses extensive experience in using the retarding field ion energy analyser and the mass spectrometer [61, 60, 205], which are both highly complementary diagnostic approaches to OES. The quantification of the ion flux characteristics by these two techniques, in combination with the expertise regarding the plasma–surface interactions previously developed in FCSEL [63, 62, 79, 80], would enable a judicious control over the thin film growth process, and hence its optimization.

9.3.2 Functional coating fabrication

The ultimate goal of the present work, devoted mainly to the characterization of the various HiPIMS discharges operated in a multitude of conditions, is to facilitate the implementation of this promising, yet emerging, technology for the fabrication of high quality functional coatings.

In Chapter 8, we have presented the high refractive index Nb_2O_5 coatings exhibiting characteristics fulfilling the optical coating requirements. In the next step of this project, Nb_2O_5 – or other high index oxide, such as Ta_2O_5 – should be combined with a low index material – for instance, SiO_2 – in the multilayer coatings, in order to prepare model interference optical filters. This can be performed in a dual magnetron set-up, where the substrate is recursively moving in between the two cathodes (e.g., Nb and Si) sputtered in the reactive O_2/Ar mixture to create the requested number of layers. The total number as well as the thicknesses of the individual layers can be designed using the OpenFilters sofware [163], developed in FCSEL.

It would be interesting to investigate the influence of Ar incorporation within the HiPIMS-deposited films on the stress-induced coating deterioration. The latter relation could be examined, for example, by the wear-, corrosion- and erosion-resistance testing, in which FCSEL has an extensive expertise [206, 207, 208, 209, 210, 211, 212, 203]. Both species-resolved plasma imaging and time- and space-resolved OES monitoring permit the evaluation of the travelling time of the working gas ions and of the expanding metal-rich plasma in between the target and the substrate. This opens a possibility to employ an appropriate substrate biasing scheme that would favor the acceleration of the arriving metal ions relatively

to the working gas ions. As suggested in Chapter 4, the substrate could be biased by a pulsed PS that is synchronized with the generator powering the sputtered cathode, with a set delay selected by the operator. The most recent bias HiPIMS generators available on the market already enable such synchronization. Furthermore, a positive bias, preventing the incorporation of the working gas ions into the substrate, such as during the ignition phase, could also be applied.

The HiPIMS discharge operation in the metal-dominated sputtering in the pure N_2 atmosphere (Chapter 5) demonstrated that the high-quality protective coatings can be fabricated with no Ar-related defects, and at the same time, with no drawback of the decreased deposition rate (Ref. [173]). This broadens the possibilities for the fabrication of high-quality nitride-based protective coatings, including the nanoscale multilayers and nanocomposites. Many years of experience and expertise that FCSEL possesses in this domain [213, 207, 208, 209, 210, 211, 212, 214] can serve as a driving force for such investigation.

9.3.3 Final remark

HiPIMS - that combines the advantages of the IPVD technique and the flexibility of the well-established magnetron sputtering with a relative ease of implementation and scale-up in the industrial process – can be considered as the current state-of-the-art deposition technology that has a great potential to outperform other commonly used coating fabrication techniques. The number of research laboratories and manufacturers investigating its capacities and limitations, as well as the number of examples demonstrating its successful application in coating preparation, are constantly growing. This huge interest from the coating community confirms that HiPIMS is a very promising technology that is definitely worth the efforts for further exploration. It is the humble believe of this candidate, that the herein presented results contribute to the general understanding of this technique and hence to its future development.

REFERENCES

[1] L. Martinu, J. Klemberg-Sapieha, and O. Zabeida, "Plasma-enhanced chemical vapor deposition of functional coatings," in *Handbook of Deposition Technologies for Films and Coatings (Third Edition)*, 3rd ed., P. M. Martin, Ed. Boston, MA: William Andrew Publishing, 2010, pp. 392 – 465. [Online]. Available: http://www.sciencedirect.com/science/article/pii/B9780815520313000053

[2] J.-O. Carlsson and P. Martin, "Chemical vapor deposition," in *Handbook of Deposition Technologies for Films and Coatings (Third Edition)*, 3rd ed., P. M. Martin, Ed. Boston, MA: William Andrew Publishing, 2010, pp. 314 – 363. [Online]. Available: http://www.sciencedirect.com/science/article/pii/B9780815520313000077

[3] M. Ohring, *Materials Science of Thin Films*, 2nd ed. San Diego, CA: Academic Press, 2002. [Online]. Available: http://www.sciencedirect.com/science/article/pii/B9780125249751500070

[4] A. Anders, "Some applications of cathodic arc coatings," in *Cathodic Arcs*, ser. Springer Series on Atomic, Optical, and Plasma Physics. New York, NY: Springer, 2008, vol. 50, pp. 1–62. [Online]. Available: http://dx.doi.org/10.1007/978-0-387-79108-1-10

[5] A. Anders, "Macroparticle filters," in *Cathodic Arcs*, ser. Springer Series on Atomic, Optical, and Plasma Physics. New York, NY: Springer, 2008, vol. 50, pp. 1–64. [Online]. Available: http://dx.doi.org/10.1007/978-0-387-79108-1-7

[6] A. Anders, "Unfiltered and filtered cathodic arc deposition," in *Handbook of Deposition Technologies for Films and Coatings (Third Edition)*, 3rd ed., P. M. Martin, Ed. Boston, MA: William Andrew Publishing, 2010, pp. 466 – 531. [Online]. Available: http://www.sciencedirect.com/science/article/pii/B9780815520313000107

[7] D. Depla, S. Mahieu, and J. Greene, "Sputter deposition processes," in *Handbook of Deposition Technologies for Films and Coatings (Third Edition)*, 3rd ed., P. M. Martin, Ed. Boston, MA: William Andrew Publishing, 2010, pp. 253 – 296. [Online]. Available: http://www.sciencedirect.com/science/article/pii/B9780815520313000053

[8] G. Bräuer, B. Szyszka, M. Vergöhl, and R. Bandorf, "Magnetron sputtering - milestones of 30 years," *Vacuum*, vol. 84, no. 12, pp. 1354 – 1359, 2010, selected Papers from the Proceedings of The Tenth International Symposium on Sputtering and Plasma Processes (ISSP 2009), 8th-10th July 2009, Kanazawa, Japan. [Online]. Available: http://www.sciencedirect.com/science/article/pii/S0042207X10000163

[9] R. F. Bunshah, "Summary, developments, and outlook," in *Handbook of Hard Coatings*, 1st ed., R. F. Bunshah, Ed. Norwich, NY: William Andrew Publishing, 2001, pp. 517 – 534.

[10] I. Petrov, P. B. Barna, L. Hultman, and J. E. Greene, "Microstructural evolution during film growth," *J. Vac. Sci. Technol. A*, vol. 21, no. 5, pp. S117–S128, 2003. [Online]. Available: http://link.aip.org/link/?JVA/21/S117/1

[11] L. Hultman, W.-D. Munz, J. Musil, S. Kadlec, I. Petrov, and J. E. Greene, "Low-energy ($\sim 100\,\mathrm{eV}$) ion irradiation during growth of TiN deposited by reactive magnetron

sputtering: Effects of ion flux on film microstructure," *J. Vac. Sci. Technol. A*, vol. 9, no. 3, pp. 434–438, 1991. [Online]. Available: http://link.aip.org/link/?JVA/9/434/1

[12] K. Sarakinos, J. Alami, and M. Wuttig, "Process characteristics and film properties upon growth of TiO_x films by high power pulsed magnetron sputtering," *J. Phys. D: Appl. Phys.*, vol. 40, no. 7, pp. 2108 – 2114, 2007. [Online]. Available: http://dx.doi.org/10.1088/0022-3727/40/7/037

[13] J. Alami, J. Gudmundsson, J. Bohlmark, J. Birch, and U. Helmersson, "Plasma dynamics in a highly ionized pulsed magnetron discharge," *Plasma Sources Sci. Technol.*, vol. 14, no. 3, pp. 525 – 31, 2005. [Online]. Available: http://dx.doi.org/10.1088/0963-0252/14/3/015

[14] A. P. Ehiasarian, J. Wen, and I. Petrov, "Interface microstructure engineering by high power impulse magnetron sputtering for the enhancement of adhesion," *J. Appl. Phys.*, vol. 101, no. 5, p. 54301, 2007. [Online]. Available: http://dx.doi.org/10.1063/1.2697052

[15] K. Bobzin, N. Bagcivan, P. Immich, S. Bolz, J. Alami, and R. Cremer, "Advantages of nanocomposite coatings deposited by high power pulse magnetron sputtering technology," *J. Mater. Process. Technol.*, vol. 209, no. 1, pp. 165 – 70, 2009. [Online]. Available: http://dx.doi.org/10.1016/j.jmatprotec.2008.01.035

[16] E. Klawuhn, G. C. D'Couto, K. A. Ashtiani, P. Rymer, M. A. Biberger, and K. B. Levy, "Ionized physical-vapor deposition using a hollow-cathode magnetron source for advanced metallization," vol. 18, no. 4. AVS, 2000, pp. 1546–1549. [Online]. Available: http://link.aip.org/link/?JVA/18/1546/1

[17] U. Helmersson, M. Lattemann, J. Bohlmark, A. P. Ehiasarian, and J. Gudmundsson, "Ionized physical vapor deposition (IPVD): A review of technology and applications," *Thin Solid Films*, vol. 513, no. 1-2, pp. 1 – 24, 2006. [Online]. Available: http://dx.doi.org/10.1016/j.tsf.2006.03.033

[18] D. Mozgrin, I. Fetisov, and G. Khodachenko, "High-current low-pressure quasi-stationary discharge in a magnetic field: experimental research," *Plasma Phys. Rep.*, vol. 21, no. 5, pp. 400 – 9, 1995.

[19] S. Bugaev, N. Koval, N. Sochugov, and A. Zakharov, "Investigation of a high-current pulsed magnetron discharge initiated in the low-pressure diffuse arc plasma," in *XVIIth International Symposium on Discharges and Electrical Insulation in Vacuum, 1996. Proceedings. ISDEIV.*, vol. 2, 1996, pp. 1074 – 1076.

[20] I. K. Fetisov, A. A. Filippov, G. V. Khodachenko, D. V. Mozgrin, and A. A. Pisarev, "Impulse irradiation plasma technology for film deposition," *Vacuum*, vol. 53, no. 1-2, pp. 133 – 136, 1999. [Online]. Available: http://www.sciencedirect.com/science/article/pii/S0042207X98004084

[21] V. Kouznetsov, K. Macak, J. M. Schneider, U. Helmersson, and I. Petrov, "A novel pulsed magnetron sputter technique utilizing very high target power densities," *Surf. Coat. Technol.*, vol. 122, no. 2-3, pp. 290 – 293, 1999. [Online]. Available: http://dx.doi.org/10.1016/S0257-8972(99)00292-3

[22] K. Macák, V. Kouznetsov, J. Schneider, U. Helmersson, and I. Petrov, "Ionized sputter deposition using an extremely high plasma density pulsed magnetron discharge,"

J. Vac. Sci. Technol. A, vol. 18, no. 4, pp. 1533 – 1537, 2000. [Online]. Available: http://dx.doi.org/10.1116/1.582380

[23] J. Bohlmark, J. Gudmundsson, J. Alami, M. Lattemann, and U. Helmersson, "Spatial electron density distribution in a high-power pulsed magnetron discharge," *IEEE Trans. Plasma Sci.*, vol. 33, no. 2, pp. 346 – 347, 2005. [Online]. Available: http://dx.doi.org/10.1109/TPS.2005.845022

[24] A. Pajdarová, J. Vlček, P. Kudláček, and J. Lukáš, "Electron energy distributions and plasma parameters in high-power pulsed magnetron sputtering discharges," *Plasma Sources Sci. Technol.*, vol. 18, no. 2, p. 025008, 2009. [Online]. Available: http://stacks.iop.org/0963-0252/18/i=2/a=025008

[25] A. Vetushka and A. P. Ehiasarian, "Plasma dynamic in chromium and titanium HIPIMS discharges," *J. Phys. D: Appl. Phys.*, vol. 41, no. 1, p. 015204, 2008. [Online]. Available: http://dx.doi.org/10.1088/0022-3727/41/1/015204

[26] J. Gudmundsson, J. Alami, and U. Helmersson, "Spatial and temporal behavior of the plasma parameters in a pulsed magnetron discharge," *Surf. Coat. Technol.*, vol. 161, no. 2-3, pp. 249 – 256, 2002. [Online]. Available: http://dx.doi.org/10.1016/S0257-8972(02)00518-2

[27] J. Gudmundsson, P. Sigurjonsson, P. Larsson, D. Lundin, and U. Helmersson, "On the electron energy in the high power impulse magnetron sputtering discharge," *J. Appl. Phys.*, vol. 105, no. 12, p. 123302, 2009. [Online]. Available: http://dx.doi.org/10.1063/1.3151953

[28] A. P. Ehiasarian, R. New, W.-D. Munz, L. Hultman, U. Helmersson, and V. Kouznetsov, "Influence of high power densities on the composition of pulsed magnetron plasmas," *Vacuum*, vol. 65, no. 2, pp. 147 – 154, 2002. [Online]. Available: http://dx.doi.org/10.1016/S0042-207X(01)00475-4

[29] J. Vlček, P. Kudláček, K. Burcalová, and J. Musil, "High-power pulsed sputtering using a magnetron with enhanced plasma confinement," *J. Vac. Sci. Technol. A*, vol. 25, no. 1, pp. 42 – 7, 2007. [Online]. Available: http://dx.doi.org/10.1116/1.2388954

[30] P. Kudláček, J. Vlček, K. Burcalová, and J. Lukáš, "Highly ionized fluxes of sputtered titanium atoms in high-power pulsed magnetron discharges," *Plasma Sources Sci. Technol.*, vol. 17, no. 2, p. 025010, 2008. [Online]. Available: http://dx.doi.org/10.1088/0963-0252/17/2/025010

[31] J. Bohlmark, J. Alami, C. Christou, A. P. Ehiasarian, and U. Helmersson, "Ionization of sputtered metals in high power pulsed magnetron sputtering," *J. Vac. Sci. Technol. A*, vol. 23, no. 1, pp. 18 – 22, 2005. [Online]. Available: http://dx.doi.org/10.1116/1.1818135

[32] J. Andersson, A. P. Ehiasarian, and A. Anders, "Observation of Ti^{4+} ions in a high power impulse magnetron sputtering plasma," *Appl. Phys. Lett.*, vol. 93, no. 7, p. 071504, 2008. [Online]. Available: http://dx.doi.org/10.1063/1.2973179

[33] J. Lazar, J. Vlček, and J. Rezek, "Ion flux characteristics and efficiency of the deposition processes in high power impulse magnetron sputtering of zirconium," *J. Appl. Phys.*, vol. 108, no. 6, p. 063307, 2010. [Online]. Available: http://link.aip.org/link/?JAP/108/063307/1

[34] A. Hecimovic and A. P. Ehiasarian, "Temporal evolution of the ion fluxes for various elements in hipims plasma discharge," *IEEE Trans. Plasma Sci.*, vol. 39, no. 4, pp. 1154 –1164, 2011. [Online]. Available: http://dx.doi.org/10.1109/TPS.2011.2106516

[35] C. Reinhard, A. P. Ehiasarian, and P. Hovsepian, "CrN/NbN superlattice structured coatings with enhanced corrosion resistance achieved by high power impulse magnetron sputtering interface pre-treatment," *Thin Solid Films*, vol. 515, no. 7-8, pp. 3685 – 92, 2007. [Online]. Available: http://dx.doi.org/10.1016/j.tsf.2006.11.014

[36] P. Hovsepian, C. Reinhard, and A. P. Ehiasarian, "CrAlYN/CrN superlattice coatings deposited by the combined high power impulse magnetron sputtering/unbalanced magnetron sputtering technique," *Surf. Coat. Technol.*, vol. 201, no. 7, pp. 4105 – 10, 2006. [Online]. Available: http://dx.doi.org/10.1016/j.surfcoat.2006.08.027

[37] P. Hovsepian, A. P. Ehiasarian, A. Deeming, and C. Schimpf, "Novel TiAlCN/VCN nanoscale multilayer pvd coatings deposited by the combined high-power impulse magnetron sputtering/unbalanced magnetron sputtering (HIPIMS/UBM) technology," *Vacuum*, vol. 82, no. 11, pp. 1312 – 1317, 2008. [Online]. Available: http://dx.doi.org/10.1016/j.vacuum.2008.03.064

[38] P. Hovsepian, A. P. Ehiasarian, and U. Ratayski, "CrAlYCN/CrCN nanoscale multilayer PVD coatings deposited by the combined high-power impulse magnetron sputtering/unbalanced magnetron sputtering (HIPIMS/UBM) technology," *Surf. Coat. Technol.*, vol. 203, no. 9, pp. 1237 – 1243, 2009. [Online]. Available: http://dx.doi.org/10.1016/j.surfcoat.2008.10.033

[39] Y. Purandare, A. P. Ehiasarian, M. Stack, and P. Hovsepian, "CrN/NbN coatings deposited by HIPIMS: A preliminary study of erosion-corrosion performance," *Surf. Coat. Technol.*, vol. 204, no. 8, pp. 1158 – 1162, 2010. [Online]. Available: http://www.sciencedirect.com/science/article/pii/S0257897209009335

[40] A. P. Ehiasarian, W.-D. Munz, L. Hultman, U. Helmersson, and I. Petrov, "High power pulsed magnetron sputtered CrN_x films," *Surf. Coat. Technol.*, vol. 163-164, pp. 267 – 272, 2003. [Online]. Available: http://dx.doi.org/10.1016/S0257-8972(02)00479-6

[41] G. Greczynski, J. Jensen, J. Böhlmark, and L. Hultman, "Microstructure control of crnx films during high power impulse magnetron sputtering," *Surf. Coat. Technol.*, vol. 205, no. 1, pp. 118 – 130, 2010. [Online]. Available: http://www.sciencedirect.com/science/article/pii/S0257897210004378

[42] M. Lattemann, U. Helmersson, and J. Greene, "Fully dense, non-faceted 111-textured high power impulse magnetron sputtering TiN films grown in the absence of substrate heating and bias," *Thin Solid Films*, vol. 518, no. 21, pp. 5978 – 5980, 2010. [Online]. Available: http://www.sciencedirect.com/science/article/pii/S0040609010007340

[43] K. Bobzin, N. Bagcivan, P. Immich, S. Bolz, R. Cremer, and T. Leyendecker, "Mechanical properties and oxidation behaviour of (Al,Cr)N and (Al,Cr,Si)N coatings for cutting tools deposited by HPPMS," *Thin Solid Films*, vol. 517, no. 3, pp. 1251 – 1256, 2008. [Online]. Available: http://dx.doi.org/10.1016/j.tsf.2008.06.050

[44] K. Bobzin, N. Bagcivan, P. Immich, S. Bolz, H. G. Fuß, and R. Cremer, "Properties of (Ti,Al,Si)N coatings for high demanding metal cutting applications deposited by

HPPMS in an industrial coating unit," *Plasma Processes Polym.*, vol. 6, no. S1, pp. S124–S128, 2009. [Online]. Available: http://dx.doi.org/10.1002/ppap.200930408

[45] K. Bobzin, N. Bagcivan, M. Ewering, R. H. Brugnara, and S. Theiß, "DC-MSIP/HPPMS (Cr,Al,V)N and (Cr,Al,W)N thin films for high-temperature friction reduction," *Surf. Coat. Technol.*, vol. 205, no. 8-9, pp. 2887 – 2892, 2011. [Online]. Available: http://www.sciencedirect.com/science/article/pii/S0257897210011205

[46] S. Konstantinidis, J. Dauchot, and M. Hecq, "Titanium oxide thin films deposited by high-power impulse magnetron sputtering," *Thin Solid Films*, vol. 515, no. 3, pp. 1182 – 1186, 2006. [Online]. Available: http://dx.doi.org/10.1016/j.tsf.2006.07.089

[47] A. Amin, D. Köhl, and M. Wuttig, "The role of energetic ion bombardment during growth of TiO_2 thin films by reactive sputtering," *J. Phys. D: Appl. Phys.*, vol. 43, no. 40, p. 405303, 2010. [Online]. Available: http://dx.doi.org/10.1088/0022-3727/43/40/405303

[48] V. Straňák, M. Quaas, H. Wulff, Z. Hubička, S. Wrehde, M. Tichý, and R. Hippler, "Formation of TiO_x films produced by high-power pulsed magnetron sputtering," *J. Phys. D: Appl. Phys.*, vol. 41, no. 5, p. 055202, 2008. [Online]. Available: http://dx.doi.org/10.1088/0022-3727/41/5/055202

[49] K. Sarakinos, J. Alami, C. Klever, and M. Wuttig, "Process stabilization and enhancement of deposition rate during reactive high power pulsed magnetron sputtering of zirconium oxide," *Surf. Coat. Technol.*, vol. 202, no. 20, pp. 5033 – 5035, 2008. [Online]. Available: http://www.sciencedirect.com/science/article/B6TVV-4SHMC9D-4/2/66911d998afba5838f424b61102c1bd2

[50] K. Sarakinos, D. Music, S. Mráz, M. to Baben, K. Jiang, F. Nahif, A. Braun, C. Zilkens, S. Konstantinidis, F. Renaux, D. Cossement, F. Munnik, and J. M. Schneider, "On the phase formation of sputtered hafnium oxide and oxynitride films," *J. Appl. Phys.*, vol. 108, no. 1, p. 014904, 2010. [Online]. Available: http://link.aip.org/link/?JAP/108/014904/1

[51] V. Sittinger, F. Ruske, W. Werner, C. Jacobs, B. Szyszka, and D. Christie, "High power pulsed magnetron sputtering of transparent conducting oxides," *Thin Solid Films*, vol. 516, no. 17, pp. 5847 – 59, 2008. [Online]. Available: http://dx.doi.org/10.1016/j.tsf.2007.10.031

[52] F. Ruske, A. Pflug, V. Sittinger, W. Werner, B. Szyszka, and D. Christie, "Reactive deposition of aluminium-doped zinc oxide thin films using high power pulsed magnetron sputtering," *Thin Solid Films*, vol. 516, no. 14, pp. 4472 – 4477, 2008. [Online]. Available: http://dx.doi.org/10.1016/j.tsf.2007.06.019

[53] "HUETTINGER Electronik," accessed: 01/07/2011. [Online]. Available: http://www.huettinger.com

[54] "MELEC GmbH," accessed: 01/07/2011. [Online]. Available: http://www.melec.de

[55] "Zpulser, LLC," accessed: 01/07/2011. [Online]. Available: http://www.zpulser.com

[56] "Solvix SA," accessed: 01/07/2011. [Online]. Available: http://www.solvix.ch

[57] "Plasma Technology Limited," accessed: 01/07/2011. [Online]. Available: http://www.plasmatechnol.com

[58] "CemeCon AG," accessed: 01/07/2011. [Online]. Available: http://www.cemecon.de

[59] "Hauzer Techno Coating BV," accessed: 01/07/2011. [Online]. Available: http://www.hauzer.nl

[60] O. Zabeida, A. Hallil, M. R. Wertheimer, and L. Martinu, "Time-resolved measurements of ion energy distributions in dual-mode pulsed-microwave/radio frequency plasma," *J. Appl. Phys*, vol. 88, no. 2, pp. 635–642, 2000. [Online]. Available: http://link.aip.org/link/?JAP/88/635/1

[61] O. Zabeida and L. Martinu, "Ion energy distributions in pulsed large area microwave plasma," *J. Appl. Phys*, vol. 85, no. 9, pp. 6366–6372, 1999. [Online]. Available: http://link.aip.org/link/?JAP/85/6366/1

[62] R. Vernhes, O. Zabeida, J. E. Klemberg-Sapieha, and L. Martinu, "Pulsed radio frequency plasma deposition of a-SiN_x:H alloys: Film properties, growth mechanism, and applications," *J. Appl. Phys.*, vol. 100, no. 6, p. 063308, 2006. [Online]. Available: http://link.aip.org/link/?JAP/100/063308/1

[63] R. Vernhes, A. Amassian, J. E. Klemberg-Sapieha, and L. Martinu, "Plasma treatment of porous SiN_x:H films for the fabrication of porous-dense multilayer optical filters with tailored interfaces," *J. Appl. Phys.*, vol. 99, no. 11, p. 114315, 2006. [Online]. Available: http://dx.doi.org/doi/10.1063/1.2202692

[64] A. Fridman, "Elementary plasma-chemical reactions," in *Plasma Chemistry.* New York, NY: Cambridge University Press, 2008, pp. 12–88.

[65] F. Chen and J. Chang, "Lecture notes on principles of plasma processing." New York, NY: Kluwer Academic/Plenum Publishers, 2003.

[66] M. A. Lieberman and A. J. Lichtenberg, *Principles of Plasma Discharges and Materials*, 1st ed. New York, NY: Wiley-Interscience, 1994.

[67] R. A. Baragiola and P. Riccardi, "Electron emission from surfaces induced by slow ions and atoms," in *Reactive Sputter Deposition*, ser. Springer Series in Materials Science, D. Depla and S. Mahieu, Eds. Heidelberg, Germany: Springer, 2008, vol. 109, pp. 43–60.

[68] A. Phelps and Z. Petrovic, "Cold-cathode discharges and breakdown in argon: surface and gas phase production of secondary electrons," *Plasma Sources Sci. Technol.*, vol. 8, no. 3, p. R21, 1999. [Online]. Available: http://stacks.iop.org/0963-0252/8/i=3/a=201

[69] D. Depla, S. Mahieu, and R. De Gryse, "Magnetron sputter deposition: Linking discharge voltage with target properties," *Thin Solid Films*, vol. 517, no. 9, pp. 2825 – 2839, 2009. [Online]. Available: http://dx.doi.org/10.1016/j.tsf.2008.11.108

[70] K. Gylfason, J. Alami, U. Helmersson, and J. Gudmundsson, "Ion-acoustic solitary waves in a high power pulsed magnetron sputtering discharge," *J. Phys. D: Appl. Phys.*, vol. 38, no. 18, pp. 3417 – 3421, 2005. [Online]. Available: http://dx.doi.org/10.1088/0022-3727/38/18/015

[71] A. Anders, "Discharge physics of high power impulse magnetron sputtering," *Surf. Coat. Technol.*, vol. 205, no. Supplement 2, pp. S1 – S9, 2011. [Online]. Available: http://www.sciencedirect.com/science/article/pii/S0257897211002702

[72] W. D. Westwood, "Methods of reactive sputtering," in *Sputter Deposition*, 1st ed., W. D. Westwood, Ed. New York, NY: AVS, 2003, pp. 239 – 385.

[73] M. Thompson, B. Farmery, and P. Newson, "The energy spectrum of ejected atoms during the high energy sputtering of gold," *Philos. Mag.*, vol. 18, p. 377, 1968.

[74] W. Eckstein, "Sputtering yields," in *Sputtering by Particle Bombardment*, ser. Topics in Applied Physics. Berlin/Heidelberg, Germany: Springer, 2007, vol. 110, pp. 33–187. [Online]. Available: http://dx.doi.org/10.1007/978-3-540-44502-9_3

[75] J. Ziegler, J. Biersack, and M. Ziegler, *computer program: TRIM-2011*, 2011. [Online]. Available: http://www.srim.org

[76] S. Berg, H.-O. Blom, T. Larsson, and C. Nender, "Modeling of reactive sputtering of compound materials," *J. Vac. Sci. Technol. A*, vol. 5, no. 2, pp. 202–207, 1987. [Online]. Available: http://link.aip.org/link/?JVA/5/202/1

[77] D. Depla, S. Heirwegh, S. Mahieu, and R. D. Gryse, "Towards a more complete model for reactive magnetron sputtering," *J. Phys. D: Appl. Phys.*, vol. 40, no. 7, p. 1957, 2007. [Online]. Available: http://stacks.iop.org/0022-3727/40/i=7/a=019

[78] D. Guttler, B. Abendroth, R. Grotzschel, W. Moller, and D. Depla, "Mechanisms of target poisoning during magnetron sputtering as investigated by real-time in situ analysis and collisional computer simulation," *Appl. Phys. Lett.*, vol. 85, no. 25, pp. 6134–6136, 2004. [Online]. Available: http://link.aip.org/link/?APL/85/6134/1

[79] A. Amassian, M. Svec, P. Desjardins, and L. Martinu, "Dynamics of ion bombardment-induced modifications of Si(001) at the radio-frequency-biased electrode in low-pressure oxygen plasmas: In situ spectroscopic ellipsometry and Monte Carlo study," *J. Appl. Phys.*, vol. 100, no. 6, pp. 063 526 – 063 526, 2006.

[80] A. Amassian, M. Dudek, O. Zabeida, S. Gujrathi, J. E. Klemberg-Sapieha, and L. Martinu, "Oxygen incorporation and charge donor activation via subplantation during growth of indium tin oxide films," *J. Vac. Sci. Technol. A*, vol. 27, no. 2, pp. 362 – 366, 2009. [Online]. Available: http://dx.doi.org/10.1116/1.3081970

[81] W. Sproul, D. Christie, and D. Carter, "Control of reactive sputtering processes," *Thin Solid Films*, vol. 491, no. 1-2, pp. 1 – 17, 2005. [Online]. Available: http://dx.doi.org/10.1016/j.tsf.2005.05.022

[82] S. Berg and T. Nyberg, "Fundamental understanding and modeling of reactive sputtering processes," *Thin Solid Films*, vol. 476, no. 2, pp. 215 – 230, 2005. [Online]. Available: http://dx.doi.org/10.1016/j.tsf.2004.10.051

[83] T. Nyberg, S. Berg, U. Helmersson, and K. Hartig, "Eliminating the hysteresis effect for reactive sputtering processes," *Appl. Phys. Lett.*, vol. 86, no. 16, p. 164106, 2005. [Online]. Available: http://dx.doi.org/10.1063/1.1906333

[84] P. J. Kelly, P. S. Henderson, R. D. Arnell, G. A. Roche, and D. Carter, "Reactive pulsed magnetron sputtering process for alumina films," *J. Vac. Sci. Technol. A*, vol. 18, no. 6, pp. 2890–2896, 2000. [Online]. Available: http://dx.doi.org/doi/10.1116/1.1319679

[85] J. Green, "Thin film nucleation, growth, and microstructural evolution: An atomic scale view," in *Handbook of Deposition Technologies for Films and Coatings (Third Edition)*, 3rd ed., P. M. Martin, Ed. Boston, MA: William Andrew Publishing, 2010,

pp. 554 – 620. [Online]. Available: http://www.sciencedirect.com/science/article/pii/B9780815520313000077

[86] L. Martinu, J. E. Klemberg-Sapieha, O. M. Küttel, A. Raveh, and M. R. Wertheimer, "Critical ion energy and ion flux in the growth of films by plasma-enhanced chemical-vapor deposition," *J. Vac. Sci. Technol. A*, vol. 12, no. 4, pp. 1360 – 1364, 1994. [Online]. Available: http://dx.doi.org/10.1116/1.579322

[87] J. E. Klemberg-Sapieha, J. Oberste-Berghaus, L. Martinu, R. Blacker, I. Stevenson, G. Sadkin, D. Morton, S. McEldowney, R. Klinger, P. Martin, N. Court, S. Dligatch, M. Gross, and R. Netterfield, "Mechanical characteristics of optical coatings prepared by various techniques: a comparative study," *Appl. Opt.*, vol. 43, no. 13, pp. 2670 – 2679, 2004. [Online]. Available: http://dx.doi.org/10.1364/AO.43.002670

[88] F. Adibi, I. Petrov, J. Greene, L. Hultman, and J. Sundgren, "Effects of high-flux low-energy (20-100 ev) ion irradiation during deposition on the microstructure and preferred orientation of $Ti_{0.5}Al_{0.5}N$ alloys grown by ultra-high-vacuum reactive magnetron sputtering," *J. Appl. Phys.*, vol. 73, no. 12, pp. 8580 – 9, 1993. [Online]. Available: http://dx.doi.org/10.1063/1.353388

[89] B. Movchan and A. Demchishin, "Study of the structure and properties of thick vacuum condensates of nickel, titanium, tungsten, aluminium oxide and zirconium dioxide," *Phys. Met. Metallogr.*, vol. 28, pp. 83–90, 1969.

[90] J. A. Thornton, "Influence of apparatus geometry and deposition conditions on the structure and topography of thick sputtered coatings," *J. Vac. Sci. Technol*, vol. 11, no. 4, pp. 666–670, 1974. [Online]. Available: http://dx.doi.org/doi/10.1116/1.1312732

[91] R. Messier, A. P. Giri, and R. A. Roy, "Revised structure zone model for thin film physical structure," *J. Vac. Sci. Technol*, vol. 2, no. 2, pp. 500–503, 1984. [Online]. Available: http://dx.doi.org/doi/10.1116/1.572604

[92] P. B. Barna and M. Adamik, "Fundamental structure forming phenomena of polycrystalline films and the structure zone models," *Thin Solid Films*, vol. 317, no. 1-2, pp. 27 – 33, 1998. [Online]. Available: http://www.sciencedirect.com/science/article/pii/S0040609097005038

[93] P. J. Kelly and R. D. Arnell, "Development of a novel structure zone model relating to the closed-field unbalanced magnetron sputtering system," *J. Vac. Sci. Technol. A*, vol. 16, no. 5, pp. 2858 – 2869, 1998. [Online]. Available: http://dx.doi.org/10.1116/1.581432

[94] S. Mahieu, P. Ghekiere, D. Depla, and R. D. Gryse, "Biaxial alignment in sputter deposited thin films," *Thin Solid Films*, vol. 515, no. 4, pp. 1229 – 1249, 2006. [Online]. Available: http://www.sciencedirect.com/science/article/pii/S004060900600784X

[95] A. Anders, "A structure zone diagram including plasma-based deposition and ion etching," *Thin Solid Films*, vol. 518, no. 15, pp. 4087 – 4090, 2010. [Online]. Available: http://dx.doi.org/10.1016/j.tsf.2009.10.145

[96] G. Janssen, "Stress and strain in polycrystalline thin films," *Thin Solid Films*, vol. 515, no. 17, pp. 6654 – 6664, 2007. [Online]. Available: http://www.sciencedirect.com/science/article/pii/S0040609007002933

[97] A. P. Ehiasarian, "Plasma surface engineering research and its practical applications," in *Reactive Sputter Deposition*, R. Wei, Ed. Kerala, India: Research Signpost, 2008, pp. 35–85.

[98] K. Sarakinos, J. Alami, and S. Konstantinidis, "High power pulsed magnetron sputtering: A review on scientific and engineering state of the art," *Surf. Coat. Technol.*, vol. 204, no. 11, pp. 1661 – 1684, 2010. [Online]. Available: http://www.sciencedirect.com/science/article/B6TVV-4XRCRJ2-1/2/ed4a46685d8a634d05243f60e16af5a0

[99] J. Gudmundsson, "Ionized physical vapor deposition (IPVD): magnetron sputtering discharges," UK, 2008, p. 082002. [Online]. Available: http://dx.doi.org/10.1088/1742-6596/100/8/082002

[100] S. Kadlec, "Simulation of neutral particle flow during high power magnetron impulse," *Plasma Processes Polym.*, vol. 4, no. S1, pp. S419–S423, 2007. [Online]. Available: http://dx.doi.org/10.1002/ppap.200731101

[101] J. Gudmundsson, "Ionization mechanism in the high power impulse magnetron sputtering (HiPIMS) discharge," *J. Phys., Conf. Ser.*, p. 082013, 2008. [Online]. Available: http://dx.doi.org/10.1088/1742-6596/100/8/082013

[102] K. Sarakinos, J. Alami, J. Dukwen, J. Woerdenweber, and M. Wuttig, "A semi-quantitative model for the deposition rate in non-reactive high power pulsed magnetron sputtering," *J. Phys. D: Appl. Phys.*, vol. 41, no. 21, p. 215301, 2008. [Online]. Available: http://dx.doi.org/10.1088/0022-3727/41/21/215301

[103] M. Samuelsson, D. Lundin, J. Jensen, M. A. Raadu, J. T. Gudmundsson, and U. Helmersson, "On the film density using high power impulse magnetron sputtering," *Surf. Coat. Technol.*, vol. 205, no. 2, pp. 591 – 596, 2010. [Online]. Available: http://www.sciencedirect.com/science/article/pii/S0257897210005633

[104] J. Vlček and K. Burcalová, "A phenomenological equilibrium model applicable to high-power pulsed magnetron sputtering," *Plasma Sources Sci. Technol.*, vol. 19, no. 6, p. 065010, 2010. [Online]. Available: http://stacks.iop.org/0963-0252/19/i=6/a=065010

[105] M. Lattemann, A. P. Ehiasarian, J. Bohlmark, P. Persson, and U. Helmersson, "Investigation of high power impulse magnetron sputtering pretreated interfaces for adhesion enhancement of hard coatings on steel," *Surf. Coat. Technol.*, vol. 200, no. 22-23, pp. 6495 – 6499, 2006. [Online]. Available: http://dx.doi.org/10.1016/j.surfcoat.2005.11.082

[106] U. Helmersson, J. Bohlmark, M. Lattemann, J. Gudmundsson, A. P. Ehiasarian, Y. Gonzalvo, and N. Brenning, "The ion energy distributions and ion flux composition from a high power impulse magnetron sputtering discharge," *Thin Solid Films*, vol. 515, no. 4, pp. 1522 – 1526, 2006. [Online]. Available: http://dx.doi.org/10.1016/j.tsf.2006.04.051

[107] A. Hecimovic, K. Burcalova, and A. P. Ehiasarian, "Origins of ion energy distribution function (IEDF) in high power impulse magnetron sputtering (HIPIMS) plasma discharge," *J. Phys. D: Appl. Phys.*, vol. 41, no. 9, p. 095203, 2008. [Online]. Available: http://dx.doi.org/10.1088/0022-3727/41/9/095203

[108] J. Vlček, P. Kudláček, K. Burcalová, and J. Musil, "Ion flux characteristics in high-power pulsed magnetron sputtering discharges," *Europhys. Lett.*, vol. 77, no. 4, p. 45002, 2007. [Online]. Available: http://dx.doi.org/10.1209/0295-5075/77/45002

[109] G. Greczynski and L. Hultman, "Time and energy resolved ion mass spectroscopy studies of the ion flux during high power pulsed magnetron sputtering of Cr in Ar and Ar/N_2 atmospheres," *Vacuum*, vol. 84, no. 9, pp. 1159 – 1170, 2010. [Online]. Available: http://dx.doi.org/10.1016/j.vacuum.2010.01.055

[110] A. Hecimovic and A. P. Ehiasarian, "Time evolution of ion energies in hipims of chromium plasma discharge," *J. Phys. D: Appl. Phys.*, vol. 42, no. 13, p. 135209, 2009. [Online]. Available: http://dx.doi.org/10.1088/0022-3727/42/13/135209

[111] A. Hecimovic and A. P. Ehiasarian, "Spatial and temporal evolution of ion energies in high power impulse magnetron sputtering plasma discharge," *J. Appl. Phys.*, vol. 108, no. 6, p. 063301, 2010. [Online]. Available: http://link.aip.org/link/?JAP/108/063301/1

[112] A. P. Ehiasarian, J. Andersson, and A. Anders, "Distance-dependent plasma composition and ion energy in high power impulse magnetron sputtering," *J. Phys. D: Appl. Phys.*, vol. 43, no. 27, p. 275204, 2010. [Online]. Available: http://stacks.iop.org/0022-3727/43/i=27/a=275204

[113] A. Mishra, G. Clarke, P. Kelly, and J. Bradley, "High temporal resolution ion energy distribution functions in hipims discharges," *Plasma Proceses Polym.*, vol. 6, no. S1, pp. 610 – 614, 2009. [Online]. Available: http://dx.doi.org/10.1002/ppap.200931601

[114] D. Christie, "Target material pathways model for high power pulsed magnetron sputtering," *J. Vac. Sci. Technol. A*, vol. 23, no. 2, pp. 330 – 335, 2005. [Online]. Available: http://dx.doi.org/10.1116/1.1865133

[115] C. Vitelaru, D. Lundin, G. D. Stancu, N. Brenning, J. Bretagne, and T. Minea, *Plasma Sources Sci. Technol.*, submitted, 2011.

[116] S. Rossnagel, "Gas density reduction effects in magnetrons," *J. Vac. Sci. Technol. A*, vol. 6, no. 1, pp. 19 – 24, 1988. [Online]. Available: http://dx.doi.org/10.1116/1.574988

[117] D. Horwat and A. Anders, "Compression and strong rarefaction in high power impulse magnetron sputtering discharges," *J. Appl. Phys.*, vol. 108, no. 12, p. 123306, 2010. [Online]. Available: http://link.aip.org/link/?JAP/108/123306/1

[118] N. Hosokawa, T. Tsukada, and H. Kitahara, "Effect of the discharge current and sustained self-sputtering," *Proceeding of the 8th International Vacuum Congress, Le Vide, Cannes*, p. 11 – 14, 1980.

[119] J. Andersson and A. Anders, "Gasless sputtering: opportunities for ultraclean metallization, coatings in space, and propulsion," *Appl. Phys. Lett.*, vol. 92, no. 22, p. 221503, 2008. [Online]. Available: http://dx.doi.org/10.1063/1.2938414

[120] A. Anders, J. Andersson, and A. Ehiasarian, "High power impulse magnetron sputtering: current-voltage-time characteristics indicate the onset of sustained self-sputtering," *J. Appl. Phys.*, vol. 102, no. 11, p. 113303, 2007. [Online]. Available: http://dx.doi.org/10.1063/1.2817812

[121] A. Anders, "Self-sputtering runaway in high power impulse magnetron sputtering: The role of secondary electrons and multiply charged metal ions," *Appl. Phys. Lett.*, vol. 92, no. 20, p. 201501, 2008. [Online]. Available: http://dx.doi.org/10.1063/1.2936307

[122] A. Anders, J. Čapek, M. Hála, and L. Martinu, "The 'recycling trap': a generalized explanation of discharge runaway in high-power impulse magnetron sputtering," *J. Phys. D: Appl. Phys.*, vol. 45, no. 1, p. 012003, 2012. [Online]. Available: http://stacks.iop.org/0022-3727/45/i=1/a=012003

[123] J. Andersson and A. Anders, "Self-sputtering far above the runaway threshold: An extraordinary metal-ion generator," *Phys. Rev. Lett.*, vol. 102, no. 4, p. 045003, 2009.

[124] J. Emmerlich, S. Mráz, R. Snyders, K. Jiang, and J. Schneider, "The physical reason for the apparently low deposition rate during high-power pulsed magnetron sputtering," *Vacuum*, vol. 82, no. 8, pp. 867 – 870, 2008. [Online]. Available: http://dx.doi.org/10.1016/j.vacuum.2007.10.011

[125] A. Anders, "Deposition rates of high power impulse magnetron sputtering: Physics and economics," *J. Vac. Sci. Technol. A*, vol. 28, no. 4, pp. 783–790, 2010. [Online]. Available: http://link.aip.org/link/?JVA/28/783/1

[126] D. Lundin, P. Larsson, E. Wallin, M. Lattemann, N. Brenning, and U. Helmersson, "Cross-field ion transport during high power impulse magnetron sputtering," *Plasma Sources Sci. Technol.*, vol. 17, no. 3, p. 035021, 2008. [Online]. Available: http://dx.doi.org/10.1088/0963-0252/17/3/035021

[127] J. Bohlmark, M. Ostbye, M. Lattemann, H. Ljungcrantz, T. Rosell, and U. Helmersson, "Guiding the deposition flux in an ionized magnetron discharge," *Thin Solid Films*, vol. 515, no. 4, pp. 1928 – 1931, 2006. [Online]. Available: http://dx.doi.org/10.1016/j.tsf.2006.07.183

[128] N. Brenning, I. Axnäs, M. Raadu, D. Lundin, and U. Helmerson, "A bulk plasma model for dc and HiPIMS magnetrons," *Plasma Sources Sci. Technol.*, vol. 17, no. 4, p. 045009, 2008. [Online]. Available: http://dx.doi.org/10.1088/0963-0252/17/4/045009

[129] E. Wallin and U. Helmersson, "Hysteresis-free reactive high power impulse magnetron sputtering," *Thin Solid Films*, vol. 516, no. 18, pp. 6398 – 6401, 2008.

[130] R. Chistyakov and B. Abraham, "Advanced pulsed DC technology for material processing applications, Part 2. plasma generator for arbitrary voltage pulse shape," *Society of Vacuum Coaters, Summer Bulletin*, pp. (32–36), 2009.

[131] V. Kouznetsov, "Method and apparatus for magnetically enhanced sputtering," U.S. Patent, US 6296742 B1, 2001, accessed: 01/07/2011.

[132] V. Kouznetsov, "Förfarande och anordning för att alstra plasma," Swedish Patent, SE 525231 C2, 2005, accessed: 01/07/2011.

[133] R. Chistyakov, "High-Power Pulsed Magnetron Sputtering," U.S. Patent, US 7147759, 2006, accessed: 01/07/2011.

[134] R. Chistyakov, "Methods and Apparatus for Generating Strongly Ionized Plasmas with Ionizational Instabilities," U.S. Patent, US 7095179, 2006, accessed: 01/08/2011.

[135] J. Lin, J. Moore, W. Sproul, B. Mishra, J. Rees, Z. Wu, R. Chistyakov, and B. Abraham, "Ion energy and mass distributions of the plasma during modulated pulse power magnetron sputtering," *Surf. Coat. Technol.*, vol. 203, no. 24, pp. 3676 – 3685, 2009. [Online]. Available: http://dx.doi.org/10.1016/j.surfcoat.2009.05.048

[136] C. M. Ferreira, J. Loureiro, and A. Ricard, "Populations in the metastable and the resonance levels of argon and stepwise ionization effects in a low-pressure argon positive column," *J. Appl. Phys.*, vol. 57, no. 1, pp. 82 –90, 1985.

[137] V. M. Donnelly, "Plasma electron temperatures and electron energy distributions measured by trace rare gases optical emission spectroscopy," *J. Phys. D: Appl. Phys.*, vol. 37, no. 19, p. R217, 2004. [Online]. Available: http://stacks.iop.org/0022-3727/37/i=19/a=R01

[138] X. M. Zhu and Y. K. Pu, "Using OES to determine electron temperature and density in low-pressure nitrogen and argon plasmas," *Plasma Sources Sci. Technol.*, vol. 17, no. 2, p. 024002, 2008. [Online]. Available: http://stacks.iop.org/0963-0252/17/i=2/a=024002

[139] N. Masoud, K. Martus, M. Figus, and K. Becker, "Rotational and vibrational temperature measurements in a high-pressure cylindrical dielectric barrier discharge (C-DBD)," *Contrib. Plasma Phys.*, vol. 45, no. 1, pp. 32 – 9, 2005. [Online]. Available: http://dx.doi.org/10.1002/ctpp.200510004

[140] A. Berchtikou, J. Lavoie, V. Poenariu, B. Saoudi, R. Kashyap, and M. R. Wertheimer, "Thermometry in noble gas dielectric barrier discharges at atmospheric pressure using optical emission spectroscopy," *IEEE Trans. Dielectr. Electr. Insul.*, vol. 18, no. 1, pp. 24 –33, 2011.

[141] J. A. Hopwood, "Plasma physics," in *Ionized Physical Vapor Deposition*, J. A. Hopwood, Ed. San Diego, CA: Academic Press, 2000, pp. 181 – 207.

[142] J. W. Coburn and M. Chen, "Optical emission spectroscopy of reactive plasmas: A method for correlating emission intensities to reactive particle density," *J. Appl. Phys.*, vol. 51, no. 6, pp. 3134–3136, 1980. [Online]. Available: http://dx.doi.org/10.1063/1.328060

[143] J. E. Greene, "Optical spectroscopy for diagnostics and process control during glow discharge etching and sputter deposition," *J. Vac. Sci. Technol. A*, vol. 15, no. 5, pp. 1718–1729, 1978. [Online]. Available: http://dx.doi.org/doi/10.1116/1.569834

[144] R. A. Gottscho and T. A. Miller, "Optical techniques in plasma diagnostics," *Pure Appl. Chem.*, vol. 56, no. 2, pp. 189–208, 1984.

[145] S. Schiller, U. Heisig, C. Korndoerfer, G. Beister, J. Reschke, K. Steinfelder, and J. Struempfel, "Reactive dc high-rate sputtering as production technology," *Surf. Coat. Technol.*, vol. 33, pp. 405 – 423, 1987. [Online]. Available: http://dx.doi.org/10.1016/0257-8972(87)90206-4

[146] R. Bracewell, *The Fourier Transform and Its Applications*, 1st ed. New York, NY: McGraw-Hill, 1965.

[147] "User manual: Princeton Instruments Acton PI-MAX/PI-MAX2 System," consulted: 01/02/2011.

[148] J. Bradley and T. Welzel, "Process diagnostics," in *Reactive Sputter Deposition*, ser. Springer Series in Materials Science, D. Depla and S. Mahieu, Eds. Heidelberg, Germany: Springer, 2008, vol. 109, pp. 43–60.

[149] A. A. Voevodin, J. G. Jones, J. S. Zabinski, and L. Hultman, "Plasma characterization during laser ablation of graphite in nitrogen for the growth of fullerene-like CN_x films," *J. Appl. Phys.*, vol. 92, no. 2, pp. 724 – 724, 2002. [Online]. Available: http://dx.doi.org/10.1063/1.1481972

[150] I. Radu, R. Bartnikas, and M. R. Wertheimer, "Dielectric barrier discharges in atmospheric pressure helium in cylinder-plane geometry: experiments and model," *J. Phys. D: Appl. Phys.*, vol. 37, no. 3, p. 449, 2004. [Online]. Available: http://stacks.iop.org/0022-3727/37/i=3/a=024

[151] R. Kumar, B. M. Novac, I. R. Smith, and C. Greenwood, "Ultrahigh-speed camera study of a plasma source for a repetitive and miniature POS," *IEEE Trans. Plasma Sci.*, vol. 36, no. 4, pp. 1266 – 1267, 2008. [Online]. Available: http://dx.doi.org/10.1109/TPS.2008.924464

[152] A. A. Lissovski and A. B. Treshchalov, "VUV-VIS imaging of high-pressure pulsed volume discharge in argon," *IEEE Trans. Plasma Sci.*, vol. 36, no. 4, pp. 958 – 9, 2008. [Online]. Available: http://dx.doi.org/10.1109/TPS.2008.925541

[153] S. A. Starostin, M. A. M. ElSabbagh, E. A., H. de Vries, M. Creatore, and M. C. M. van de Sanden, "Formation and expansion phases of an atmospheric pressure glow discharge in a PECVD reactor via fast ICCD imaging," *IEEE Trans. Plasma Sci.*, vol. 36, no. 4, pp. 968 – 969, 2008. [Online]. Available: http://dx.doi.org/10.1109/TPS.2008.924622

[154] J. Gunnars and U. Wiklund, "Determination of growth-induced strain and thermo-elastic properties of coatings by curvature measurements," *Mater. Sci. Eng. A*, vol. 336, no. 1-2, pp. 7 – 21, 2002. [Online]. Available: http://www.sciencedirect.com/science/article/pii/S0921509301019797

[155] W. Oliver and G. Pharr, "Improved technique for determining hardness and elastic modulus using load and displacement sensing indentation experiments," *J. Mater. Res.*, vol. 7, no. 6, pp. 1564 – 1580, 1992.

[156] Y. Golovin, M. Isaenkova, O. Krymskaya, V. Vasyukov, R. Stolyarov, A. Shuklinov, and L. Polyakov, "The size effects in hardness of polycrystalline niobium," *Tech. Phys. Lett.*, vol. 36, pp. 369–370, 2010. [Online]. Available: http://dx.doi.org/10.1134/S1063785010040231

[157] G. E. Jellison, "Data analysis for spectroscopic ellipsometry," in *Handbook of ellipsometry*, 1st ed., H. Tompkins and E. A. Irene, Eds. New York, NY: William Andrew Publishing, 1994, pp. 237 – 296.

[158] J. Alami, K. Sarakinos, F. Uslu, and M. Wuttig, "On the relationship between the peak target current and the morphology of chromium nitride thin films deposited by reactive high power pulsed magnetron sputtering," *J. Phys. D: Appl. Phys.*, vol. 42, no. 1, p. 015304 (7 pp.), 2009. [Online]. Available: http://dx.doi.org/10.1088/0022-3727/42/1/015304

[159] J. Alami, P. Persson, D. Music, J. Gudmundsson, J. Bohlmark, and U. Helmersson, "Ion-assisted physical vapor deposition for enhanced film properties on nonflat surfaces," *J. Vac. Sci. Technol. A*, vol. 23, no. 2, pp. 278 – 80, 2005. [Online]. Available: http://dx.doi.org/10.1116/1.1861049

[160] E. Oks and A. Anders, "Evolution of the plasma composition of a high power impulse magnetron sputtering system studied with a time-of-flight spectrometer," *J. Appl. Phys.*, vol. 105, no. 9, pp. 093 304 –, 2009. [Online]. Available: http://dx.doi.org/10.1063/1.3125443

[161] P. Vašina, M. Meško, J. Imbert, M. Ganciu, C. Boisse-Laporte, L. De Poucques, M. Touzeau, D. Pagnon, and J. Bretagne, "Experimental study of a pre-ionized high power pulsed magnetron discharge," *Plasma Sources Sci. Technol.*, vol. 16, no. 3, pp. 501 – 510, 2007. [Online]. Available: http://dx.doi.org/10.1088/0963-0252/16/3/009

[162] M. Hala, N. Viau, O. Zabeida, J. E. Klemberg-Sapieha, and L. Martinu, "Dynamics of reactive high-power impulse magnetron sputtering discharge studied by time- and space-resolved optical emission spectroscopy and fast imaging," *J. Appl. Phys.*, vol. 107, no. 4, p. 043305, 2010. [Online]. Available: http://link.aip.org/link/?JAP/107/043305/1

[163] S. Larouche and L. Martinu, "OpenFilters: open-source software for the design, optimization, and synthesis of optical filters," *Appl. Opt.*, vol. 47, no. 13, pp. C219–C230, 2008. [Online]. Available: http://ao.osa.org/abstract.cfm?URI=ao-47-13-C219

[164] J. Vlček, A. Pajdarová, P. Belský, J. Lukáš, P. Kudláček, and J. Musil, "Characterization of high-power pulsed dc magnetron discharges for ionized high-rate sputtering of copper films," *Society of Vacuum Coaters 48th Annual Technical Conference Proceedings*, p. 465, 2005.

[165] L. de Poucques, J.-C. Imbert, C. Boisse-Laporte, J. Bretagne, M. Ganciu, L. Teule-Gay, P. Vasina, and M. Touzeau, "Analysis of the transport of ionized titanium atoms in a highly ionized sputter deposition process," *Plasma Processes Polym.*, vol. 4, no. SUPPL.1, pp. S424 – S429, 2007. [Online]. Available: http://dx.doi.org/10.1002/ppap.200731102

[166] P. Vasina, M. Mesko, L. de Poucques, J. Bretagne, C. Boisse-Laporte, and M. Touzeau, "Study of a fast high power pulsed magnetron discharge: role of plasma deconfinement on the charged particle transport," *Plasma Sources Sci. Technol.*, vol. 17, no. 3, p. 035007, 2008. [Online]. Available: http://dx.doi.org/10.1088/0963-0252/17/3/035007

[167] D. Benzeggouta, M. Hugon, and J. Bretagne, "Study of a hppms discharge in Ar/O_2 mixture: Ii. plasma optical emission and deposited RuO_x film properties," *Plasma Sources Sci. Technol.*, vol. 18, no. 4, p. 045026, 2009. [Online]. Available: http://dx.doi.org/10.1088/0963-0252/18/4/045026

[168] J. Bohlmark, U. Helmersson, M. VanZeeland, I. Axnäs, J. Alami, and N. Brenning, "Measurement of the magnetic field change in a pulsed high current magnetron discharge," *Plasma Sources Sci. Technol.*, vol. 13, no. 4, pp. 654 – 661, 2004. [Online]. Available: http://dx.doi.org/10.1088/0963-0252/13/4/014

[169] D. Benzeggouta, M. Hugon, J. Bretagne, and M. Ganciu, "Study of a hppms discharge in ar/o2 mixture: I. discharge characteristics with ru cathode," *Plasma*

Sources Sci. Technol., vol. 18, no. 4, pp. 045 025 –, 2009. [Online]. Available: http://dx.doi.org/10.1088/0963-0252/18/4/045025

[170] S. Konstantinidis, J. Dauchot, M. Ganciu, and M. Hecq, "Transport of ionized metal atoms in high-power pulsed magnetron discharges assisted by inductively coupled plasma," *Appl. Phys. Lett.*, vol. 88, no. 2, p. 21501, 2006. [Online]. Available: http://dx.doi.org/10.1063/1.2162671

[171] D. Lundin, N. Brenning, D. Jadernas, P. Larsson, E. Wallin, M. Lattemann, M. Raadu, and U. Helmersson, "Transition between the discharge regimes of high power impulse magnetron sputtering and conventional direct current magnetron sputtering," *Plasma Sources Sci. Technol.*, vol. 18, no. 4, p. 045008 (6 pp.), 2009. [Online]. Available: http://dx.doi.org/10.1088/0963-0252/18/4/045008

[172] J. Vlček, B. Zustin, J. Rezek, K. Burcalová, and J. Tesař, "Pulsed magnetron sputtering of metallic films using a hot target," *Society of Vacuum Coaters 52nd Annual Technical Conferenece Proceedings (Santa Clara, CA)*, pp. (219–223), 2009.

[173] M. Hala, N. Viau, O. Zabeida, J. E. Klemberg-Sapieha, and L. Martinu, "Time- and space-resolved optical emission spectroscopy study of reactive HIPIMS discharges," *Society of Vacuum Coaters 52nd Annual Technical Conferenece Proceedings (Santa Clara, CA)*, pp. 228 – 233, 2009.

[174] A. Hecimovic and A. P. Ehiasarian, "Spatial and temporal evolution of ions energies in hipims plasma discharge," *Society of Vacuum Coaters 52nd Annual Technical Conferenece Proceedings (Santa Clara, CA)*, pp. 240–247, 2009.

[175] M. Hála, O. Zabeida, B. Baloukas, J. E. Klemberg-Sapieha, and L. Martinu, "Time- and species-resolved plasma imaging as a new diagnostic approach for HiPIMS discharge characterization," *IEEE Trans. Plasma Sci.*, vol. 38, no. 11, pp. 3035 –3039, Nov. 2010.

[176] B. Liebig, N. S. J. Braithwaite, P. Kelly, and J. Bradley, "Spatial and temporal investigation of high power pulsed magnetron discharges by optical 2D-imaging," *Thin Solid Films*, vol. 519, no. 5, pp. 1699 – 1704, 2010. [Online]. Available: http://www.sciencedirect.com/science/article/B6TW0-50F8BPX-1/2/fb57e41b1db6c8abedb2627c19502530

[177] J. Čapek, M. Hála, O. Zabeida, J. E. Klemberg-Sapieha, and L. Martinu, "Steady state discharge optimization in high-power impulse magnetron sputtering through the control of the magnetic field," *J. Appl. Phys.*, vol. 111, no. 2, p. 023301, 2012. [Online]. Available: http://link.aip.org/link/?JAP/111/023301/1

[178] "SVS Vacuum Coating Technologies GmbH," accessed: 01/07/2011. [Online]. Available: http://www.svs-vct.com

[179] "Richter Precision Inc." accessed: 01/07/2011. [Online]. Available: http://www.richterprecision.com

[180] "Acree Technologies Inc," accessed: 01/07/2011. [Online]. Available: http://www.acreetech.com

[181] "R.L. Kurucz and B. Bell, 1995 atomic line data, Kurucz CD-ROM, No. 23, Cambrige, MA," accessed: 01/02/2011. [Online]. Available: {Harvard-SmithsonianCenterforAstrophysics},{http://cfa-www.harvard.edu/amdata/ampdata/kurucz23/sekur.html}

[182] "National Institute of Standards," accessed: 01/02/2011. [Online]. Available: http://www.nist.gov/pml/data/asd.cfm

[183] A. Anders, "Physics of arcing, and implications to sputter deposition," *Thin Solid Films*, vol. 502, pp. 22–28, 2006.

[184] M. Hála, J. Čapek, O. Zabeida, J. E. Klemberg-Sapieha, and L. Martinu, "Hysteresis-free deposition of niobium oxide films by HiPIMS using different pulse management strategies," *J. Phys. D: Appl. Phys.*, accepted, 2011.

[185] L. Meng, A. N. Cloud, S. Jung, and D. N. Ruzic, "Study of plasma dynamics in a modulated pulsed power magnetron discharge using a time-resolved langmuir probe," *J. Vac. Sci. Technol. A*, vol. 29, no. 1, p. 011024, 2011. [Online]. Available: http://link.aip.org/link/?JVA/29/011024/1

[186] D. Horwat and A. Anders, "Ion acceleration and cooling in gasless self-sputtering," *Appl. Phys. Lett.*, vol. 97, no. 22, p. 221501, 2010. [Online]. Available: http://link.aip.org/link/?APL/97/221501/1

[187] C. Steinbrüchel, "A simple formula for low-energy sputtering yields," *Applied Physics A: Materials Science & Processing*, vol. 36, pp. 37–42, 1985. [Online]. Available: http://dx.doi.org/10.1007/BF00616458

[188] J. Lin, J. Moore, W. Sproul, B. Mishra, and Z. Wu, "Modulated pulse power sputtered chromium coatings," *Thin Solid Films*, vol. 518, no. 5, pp. 1566 – 1570, 2009, proceedings of the 36th International Conference on Metallurgical Coatings and Thin Films. [Online]. Available: http://www.sciencedirect.com/science/article/B6TW0-4XCYJ9M-5/2/aca74a958c6a0c9e188af934f6ea65d6

[189] Y. Purandare, A. P. Ehiasarian, and P. Hovsepian, "Deposition of nanoscale multilayer CrN/NbN physical vapor deposition coatings by high power impulse magnetron sputtering," *J. Vac. Sci. Technol. A*, vol. 26, no. 2, pp. 288 – 296, 2008. [Online]. Available: http://dx.doi.org/10.1116/1.2839855

[190] J. Alami, K. Sarakinos, F. Uslu, C. Klever, J. Dukwen, and M. Wuttig, "On the phase formation of titanium oxide films grown by reactive high power pulsed magnetron sputtering," *J. Phys. D: Appl. Phys.*, vol. 42, no. 11, p. 115204, 2009. [Online]. Available: http://dx.doi.org/10.1088/0022-3727/42/11/115204

[191] J. Lin, J. Moore, W. Sproul, B. Mishra, Z. Wu, and J. Wang, "The structure and properties of chromium nitride coatings deposited using dc, pulsed dc and modulated pulse power magnetron sputtering," *Surf. Coat. Technol.*, vol. 204, no. 14, pp. 2230 – 2239, 2010. [Online]. Available: http://www.sciencedirect.com/science/article/pii/S025789720901038X

[192] M. Audronis and V. Bellido-Gonzalez, "Hysteresis behaviour of reactive high power impulse magnetron sputtering," *Thin Solid Films*, vol. 518, no. 8, pp. 1962 – 1965, 2010. [Online]. Available: http://www.sciencedirect.com/science/article/pii/S0040609009019932

[193] T. Kubart, M. Aiempanakit, J. Andersson, T. Nyberg, S. Berg, and U. Helmersson, "Studies of hysteresis effect in reactive hipims deposition of oxides," *Surf. Coat. Technol.*, vol. 205, no. Supplement 2, pp. S303 – S306, 2011, PSE

2010 Special Issue, Proceedings of the 12th International Conference on Plasma Surface Engineering, Garmisch-Partenkirchen, Germany. [Online]. Available: http://www.sciencedirect.com/science/article/pii/S0257897211000314

[194] M. Aiempanakit, T. Kubart, P. Larsson, K. Sarakinos, J. Jensen, and U. Helmersson, "Hysteresis and process stability in reactive high power impulse magnetron sputtering of metal oxides," *Thin Solid Films*, vol. 519, no. 22, pp. 7779 – 7784, 2011. [Online]. Available: http://dx.doi.org/10.1016/j.tsf.2011.06.021

[195] A. Brenner and S. Senderoff, "Calculation of stress in electrodeposits from curvature of plated strip," *J. Research US Bureau of Standards*, vol. 42, no. 2, pp. 105 – 123, 1949.

[196] D. Depla, S. Heirwegh, S. Mahieu, J. Haemers, and R. De Gryse, "Understanding the discharge voltage behavior during reactive sputtering of oxides," *J. Appl. Phys.*, vol. 101, no. 1, p. 13301, 2007. [Online]. Available: http://dx.doi.org/10.1063/1.2404583

[197] M. Audronis, V. Bellido-Gonzalez, and B. Daniel, "Control of reactive high power impulse magnetron sputtering processes," *Surf. Coat. Technol.*, vol. 204, no. 14, pp. 2159 – 2164, 2010. [Online]. Available: http://www.sciencedirect.com/science/article/pii/S0257897209009906

[198] M. Hála, J. Čapek, O. Zabeida, J. E. Klemberg-Sapieha, and L. Martinu, "Pulse management in high power pulsed magnetron sputtering of niobium," *Surf. Coat. Technol.*, submitted, 2011.

[199] M. Seah and T. Nunney, "Sputtering yields of compounds using argon ions," *J. Phys. D: Appl. Phys.*, vol. 43, no. 25, p. 253001 (13 pp.), 2010. [Online]. Available: http://dx.doi.org/10.1088/0022-3727/43/25/253001

[200] T. Kubart, T. Nyberg, and S. Berg, "Modelling of low energy ion sputtering from oxide surfaces," *J. Phys. D: Appl. Phys.*, vol. 43, no. 20, p. 205204 (6pp.), 2010. [Online]. Available: http://dx.doi.org/10.1088/0022-3727/43/20/205204

[201] E. Taglauer and W. Heiland, "Mass and energy dependence of the equilibrium surface composition of sputtered tantalum oxide," *Appl. Phys. Lett.*, vol. 33, no. 11, pp. 950–952, 1978. [Online]. Available: http://link.aip.org/link/?APL/33/950/1

[202] C. C. Lee, C. L. Tien, and J. C. Hsu, "Internal stress and optical properties of Nb_2O_5 thin films deposited by ion-beam sputtering," *Appl. Opt.*, vol. 41, no. 10, pp. 2043–2047, 2002. [Online]. Available: http://ao.osa.org/abstract.cfm?URI=ao-41-10-2043

[203] E. Çetinörgü, B. Baloukas, O. Zabeida, J. E. Klemberg-Sapieha, and L. Martinu, "Mechanical and thermoelastic characteristics of optical thin films deposited by dual ion beam sputtering," *Appl. Opt.*, vol. 48, no. 23, pp. 4536–4544, 2009. [Online]. Available: http://ao.osa.org/abstract.cfm?URI=ao-48-23-4536

[204] C. Davis, "A simple model for the formation of compressive stress in thin films by ion bombardment," *Thin Solid Films*, vol. 226, no. 1, pp. 30 – 34, 1993. [Online]. Available: http://www.sciencedirect.com/science/article/B6TW0-46NYF47-217/2/ddcb3d718d84ca8dd08194de977ae4f7

[205] A. Hallil, O. Zabeida, M. R. Wertheimer, and L. Martinu, "Mass-resolved ion energy distributions in continuous dual mode microwave/radio frequency plasmas in argon and nitrogen," *J. Vac. Sci. Technol. A*, vol. 18, no. 3, pp. 882 – 90, 2000. [Online]. Available: http://dx.doi.org/10.1116/1.582271

[206] P. Jedrzejowski, J. Cizek, A. Amassian, J. E. Klemberg-Sapieha, J. Vlcek, and L. Martinu, "Mechanical and optical properties of hard SiCN coatings prepared by PECVD," vol. 447-448, Switzerland, 2004, pp. 201 – 207. [Online]. Available: http://dx.doi.org/10.1016/S0040-6090(03)01057-5

[207] J. E. Klemberg-Sapieha, P. Jedrzejowski, and L. Martinu, "Mechanical and optical characteristics of superhard nanocomposite TiN/a-Si_3N_4 and TiCN/a-SiCN coatings produced by PECVD," *J. Superhard Mater.*, vol. 29, pp. 147–152, 2007. [Online]. Available: http://dx.doi.org/10.3103/S1063457607030069

[208] E. Bousser, M. Benkahoul, L. Martinu, and J. E. Klemberg-Sapieha, "Effect of microstructure on the erosion resistance of Cr-Si-N coatings," *Surf. Coat. Technol.*, vol. 203, no. 5-7, pp. 776 – 780, 2008. [Online]. Available: http://dx.doi.org/10.1016/j.surfcoat.2008.08.012

[209] S. Hassani, J. E. Klemberg-Sapieha, M. Bielawski, W. Beres, L. Martinu, and M. Balazinski, "Design of hard coating architecture for the optimization of erosion resistance," *Wear*, vol. 265, no. 5-6, pp. 879 – 887, 2008. [Online]. Available: http://dx.doi.org/10.1016/j.wear.2008.01.021

[210] M. Benkahoul, P. Robin, L. Martinu, and J. E. Klemberg-Sapieha, "Tribological properties of duplex Cr-Si-N coatings on SS410 steel," *Surf. Coat. Technol.*, vol. 203, no. 8, pp. 934 – 940, 2009. [Online]. Available: http://dx.doi.org/10.1016/j.surfcoat.2008.07.036

[211] S. Guruvenket, D. Li, J. E. Klemberg-Sapieha, L. Martinu, and J. Szpunar, "Mechanical and tribological properties of duplex treated TiN, nc-TiN/a-SiNx and nc-TiCN/a-SiCN coatings deposited on 410 low alloy stainless steel," *Surf. Coat. Technol.*, vol. 203, no. 19, pp. 2905 – 11, 2009. [Online]. Available: http://dx.doi.org/10.1016/j.surfcoat.2009.03.009

[212] M. Azzi, M. Benkahoul, J. A. Szpunar, J. E. Klemberg-Sapieha, and L. Martinu, "Tribological properties of CrSiN-coated 301 stainless steel under wet and dry conditions," *Wear*, vol. 267, no. 5-8, pp. 882 – 889, 2009. [Online]. Available: http://dx.doi.org/10.1016/j.wear.2009.01.027

[213] P. Jedrzejowski, J. E. Klemberg-Sapieha, and L. Martinu, "Quaternary hard nanocomposite TiC_xN_y/SiCN coatings prepared by plasma enhanced chemical vapor deposition," *Thin Solid Films*, vol. 466, no. 1-2, pp. 189 – 196, 2004. [Online]. Available: http://dx.doi.org/10.1016/j.tsf.2004.03.043

[214] J. Houska, J. E. Klemberg-Sapieha, and L. Martinu, "Atomistic simulations of the characteristics of TiSiN nanocomposites of various compositions," *Surf. Coat. Technol.*, vol. 203, no. 22, pp. 3348 – 3355, 2009. [Online]. Available: http://dx.doi.org/10.1016/j.surfcoat.2009.04.021

APPENDIX A Steady state HiPIMS discharge optimization through the control of the magnetic field

Steady state HiPIMS discharge optimization through the control of the magnetic field

Authors: J. Čapek, M. Hála, O. Zabeida, J.E. Klemberg-Sapieha, L. Martinu

Article published: Journal of Applied Physics, vol. 111, p. 023301, Jan. 2012.

Abstract:

High power impulse magnetron sputtering (HiPIMS) is a pulsed DC sputtering technique utilizing high power density peaks of typically more than $100\,\mathrm{W\,cm^{-2}}$. The discharge operation at such elevated powers can be hindered by the magnetron configuration (size and magnetic field) and/or the target conditions (e.g. material and thickness). In addition, target erosion is an important issue significantly affecting process reproducibility. In the present work, we propose a simple approach for the stabilization of the HiPIMS discharge by controlling the target magnetic field using paramagnetic spacers with different thicknesses in between the magnetron surface and the target. We demonstrate a straightforward discharge optimization, while using various target materials, such as Nb, Ta, Cr, Al, Ti, Si, and even C (graphite). The existence of a steady state high density discharge above the graphite target and the other targets in general is discussed in terms of the magnetic field configuration and the gas rarefaction effect.

A.1 Introduction

High power impulse magnetron sputtering (HiPIMS) is a pulsed DC sputtering technique utilizing high power density peaks of typically more than $100\,\mathrm{W\,cm^{-2}}$ at a sufficiently low time-averaged power density in order to avoid target overheating. This results in a high density discharge and, consequently, in a high degree of ionization of the sputtered material. This makes HiPIMS a very attractive deposition technique for enhancing and tailoring coating properties.[1, 2]

Recently, Anders *at al.* described[3] that specific conditions have to be met in order to reach a high density (HD) discharge. Probably, the most important criterion is the sufficiently high pulse voltage value, U_c. If U_c is lower than a certain threshold, U_th, a low density (LD) discharge is observed [see Fig. A.1 (dotted line)], such as in DC magnetron sputtering (DCMS).

At time $t = 0\,\mu\mathrm{s}$, the target is surrounded only by Ar atoms at a preset pressure, thus the initial current density growth can be mostly attributed to Ar ions impacting on the target. However, the sputtered atoms transfer their momentum through collisions to the surrounding gas. This results in heating and consequently in rarefaction of the Ar atoms.[4] It is to be noted that a similar effect can also be caused by an elevated temperature of the target surface.[5] Since Ar ions are the principle particles generating secondary electrons (SE) in the LD plasma (due to their high potential energy[3]), the discharge current density starts to decrease at some point to a steady state value reached after several tens of microseconds. The resulting current density is mainly determined by the reduced concentration of Ar atoms close to the target surface.[6]

For U_c higher than U_th [Fig. A.1 (solid line)] the number and the energy of SE are sufficient to ionize an important fraction of the sputtered atoms. The target ions can then be attracted back to the target by the large potential fall across the plasma (pre)sheath. Although the rarefaction of the working gas is even more pronounced at higher powers, the back-attracted excited target ions, and especially the doubly ionized target atoms, are able to partially substitute the role of Ar ions in the generation of the SE.[7, 8] The latter process is crucial for sustaining the HD discharge. As a consequence, the HD discharge

reaches a steady state, which is characterized by a substantially higher value of the current density compared to the LD case.

In some specific conditions, the ions of the sputtered material are able to take over the role of the Ar ions completely, thus the background Ar gas can be omitted without loosing the HD discharge regime.[9, 10, 11] The condition for such a mode, termed "sustained self sputtering", or "gasless sputtering", was originally introduced by Hosokawa[12] *at al.* as

$$\Pi \equiv \alpha\,\beta\,\gamma_{\rm ss} = 1, \tag{A.1}$$

where, α is the probability that a sputtered atom becomes ionized, β is the probability that the newly formed ion returns to the target, and, γ_{ss} is the self sputtering yield. Since $\alpha < 1$ and $\beta < 1$, it is necessary that $\gamma_{\rm ss} > 1$. One of the advantages of such a HD discharge is the deposition of dense coatings without any contamination by the working gas.

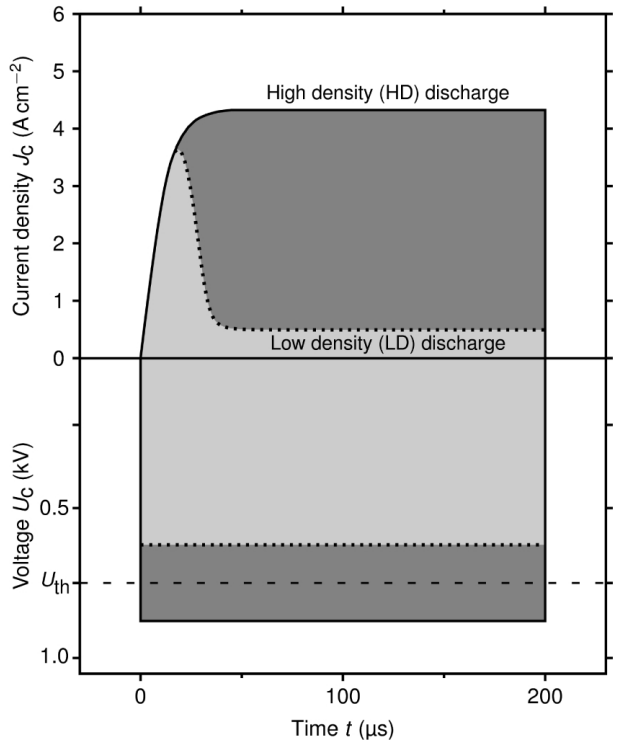

Figure A.1 Schematic waveforms of the pulse voltage $U_{\rm c}$ and the target current density, $J_{\rm c}$, for a case that $U_{\rm c} < U_{\rm th}$ (dotted line) and $U_{\rm c} > U_{\rm th}$ (solid line), where $U_{\rm th}$ is a threshold for the high density plasma (dashed line).

However, an additional source of metal ions (e.g., pulsed cathodic arc[11]) is needed to initiate the discharge at every high voltage pulse.

Despite of the effort that has been devoted to the understanding of the HiPIMS processes in the last years, its practical implementation may be complicated due to several types of problems: (i) HiPIMS power supply overloading, (ii) excessive arcing, and (iii) strong effect of target erosion. In the present work, we discuss in more detail on the above issues, and we propose a straightforward solution based on the magnetron's magnetic field control. In addition, we demonstrate the significance of the gas rarefaction effect on the HiPIMS discharges by providing the experimental evidence for various target materials, including those with a low sputtering yield such as carbon (graphite).

A.2 Experimental setup

All experiments were performed in a vacuum deposition system illustrated in Fig. A.2 using a grounded stainless steel chamber, in a pure Ar atmosphere, and a pressure, $p = 1\,\mathrm{Pa}$. An unbalanced magnetron (5 cm in diameter unless otherwise specified) was powered by a HÜTTINGER Electronics HMP2/1 power supply (2 kW maximum average power) working in the frequency range from 2 to 500 Hz, at a voltage pulse duration between 1 and 200 µs and with a maximum voltage and peak current of 2 kV and 1000 A, respectively. A repetition

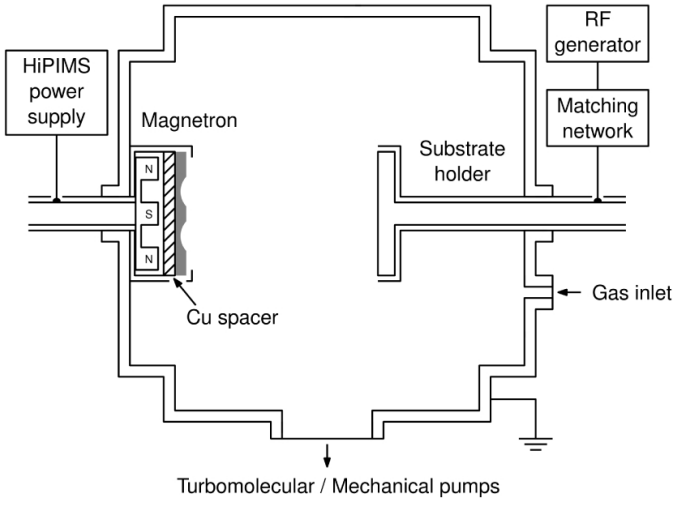

Figure A.2 Schematic diagram of the experimental setup.

frequency $f_r = 50\,\text{Hz}$ and a pulse duration $t_p = 200\,\mu\text{s}$ were used in order to be able to reach a steady state HD discharge without overheating the magnetron. We intentionally used such a small-size magnetron since it allowed us to achieve very high power densities during the pulses at lower total (average) powers.

The magnetron's magnetic field is shown in Fig. A.3. This measurement of the field distribution was performed by a home-made mapping system where the position of a LakeShore HMNT-4E04-VR Hall probe was controlled by a x–y movable stage. More details concerning the measurement and properties of the magnetic field are presented in Appendix AA. The substrate holder (surface area $\sim 50\,\text{cm}^2$; target-to-substrate distance $d = 10\,\text{cm}$) was biased at a low power ($\sim 10\,\text{W}$) to obtain a negative bias voltage of $-20\,\text{V}$ by an additional RF power supply in order to facilitate the discharge ignition.

In this work, different target materials have been tested; this includes: Ta, Nb, Cr, Ti, Al (6.35 mm thick), n-doped Si (total thickness 3.18 mm Si + 3.18 mm copper bonding), and C–graphite (3.18 mm thick). Copper spacers placed in between the target and the magnetron head were used to modify the magnetic field strength. The thickness, d_s, of the spacers was

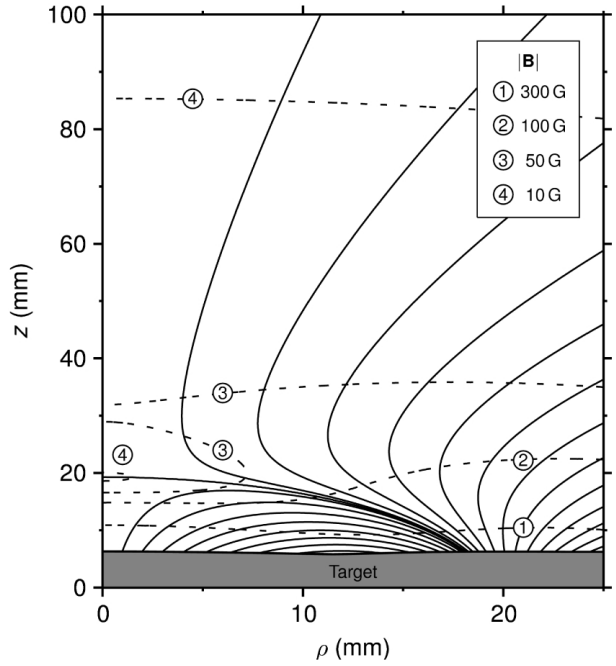

Figure A.3 Magnetic field lines (solid lines) and contours of the magnetic field, $|\mathbf{B}|$, (dashed lines) corresponding to the magnetic field of the 50 mm diameter unbalanced magnetron used in this work.

in the range of 0 to 5 mm. The target erosion was measured as a ratio between the depth of the race track and the thickness of a new target.

Waveforms of the cathode voltage and discharge current were measured by a Tektronix P6015A voltage probe and a Pearson 301X current monitor, respectively, and recorded by a Tektronix TDS2014B digital oscilloscope.

Optical emission from the discharge was collected by an optical fibre probe mounted within the reactor overlooking the discharge at a distance of $d \approx 1$ cm parallel with the target surface. The time-averaged optical spectra were analyzed by Ocean Optics USB2000 spectrometer.

A.3 Common issues in the HiPIMS process implementation

In this section we discuss various general problems related to the implementation of a HiPIMS discharge in deposition systems; this includes HiPIMS power supply overloading, excessive arcing, and the strong effect of target erosion. Possible solutions are also outlined.

A.3.1 HiPIMS power supply overloading

The steady state HD discharge (depicted in Fig. A.1) can be reached only in the case when the HiPIMS power supply can sustain a constant voltage ($U_c > U_{th}$) during the whole pulse. If the resulting HD discharge current value is too high (due to a large target surface, a strong magnetron's magnetic field or a high emission of SE from the target) the steady state cannot be reached. Instead, a peak-shaped current waveform is observed (as exemplified Fig. A.4).

Here, high current values at the beginning of the pulse significantly reduce the charge stored in the pulse unit capacitors of the HiPIMS power supply. As a consequence, the U_c starts to decrease at $t_1 = 30\,\mu s$ (as indicated by the time line no. 1 in Fig. A.4), followed by the U_c maximum, and consequently by the drop of the HD current. Moreover, beyond $t_2 = 130\,\mu s$ (time line no. 2) an even more rapid fall of the current is observed. The latter effect is caused by a voltage drop below the voltage threshold for the sustained HD discharge.[13]

It should be highlighted that due to the power supply overloading neither the voltage nor the current levels are stable. This complicates understanding and modeling of the discharge.

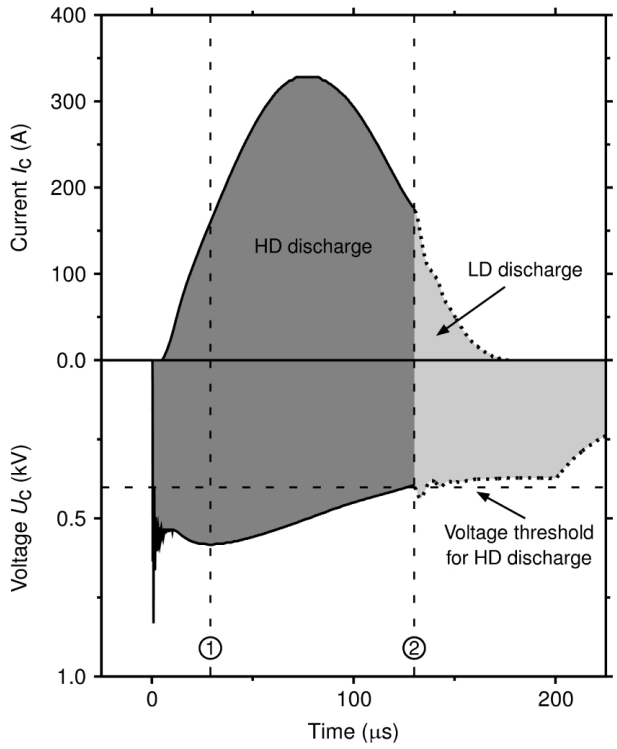

Figure A.4 Waveforms of the magnetron voltage U_c and the target current, I_c, for a Ti target. The line no. 1 denotes the time at which the pulse voltage starts to decrease because of insufficient charge stored in the pulse unit capacitors of the HiPIMS power supply. The line no. 2 represents the time at which the HD discharge is lost due to the drop of the voltage under a threshold for HD plasma.

A.3.2 Excessive arcing

The number and the energy of the emitted SE are very important discharge parameters. Furthermore, the production mechanism of the SE is crucial as well. A typical discharge in plasma processing is operated in a glow or an abnormal glow discharge regime where the SE are individually emitted by the impacting ions. However, the HiPIMS process is characterized by a high target ion current density, J_{ci}, that narrows the sheath thickness, x_c, accordingly to the Child's law. For instance, the collisionless Child's law results in a sheath thickness $x_{c,DCMS} = 300\,\mu m$ for a typical DCMS discharge ($J_{ci} = 50\,mA\,cm^{-2}$, $U_c = 0.3\,kV$) and $x_{c,HiPIMS} = 45\,\mu m$ for a typical HiPIMS discharge ($J_{ci} = 4\,A\,cm^{-2}$, $U_c = 0.6\,kV$) above a Nb target. The thinner sheath significantly increases the electrical field intensity, E, close to the target surface from $E_{DCMS} = 1.0 \times 10^6\,V\,m^{-1}$ to $E_{HiPIMS} = 1.3 \times 10^7\,V\,m^{-1}$. Such a rise in E may substantially enhance the probability of electron field emission at target

defects (i.e. grain boundaries, inclusions).[14] Hence, HiPIMS discharge is much more prone to a transition to the collective field and thermal electron emission regimes. In such a case, the large scale discharge collapses into a small cathodic spot through which a high current density may flow. The latter discharge is known as an arc.

Arcing during the deposition process is a serious issue. Despite the fact that arc handling is now a standard feature of commercial HiPIMS power supplies, there can be some residual energy in the discharge circuit even after the arc detection. This may lead to the ejection of macroparticles from the sputtered target, and thus to a possible deterioration of the coating quality.

A.3.3 Strong effect of target erosion

Figure A.5 shows the steady state current as a function of the pulse voltage for different erosion states (6 and 80 %) of a Nb target. Transition from the LD to the HD discharge is characterized by a jump in the current, and consequently by a change in the curve slope.[15, 16] Interestingly, a zero or even a negative slope can be observed during the HD discharge for some combinations of the magnetron's magnetic field configuration and the target material (see Fig. A.5). One possible explanation of the observed flattening of the I–V curve is a lower SE confinement by the magnetic field of the magnetron at elevated voltage values.[17, 15] As a result, a significant portion of these electrons will be lost without contributing to the plasma density. This effect may be further enhanced by an increased magnetic deconfinement due to the rise of the Hall current upon a transition from the LD to the HD regime.[18, 19]

This phenomenon is not a problem by itself, but it will negatively affect the long-term reproducibility (e.g. the constant deposition rate) of the deposition process. As illustrated in Figure A.5, the progressing target erosion can result in a substantial rise of the HD current level. In such a situation, it is impossible to reach the original (low level) current without a loss of the HD discharge. Consequently, the deposition conditions are irreversibly altered.

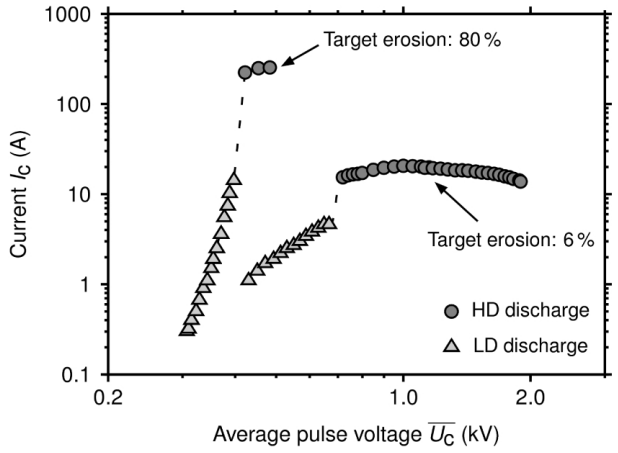

Figure A.5 Current–voltage characteristics corresponding to different erosion states (6 and 80 %) of the Nb target.

A.3.4 Possible solutions

The difficulties with the application and implementation of the HiPIMS described above indicate a need for process optimization. An adequate solution should permit: (i) to sustain the HD discharge during most of the duration of the HiPIMS pulse, (ii) to minimize arcing, and (iii) to enhance the process reproducibility.

A possible answer to the above requirements is the ability to adjust the current level during the HD discharge. This may be performed by modifying the magnetron's magnetic field by one of the following approaches: (i) use of a magnetron equipped by electromagnets,[10] (ii) replacement of the permanent magnets inside the magnetron,[20] (iii) application of an external magnetic field (i.e. additional coil[21] or permanent magnets[22]), or (iv) adjustment of the distance between the target surface and the permanent magnets.[23] In this work, we utilize the latter approach by inserting paramagnetic (copper) spacers of different thicknesses between the target and the magnetron head.

A.4 Optimization of the high density discharge

In this section we study the effect of target erosion on the HiPIMS discharge characteristics above a Nb target for the case when the HD current level is independent of the pulse voltage. We then demonstrate application of the copper spacers for the control of the mag-

netic field and the consequent steady state HD discharge optimization. Finally, we present model examples of the optimized HiPIMS discharge for Ta, Cr, Al, Ti, Si, and C targets.

A.4.1 Control of the HiPIMS discharge through the optimization of the magnetic field

The HiPIMS discharge characteristics in front of the Nb target depend on the level of target erosion and on the thickness of the inserted spacer. The distribution of the radial component, $|B_\rho|$, of the magnetic field around the Nb target at different stages of erosion is illustrated in Fig. A.6. The corresponding current waveforms for various preset voltages are shown in Figure A.7 (a – c).

For a low target erosion of 6 %, a radial magnetic field at the target surface $B_\rho = 550\,\mathrm{G}$ (Fig. A.6) and a racetrack area $A_\mathrm{r} = 9.3\,\mathrm{cm}^2$ lead to a typical LD discharge for pulse voltages $U_\mathrm{c} < U_\mathrm{th} = 0.7\,\mathrm{kV}$ [Fig. A.7 (a)]. Pulse voltages higher than this U_th threshold result in a steady state HD discharge at a maximum current value of approximately 20 A at $U_\mathrm{c} = 1\,\mathrm{kV}$. Surprisingly, the HD current does not rise even for very high voltages (e.g. $U_\mathrm{c} > 1\,\mathrm{kV}$). Instead, we observe a slow decrease of the steady state HD current level to 14 A at $U_\mathrm{c} = 2\,\mathrm{kV}$, such as previously illustrated in Fig. A.5. This behavior can probably be attributed to an enhanced energy of the SE at these voltages, as previously discussed in section A.3.3.

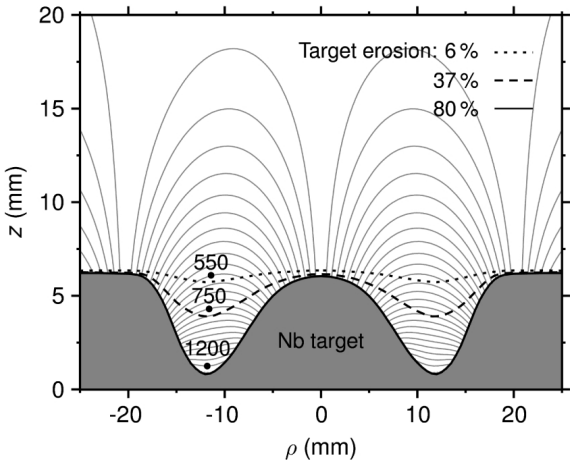

Figure A.6 Niobium target profiles at different erosion states (6, 37, and 80 %) presented together with the absolute values of the radial component $|B_\rho|$ of the magnetron's magnetic field (in Gauss).

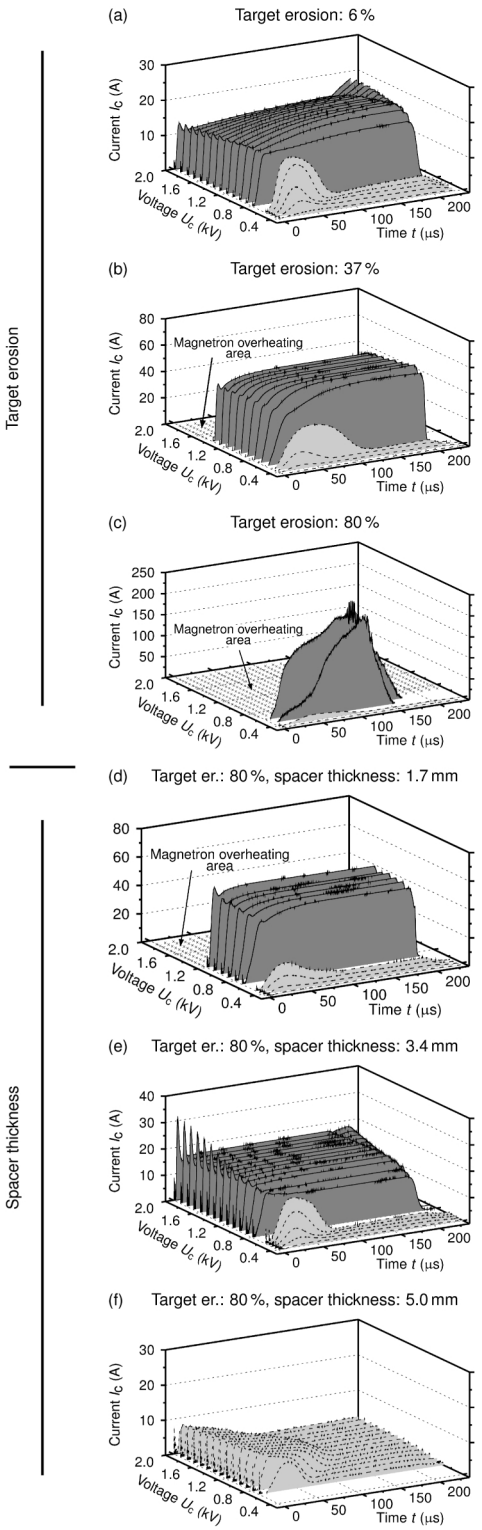

Figure A.7 Waveforms of the target current I_c as a function of a preset HiPIMS pulse voltage applied to a Nb target at different erosion states: 6 % (a), 37 % (b), and 80 % (c), and at 80 % of erosion state but for different thicknesses of spacers: 1.7 mm (d), 3.4 mm (e), and 5.0 mm (f).

The discharge behavior at a target erosion of 37 % [Fig. A.7 (b)] is similar to the previous case. Clearly, a stronger magnetic field $B_\rho = 750\,\mathrm{G}$ (Fig. A.6) and a larger surface of the racetrack $A_\mathrm{r} = 11.9\,\mathrm{cm}^2$ lead to a higher current level. For instance, the steady state value of the HD discharge current at $U_\mathrm{c} = 1.0\,\mathrm{kV}$ is 53 A in this case. Moreover, the HD plasma threshold U_th decreases from 0.7 to 0.6 kV. In these experiments, voltages higher than 1.4 kV cannot be used in order to avoid overheating the magnetron.

For a high target erosion of 80 % the magnetic field is about two times stronger ($B_\rho = 1200\,\mathrm{G}$ in Fig. A.6) and the surface area 50% larger ($A_\mathrm{r} = 15.1\,\mathrm{cm}^2$) as compared to a new target. These conditions lead to a low voltage threshold $U_\mathrm{th} = 0.5\,\mathrm{kV}$ and give rise to large HD current peaks reaching a maximum value of up to 215 A at $U_\mathrm{c} = 0.6\,\mathrm{kV}$ (the maximum voltage that can be applied without the magnetron overheating) [Fig. A.7 (c)]. These elevated discharge current values lead to power supply overloading and a higher probability of arc development (section A.3). It should also be mentioned that the HD current above a progressively eroded target may be affected by additional phenomena, such as possible change in the sputtered material angular distribution towards the substrate.[24, 25] However, this effect is beyond the scope of this paper.

Since the high density current is independent of the pulse voltage it is necessary to decrease the magnetic field strength in order to reproduce the desired steady state HD discharge. This has been accomplished by the introduction of a metallic (Cu) spacer in between the target and the magnetron that allows one to effectively compensate the effects of the stronger magnetic field and the larger surface area of the racetrack. As an example, the modification of the discharge characteristics for the highly eroded target (80 %) is demonstrated with the application of three different spacers with thicknesses $d_\mathrm{s} = 1.7$, 3.4, and 5.0 mm [Fig. A.7 (d)–(f)].

For $d_\mathrm{s} = 1.7$ and 3.4 mm, a stable HD discharge is obtained even for a highly eroded target. It should be stressed that the HD discharge currents for $d_\mathrm{s} = 3.4\,\mathrm{mm}$ are similar to the current levels obtained for a new or slightly eroded target. However, some minor differences in the shape of the current waveforms can be noted, particularly during the first 20 µs of the pulse. This effect may be explained by the modified surface and shape of the racetrack (erosion state 80 % vs 6 %), and the related gas dynamics. When the resulting magnetic field

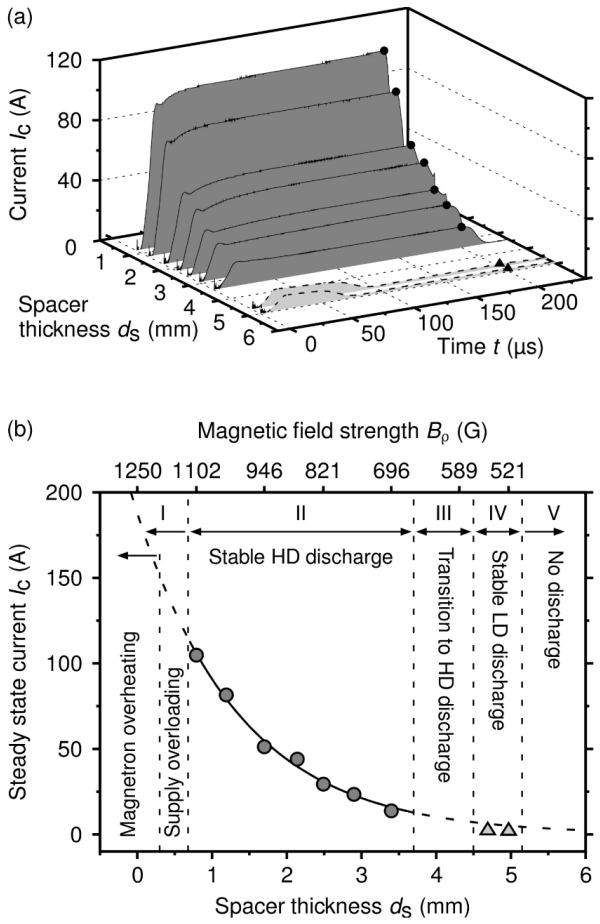

Figure A.8 Waveforms of the target current I_c at constant pulse voltage $U_c = 0.8\,\mathrm{kV}$ as a function of the copper spacer thickness d_s positioned in between the Nb target (80 % of target erosion) and the magnetron head (a). The corresponding steady state current values I_c [at $t = 200\,\mu\mathrm{s}$, as highlighted by solid symbols in (a)] are plotted as a function of the spacer thickness d_s, and various discharge modes are indicated (b).

is too weak (spacer thickness $d_s = 5.0\,\mathrm{mm}$) the transition to the HD discharge is inhibited due to a low SE confinement.

Figure A.8 shows the obtained steady state current for a fixed $U_c = 0.8\,\mathrm{kV}$ as a function of the magnetic field strength (spacer thickness). The decreasing current level illustrates the strong effect of the magnetic field on the HD discharge current [Fig. A.8 (a)]. Subsequently, different discharge regimes (e.g. “Stable HD discharge”, “Transition to LD discharge”, and “Stable LD discharge”) can be identified as illustrated in Fig. A.8 (b).

One can clearly see that the HD discharge current can be adjusted within a large range of values spanning from 105 A down to 14 A. This demonstrates the possibility to operate

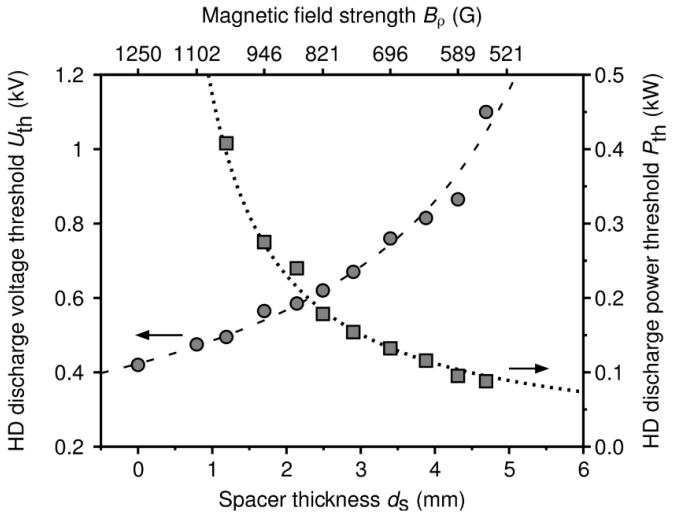

Figure A.9 Threshold U_{th} and corresponding minimum power P_{th} for the HD discharge as a function of the copper spacer thickness d_{s} positioned in between the Nb target (80 % of target erosion) and the magnetron head.

the HD discharge at low currents, and hence to eliminate and avoid the problems discussed in section A.3.

In addition, the voltage threshold U_{th} simultaneously increases with the decreasing magnetic field, such as demonstrated in Fig. A.9. Since the HD current (Fig. A.8) is more sensitive to the magnetic field strength alteration than is U_{th} (Fig. A.9), one has an option to effectively minimize the HD discharge power threshold, P_{th}, as well (see Fig. A.9). This feature allows one to avoid magnetron overheating at a given pulse length and repetition frequency.

A.4.2 Optimization of the HiPIMS discharge for various target materials

In the above section we have described the importance of the magnetic field on the steady state HD discharge for the specific case of a Nb target. In this section, we extend this work for the sputtering other target materials.

Figure A.10 shows current waveforms of the HD discharges operated above various target materials: Ta, Cr, Al, Ti, Si, and C ($\sim$ 5 % of target erosion) for which the HD discharge current was minimized through the control of the magnetic field. The shape of the corresponding current waveforms varies significantly from one material to another, which indicates differences in the discharge dynamics.

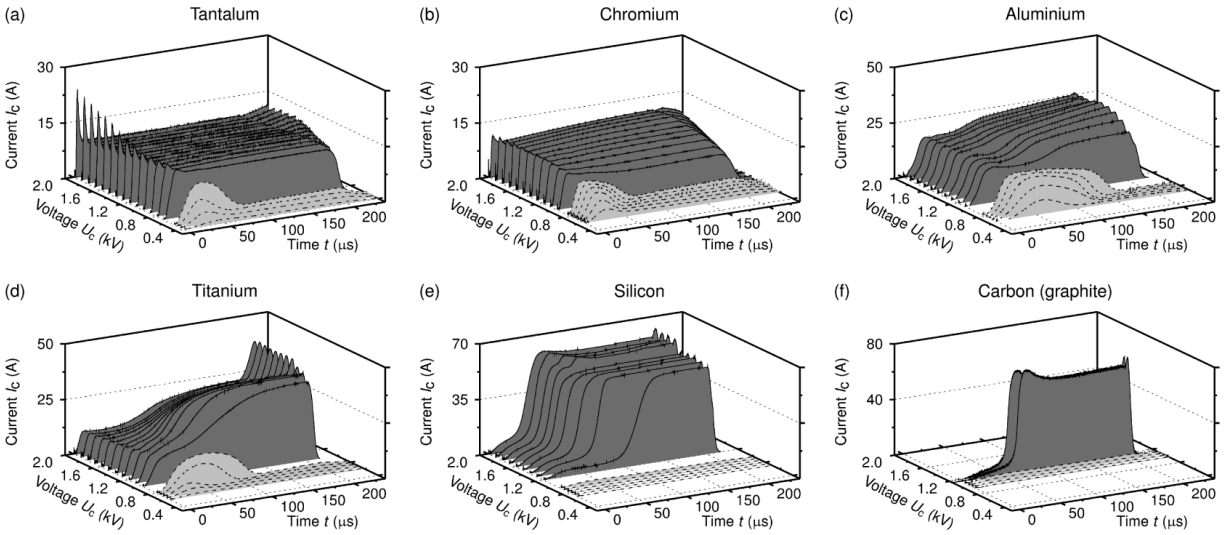

Figure A.10 Waveforms of the target current I_c as a function of the preset HiPIMS pulse voltage applied to different target materials: Ta (a), Cr (b), Al (c), Ti (d), Si (e), and C (f).

The rectangular-shape current waveforms of the discharges above the Ta and Cr targets [Fig. A.10 (a) and (b)] are very similar to those of the discharges above the Nb target [Fig. A.7 (a)]. In these three cases, the optimization process was fairly simple and often unnecessary; for instance, for a new target, for which the steady state HD discharge currents were already low (e.g., 20 A). In contrast, the HD discharge above the Al, and especially the Ti targets [Fig. A.10 (c) and (d)], requires a longer time ($\sim$ 100 µs) to stabilize and reach steady state conditions. Moreover, the discharge optimization was more difficult, i.e., the reached minimum HD currents were $\approx$ 25 A and $\approx$ 35 A for the Al and the Ti targets, respectively. Surprisingly, the discharges above the Si and even the C targets [Fig. A.10 (e) and (f)] were also operated in the steady state HD discharge, even though with a significant delay ($t \approx 50$ µs) of the HD current at the beginning of the pulse. In fact, for both of these materials, contrary to the previously discussed targets, it is essentially impossible to reach conditions for sustained self sputtering [Eq. (A.1)]. This is due to the low sputtering yield of these materials, for which $\gamma_{ss} = 0.71$ for Si and $\gamma_{ss} = 0.27$ for C targets at an ion energy of 1 keV.[26] Here, let us note that the optimization process of these two discharges was the most complicated and the least effective. Particularly, the C target required a very low magnetic field strength in order to avoid arc occurrences. Even then, the resulting minimum steady state HD current was still relatively high ($\approx$ 65 A).

A.5 High density discharge and gas rarefaction effect

In the previous section we have demonstrated the optimization of a steady state HiPIMS discharge through the control of the magnetic field for various target materials. In this section we discuss in more detail the importance of the magnetic field configuration and the gas rarefaction effect on the HD discharge current level.

In order to better understand the HD discharges operated above the C target, and the other target materials in general, the plasma composition was investigated using optical emission spectroscopy (OES). Figure A.11 shows the OES spectra recorded from the LD and HD discharges operated above Nb and C targets. The plasma emission is dominated by sputtered species in the case of Nb discharges. In addition, the HD spectra exhibit a substantially higher emission from the ionized Nb lines than the LD spectra, and also a much lower intensity of the Ar emission lines. This is a consequence of the significant Ar (39.95 amu) rarefaction by the high fluxes of heavy Nb atoms (92.91 amu), and of the self sputtering mechanism during which an important fraction of the sputtered material gets ionized.

In contrast, the spectra of the LD discharge above the C target exhibit only neutral Ar emission lines. The transition to the HD regime is then accompanied by a significant rise of the emission from the ionized Ar atoms. This observation provides evidence that Ar atoms play a dominant role in both LD and HD discharges. The above results can be interpreted by the low sputtering yield and the low mass of C atoms (12.01 amu) that result in a lower level of working gas rarefaction as compared to heavier elements with a high sputtering yield.[4] It should be noted that a similar observation of the dominant Ar ions emission was also detected in the steady state HiPIMS discharges operated above highly poisoned metal targets.[27]

Generally, a steady state discharge governed by Ar species can be described as follows:

$$\Pi_{\mathrm{g}} \equiv \gamma_{\mathrm{se}}\, \kappa_{\mathrm{e\text{-}g}}\, \beta_{\mathrm{g}} = 1, \tag{A.2}$$

where γ_{se} is the ion induced yield of SE, $\kappa_{\mathrm{e\text{-}g}}$ is the number of ionization collisions per one emitted SE, and β_{g} is the probability that the newly formed Ar ion is attracted towards the target. Since $\gamma_{\mathrm{se}} \approx 0.1$ (for metals[28]) and $\beta_{\mathrm{g}} < 1$, it is necessary that $\kappa_{\mathrm{e\text{-}g}} \approx 10$.

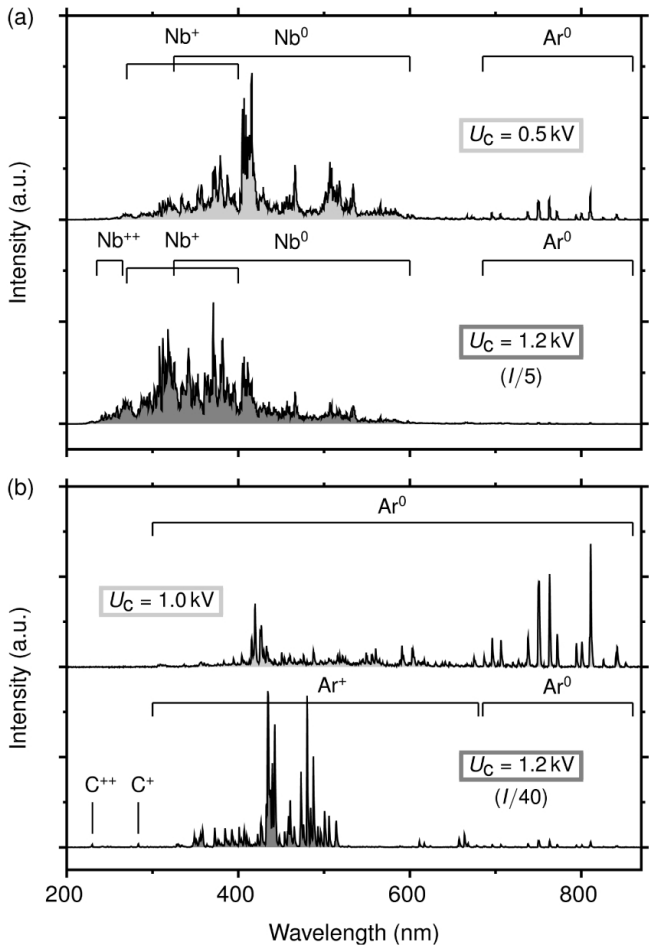

Figure A.11 Optical emission intensities from steady state LD (upper curves) and HD (lower curves) discharges operated above Nb (a) and C (b) targets. The optical emission probe was situated at $d = 1\,\mathrm{cm}$ from the target.

The quantity $\kappa_{\text{e-g}}$ can be further expressed in terms of specific discharge characteristics:

$$\kappa_{\text{e-g}} = n_{\text{g}}\ \sigma_{\text{e-g}}(E_{\text{e}})\ l(\mathbf{B}), \tag{A.3}$$

where n_{g} is the concentration of neutral Ar atoms close to the target surface, $\sigma_{\text{e-g}}$ is the cross section for ionization of the Ar atom by an impacting SE (function of the electron energy, E_{e}), and l is the length of a lifetime trajectory of a SE (function of the magnetic field $\mathbf{B}$). In principle, condition $\kappa_{\text{e-g}} \geq 10$ is not difficult to attain since l can be substantially increased by a suitable magnetic field configuration of the magnetron.[29] Nevertheless, the working gas rarefaction lowers n_{g} in front of the target. In addition, the discharge current reduces average l

due to the superimposed Hall current that modifies the magnetic field configuration[18, 19] in such a way that the most energetic electrons are no longer confined. As will be discussed below for the specific case of the HD discharges, these two effects limit the resulting steady state current. The transition from the LD to the HD discharge is governed by several phenomena, e.g. generation of multiply ionized gas atoms and/or gas recycling mechanism.[30]

It has already been discussed in section A.4.2 that the optimization (minimization) of the HD current through the control of the magnetic field was more difficult for some target materials. This observation indicates that the effect of the magnetic field on the SE confinement is accompanied by another important effect that influences the final value of the steady state HD current. The latter phenomenon can be related to the atomic mass and sputtering yield of the target material, which are, in fact, the two fundamental parameters in Ar gas rarefaction by the flux of sputtered material. In order to illustrate this assumption, the minimized steady state HD current was plotted in Fig. A.12 as a function of the normalized Ar gas density, K, which is defined as

$$K = \frac{n_{\mathrm{r}}}{n_0}, \tag{A.4}$$

where n_{r} is the reduced density of gas atoms close to the target surface, and n_0 is the density of gas atoms close to the wall of the system. The former quantity was calculated according to the model of Rossnagel,[4] as specified in detail in Appendix AB.

The HD discharge current is largely affected by n_{r}, mainly due to the substantially higher coefficient of SE emission of Ar ions, as compared to the majority of the sputtered material ions.[8] This means that a higher value of n_{r}, and a consequent higher working gas ionization, result in an elevated discharge current. The correlation of the HD current level and of n_{r} (illustrated in Fig. A.12) can thus be interpreted by the Ar gas rarefaction effect: For low values of K (< 0.07), the Ar gas is highly diluted by the flux of the sputtered material, and an almost pure self sputtering discharge can be reached (Nb, Ta). When K is increased, the contribution of Ar ions to the resulting current is more significant, and the sputtering mechanism of the HD discharge is gradually transformed from the self sputtering mode to the gas sputtering mode (Si, C). This observation confirms that Ar gas rarefaction by the sputtered particles is

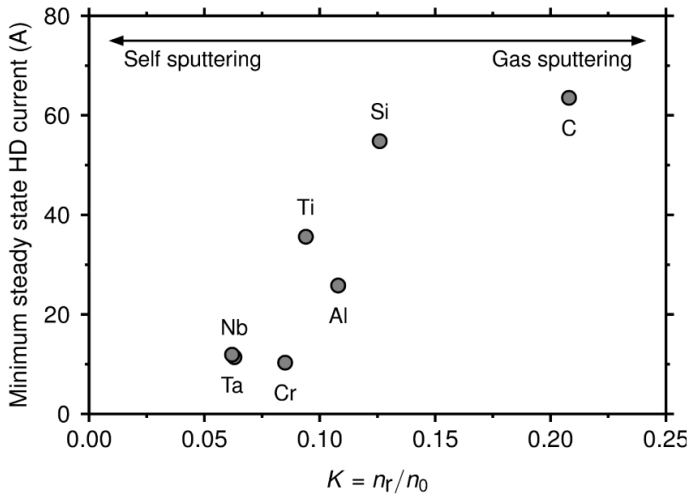

Figure A.12 Minimized steady state HD current at $U_c = 1.2\,\mathrm{kV}$ as a function of the normalized density of the Ar gas in front of the target by sputtered particles of various materials (Ta, Nb, Cr, Al, Ti, Si, and C). The prevalent sputtering mechanisms are indicated.

an important material-dependent phenomenon which governs the HD current level. It should be also noted that an elevated target surface temperature during the high power pulse may also cause the Ar gas density rarefaction.[5] Nevertheless, this effect was neglected during the presented calculation of the reduced Ar gas density.

It has been already mentioned in Section A.1 that in the HD discharge a portion of the sputtered target atoms is ionized, attracted back to the target, and they eventually (if their potential energy is sufficiently high[8]) produce SE as well. Hence, the decrease in the SE production by the bombarding Ar ions can be partially or even completely compensated by the back-attracted ions, especially for the high sputtering yield target materials. Consequently, the measured HD current may be higher than the predicted theoretical value corresponding to the Ar ion fluxes.[6]

In a general case, the contribution of both gas sputtering and self sputtering mechanisms to the resulting HD discharge should be considered. Therefore, the condition for the steady state HD discharge dominated by Ar ions (Eq. A.2) is not complete by itself, and it should be combined with the condition for the self sputtering mode (Eq. A.1). In complement to our present work, a general criterion for a transition from the LD to the HD discharge is presented and discussed in more detail in a separate publication.[30]

A.6 Summary and Conclusions

In this paper, we discussed the concept of the optimization of HiPIMS discharges operated above different elemental targets [Ta, Nb, Cr, Al, Ti, Si, and C (graphite)]. First, we described various problems related to the HiPIMS discharge implementation in the deposition systems, such as (i) HiPIMS power supply overloading, (ii) excessive arcing, and (iii) strong effect of target erosion. Second, we proposed a simple approach for the HiPIMS discharge optimization based on the application of copper (paramagnetic) spacers in between the magnetron and the target. This technique was demonstrated by an example of the HD discharge above a 80 % eroded Nb target; It was shown that the level of the steady state HD current can be controlled in a large range of 14 – 105 A. Furthermore, we have shown successful stabilization of the HD mode at the lowest accessible discharge current for different materials, including Si and C. The observation of a steady high current level above the C target, supported by optical emission spectroscopy monitoring, indicated the dominant role of Ar ions in HD discharges above low yield target materials. Finally, we offered a correlation between the gas rarefaction effect and the HD discharge current value.

Acknowledgments

The authors wish to thank Mr. Francis Turcot and Mr. Sébastien Chenard for their expert technical assistance. The financial support of NSERC of Canada within the CRDPJ 38074-08 project is gratefully acknowledged.

REFERENCES

[1] K. Sarakinos, J. Alami., and S. Konstantinidis, Surf. Coat. Technol. **204**, 1661 (2010).

[2] A. Ehiasarian, "Plasma surface engineering research and its practical applications," (Kerala, India, 2008) Chap. Fundamentals and applications of HIPIMS, p. 35.

[3] A. Anders, J. Andersson, and A. Ehiasarian, J. Appl. Phys. **102**, 113303 (2007).

[4] S. Rossnagel, J. Vac. Sci. Technol. A **6**, 19 (1988).

[5] A. Anders, Surf. Coat. Technol. **205**, S1 (2011).

[6] S. Rossnagel, J. Vac. Sci. Technol. A **6**, 223 (1988).

[7] J. Vlček and K. Burcalová, Plasma Sources Sci. Technol. **19**, 065010 (2010).

[8] A. Anders, Appl. Phys. Lett. **92**, 201501 (2008).

[9] W. Posadowski and Z. Radzimski, J. Vac. Sci. Technol. A **11**, 2980 (1993).

[10] S. Kadlec and J. Musil, Vacuum **47**, 307 (1996).

[11] J. Andersson and A. Anders, Appl. Phys. Lett. **92**, 221503 (2008).

[12] N. Hosokawa, T. Tsukada, and H. Kitahara, Proceedings of the Eighth International Vacuum Congress, Le Vide, Cannes, France, 11(1980).

[13] M. Hála, N. Viau, O. Zabeida, J. Klemberg-Sapieha, and L. Martinu, J. Appl. Phys. **107**, 043305 (2010).

[14] A. Anders, Thin Solid Films **502**, 22 (2006).

[15] A. Ehiasarian, R. New, W.-D. Münz, L. Hultman, U. Helmersson, and V. Kouznetsov, Vacuum **65**, 147 (2002).

[16] J. Alami, K. Sarakinos, G. Mark, and M. Wuttig, Appl. Phys. Lett. **89**, 154104 (2006).

[17] J. Thornton, J. Vac. Sci. Technol. **15**, 171 (1978).

[18] J. Bohlmark, U. Helmersson, M. VanZeeland, I. Axnäs, J. Alami, and N. Brenning, Plasma Sources Sci. Technol. **13**, 654 (2004).

[19] S. Abolmasov and A. Bizyukov, IEEE Trans. Plasma Sci. **33**, 1447 (2005).

[20] J. Sags, L. Fontana, and H. Maciel, Vacuum **85**, 705 (2011).

[21] I. Ivanov, P. Kazansky, L. Hultman, I. Petrov, and J.-E. Sundgren, J. Vac. Sci. Technol. A **12**, 314 (1994).

[22] J. Musil, K. Rusňák, V. Ježek, and J. Vlček, Vacuum **46**, 341 (1995).

[23] T. Nakamura, S. Kato, and H. Nishiyama, "Magnetron sputtering apparatus," (1982), US patent US4309266.

[24] G. Turner, S. Rossnagel, and J. Cuomo, J. Appl. Phys. **75**, 3611 (1994).

[25] W. Westwood, *Sputter deposition* (AVS, 2003) p. 116.

[26] W. Eckstein, *Sputtering by Particle Bombardment*, Vol. 110 (Springer Berlin / Heidelberg, 2007) pp. 33–187.

[27] M. Hála, J. Čapek, O. Zabeida, J. Klemberg-Sapieha, and L. Martinu, accepted for publication in J. Phys. D (2011).

[28] D. Depla, S. Heirwegh, S. Mahieu, J. Haemers, and R. D. Gryse, J. Appl. Phys. **101**, 013301 (2007).

[29] T. Sheridan, M. Goeckner, and J. Goree, J. Vac. Sci. Technol. A **8**, 30 (1990).

[30] A. Anders, J. Čapek, M. Hála, and L. Martinu, J. Phys. D **45**, 012003 (2012).

[31] D. Meeker, *computer program: Finite Element Method Magnetics 4.2* (2009).

[32] I. Svadkovski, D. Golosov, and S. Zavatskiy, Vacuum **68**, 283 (2003).

[33] E. Clementi, D. Raimondi, and W. Reinhardt, J. Chem. Phys. **47**, 1300 (1967).

[34] J. Ziegler, J. Biersack, and M. Ziegler, *computer program: TRIM-2011* (2011).

Appendix AA Assessment of the magnetic field in front of the target

The axial (B_z) and radial (B_ρ) components of the magnetic field **B** (Fig. A.3) were measured in the central plane in front of the magnetron head assuming that the magnetic field is axisymmetrical. The magnetron magnetic field was also simulated by using the finite element software package FEMM[31] and the resulting map was fitted to the experimental data of **B**. This approach enables one to calculate the magnetic vector potential, **A**, defined as:

$$\mathbf{B} = \nabla \times \mathbf{A} \tag{A.5}$$

and consequently, the magnetic field in an arbitrary point. In the general 3D case, **A** is a vector with three components. However, in the 2D planar and axisymmetric case, two of these three components are zero, leaving just one none-zero component in the "out of the page" direction. In such case, magnetic field lines can be plotted as contours of the magnetic potential A or of the quantity, A^*, where:

$$A^* = \frac{A}{\sqrt{|A|}} \tag{A.6}$$

for a more detailed representation of a decaying magnetic field (e.g. close to the substrate holder).

The maximum radial magnetic field component B_ρ at the surface of a new 6.35 mm thick target reached a value of 550 G at a distance of 12.0 mm from the center, and the axial component B_z changed its direction at a distance $Z_0 = 13.1$ mm from the target surface. The level of unbalancing of the magnetron's magnetic field can be expressed by the unbalance coefficient, K, of the magnetron[32], defined as:

$$K = \frac{\Phi_o}{\Phi_i}, \tag{A.7}$$

where Φ_i and Φ_o denote magnetic fluxes from the inner and outer magnets on the target surface. In our case $K = 4.8$, while $K = 1$ for a perfectly balanced magnetron.

Appendix AB Determination of gas atom density close to the target surface

According to the model of Rossnagel,[4] the reduced Ar gas density n_r in front of the target caused by the flux of the sputtered material can be expressed as a function of the HD discharge current I_c as

$$n_\mathrm{r} = \frac{-T_0 + (T_0^2 + \beta I_\mathrm{c})^{1/2}}{\gamma I_\mathrm{c}}, \tag{A.8}$$

where

$$\beta = \frac{\overline{E_\mathrm{a}} Y \sigma n_0 T_0}{\pi K_\mathrm{g} f e} \tag{A.9}$$

and

$$\gamma = \frac{\overline{E_\mathrm{a}} Y \sigma}{2\pi K_\mathrm{g} f e}. \tag{A.10}$$

Here, n_0 and T_0 are the gas concentration and the gas temperature close to the chamber wall, $\overline{E_\mathrm{a}}$ is the average energy of the sputtered particles, Y is the sputtering yield, σ is the collision cross section for momentum transfer, e is the elementary charge, K_g is the thermal conductivity of the gas, and f is a constant.

In order to calculate n_r from Eq. (A.8), the steady state HD current value corresponding to $U_\mathrm{c} = 1.2\,\mathrm{kV}$ was used as an input parameter for the investigated target materials. A simplified assumption was used that the sputtering process is performed only by Ar ions. Furthermore, the cross section for momentum transfer σ was estimated by considering the "hard-sphere model" as

$$\sigma = \pi(a_\mathrm{s} + a_\mathrm{g})^2, \tag{A.11}$$

where a_s and a_g are atomic diameters of sputtered and gas particles.[33] The sputtering yield Y and the average energy of sputtered atoms $\overline{E_\mathrm{a}}$ were calculated using the TRIM computer program.[34] The value of the constant f was supposed to be 3, the wall temperature was 300 K, the thermal conductivity of Ar gas K_g was $1.79\times10^{-2}\,\mathrm{W\,K^{-1}\,m^{-1}}$, and the pressure was 1 Pa.